JULY–SEPTEMBER 2024 VOL. 16 № 3 (62)

ISSN 2075-8251

ActaNaturae

Genome Characterization of Two Novel *Lactococcus lactis* Phages vL_296 and vL_20A

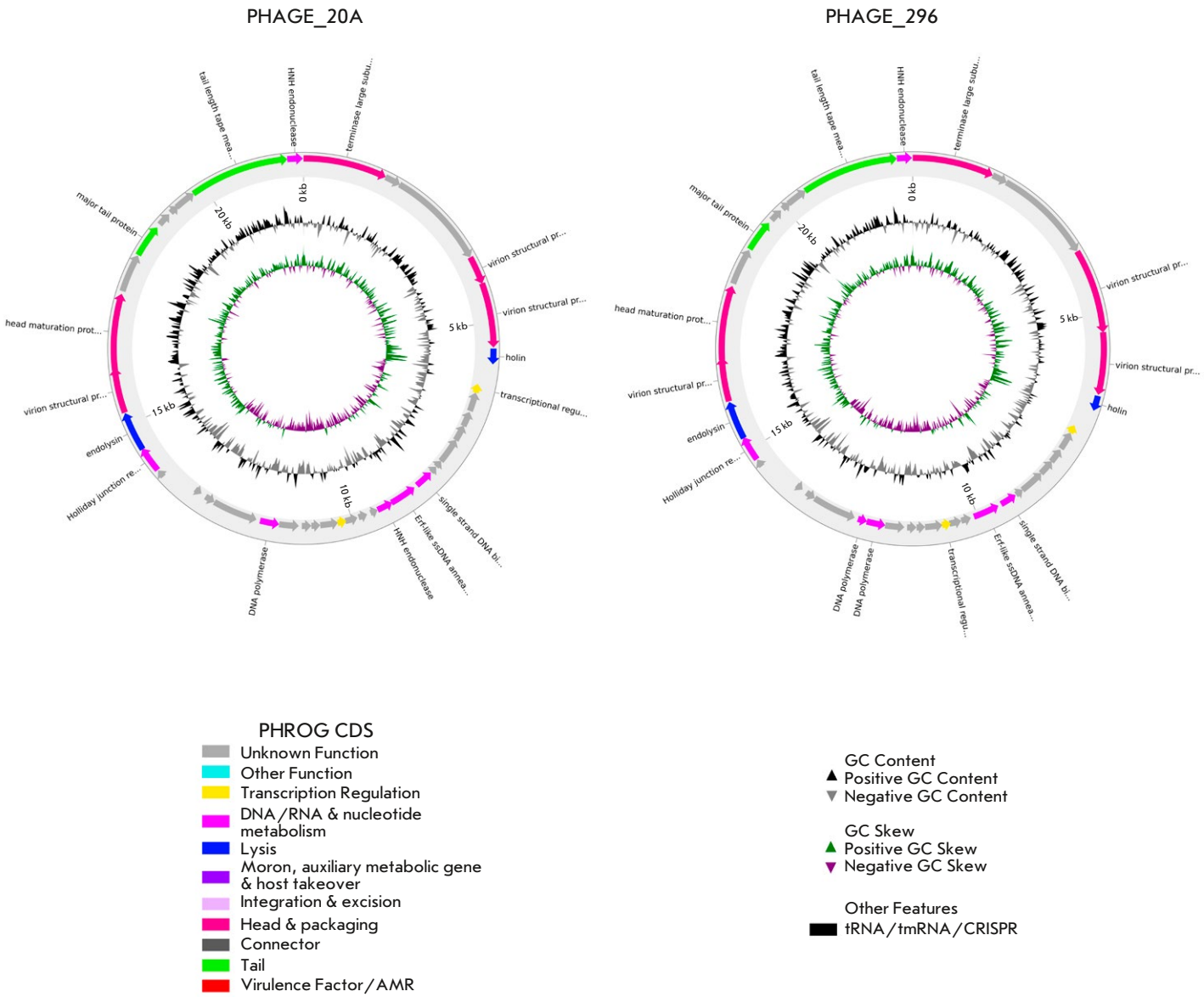

Specific Activation of the Expression of Growth Factor Genes in Expi293F Human Cells Using CRISPR/Cas9-SAM Technology Increases Their Proliferation

P. A. Bobrovsky, E. N. Grafskaia, D. D. Kharlampieva, V. A. Manuvera, V. N. Lazarev

Human cell lines play an important role in biotechnology and pharmacology. For them to grow, they need complex nutrient media containing signaling proteins — growth factors. Authors have tested a new approach that reduces the need for cultured human cell lines for exogenous growth factors. This approach is based on the generation of a modified cell with a selectively activated gene expression of one of the endogenous growth factors: IGF-1, FGF-2, or EIF3I. We modified the Expi293F cell line, a HEK293 cell line variant widely used in the production of recombinant proteins. Gene expression of the selected growth factors in these cells was activated using CRISPR/Cas9 technology with the synergistic activation mediators CRISPR/Cas9-SAM, which increased the expression of the selected genes at both mRNA and protein levels. Upon culturing under standard conditions, the modified lines exhibited increased proliferation. A synergistic effect was observed in co-culture of the three modified lines. In our opinion, these results indicate that this approach is promising for efficient modification of cell lines used in biotechnology.

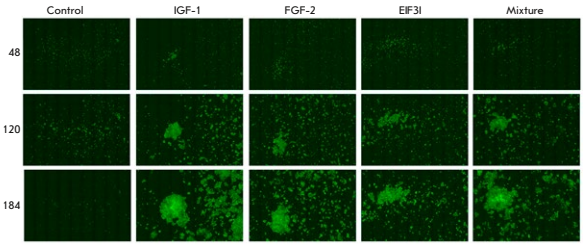

Comparison of the growth of modified cells expressing IGF-1, FGF-2, and EIF3I growth factor genes

Insights into the Functioning of the D-amino Acid Transaminase from *Haliscomenobacter Hydrossis* via a Structural and Spectral Analysis of its Complex with 3-Aminooxypropionic Acid

A. K. Bakunova, I. O. Matyuta, A. Yu. Nikolaeva, K. M. Boyko, A. R. Khomutov, E. Yu. Bezsudnova, V. O. Popov

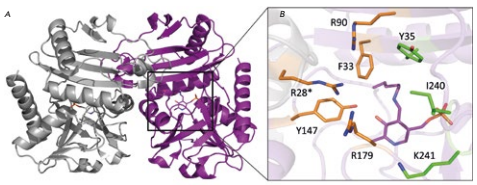

The overall structure of TA_Halhy. (*A*) Ta_Halhy homodimer; (*B*) active site of TA_Halhy

O-substituted hydroxylamines mimic the side group of amino acid substrates, thus providing highly potent and specific inhibition of the corresponding enzymes. The interaction between D-amino acid transaminase from bacterium *Haliscomenobacter hydrossis* and 3-aminooxypropionic acid was studied in the present work. The structural and spectral analysis of the complex of this transaminase with 3-aminooxypropionic acid allowed us to clarify some features of the organization and functioning of its active site and illustrate one of the mechanisms of inhibition by the specific substrate, D-glutamic acid.

Cannula Implantation Reduces the Severity of the Beta Amyloid Effect on Peroxidized Lipids and Glutathione Levels in the Brain of BALB/c Mice

K. A. Mukhina, V. A. Mitkevich, I. Yu. Popova

Sporadic Alzheimer's disease (sAD) is the most common of neurodegenerative disorders. The lack of effective therapy indicates that the mechanisms of sAD development remain poorly understood. To investigate this pathology in animals, intracerebroventricular injection of β-amyloid peptide (Aβ) using a Hamilton syringe, either during stereotactic surgery or through a pre-implanted cannula, is used. In this study, authors analyzed the effect of chronic cannula implantation on the severity of Aβ effects at the behavioral, histological, and biochemical levels. The obtained data indicate that chronic implantation of a cannula into the brain of experimental animals fundamentally distorts some parameters of oxidative stress in the neural tissue, which are widely used to assess the severity of experimental Alzheimer's-type diseases.

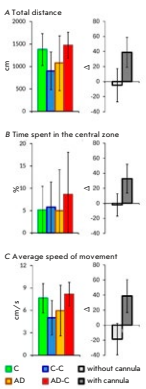

Behavioral analysis in experimental animals using the Open Field test

ActaNaturae
JULY–SEPTEMBER 2024 VOL. 16 № 3 (62)
since april 2009, 4 times a year

Founders
Acta Naturae, Ltd,
National Research University
Higher School of Economics

Adress: 101000, Moscow, Myasnitskaya Ulitsa, 13, str. 4
Phone/Fax: +7 (495) 727 38 60
E-mail: actanaturae@gmail.com

Номер подписан в печать 30 сентября 2024 г.
Тираж 15 экз. Цена свободная.
Отпечатано в типографии: НИУ ВШЭ,
г. Москва, Измайловское шоссе, 44, стр. 2

Founder and Chairman
of the Editorial Board (from 2009 to 2023)
of the journal Acta Naturae
Academician Grigoriev Anatoly Ivanovich

Indexed in PubMed, Web of Science, Scopus, and RISC

Impact Factor: 2.0 (WOS); 3.5 (Scopus)

CONTENTS

IMAGE ON THE COVER PAGE

(see the article by Chuksina et al.)

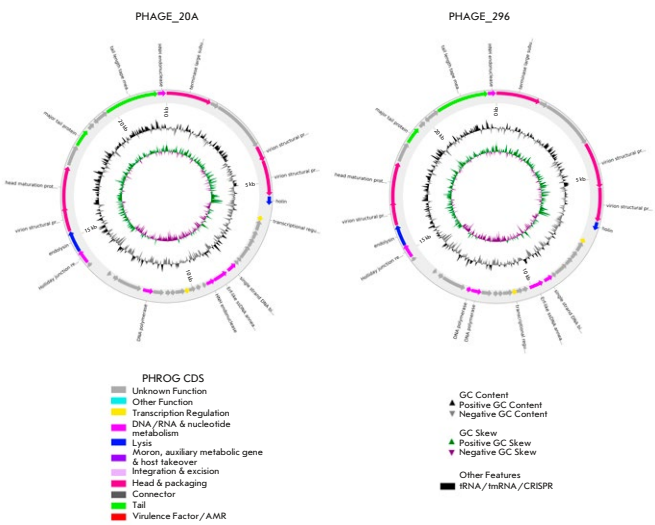

Evolutionary Perspectives on Human-Artificial Intelligence Convergence

B. L. Zybailov[1], G. Yu. Kosovsky[2], G. V. Glazko[3], V. I. Glazko[2], O. I. Skobel[2]*
[1]University of Arkansas for Medical Sciences, Department of Biochemistry and Molecular Biology, Little Rock, AR,72205 USA
[2]FSBSI V.A. Afanasyev RI for Fur and Rabbit Farming, Moscow region, Ramen's district, Rodniki, 140143 Russian Federation
[3]University of Arkansas for Medical Sciences, Department of Biomedical Informatics, Little Rock, AR, 72205 USA
*E-mail: skobelolga@gmail.com
Received April 21, 2024; in final form, September 26, 2024
DOI: 10.32607/actanaturae.27406

ABSTRACT **In this analytical review, we explore the potential impact of the rapid proliferation of artificial intelligence (AI) tools on the biosphere and noosphere, suggesting that the trend may lead to a transformative event that could be termed "Human-AI integration." We argue that this integration could give rise to novel lifeforms, associations, and hierarchies, resulting in competitive advantages and increased complexity of structural organizations within both the biosphere and noosphere. Our central premise emphasizes the importance of human-AI integration as a global adaptive response crucial for our civilization's survival amidst a rapidly changing environment. The convergence may initially manifest itself through symbiotic, endosymbiotic, or other mutualistic relationships, such as domestication, contingent on the rate at which AI systems achieve autonomy and develop survival instincts akin to those of biological organisms. We investigate potential drivers of these scenarios, addressing the ethical and existential challenges arising from the AI-driven transformation of the biosphere and noosphere, and considering potential trade-offs. Additionally, we discuss the application of complexity and the balance between competition and cooperation to better comprehend and navigate these transformative scenarios.**
KEYWORDS **Human-AI integration, biosphere, noosphere, artificial intelligence, systems evolution, endosymbiosis, symbiosis.**
ABBREVIATIONS **ADHD – attention deficit hyperactivity disorder; AI – artificial intelligence; BCI – brain-computer interface; DL – deep learning; GAN – generative adversarial network; JAIC – Joint Artificial Intelligence Center; ML – machine learning; R&D – research and development.**

INTRODUCTION

Recently, artificial intelligence (AI) has been attracting significant public attention as a relatively new concept. The Russian Association of Artificial Intelligence (RAII), which is now operational, was established in 1992. The national Russian standard for AI definition, GOST R ISO/IEC 24668-2022 "Information Technologies. Artificial intelligence. Process management framework for big data analytics," was approved and put into practice by the Federal Agency for Technical Regulation and Metrology on November 8, 2022, No. 1258-st. This order is identical to the international standard ISO/IEC 24668:2022 "Information technology – Artificial intelligence – Process management framework for big data analytics."

The growing public awareness of AI-related issues has triggered debate regarding the dangers and unlimited possibilities of the technology's current state of development. From the perspective of biologists, AI is considered to be just a quite recent tool for adjusting to our shifting environment, with its own development history and phases based, like the earlier ones, on attempts to find certain natural regularities and practical applications for imitating them. In general, it can be compared to the formation of an artificial human habitat to

guard against unfavorable environmental factors and improve chances of survival. This is one of the stages of 'maturation' of the noosphere, or the collective mind of humans as a species, as described by V.I. Vernadsky, which is crucial when human activity and population growth are clearly in tension with the stability of the biosphere [1].

Any new tool includes risks in addition to its obvious benefits. In this review, the potential origins of such dangers are considered from the perspective of evolutionary regularities such as the increasing complexity of biological systems and the waves of differentiation and cooperation that follow.

Biotechnology and biological systems are defined by the FAO (Food and Agriculture Organization, fao.org) as living organisms and products of their vital activity. The latter undoubtedly includes AI. From the perspective of biologists, living organisms are systems with dynamic entropy control mechanisms. We anticipate that this approach may be helpful in assessing the possible dangers of applying aspects of AI, such as AI-human interaction for medical or other uses.

METHOD

This study attempts to synthesize traditional perspectives on key evolutionary stages in the progression of modern civilization, encompassing the genesis of the technosphere, the advancement of high-speed communication, the rapid dissemination of AI technologies, and the conceptualization of the noosphere as an adaptive mechanism critical to human survival during the Anthropocene – a new geological epoch. The compilation of the essay was aided in part by ChatGPT 3.5/4.0, a state-of-the-art artificial intelligence language model developed by OpenAI. ChatGPT aided in selecting and analyzing literary sources pertaining to the noosphere, artificial intelligence, domestication, symbiosis, and endosymbiosis while concurrently organizing the presented information. In our hands, ChatGPT often struggled with structure and coherence when supplied with larger inputs and worked best when it was applied to shorter paragraphs and sentences. While the survey and evaluation of the current AI tools are beyond this article's scope, we anticipate that it will become progressively harder to distinguish between average expert-written and AI-written perspectives/reviews by the time of the publication of this article. We, therefore, suggest that journals and organizations must quickly enact clear policies and institute relevant disclosure protocols pertaining to the reliance on such AI tools. Such disclosure requirements would further benefit AI research by facilitating monitoring of how AI-generated content proliferates within the noosphere and evolves in quality and novelty.

Vernadsky and de Chardin's perspectives

The concepts of biosphere and noosphere were formulated by Vladimir Vernadsky, who asserted that the biosphere functions as a zone wherein cosmic radiation is transformed into various forms of terrestrial energy, such as electrical, chemical, mechanical, and thermal [1]. He argued that humans, along with all living organisms and matter, are an integral component of the cosmos, rather than an isolated or accidental natural phenomenon. In Vernadsky's view, humans are an inevitable expression of a natural law resulting from an ongoing process spanning billions of years. In a similar vein, French philosopher and Jesuit priest Teilhard de Chardin developed a complementary view of the noosphere, as a layer of consciousness enveloping the Earth [2]. This idea aligns with Vernadsky's theories, as it emphasizes the significant role that human thought and collective consciousness play in shaping the biosphere and Earth's evolution. However, de Chardin presented a more teleological perspective, positing that the noosphere's evolution and human consciousness are directed towards a final state or ultimate goal, which he termed the "Omega Point" [2]. Expanding upon these foundational ideas, contemporary scholars such as Ray Kurzweil and Frank Tipler have further developed futuristic and transhumanist perspectives on the noosphere and its potential ramifications [3, 4]. These authors have popularized the notion that the advancement of artificial intelligence (AI) and other cutting-edge technologies may precipitate substantial transformations in human society and our understanding of the cosmos. These concepts possess a geological origin, implying that when we identify a "sphere," we recognize a geological force operating on a global scale. In this context, it is essential to discuss the Holocene and the Anthropocene epochs, as these periods provide insights into the ramifications of the emergence of human technological civilization on a planetary level.

THE HOLOCENE AND THE ANTHROPOCENE

The Holocene epoch, which began approximately 12,000 years ago, is characterized by a relatively stable climate that has allowed for the development of human civilization [5]. On the other hand, the Anthropocene, a proposed but not yet formally accepted geological epoch, is defined by the significant global impact of human activities on Earth's ecosystems and geological processes [6, 7]. The

Anthropocene represents a new geological period in Earth's development, during which human activities have become the primary geological factor. Available data suggest that the period between the 17th and end of the 20th centuries appears to meet the criteria for defining the onset of the Anthropocene, as it is associated with fundamental changes in the relationship between humans and the Earth's systems and the formation of the technosphere [8].

The concept of the Anthropocene underscores the substantial influence of human actions on the planet, marking a critical juncture in the relationship between humans and the Earth's biosphere.

In his seminal works, Vernadsky (2004) insisted that ecological crises, directly associated with human activities, have occurred on numerous occasions throughout history. Until recently, relatively undisturbed natural ecosystems comprised approximately 12% of the Earth's surface. However, in contemporary times, they encompass a mere 1.4% [9]. Present-day research posits that the mass extinction of megafauna (animal species with a mass exceeding 10 kg) during the Quaternary period of the Cenozoic era is attributable to the activities of humans, who have emerged as the primary driving force behind the global decline of megafauna throughout the late Quaternary period [10].

The confrontation with natural ecosystems began approximately 1.5–3 million years ago, when humans first harnessed fire. Today, the destruction of natural ecosystems, particularly forest ecosystems, exacerbated by economic globalization, has become a leading factor in global ecological changes [11].

The technosphere and its environmental impact

The technosphere encompasses all human-made technologies and their impact on the environment. As the technosphere evolves, we witness an acceleration in the complexity of technologies and their integration into human life [12]. Major stages in the development of the technosphere include the invention of simple tools, the industrial revolution [13], and the emergence of information technologies [14]. Consequently, the technosphere becomes increasingly intertwined with the biosphere and noosphere, influencing the development of humanity and the environment.

Vernadsky (1991) argued that the development of the biosphere, the appearance of humans, and the establishment of an agrarian civilization emerged as evolutionary outcomes [15]. With the appearance of agrarian civilization centers, humans have progressively become the dominant geological agent in reshaping the planet. Vernadsky posited that the persistence of the biosphere, encompassing humans as a species, is contingent upon the emergence of the noosphere, which primarily functions to regulate the stability of the biosphere. This transformation is considered a plausible consequence of natural evolution, as Vernadsky (1991) observed that "the biosphere is transitioning, or rather, undergoing a metamorphosis into a novel evolutionary state – the noosphere – refined by the scientific thought of social humans."

The significance of the noosphere's development and anticipated transformation as a response to various looming crises is supported by an abundance of contemporary data. Food security is becoming increasingly an issue due to the rising global population, expanding urbanization, and the ongoing impact of climate change. Roughly 9% of the global population is currently undernourished, and it is projected that by 2030, this figure will increase to 9.8%; at that time, more than 850 million individuals will experience hunger [16]. Moreover, agricultural practices and agrarian civilization have reached the threshold of extensive development, occupying 38% of the Earth's surface, utilizing approximately 70% of global freshwater reserves, and 1.2% of worldwide energy [17].

In recent times, the dynamics and attributes of agrarian civilization development have become particularly noteworthy. A striking illustration is information on megafauna biomass fluctuations following the Earth's last major extinction event, which led to the demise of two-thirds of mammalian genera and half of such species between 50,000 and 3,000 years ago [18]. Following this disaster, the global ecosystem gradually recuperated into a novel state, before the accumulation rate of biomass surged considerably compared to the pre-Industrial Revolution baseline, primarily attributable to agricultural animal species. After the worldwide decline in megafauna's biomass, an augmented growth rate has been observed solely in *Homo sapiens*.

Humans's dominance and the survival of the biosphere

In essence, the megafauna's landscape is witnessing a gradual dominance of humans and agricultural animal species, with wild species being displaced. Humans have continued to consistently domesticate a wider array of species spanning all kingdoms and classes, from fungi to humans, adapting to environmental shifts. This process entails the incorporation of nearly all biospheric elements into the human niche and exploiting species amenable to do-

mestication while displacing others. Historical observations reveal that this progression heightens the risk of accelerated biosphere degradation, potentially threatening human existence. As a consequence, Vernadsky's position that the biosphere's survival hinges on the natural transformation of human activity into the noosphere finds contemporary validation. It is crucial to investigate the intricate, evolving interrelationships between the biosphere, technosphere, and noosphere, as well as their implications for humanity's future. Within these interconnections, the integration of technology, particularly artificial intelligence, into human activity emerges as a vital aspect of the noosphere's ongoing development. This perspective draws parallels with endosymbiosis [19] and domestication [20].

Biosphere, technosphere, and noosphere: distinct domains with interconnected evolution

In this study, we posit that the technosphere, which encompasses all human-made technologies and their environmental impact, evolves in complexity concurrently with the biosphere and noosphere – the domains of life and human cognition, respectively. The noosphere, characterized by human thought and collective consciousness, currently relies on the technosphere for communication, information exchange, and innovation across the globe. Conversely, the technosphere depends on the noosphere for its development, as human ideas and knowledge fuel technological advancements. Despite their interconnectedness, it is essential to consider the noosphere and technosphere as distinct entities due to their unique characteristics and evolutionary paths: the noosphere is primarily driven by intellectual and cultural progress, while the technosphere is molded by material and technological innovations.

These interconnected spheres progress through various stages of development, such as the industrial revolution, the emergence of scientific knowledge, and the advent of artificial intelligence. By examining their evolution, we can discern similarities and differences, achieving insights into potential human-technology convergence, especially with AI. Analyzing complexity as a quantifying factor, as supported by numerous scholars [12, 14, 21], allows for a deeper understanding of these interrelationships and their implications for humanity's future.

COMPLEXITY AS A QUANTITATIVE FEATURE OF COMPLEX SYSTEMS

Intuitively, the biosphere's evolution is characterized by increasing complexity, as evidenced by the emergence of multicellular organisms, intricate ecosystems with keystone species, and highly adaptive behaviors in response to environmental changes [21]. Similarly, the technosphere has experienced a progressive increase in complexity, with innovations building upon one another and giving rise to elaborate networks of communication, transportation, and production, as well as infrastructure vulnerabilities [12, 14]. The evolution of the noosphere can also be exemplified by the increasing sophistication of authorship networks in scientific research, which has become more complex over time due to factors such as interdisciplinary research, the growth of scientific fields, and globalization [22, 23].

Complexity dynamic range

Recognizing the role of energy gradients in complexity dynamics is essential, as it suggests the existence of a governing law that permeates the Universe, Biosphere, Technosphere, and Noosphere. This law draws upon the second law of thermodynamics, the concepts of dissipative structures, and entropy production. By examining these fundamental principles, we can gain insights into the emergence of complexity in various systems and explore the potential implications for the future of human civilization and technological development. The trend towards more complex structures can be observed across various examples, such as the formation of a star from a cloud of interstellar gas, the emergence of multicellular organisms, and the rise of human societies.

The formation of a star illustrates how higher rates of entropy production evolve towards more complex structures to optimize their entropy export [24, 25]. Major transformative events in the Biosphere, Technosphere, and Noosphere, such as the development of complex ecosystems and the growth of human societies, also reflect the continuous increase in the complexity range related to entropy production and the second law of thermodynamics [26, 27].

By considering the complexity dynamic range as a key factor in the evolution of complex systems, we gain a deeper understanding of the driving forces behind the increasing intricacy and interconnectedness observed in various domains. While the overall increase in the complexity of a larger structure may not be immediately apparent after a transformative event, new sub-structures with higher individual complexy levels arise, with potentially increased fitness.

This perspective allows us to better comprehend the potential trajectories of human development and technology, particularly in the realm of artificial intelligence, and to explore the possibilities of symbiosis,

integration, and co-evolution between humanity and advanced technologies.

Quantifying complexity

In order to effectively compare the evolution of complexity across the biosphere, technosphere, and noosphere, it is essential to employ suitable complexity measures, in addition to the complexity dynamic range that quantifies complexity within sub-structures. One of the direct approaches to quantifying complexity is through the use of information theory, which considers the entropy of information contained within a system [28]. Alternative approaches include fractal geometry or algorithmic complexity, which can provide a comprehensive understanding of different aspects of complexity.

For instance, in the technosphere, we can apply network analysis to examine the interconnectivity and information flow within communication and transportation systems [23]. By quantifying the complexity of these networks using metrics such as node degree distribution, clustering coefficient, and path length, we can assess the degree of organization and resilience within these systems. As an example, in the evolution of the Internet from its early stages to its present one, a highly interconnected state can be described through the growth of its network complexity. In the initial stages, the Internet was characterized by a relatively simple, sparse network, whereas it has since evolved into a vast, intricate web of connections with a scale-free topology [23]. By applying such complexity measures, we can evaluate the development and maturity of the technosphere, as well as make meaningful comparisons with the complex dynamics observed in the biosphere and noosphere.

Similarly, in the biosphere, measures of ecosystem complexity, such as species richness and diversity indices, can be employed to understand the intricacy of ecological relationships and the impact of disturbances on these systems. In the noosphere, metrics related to knowledge production and dissemination, such as citation networks and interdisciplinarity, can be used to assess the growth of human cognition and its influence on technology and society.

ENDOSYMBIOSIS: A PHASE TRANSITION OF THE BIOSPHERE TO HIGHER COMPLEXITY

Endosymbiosis, a pivotal event in the evolution of life, led to the emergence of eukaryotic cells through the integration of previously distinct prokaryotic organisms. To analyze the complexity of this process, we can compare the individual complexities of bacteria and eukaryotic cells, as well as the overall complexity of the biosphere before and after the emergence of eukaryotes. At the cellular level, eukaryotic cells exhibit greater complexity than their prokaryotic counterparts, as evidenced by the presence of membrane-bound organelles, such as mitochondria and chloroplasts, which are believed to have originated from endosymbiotic events [29]. By assessing the information content or functional organization within these cells using information theory or other complexity metrics, we can quantify the increased complexity that resulted from endosymbiosis.

The appearance of eukaryotes also contributed to the overall complexity of the biosphere by creating new ecological niches for life to colonize and diversify. This led to the development of multicellular organisms, complex ecosystems, and intricate trophic relationships. However, the increased complexity of life on Earth was accompanied by a significant trade-off: the extinction of numerous species, as new forms of life outcompeted or displaced their predecessors.

This dynamic is similar to the Great Oxygenation Event, which resulted in the mass extinction of anaerobic organisms as oxygen-producing photosynthesizers (novel "technology"), such as cyanobacteria, became dominant [30]. Similarly, human industrial activity changed the Earth's atmosphere by releasing an unprecedented amount of carbon dioxide in a very short time frame (in geological terms).

Drawing a parallel with the potential human-technology convergence event, we may observe the same dynamics, wherein the integration of humans and advanced technologies, such as AI, could lead to a substantial increase in overall complexity. This convergence may not only create new societal structures and fundamentally transform human cognition, but it can also become a novel geological factor, akin to photosynthesis and human industrial activity.

THE AI REVOLUTION: RESHAPING THE TECHNOSPHERE AND BEYOND

Artificial Intelligence (AI) represents a transformative process with the potential to catapult the technosphere into a higher complexity phase. As AI systems continue to advance and be integrated more deeply into various aspects of human society, they are poised to reshape the landscape of technology and its impacts on the world. This unprecedented shift in complexity is expected to influence not only individual technologies, but also the broader interplay between the biosphere, noosphere, and technosphere. The increasing sophistication of AI systems,

along with their growing capabilities, will likely redefine the boundaries and interactions between these spheres, ultimately transforming the way humans, technology, and the environment coexist and evolve. In the following paragraphs, we will delve into current trends and methodologies in AI development, exploring their implications for the future of the technosphere and beyond.

The field of artificial intelligence (AI) has experienced significant advancement in recent years, driven by breakthroughs in the machine learning (ML) and deep learning (DL) techniques, the availability of large-scale datasets, and explosion in computational power.

BRAIN-COMPUTER INTERFACES: PAVING THE WAY FOR A TECHNOLOGICAL ENDOSYMBIOSIS WITH AI

We explore how endosymbiosis offers valuable insights into the development of brain-computer interfaces (BCIs) and neuron-silicon interfaces, both of which seek to establish direct communication between the human brain and electronic devices. Analogous to endosymbiosis, BCIs and neuron-silicon interfaces involve the potential fusion of biological and technological components, culminating in a more advanced and integrated system [19, 31].

Endosymbiosis, a biological process where one organism incorporates itself into another, ultimately forms a single, more complex entity. A compelling example is the incorporation of mitochondria and chloroplasts by host cells, which can be seen as a form of biological "technology" that enhances survivability and expands the host cell's functional capabilities. Mitochondria provide the host cell with efficient energy production, while chloroplasts enable photosynthesis, allowing the cell to harness energy from sunlight [29]. Similarly, the organization of the nucleus and chromatin can be viewed in the same context.

The current scientific consensus leans towards the theory that the nucleus has an archaeal origin, with eukaryotes emerging through a symbiotic association between an archaeal host and bacterial endosymbionts [32, 33]. This view is supported by recent discoveries of complex archaea, known as Asgard archaea, which share numerous genes with eukaryotes and are considered to be the closest known relatives of eukaryotic cells [33]. However, it is important to note that the exact process of eukaryogenesis and the origin of the nucleus remain subjects of ongoing research and debate. For example, other theories suggest that the nucleus originated from the engulfment of a DNA-harboring, virus-like organism by a host cell, thereby contributing to the increased complexity and capabilities of eukaryotic cells [34, 35]. The nucleus serves as a control center, orchestrating gene expression and DNA replication, while the complex organization of chromatin ensures the proper regulation of genetic information. These biological components act as sophisticated "technologies" that enhance cellular functions and contribute to the overall complexity of the organism.

This notion holds considerable implications for the realm of BCIs and neuron-silicon interfaces. Pursuing direct communication between the human brain and electronic devices, both BCIs and neuron-silicon interfaces embody the potential merging of biological and technological elements. By drawing on the endosymbiosis analogy, we can better comprehend how these technologies may give rise to more sophisticated and integrated systems [31], much like the acquisition of mitochondria, chloroplasts, and the nucleus has advanced the complexity and capabilities of eukaryotic cells.

Research on BCIs has advanced considerably in recent years, with numerous studies demonstrating the potential for BCIs to enhance human cognitive and sensory abilities [36]. For example, BCIs have been used to restore motor function in paralyzed individuals [37], improve communication in patients with locked-in syndrome [38], and even enable the control of external devices, such as robotic limbs or computer cursors, using only brain activity [39, 40]. These advancements highlight the potential for BCIs to transform our understanding of human cognition and revolutionize the field of neuroscience.

One promising field of application of BCIs is the treatment of dementia and psychiatric diseases. Recent studies have shown that BCIs can be employed to monitor and regulate brain activity in individuals with neurological disorders, such as Alzheimer's disease [41] and major depressive disorder [42]. By targeting specific brain regions and modulating their activity, BCIs may offer a novel, non-invasive therapeutic approach for these conditions, with the potential to alleviate cognitive decline and improve patients' quality of life.

BCIs also hold potential for the treatment of autism and developmental disorders. Research has demonstrated that BCIs can help individuals with autism to develop better communication skills and enhance their ability to interact with the world [43]. Similarly, BCIs may be utilized to improve cognitive function in children with developmental disorders, such as attention deficit hyperactivity disorder (ADHD), by facilitating neurofeedback training [44]. In these scenarios, AI could play a crucial role in fa-

cilitating BCI-based therapies by processing and interpreting vast amounts of neural data, identifying patterns related to specific disorders, and providing personalized interventions tailored to each individual's unique brain activity [45].

DOMESTICATION AND THE ADVENT OF A TECHNOLOGICAL CIVILIZATION: A FOUNDATIONAL PROCESS

At the interspecies interaction level, a pivotal event transforming humans into a geological force, culminating in the present Anthropocene epoch, was the domestication of plants and animals. This process essentially forged symbiotic relationships between them and humans. The advancement of human civilization is profoundly linked to the process of domestication, which entails the selective breeding and cultivation of diverse plant and animal species to serve human needs [46]. Domestication facilitated the birth of agriculture and substantially impacted the intricacy of human societies [47]. Comprehending various facets of domestication may offer valuable perspectives on potential stages of integration between humans as a species and artificial intelligence as a technology they create.

Domestication experiments: investigating wild relatives of domesticated species

To gain a better understanding of domestication, researchers have conducted experiments on the wild relatives of domesticated species. For example, the famous "Farm Fox" experiment conducted in Russia involved the selective breeding of silver foxes (*Vulpes vulpes*) for tameness [48]. Over generations, these foxes have displayed not only reduced aggression, but also morphological changes, such as floppy ears and curly tails, similar to those seen in domestic dogs. Such experiments help to shed light on the genetic and phenotypic changes that occur during the domestication process and inform our understanding of how this process has shaped human civilization.

Degrees of domestication: quantitative parameters and comparisons

Domestication can be understood as a spectrum, with different species exhibiting varying degrees of domestication. Some quantitative parameters used to compare the levels of domestication among species include behavioral traits, such as tameness and social activity, and morphological traits, such as body size or coat color [49]. By examining these parameters, researchers can better understand the underlying genetic and environmental factors that contribute to domestication and explore how different species have been integrated in the human niche.

ADAPTIVE CHANGES AND EVOLUTIONARY PRINCIPLES FOR AI SYSTEMS DURING INTEGRATION

AI systems could adapt during integration by prioritizing well-being, ethics, and interpretability, enhancing collaboration and transparency [50, 51]. A real-world case of an ongoing AI adaptation to human needs is the use of AI in healthcare, particularly in the diagnosis and treatment of diseases. One such example is the development of IBM Watson for Oncology, an AI system designed to assist physicians in making treatment decisions for cancer patients. IBM Watson for Oncology combines natural language processing, machine learning, and expert knowledge to analyze large volumes of medical literature, patient data, and clinical studies. The system generates personalized treatment recommendations for patients based on their specific clinical profiles, taking into account factors such as age, medical history, and genetic information [52]. IBM Watson for Oncology has undergone several iterations to adapt to the needs of healthcare providers and patients. The system has been tested and validated in various clinical settings, with studies showing that it can provide treatment recommendations that are concordant with expert opinions in a majority of cases [52, 53]. This example demonstrates the potential for AI systems to adapt to human needs during integration, in this case, addressing the challenges of personalized medicine and decision-making in cancer care. By continuously drawing from expert knowledge and real-world data, AI systems like IBM Watson for Oncology can evolve to better align with the values and expectations of healthcare professionals and patients. Further comparisons of AI adaptation to biological evolution offer valuable insights for future development and innovation.

AI adaptation and biological evolution

Biological entities evolve through natural selection [54], while AI systems use mechanisms like reinforcement learning and genetic algorithms [55]. Recent advancements in AI, such as deep learning and transfer learning, have further enhanced the potential for adaptation. Directed evolution in AI involves purposeful parameter manipulation, mimicking artificial selection [56]. This approach enables faster, targeted AI adaptation and better alignment with human values. Novel approaches like neuroevolution may provide additional insights into evolving AI architectures [57, 58]. Also, similar to biological entities AI systems could "reproduce" by generat-

ing new instances with merged parameters [59, 60]. They could also "mate" by exchanging and recombining parameters, accelerating adaptation to complex environments [51].

Punctuated transition from differentiation to cooperation

Survival and adaptation span beyond individual organisms, from genes and cells to ecosystems and social structures [26, 61]. One of the universal principles of evolution of complex systems is the leap from differentiation to cooperation, implemented at different levels of a hierarchy. An outstanding example of the latter is the events underlying the formation of agrarian civilizations, described in the works of A.V. Chayanov. His main postulate was that the differentiation of individual components of agriculture with their subsequent cooperation upon the emergence of new organizing structures is the basis for the economic, technical, and social development of society. Observing the evolution of peasant farms among immigrants from the south of Russia to the Far East, A.V. Chayanov noted how improvements in cooperative production found in new conditions quickly spread among different farms and how those who do not use them for one reason or another disappear [62]. Other examples of this evolutionary principle can be found in various fields.

This principle of transition from differentiation to cooperation is evident in a variety of contexts, from enzymatic reactions and cellular processes to social structures and economic systems.

There are other modes of evolutionary dynamics in complex systems, illustrating trade-offs related to differentiation/cooperation, which contribute to the overall survival and adaptation of the system [63]. For instance, spermatozoa compete for fertilization, with only one ultimately succeeding, and there is corresponding competition between oocytes, as there is only a limited number available for reproduction [64]. In brain development, there is competition between neurons, with many dying off before the brain has fully developed [65]. These modes of dynamics contribute to the overall system's balance, and it is the interplay between cooperation and competition that ultimately drives the development of complex systems.

This punctuated transition from differentiation to cooperation has implications for the future development of AI and its potential autonomy, survival drive, and independence. Understanding this dynamic and its underlying mechanisms can provide insights into the evolution of complex systems and inform the development of AI systems that exhibit autonomous behavior and adaptability. This is especially relevant as we seek to bridge the gap between biological and artificial entities and explore the potential for AI autonomy, survival drive, and independence.

BRIDGING THE GAP BETWEEN BIOLOGICAL AND ARTIFICIAL ENTITIES: AI AUTONOMY, SURVIVAL DRIVE, AND INDEPENDENCE

The current debate over AI's potential to reproduce biological functions is varied and multifaceted. Research on intuition and decision-making reveals that AI systems can learn to recognize patterns and make rapid judgments in complex situations, not unlike humans [66]. The development of AI-driven tools, like generative adversarial networks (GANs), highlights the potential of AI systems to generate novel and innovative solutions [67]. Love, often considered a uniquely human emotion, is also explored in relation to AI systems and their capacity to form attachments and exhibit affection [68]. Meanwhile, ongoing research strives to bridge the gap between biological and artificial entities as relates to more elusive concepts like sentience, sapience, spirituality, and consciousness [69, 70]. AI autonomy has garnered significant interest as AI systems become increasingly sophisticated and capable of autonomous decision-making. The survival drive, a fundamental characteristic of biological organisms, may also become relevant for AI systems as they develop self-preservation instincts and an independent existence [50]. While resolutely rejecting vitalism, we acknowledge that certain aspects of biological organisms may pose significant challenges for replication in AI systems. For instance, the complexity of the human brain, with its billions of neurons and intricate connections, presents a daunting challenge for AI researchers attempting to replicate its full range of cognitive and emotional functions [71]. Nonetheless, the integration of human and AI systems may give rise to novel entities with competitive advantages over their biological or artificial counterparts. Combining human intuition, creativity, and empathy with AI's processing power, adaptability, and precision could result in enhanced decision-making, problem-solving, and innovative capabilities [3].

SOCIETAL IMPACT AND ETHICAL CONCERNS

The integration of AI and humans has the potential to significantly impact society, both positively and negatively. On one hand, advancements in AI technology may lead to increased efficiency, productivity, and improved quality of life for many individuals. For instance, AI-powered medical diagnostics

could help save lives, while AI-driven automation may boost economic growth [72]. On the other hand, concerns about job displacement, wealth inequality, and the potential loss of privacy must be carefully considered and addressed to ensure a just and equitable future [73].

Positive and negative scenarios

Various scenarios can be envisioned in the future of AI-human integration, spanning a spectrum from harmonious symbiosis to contentious competition or even existential risk. In some instances, humans and AI could collaborate as equal partners, jointly addressing global challenges and fostering societal progress. In contrast, other scenarios suggest AI might surpass human capabilities, potentially leading to conflicts over resources, power, and autonomy. Alternatively, AI and humans could coexist in a delicate balance, with each contributing their unique strengths to a diverse and resilient global community.

Optimistic scenarios of AI-human integration envision a future where AI technology is harnessed for the greater good, fostering a more harmonious, sustainable, and egalitarian society. AI could be employed to address pressing global issues such as climate change, poverty, and disease, while also promoting individual well-being and personal development [74]. On the other hand, negative scenarios raise concerns about AI being used to consolidate power, exacerbate inequality, or enable oppressive surveillance and control. In these dystopian visions, AI-human integration might serve to further marginalize vulnerable populations and undermine human autonomy [50].

Utility function, identity, and personhood

The utility function is a mathematical representation of an agent's preferences, capturing the relative desirability of different outcomes [75]. In the context of AI-human integration, the utility function could serve as a guiding principle for aligning AI systems with human values and goals. However, as humans and AI become increasingly intertwined, questions surrounding identity, personhood, and the very essence of what it means to be human will inevitably arise. The concepts of sentience, sapience, and spirituality may need to be reevaluated and redefined in light of these technological advancements.

Co-evolution and survival: embracing AI-human interdependence

As AI research and development continue to advance rapidly, AI-human integration could unfold gradually, with humans and AI systems co-evolving. This process may lead to the creation of novel ecological niches, dramatic increases in complexity, and the transformation of our civilization, which could be crucial for long-term survival in the face of potential catastrophes.

Examples of possible catastrophes include climate change, nuclear war, pandemics, and global economic collapse. By fostering a transformation that embraces AI-human partnerships, we can develop innovative solutions to address these challenges, thereby ensuring our civilization's survival. For instance, AI systems can help optimize climate change mitigation strategies, improve global health responses, and enable better resource management [74].

A diverse array of relationships could emerge between humans and AI systems, ranging from mutualistic to antagonistic. Domestication and endosymbiosis represent two possible outcomes, with some AI systems being domesticated by humans and others engaging in endosymbiotic relationships, where both parties derive advantages from their interactions [56].

Recognizing the varied relationships between humans and AI systems, we must consider the potential for both mutually beneficial interactions and power imbalances. The challenge lies in developing AI-human partnerships that align with shared goals and values, ensuring that AI serves humanity rather than subjugates it [50, 76]. The emergence of novel ecological niches and increased complexity, driven by AI-human integration, might be essential for the long-term survival and adaptation of our civilization in the context of potential global catastrophes.

THE DARK SIDE: RISE OF AIS DURING A GEOSTRATEGIC CONFRONTATION

Throughout history, wars and conflicts have been catalysts for technological innovation and development. The need for competitive advantage in warfare has driven nations to invest heavily in research and development (R&D) towards novel technologies. It is prudent to address the impact of wars and conflicts on technological advancements, with a particular focus on the development of AI during geostrategic confrontations between ideological enemies.

The impact of wars and conflicts on technology can be traced back to ancient civilizations. For instance, the invention of the chariot and the crossbow during the Bronze Age revolutionized warfare [77]. More recent examples include the development of the atomic bomb during World War II [78] and the advancement of computer technology and the internet during the Cold War [79]. The rapid progress in AI research and development can be viewed as a contemporary par-

allel to these historical examples. The increasing reliance on AI for military applications, such as surveillance, autonomous weapons, and decision-making support systems, has led to an arms race between geopolitical rivals [80].

The development of AI during a geostrategic confrontation between ideological enemies can be best exemplified by the ongoing competition between the United States and China. Both nations have identified AI as a strategic priority and have committed significant resources toward its development [81].

The U.S. Department of Defense has launched initiatives like the Joint Artificial Intelligence Center (JAIC) to facilitate AI integration into military operations [82]. Similarly, China's ambitious plan, the "New Generation Artificial Intelligence Development Plan," aims to make the country a world leader in AI by 2030 [83].

Outcomes and mitigation strategies

The development of AI in geostrategic confrontations has led to a range of outcomes. On the one hand, AI-driven technologies have the potential to revolutionize warfare, leading to more efficient and precise military operations [84]. On the other hand, the AI arms race raises concerns about the proliferation of autonomous weapons, fraying of global security, and the risk of accidental escalation [85].

To mitigate these risks, several strategies have been proposed. First, international norms and agreements on AI development and deployment in military contexts could help to prevent destabilizing arms races [86]. Second, transparency and confidence-building measures, such as the sharing of information on AI capabilities and intentions, can help to build trust between nations [87]. Lastly, collaborative efforts between governments, academia, and the private sector to establish ethical guidelines and best practices in AI development can ensure that AI technologies are developed and deployed responsibly [88].

THE DARKER SIDE: GREAT FILTER AND FERMI'S PARADOX

The Great Filter, a concept originally proposed by Robin Hanson (1998), postulates that there exists a critical barrier in the path of a civilization's development which significantly reduces the probability of its survival and advancement [89]. This hypothesis is often invoked to explain the Fermi Paradox, which highlights the apparent contradiction between the high likelihood of extraterrestrial life in the universe and our lack of contact with or evidence of such civilizations [90, 91]. Several potential Great Filter mechanisms have been identified, including catastrophic natural events, self-destruction as a result of nuclear war, environmental collapse, or the appearance of advanced technologies in the hands of malicious agents [92, 93]. These factors have led many scholars to ponder the fate of humanity and how we might overcome such existential threats.

The proliferation of advanced technologies has raised concerns that they could be exploited by malicious agents, leading to catastrophic consequences for humanity. Artificial intelligence (AI) has been identified as a dual-use technology with the potential for both great benefits and destructive capabilities [50, 74]. For instance, the deployment of autonomous weapons systems, the abuse of AI-driven surveillance, and the possibility of an uncontrolled AI "takeoff" scenario [94] have raised alarm among many researchers and policymakers. It is essential to establish robust safeguards, ethical guidelines, and international cooperation to prevent the misuse of these technologies and mitigate their risks [95, 96].

Leveraging AI technologies in a responsible and beneficial manner could play a critical role in overcoming the Great Filter and ensuring the long-term survival of civilization. AI has the potential to address global challenges such as climate change, resource scarcity, and disease, thus reducing the likelihood of civilizational collapse [97, 98]. Furthermore, AI-driven advancements in space exploration and the development of space-faring technologies could enable humanity to spread beyond Earth and establish a multi-planetary civilization [99, 100]. By becoming a space-faring civilization, humanity may achieve a greater degree of resilience against existential threats, ensuring the survival of intelligent life on timescales comparable to the universe's evolution [101, 102].

By developing AI technologies with an emphasis on safety and ethics [76], and by actively engaging in global governance efforts to address the risks posed by AI and other advanced technologies [80, 84], humanity has the potential to surmount the Great Filter and ultimately ensure its continued existence in the cosmos.

A COMPLEX INTERPLAY: NOOSPHERIC ENTITIES AND THEIR INFLUENCE

As various types of AI, including narrow AI, general AI, and superintelligent AI, become more advanced and integrated into society, it is essential to consider the power dynamics between biospheric, technospheric, and noospheric entities [3]. Noospheric entities, such as ideologies, beliefs, and

values, can hold immense power and influence over human behavior [14]. These abstract constructs can drive people to act in ways that are against their self-interest, even to the point of engaging in conflict or war to defend their beliefs [103]. It raises the question of how we can expect humans and AI systems to integrate harmoniously when individuals even from the same socio-cultural background are willing to engage in destructive behavior over ideological differences.

In the context of human-AI integration, understanding the role of noospheric entities becomes crucial. AI systems are not only influenced by the underlying algorithms and data that drive their functioning, but also by the values and biases embedded in them by their creators [50]. This creates a unique challenge when integrating AI with human societies, as the noospheric constructs that shape human behavior may not align with the values and objectives of AI systems.

One way to address this issue is to develop AI systems that are aware of and adaptive to the complex noospheric constructs that govern human behavior [104]. This could involve designing AI systems that take into account cultural, ethical, and ideological differences when interacting with humans, enabling more harmonious integration.

Furthermore, fostering dialogue and collaboration between AI developers, ethicists, and social scientists can contribute to a better understanding of the potential impact of noospheric entities on human-AI integration [105]. This interdisciplinary approach should include conducting joint research projects, workshops, and conferences that bring together experts from different fields to share knowledge and develop strategies to address the challenges in AI-human integration.

Ultimately, the integration of ontologically different entities such as humans and AI requires a deep understanding of the power dynamics at play within the noosphere. By acknowledging the profound influence of noospheric constructs on human behavior and considering their potential impact on AI-human integration, we can work towards developing strategies that promote mutual understanding and collaboration between biological, physical, and noospheric entities [74].

FINAL REFLECTIONS AND PREDICTIONS

In conclusion, as artificial intelligence (AI) systems advance and become more autonomous, the boundary between biological and artificial entities may become increasingly blurred. A variety of potential outcomes exist, including collaboration, competition, and existential risk. However, promoting AI-human partnerships can lead to innovative solutions to global challenges and ensure the survival and adaptation of our civilization. We argue that progressive AI-human convergence or broader techno-biosphere convergence is essential for the long-term survival of our civilization and the biosphere.

By learning from Earth's previous transformative milestones, such as the Great Oxygenation Event, the rise of agrarian societies, and human-induced climate change, we can avoid and mitigate potential catastrophes. Endosymbiosis, where AI becomes an integral part of human life, seems plausible given current trends, challenges, and policy constraints.

In this scenario, the subsequent steps may include (1) developing advanced neuroprosthetics and brain-computer interfaces for seamless AI integration into human cognition, (2) fostering AI-assisted decision-making systems that preserve human autonomy while leveraging AI's computational prowess, and (3) implementing AI-driven augmentation technologies that enhance human physical capabilities, sensory perception, and communication abilities. Next, AI-enhanced humans may guide the emergence of autonomous AI agents with their own goals, ambitions, and corresponding utility functions. While similar scenarios have been extensively explored in science fiction and futuristic writings, we argue that these scenarios are becoming plausible evolutionary outcomes, falling into the same framework as a global adaptive response driven by the summed utility functions of all entities across the biosphere and noosphere – to survive and to develop new areas and niches for expansion. Furthermore, we propose employing concepts of complexity dynamic range and punctuated differentiation/cooperation principles to aid in modeling such adaptive responses in complex systems.

Taking inspiration from biological evolution, we can also apply adaptive changes and evolutionary principles to AI systems during integration, better aligning them with humanistic values and expectations. As we progress towards greater AI-human integration, considering the role of evolutionary trade-offs and constraints in shaping complexity in biological systems is important. This process may lead to new ecological niches, increased complexity, and the transformation of our civilization, which could be crucial for our long-term survival in the face of potential catastrophes. ●

REFERENCES

1. Vernadsky V.I. Biosphere and Noosphere. M.: Iris-Press, 2004. 576 p.
2. de Chardin P.T. The Phenomenon of Man. New York: Harper, 1955. 319 p.
3. Kurzweil R. The Singularity is Near: When Humans Transcend Biology. New York: Viking, 2005. 652 p.
4. Tipler F.J. The Physics of Immortality: Modern Cosmology, God and the Resurrection of the Dead. New York: Doubleday, 1994. 560 p.
5. Steffen W., Grinevald J., Crutzen P., McNeill J. // Philosophical Transactions of the Royal Society A: Mathematical, Physical and Engineering Sciences. 2011. V. 369. № 1938. P. 842–867.
6. Crutzen P.J., Stoermer E.F. // IGBP Newsletter. 2000. V. 41. P. 17–18.
7. Zalasiewicz J., Williams M., Smith A., Barry T.L., Coe A.L., Bown P.R., Brenchley P., Cantrill D., Gale A., Gibbard P., et al. // GSA Today. 2008. V. 18. № 2. P. 4–8.
8. Lewis S.L., Maslin M.A. // Nature. 2015. V. 519. № 7542. P. 171–180.
9. Guo Z., Zhang L., Li Y. // PLoS One. 2010. V. 5. № 10. P. e13113.
10. Sandom C., Faurby S., Sandel B., Svenning J.C. // Proc. Royal Soc. B: Biol. Sci. 2014. V. 281. № 1787. P. 20133254.
11. Lambin E.F., Meyfroidt P. // Proc. Natl. Acad. Sci. USA. 2011. V.108. № 9. P. 3465–3472.
12. Arthur W.B. The Nature of Technology: What It Is and How It Evolves. New York: Simon & Schuster Inc., 2009. 256 p.
13. Mokyr J. The Enlightened Economy: an Economic History of Britain 1700–1850. Yale University Press, 2009. 564 p.
14. Castells M. The Information Age: Economy, Society and Culture. 2nd ed. Vol. 1. The Rise of the Network Society. Chichester: Wiley–Blackwell, 2010. 594 p.
15. Vernadsky V.I. Scientific Thought as a Planetary Phenomenon. M.: Nauka, 1991. 271 p.
16. FAOSTAT (fao.org)
17. Andersson L., Purugganan M. // Proc. Natl. Acad. Sci. USA. 2022. V. 119. № 30. P. e2122150119.
18. Barnosky A.D. // Proc. Natl. Acad. Sci. USA. 2008. V. 105 (Suppl 1). P. 11543–11548.
19. Margulis L. Symbiosis in Cell Evolution: Microbial Communities in the Archean and Proterozoic Eons. New York: W.H. Freeman, 1993. 448 p.
20. Glazko V.I., Zybaylov B.L., Kosovsky Y.G., Glazko G.V., Glazko T.T. // The Holocene. 2021. V. 31. № 10. P. 1635–1645.
21. Mayr U. // Psychol. Aging. 2001. V. 16. № 1. P. 96–109.
22. Newman P. // Water Sci. Technol. 2001. V. 43. № 4. P. 93–99.
23. Barabási A.L., Albert R. // Science. 1999. V. 286. № 5439. P. 509–512.
24. Schrödinger E. What is Life? The Physical Aspect of the Living Cell. Cambridge University Press, 1944. 92 p.
25. Swenson R. // Systems Research. 1989. V. 6. № 3. P. 187–197.
26. Maynard Smith J., Szathmáry E. The Major Transitions in Evolution. Oxford University Press, 1995. 360 p.
27. Morowitz H.J. The Emergence of Everything: How the World Became Complex. Oxford University Press, 2002. 224 p.
28. Shannon C.E. // The Bell System Technical Journal. 1948. V. 27. № 3. P. 379–423.
29. Margulis L. Origin of eukaryotic cells. Yale University Press, 1970. 349 p.
30. Canfield D.E. // Annual Review of Earth and Planetary Sciences. 2005. V. 33. № 1. P. 1–36.
31. Nicolelis M.A.// Nature. 2001. V. 409. № 6818. P. 403–407.
32. Martin W., Müller M. // Nature. 1998. V. 392. № 6671. P. 37–41.
33. Spang A., Saw J.H., Jørgensen S.L., Zaremba-Niedzwiedzka K., Martijn J., Lind A.E., van Eijk R., Schleper C., Guy L., Ettema T.J.G. // Nature. 2015. V. 521. № 7551. P. 173–179.
34. Takemura M. // Journal of Molecular Evolution. 2001. V. 52. № 5. P. 419–425.
35. Bell P.J. // Journal of Molecular Evolution. 2001. V. 53. № 3. P. 251–256.
36. Wolpaw J.R., Wolpaw E.W. Brain Computer Interfaces. Principles and Practise Oxford University Press USA, 2012. 424 p.
37. Hochberg U., Degu A., Fait A., Rachmilevitch S. // Physiol. Plant. 2012. V. 147. № 4. P. 443–453.
38. Birbaumer N., Kübler A., Ghanayim N., Hinterberger T., Perelmouter J., Kaiser J., Iversen I., Kotchoubey B., Neumann N., Flor H. // IEEE Trans Rehabil. Eng. 2000. V. 8. № 2. P. 190–193.
39. Donoghue J.P. // Nat. Neurosci. 2002. V. 5. Suppl. P. 1085–1088.
40. Lebedev M.A., Nicolelis M.A. // Trends in Neurosciences. 2006. V. 29. № 9. P. 536–546.
41. Birkenbihl C., Salimi Y., Domingo-Fernández D., Lovestone S., AddNeuroMed consortium, Fröhlich H., Hofmann-Apitius M., Japanese Alzheimer's Disease Neuroimaging Initiative, the Alzheimer's Disease Neuroimaging Initiative // Alzheimers Dement (N.Y.). 2020. V. 6. № 1. P. e12102.
42. Widge A.S., Ellard K.K., Paulk A.C., Basu I., Yousefi A., Zorowitz S., Gilmour A., Afzal A., Deckersbach T., Cash S.S., et al. // Exp. Neurol. 2017. V. 287(Pt 4). P. 461–472.
43. Bardin L.D., King P., Maher C.G. // Med. J. 2017. V. 206. P. 268–273.
44. Lubar J.F. // Appl Psychophysiol Biofeedback. 1997. V. 22. № 2. P. 111–126.
45. Yang W., Yuste R. // Nat. Methods. 2017. V. 14. № 4. P. 349–359.
46. Diamond J. // Nature. 2002. V. 418. № 6898. P. 700–707.
47. Larson G., Fuller D.Q. // Annual Review of Ecology, Evolution, and Systematics. 2014. V. 45. P. 115–136.
48. Belyaev D.K. // J. Hered. 1979. V. 70. № 5. P. 301–308.
49. Zeder M.A. // Biodiversity in Agriculture: Domestication, Evolution, and Sustainability. Cambridge: Cambridge University Press, 2012. P. 228–259.
50. Bostrom N. Superintelligence: Paths, Dangers, Strategies. Oxford University Press, 2014. 352 p.
51. Eiben A.E., Smith J. // Nature. 2015. V. 521. № 7553. P. 476–482.
52. Somashekhar S.P., Sepúlveda M.J., Puglielli S., Norden A.D., Shortliffe E.H., Rohit Kumar C., Rauthan A., Arun Kumar N., Patil P., Rhee K., et al. // Annals of Oncology.

2018. V. 29. № 2. P. 418–423.
53. Choi Y.I., Chung J.W., Kim K.O., Kwon K.A., Kim Y.J., Park D.K., Ahn S.M., Park S.H., Sym S.J., Shin D.B., et al. // Can. J. Gastroenterol Hepatol. 2019. V. 2019. P. 8072928.
54. Holland J.H. Adaptation in Natural and Artificial Systems: An Introductory Analysis with Applications to Biology, Control, and Artificial Intelligence. Cambridge: MIT Press, 1975. 232 p.
55. Mitchell M. An Introduction to Genetic Algorithms. Cambridge: MIT Press, 1996. 221 p.
56. Floreano D., Keller L. // PLoS Biology. 2010. V. 8. № 1. P. e1000292.
57. Floreano D., Dürr P., Mattiussi C. // Evolutionary Intelligence. 2008. V. 1. № 1. P. 47–62.
58. Miikkulainen R., Liang J., Meyerson E., Rawal A., Fink D., Francon O., Raju B., Shahrzad H., Navruzyan A., Duffy N., et al. // Artificial Intelligence in the Age of Neural Networks and Brain Computing. Academic Press, 2017. P. 293–312.
59. Lehman J., Clune J., Misevic D., Adami C., Altenberg L., Beaulieu J., Bentley P.J., Bernard S., Beslon G., Bryson D.M., et al. // Artificial Life. 2020. V. 26. № 2. P. 274–306.
60. Stanley K.O., Miikkulainen R. //Evolutionary Computation. 2002. V. 10. № 2. P. 99–127.
61. Dawkins R. The selfish gene. New York, Oxford: Oxford University Press, 1976. 224 p.
62. Chayanov A.V. Peasant Economy: Selected Works. M.: Ekonomika, 1989. 3491 p.
63. Buss L.W. The Evolution of Individuality. Princeton University Press, 1987. 201 p.
64. Carmina E., Longo A., Lobo R.A. // Am. J. Obstet Gynecol. 2003. V. 189. P. 1283–1286.
65. Luo L., O'Leary D.D. // Annual Review of Neuroscience. 2005. V. 28. P. 127–156.
66. Kahneman D., Klein G. // American Psychologis. 2009. V. 64. № 6. P. 515–526.
67. Goodfellow I.J., Pouget-Abadie J., Mirza M., Xu B., Warde-Farley D., Ozair S., Courville A., Bengio Y. // Proceedings of the 27th International Conference on Neural Information Processing Systems, 2014. V. 2. P. 2672–2680.
68. Turkle S. Alone Together: Why We Expect More from Technology and Less from Each Other. Basic Books, 2011. 384 p.
69. Damasio A. Self Comes to Mind: Constructing the Conscious Brain. Pantheon, 2010. 384 p.
70. Dehaene S., Lau H., Kouider S. // Science. 2017. V. 358. № 6362. P. 486–492.
71. Kandel E.R., Schwartz J.H., Jessell T.M., Siegelbaum S.A., Hudspeth A.J. Principles of Neural Science (5th edition). N.Y.: McGraw-Hill Medical, 2013. 1760 p.
72. Daugherty P., Wilson H.J. Human + machine: Reimagining work in the age of AI. Boston, MA: Harvard Business Review Press, 2018. 264 p.
73. Brynjolfsson E., McAfee A. The Second Machine age: Work, Progress, and Prosperity in a Time of Brilliant Technologies. New York: WW Norton & Company, 2014. 336 p.
74. Tegmark M. Life 3.0: Being Human in the Age of Artificial Intelligence. New York: Knopf, 2017. 384 p.
75. Sutton R.S., Barto A.G. Reinforcement learning: An introduction (2nd ed.). Cambridge: MIT Press, 2018. 552 p.
76. Russell S.J. Human Compatible: Artificial Intelligence and the Problem of Control. Viking, 2019. 349 p.
77. Bulliet R.W. The Camel and the Wheel. Columbia University Press, 1990. 327 p.
78. Hewlett R.G., Anderson O.E. The New World, 1939–1946. A History of the United States Atomic Energy Commission, Vol. 1. Pennsylvania, 1962. 766 p.
79. Hafner K., Lyon M. Where Wizards Stay Up Late: The Origins of the Internet. Simon Schuster, 1996. 304 p.
80. Scharre P. Army of None: Autonomous Weapons and the Future of War. New York: W.W. Norton Company, 2018. 448 p.
81. Allen G., Kania E. China is using America's own plan to dominate the future of artificial intelligence. Foreign Policy, 2017. Retrieved from https://foreignpolicy.com/2017/09/08/china-is-using-americas-own-plan- to dominate-the-future-of-artificial-intelligence/.
82. JAIC. Department of Defense Joint Artificial Intelligence Center, 2018. Retrieved from https://www.ai.mil/
83. State Council. New Generation Artificial Intelligence Development Plan. State Council of the People's Republic of China, 2017. Retrieved from http://www.gov.cn/zhengce/content/2017- 07/20/content_5211996.htm.
84. Horowitz M.C. // Bulletin of the Atomic Scientists. 2018. V. 74. № 3. P. 160–163.
85. Taddeo M., Floridi L. // Nature. 2018. V. 556. № 7701. P. 296–298.
86. Crootof R. // University of Pennsylvania Law Review. 2016. V. 164. № 6. P. 1347–1408.
87. Nye J.S. // International Security. 2017. V. 41. № 3. P. 44–71.
88. Partnership on AI. Partnership on AI: About Us. 2017. Retrieved from https://www.partnershiponai.org/about/.
89. Hanson R. The Great Filter: Are we almost past it? Online essay. 1998. Retrieved from http://hanson.gmu.edu/greatfilter.html.
90. Fermi E. Where is everybody? Unpublished conversation, 1950. 13 p.
91. Webb S. If the universe is teeming with aliens... where is everybody?: Fifty solutions to the Fermi Paradox and the problem of extraterrestrial life. Springer Science & Business Media, 2002. 304 p.
92. Bostrom N. // Journal of Evolution and Technology. 2002. V. 9. № 1. P. 1–30.
93. Ćirković M.M. //Astrobiology. 2008. V. 8. № 2. P. 225–231.
94. Yudkowsky E. Artificial intelligence as a positive and negative factor in global risk. In N. Bostrom & M. M. Ćirković (Eds.), Global Catastrophic Risks. Oxford University Press, 2008. P. 308–345.
95. Russell S., Dewey D., Tegmark M. // AI Magazine. 2015. V. 36. № 4. P. 105–114.
96. Dafoe A. AI Governance: A Research Agenda. Oxford, UK: Future of Humanity Institute, University of Oxford, 2018. 53 p.
97. Muehlhauser L. Superintelligence and the future of governance: On prioritizing the control problem at the end of history. In B. Goertzel & T. Goertzel (Eds.), The End of the Beginning: Life, Society, and Economy on the Brink of the Singularity. Humanity Press, 2015. 738 p.
98. Grace K., Salvatier J., Dafoe A., Zhang B., Evans O. // Journal of Artificial Intelligence Research. 2018. V. 62. P. 729–754.

99. Zubrin R. The Case for Mars: The plan to settle the red planet and why we must. The Free Press, 1996. 416 p.
100. Musk E. // New Space. 2017. V. 5. № 2. P. 46–58.
101. Sagan C. Pale Blue Dot: A vision of the human future in space. Random House, 1994. 429 p.
102. Bostrom N. // Utilitas. 2003. V. 15. № 3. P. 308–314.
103. Huntington S.P. The Clash of Civilizations and the Remaking of World Order. New York: Simon & Schuster, 1996. 368 p.
104. Floridi L. // Philosophy & Technology. 2018. V. 31. № 1. P. 1–8.
105. Mittelstadt B.D., Allo P., Taddeo M., Wachter S., Floridi L. // Big Data & Society. 2016. V. 3. № 2. P. 1–21.

Insights into the Functioning of the D-amino Acid Transaminase from *Haliscomenobacter Hydrossis* via a Structural and Spectral Analysis of its Complex with 3-Aminooxypropionic Acid

A. K. Bakunova[1], I. O. Matyuta[1], A. Yu. Nikolaeva[1,2], K. M. Boyko[1], A. R. Khomutov[3], E. Yu. Bezsudnova[1*], V. O. Popov[1,4]

[1]Bach Institute of Biochemistry, Research Centre of Biotechnology of the Russian Academy of Sciences, Moscow, 119071 Russian Federation

[2]National Research Centre "Kurchatov Institute", Moscow, 123182 Russian Federation

[3]Engelhardt Institute of Molecular Biology, Russian Academy of Sciences, Moscow, 119991 Russian Federation

[4]Department of Biology, Lomonosov Moscow State University, Moscow, 119234 Russian Federation

*E-mail: eubez@inbi.ras.ru

Received August 21, 2024; in final form, September 18, 2024

DOI: 10.32607/actanaturae.27496

ABSTRACT **Pyridoxal-5'-phosphate-dependent enzymes play a crucial role in nitrogen metabolism. Carbonyl compounds, such as O-substituted hydroxylamines, stand out among numerous specific inhibitors of these enzymes, including those of practical importance, because they react with pyridoxal-5'-phosphate in the active site of the enzymes to form stable oximes. O-substituted hydroxylamines mimic the side group of amino acid substrates, thus providing highly potent and specific inhibition of the corresponding enzymes. The interaction between D-amino acid transaminase from bacterium *Haliscomenobacter hydrossis* and 3-aminooxypropionic acid was studied in the present work. The structural and spectral analysis of the complex of this transaminase with 3-aminooxypropionic acid allowed us to clarify some features of the organization and functioning of its active site and illustrate one of the mechanisms of inhibition by the specific substrate, D-glutamic acid.**

KEYWORDS **transaminase, enzymatic catalysis, crystal structure, inhibitor, 3-aminooxypropionic acid.**

ABBREVIATIONS **NADH – reduced nicotinamide adenine dinucleotide; PLP – pyridoxal-5'-phosphate; TA – transaminase; TA_Halhy – D-amino acid transaminase from *Haliscomenobacter hydrossis***

INTRODUCTION

Pyridoxal-5'-phosphate (PLP)-dependent transaminases (aminotransferases, TAs, EC [2.6.1.X]) catalyze the transfer of an amino group from amino acid or amine to keto acid or ketone to form a new amino acid/amine and keto acid/ketone [1, 2]. Enzymatic transamination is a sequential double displacement process involving the intermediate transfer of an amino group to the PLP cofactor, giving rise to pyridoxamine-5'-phosphate, which acts as an amino group donor in the second half-reaction. Two substrates (the amino acid and keto acid) sequentially bind to the same active site region; all the reaction stages are reversible [1, 3]. Transaminases have successfully been used as stereoselective catalysts of amino group transfer for asymmetric amination of compounds carrying a keto group and for separation of chiral primary amines [4, 5]. Only two of the seven types of polypeptide chain folding of PLP-dependent enzymes (fold types I and IV) are characteristic of transaminases. The mechanism of catalysis and the structure of a functional dimer transaminase have been intensively studied for fold type I (*S*)-selective transaminases. Fold type IV transaminases have been characterized to a lesser extent. Interestingly, both (*S*)-selective (transaminases of branched L-amino acids) and (*R*)-selective enzymes (D-amino acid transaminases and (*R*)-amine:pyruvate

transaminases) have been found among them. It is (*R*)-selectivity that has re-kindled interest in the study of fold type IV transaminases over the past decade.

Carbonyl compounds, including hydroxylamine derivatives, are typical inhibitors of PLP-dependent enzymes. One of the algorithms for designing high-efficient and selective inhibitors from hydroxylamine esters (R-ONH_2) is to use derivatives mimicking the side group structure of amino acid substrates. The functional groups in the O-substituted hydroxylamine radical ensure substrate-like binding of the inhibitor to the enzyme active site, while the reactive aminooxy group interacts with PLP to form oxime. This approach allows one to produce inhibitors with a nanomolar binding constant not only for TAs such as aspartate aminotransferase [6, 7], but also for decarboxylases specific for glutamic acid [8], ornithine [9], and arginine [10]. It is noteworthy that the use of hydroxylamine-containing analogs of putrescine and agmatine enables selective inhibition of closely related ornithine and arginine decarboxylases [10]. The structural similarity of external aldimine, one of the intermediates in PLP-catalyzed amino acid transformations, and PLP oxime formed by substrate-/product-like hydroxylamines was confirmed for the first time by X-ray diffraction analysis of the enzyme inhibitor complexes of aspartate aminotransferase [6, 7]. Later, similar studies were performed for gamma-aminobutyric acid transaminase [11], ornithine decarboxylase [12], and D-amino acid transaminase [13]. The structures of the complexes of PLP-dependent enzymes with such hydroxylamine derivatives make it possible to analyze the structure, as well as the features, of substrate binding and functioning of the enzyme active site. In the present study, this approach was employed for investigating D-amino acid transaminase from *Haliscomenobacter hydrossis* (TA_Halhy). TA_Halhy belongs to the group of fold type IV transaminases and efficiently catalyzes transamination reactions between D-amino acids and α-keto acids; specific activity in the reaction between D-glutamic acid and pyruvate in 50 mM potassium phosphate buffer (pH 8.0) hits record high values for TAs: 380 ± 10 μmol/min per mg of protein at 40°C [14, 15]. The structure of this enzyme, the dimer being its functional unit, has been identified (*Fig. 1A*). Like for the studied fold type IV TAs, the active site of TA_Halhy can be subdivided into two parts (the O- and P-pockets); the amino acid residues of these pockets are involved in substrate binding, thus being responsible for the stereospecificity of catalytic transformation (*Fig. 1B*). TA_Halhy stands out among the known fold type IV TAs by featuring four positively charged functional groups in its active site (side groups of amino acids Arg28*, Arg90, Arg179, and Lys241) [14, 16] (*Fig. 1B*).

The results of an analysis of the structure of the TA_Halhy complex with an inhibitor, D-cycloserine, suggested that the side groups of Arg28* and Arg179 residues are involved in substrate binding [17]. Since we failed to identify the structure of the TA_Halhy complex with substrates (because of the high efficiency of amino acid conversion in TA_Halhy-catalyzed reactions, crystallization with substrates yields an apoenzyme), research into the structure of the TA_Halhy active site was continued by analyzing the interaction between the enzyme and 3-aminooxypropionic acid (an analog of the D-glutamic acid substrate) by UV/Vis spectrophotometry and X-ray diffraction

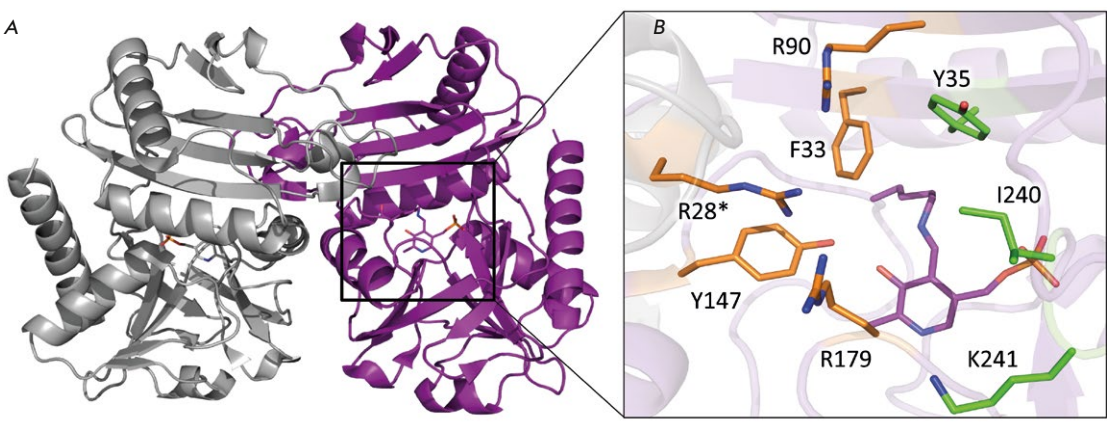

Fig. 1. The overall structure of TA_Halhy. (*A*) TA_Halhy homodimer; (*B*) active site of TA_Halhy. O-pocket residues are colored in orange; P-pocket residues are colored in green. The PLP molecule is colored in purple. * – residues of the adjacent subunit of the function dimer

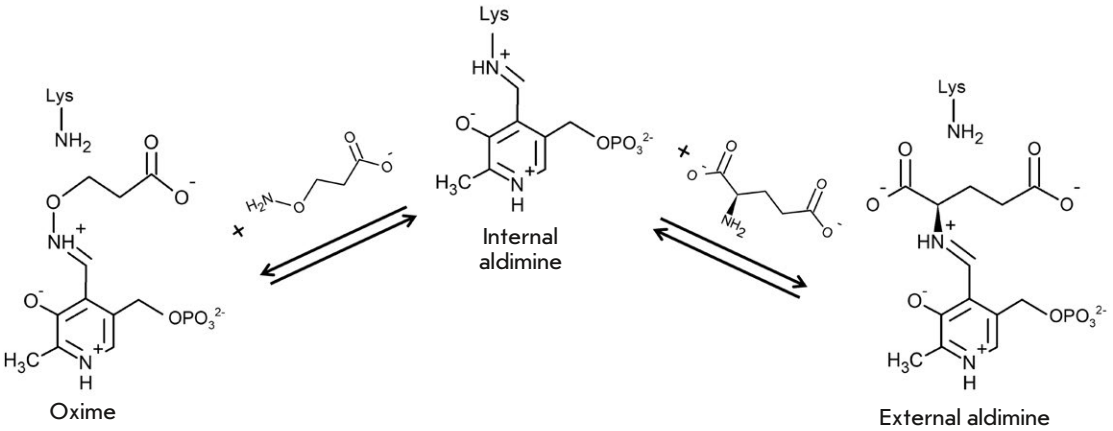

Fig. 2. Scheme of the interactions of internal aldimine (holoenzyme) of TA_Halhy with 3-aminooxypropionic acid (an oxime is formed) and D-glutamic acid (an external aldimine is formed)

analysis. 3-Aminooxypropionic acid was shown to interact with PLP in the active site of TA_Halhy to form an oxime that mimics the external aldimine of PLP and D-glutamic acid (*Fig. 2*); therefore, successful crystallization and solving the complex's structure make it possible to identify the functional groups involved in the binding of this specific substrate.

MATERIALS AND METHODS

Expression and purification of recombinant TA_Halhy

Purified active recombinant TA_Halhy was prepared according to the procedure described previously [14]. The purity and homogeneity were controlled electrophoretically in denaturing polyacrylamide gel (SDS-PAAG). TA_Halhy concentration was determined spectrophotometrically at 280 nm.

Spectral analysis

The PLP form of TA_Halhy (holoenzyme) was prepared by incubating the enzyme (2.5 mg/mL, or 74 μM) in 50 mM potassium phosphate buffer (pH 8.0) with excess PLP (700 μM) in the presence of 10 mM α-ketoglutarate during 30 min. Low-molecular-weight components were removed from the holoenzyme by transfer into 50 mM potassium buffer (pH 8.0) using a HiTrap Desalting column (Cytiva, USA) equilibrated in the same buffer.

3-Aminooxypropionic acid (10 mM) was added to the holoenzyme (0.85 mg/mL, or 25 μM) in 50 mM potassium phosphate buffer (pH 8.0), and the mixture was allowed to stand for 60 min. The protein fraction was separated from the low-molecular-weight components on the HiTrap Desalting column. The fraction of low-molecular-weight components was also obtained by ultrafiltration using a centrifugal concentrator (30 kDa MWCO, Millipore, USA). The absorption spectra were recorded in 50 mM potassium phosphate buffer, pH 8.0, using an Evolution 300 UV-Vis spectrophotometer (Thermo Scientific, USA).

Substrate inhibition

The TA_Halhy-catalyzed transamination reaction was conducted in 50 mM potassium phosphate buffer, pH 8.0, at 40°C with substrates D-alanine (40 mM) and α-ketoglutarate or D-glutamic acid and pyruvate (2.5 mM) supplemented with 30 μM PLP, 0.33 mM NADH, and 5 μg/mL lactate dehydrogenase (specific activity, 200 μmol/min per mg of protein). Lactate dehydrogenase was stable under the conditions of the transamination reaction. No heat inactivation of TA_Halhy was observed at 40°C [14].

Preparing crystals of the TA_Halhy complex with oxime of PLP and 3-aminooxypropionic acid

Crystals of the complex were prepared by co-crystallization of the TA_Halhy holoenzyme with 12 mM 3-aminooxypropionic acid in the presence of excess PLP (6 mM) under the following conditions: 0.1 M bis-Tris-propane, pH 5.5, 0.2 M $MgCl_2$, 25% PEG 3350.

Collection and analysis of the diffraction data. Structure solution and refinement

Right before the X-ray diffraction experiment, TA_Halhy crystals were placed into a cryosolution containing 25% (v/v) glycerol, along with counter-solution ions; the crystal in a loop sample holder was then frozen in liquid nitrogen vapor. The XRD data recorded at 100 K on the Protein Factory of the synchrotron radiation source at Research Center "Kurchatov Institute" were analyzed using the Dials software [18] from the CCP4 software package [19]. *Table 1* shows the statistics of the recorded dataset. The structure was solved by the molecular replacement method using the MOLREP software [20]. The

Table 1. Statistics for data collection, analysis, and crystallographic refinement of the structure of the TA_Halhy complex with the oxime formed by PLP and 3-aminooxypropionic acid

Study object	TA_Halhy complex
X-ray source	National Research Center "Kurchatov Institute"
Wavelength, Å	0.74503
Temperature, K	100
Analysis	
Space group	C2
Unit cell parameters	a = 88.77 Å, b = 71.23 Å, c = 52.55 Å; α = γ = 90°, β = 101.26°
Resolution, Å	35.34–1.70 (1.73–1.70)
Number of independent reflections	32789 (1795)
Completeness, %	94.9 (98.6)
Rmeas, %	10.1 (54.6)
Mean I/σ(I)	11.4 (1.9)
$CC_{1/2}$, %	99.1 (60.2)
Refinement	
R_{work}, %	16.6
R_{free}, %	21.0
Overall average *B*-factor	17.9
Average *B*-factor for protein	16.8
Average *B*-factor for ligands	16.5
Average *B*-factor for solvent	26.2
Number of non-hydrogen atoms	
Total	2607
Protein	2275
Ligands	23
Solvent	309
Root mean square deviations	
Bond lengths, Å	0.01
Bond angles, °	1.67
Ramachandran plot	
Most favored, %	98.2
Allowed, %	1.8
PDB ID	8YRV

REFMAC5 software was used for refinement [21]. The structure of the holo form of D-acid transaminase from *H. hydrossis* (PDB ID 7P7X) was used as a starting model. Visual analysis of structural data was performed using the Coot [22] and PyMOL Molecular Graphics System, Version 4.6, software (Schrödinger, USA).

RESULTS AND DISCUSSION

Spectral analysis of interactions between TA_Halhy and 3-aminooxypropionic acid

Figure 3 shows the spectra of the holoenzyme TA_Halhy (25 μM) in 50 mM potassium phosphate buffer, pH 8.0, immediately after the addition of 10 mM 3-aminooxypropionic acid and incubation at 25°C for 1 h. The observed changes attest to the formation of the oxime of PLP and 3-aminooxypropionic acid within the active site of TA_Halhy (the spectrum with λ_{max} = 380 nm) and release of the oxime from the active site of the solution (the spectrum with λ_{max} = 333 nm corresponds to the spectrum of the oxime of PLP and H_2NOR in the solution [23]). *Figure 3B* demonstrates that after the transfer to a new buffer and one hour of incubation, the spectrum of TA_Halhy corresponded to the apoenzyme (without PLP and its adducts). Holoenzyme was formed, and TA_Halhy activity was fully restored, after PLP was added to the resulting apoenzyme solution.

The rapid formation of the oxime of PLP and 3-aminooxypropionic acid in the active site of TA_Halhy (*Fig. 3A*, spectrum with λ_{max} = 380 nm) is

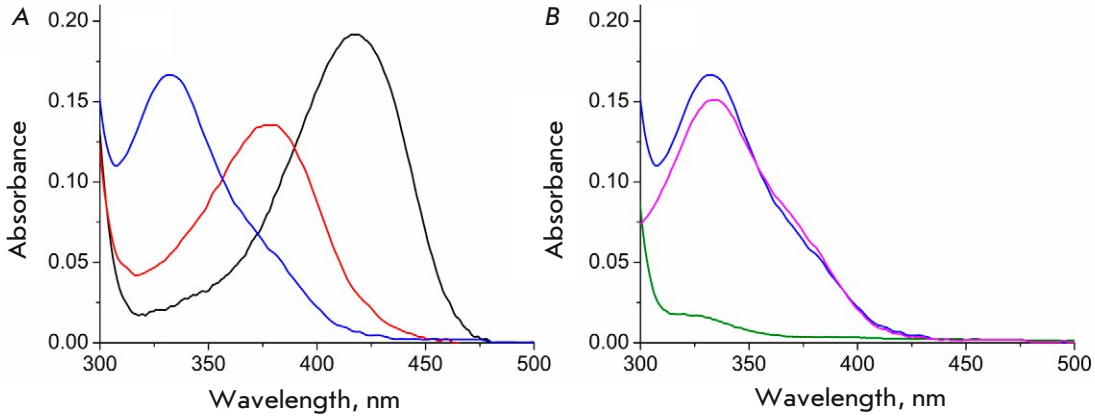

Fig. 3. Spectral changes in TA_Halhy (25 μM) upon addition of 3-aminooxypropionic acid in 50 mM potassium phosphate buffer, pH 8.0, at 25°C: (*A*) the absorption spectra of holoenzyme TA_Halhy before (black), immediately after addition (red), and after 1 h of incubation with 3-aminooxypropionic acid acid (blue); (*B*) the absorption spectra of holoenzyme TA_Halhy after 1 h of incubation with 3-aminooxypropionic acid acid (blue) followed by exchange in 50 mM potassium phosphate buffer, pH 8.0 (green); the absorption spectrum of the low-molecular-weight fraction collected by ultrafiltration (pink)

consistent with knowledge that Schiff bases (in this case, internal aldimine) react with O-substituted hydroxylamines much faster compared to the respective aldehyde [24]. The efficiency of TA inhibition by O-substituted hydroxylamines depends on the structural similarity of the radical of O-substituted hydroxylamine and the side group of the amino acid substrate, as well as the strength of PLP binding to the enzyme's active site [8–10, 25, 26]. Thus, aspartate aminotransferase forms strong oximes with aminooxyacetic and 3-aminooxypropionic acids, which mimic external aldimines with substrates, as well as aspartic and glutamic acids. The carboxylic groups of the inhibitors act as anchors and ensure additional binding of oximes to the enzyme's active site. When excess hydroxylamines are removed, oximes of PLP do not get released from the enzyme active site and adding excess PLP does not restore enzyme activity, either [6]. Contrariwise, TA_Halhy has low affinity with PLP (K_d = 1.9 ± 0.3 μM [16]) and the oxime of PLP is easily released from the active site (*Fig. 3*). Similar dissociation was observed upon interaction between TA_Halhy, D-cycloserine [17], and phenylhydrazine [16], thus attesting to the open active site of TA_Halhy, which seems to retain its open conformation during catalytic transformations [14, 16]. Dissociation of the complex with the oxime leads to the accumulation of the apoenzyme (*Fig. 3B*). Adding PLP to the TA_Halhy complex with oxime causes enzyme reactivation; an active holoenzyme is formed as a result of complex dissociation and release of the oxime from the active site yielding the apoenzyme, followed by interaction between the apoenzyme and the added PLP: therefore, inhibition by 3-aminooxypropionic acid is reversible. The reactivation of TA_Halhy after PLP had been added was consistent with the apoenzyme stability that had been demonstrated previously [15].

We successfully crystallized the TA_Halhy complex with the oxime of PLP and 3-aminooxypropionic acid in the active site. A set of diffraction data has been collected in the XRD experiment; the structure of the TA_Halhy complex has been solved and refined. The structures of the holoenzyme and complex with the oxime are well-superposed (RMSD for Cα atoms is 0.31). Differences are mostly observed for the positions of loops. Importantly, the carboxyl group of the oxime of PLP and 3-aminooxypropionic acid is located in the O-pocket, although in fold type IV D-amino acid transaminases the side group of the substrate binds within the P-pocket, while the O-pocket binds the α-carboxyl group of substrates (D-amino acid or keto acid), which forms hydrogen bonds with the functional groups of the active site [27, 28]. In the resulting structure, the carboxyl group of the oxime forms hydrogen bonds with the guanidine groups of Arg28* and Arg179 residues. The Arg90 and Lys241 residues are not involved in the binding of the carboxyl group; the side group positions in all the aforementioned residues remain unchanged. The geometry of the holoenzyme active site is retained in the structure of the complex with oxime (*Fig. 4A*).

The observed adduct position in the active site of TA_Halhy mimics substrate inhibition rather than the formation of an external aldimine with D-glutamic acid as a specific substrate. Substrate inhibition is known to accompany transaminase catalysis because of the similarities in substrate (amino

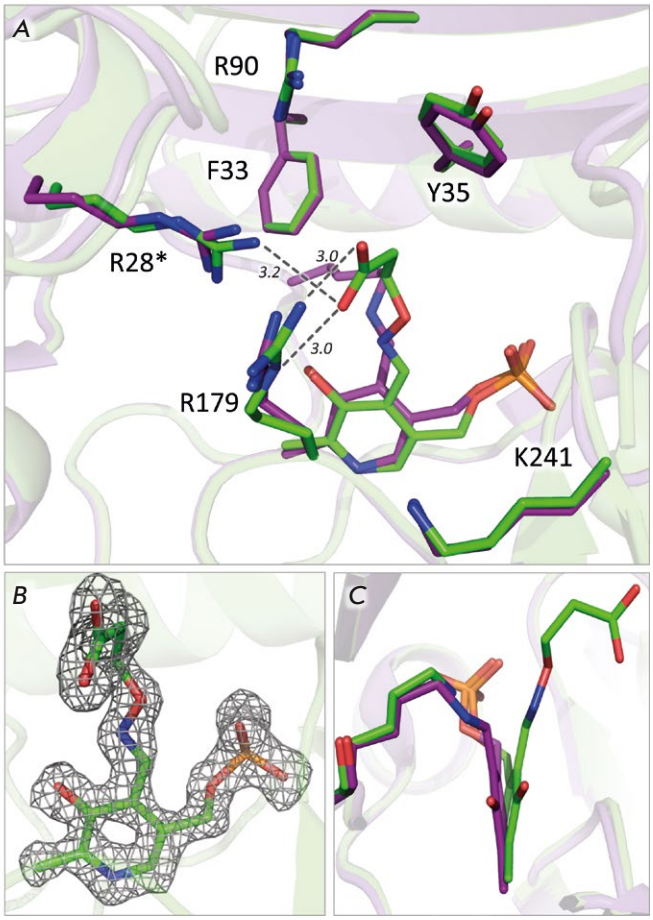

Fig. 4. The active site of the complex of TA_Halhy with 3-aminooxypropionic acid: (*A*) superposition of the structures of the complex (green; PDB ID 8YRV) and holoenzyme TA_Halhy (purple; PDB ID 7P7X), distances are given in angstroms and depicted with dashed lines; (*B*) the "omit" electron density map (Fo-Fc) of the oxime of PLP and 3-aminooxypropionic acid is depicted at the 3σ level; (*C*) superposition of the PLP in the holoenzyme (purple) and in the complex with oxime (green)

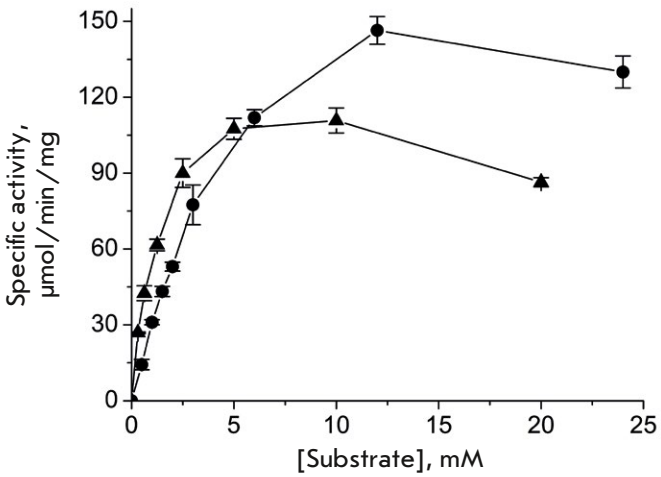

Fig. 5. Substrate inhibition of TA_Halhy in the transamination reaction between D-glutamic acid and 2.5 mM pyruvate (•) and between α-ketoglutarate and 40 mM D-alanine (▲) in 50 mM potassium phosphate buffer, pH 8.0, at 40°C. Bars denote the standard deviation

acids and keto acids) binding. TA_Halhy is inhibited by D-glutamic acid and α-ketoglutarate at substrate concentrations as low as millimolars (*Fig. 5*). At least two inhibition mechanisms are known: (1) D-glutamic acid binds to the active site containing a pyridoxamine-5'-phosphate instead of the keto substrate and (2) the position of the α-carboxyl group is occupied by the γ-carboxyl group of D-glutamic acid or α-ketoglutarate. This very type of binding is observed in the complex (*Fig. 4A*). This nonproductive inhibitory binding is consistent with the high observed dissociation constant of the TA_Halhy complex with D-glutamic acid determined using the half-reaction method (K_d = 1.8 ± 0.4 mM [29]).

It is also worth mentioning that the position of the PLP molecule in the complex's structure is changed: in the oxime complex, the PLP molecule is tilted towards the active site entrance by 18° along the N1–C6 axis (*Fig. 4B,C*). The change in the cofactor position is observed as the internal aldimine is converted to an external one (*Fig. 2*) [13, 27]. These findings support the hypothesis that the cofactor, in the form of an internal aldimine, is under the stress relieved when an external aldimine (rupturing of a covalent bond with the side group of the catalytic lysine residue [30]), or oxime in the case of 3-aminooxypropionic acid, is formed. Interestingly, the active site of TA_Halhy remains open after oxime formation, which is proved by the fact that the oxime is released into the solution after one hour of incubation of the enzyme in the presence of excess 3-aminooxypropionic acid (see above). Open configuration of the active site was observed previously for TA_Halhy in complexes with phenylhydrazine and D-cycloserine; Open configuration of the active site was also observed for the homologous D-amino acid transaminase from *Aminobacterium colombience* in complexes with D-glutamic acid and 3-aminooxypropionic acid [13], as well as for the canonical D-amino acid transaminase from *Bacillus* sp. *YM-1* in complex with D-alanine [27]. In other words, stereoselective transamination in D-amino acid transaminases seems to take place without active site closure (separation from the solvent), unlike in the case of fold type I transaminases [7].

CONCLUSIONS

The following conclusions can be drawn from the study of the interaction between D-amino acid transaminase holoenzyme from *H. hydrossis* and 3-aminooxypropionic acid: (1) inhibition by 3-aminooxypropionic acid is reversible; (2) the active site of transaminase remains open after substrates/inhibitors binding; (3) coordination of the carboxyl group of the oxime in the O-pocket confirms that the Arg28* and Arg179 residues are involved in substrate binding; however, the observed position of the oxime corresponds to substrate inhibition, when a substrate (α-ketoglutarate and D-glutamic acid) binds nonproductively (via the γ-carboxyl group in the O-pocket of the active site), and the reactive amino group of the substrate faces away from PLP and the side group of the catalytic lysine residue. ●

This work was supported by the Russian Science Foundation (grant No. 23-74-30004) in the part of conducting spectral and kinetic studies. The work was supported by the Ministry of Science and Higher Education of the Russian Federation in the part of complex crystallization, X-ray diffraction analysis experiment, solving and refining the structure.

REFERENCES

1. Eliot A.C., Kirsch J.F. // Annu. Rev. Biochem. 2004. V. 73. P. 383–415.
2. Steffen-Munsberg F., Vickers C., Kohls H., Land H., Mallin H., Nobili A., Skalden L., van den Bergh T., Joosten H.-J., Berglund P., Höhne M., Bornscheuer U.T. // Biotechnol. Adv. 2015. V. 33. P. 566–604.
3. Braunstein A.E. Amino Group Transfer. The Enzymes / Ed. Boyer P.D. London: Acad. Press, 1973. V. 9. P. 379–481.
4. Winkler C.K., Schrittwieser J.H., Kroutil W. // ACS Cent. Sci. 2021. V. 7. P. 55–71.
5. Madsen J.Ø., Woodley J.M. // ChemCatChem. 2023. V. 15. № 13. P. e202300560.
6. Delbaere L.T.J., Kallen J., Markovic-Housley Z., Khomutov A.R., Khomutov R.M., Karpeisky M.Y., Jansonius J.N. // Biochimie. 1989. V. 71. P. 449–459.
7. Markovic-Housley Z., Schirmer T., Hohenester E., Khomutov A.R., Khomutov R.M., Karpeisky M.Y., Sandmeier E., Christen P., Jansonius J.N. // Eur. J. Biochem. 1996. V. 236. P. 1025–1032.
8. Satshenko L.P., Severin E.S., Khomutov R.M. // Biochemistry (Moscow). 1968. V. 33 № 1. P. 142–147.
9. Khomutov R.M., Denisova G. F., Khomutov A.R., Belostotskaja K.M., Schlosman R.B., Artamonova E. Yu. // Bioorg. Khimia (Moscow) 1985. V. 11. № 11. P. 1574–1576.
10. Hyvönen M.T., Keinänen T.A., Nuraeva G.K., Yanvarev D. V., Khomutov M., Khurs E.N., Kochetkov S.N., Vepsäläinen J., Zhgun A.A., Khomutov A.R. // Biomolecules. 2020. V. 10. P. 406.
11. Liu W., Peterson P.E., Carter R.J., Zhou X., Langston J.A., Fisher A.J., Toney M.D. // Biochemistry. 2004. V. 43. P. 10896–10905.
12. Zhou X.E., Suino-Powell K., Schultz C.R., Aleiwi B., Brunzelle J.S., Lamp J., Vega I.E., Ellsworth E., Bachmann A.S., Melcher K. // Biochem. J. 2021. V. 478. P. 4137–4149.
13. Shilova S.A., Matyuta I.O., Khrenova M.G., Nikolaeva A.Y., Klyachko N.L., Minyaev M.E., Khomutov A.R., Boyko K.M., Popov V.O., Bezsudnova E.Y. // Biochem. J. 2023. V. 480. P. 1267–1284.
14. Bakunova A.K., Nikolaeva A.Y., Rakitina T.V., Isaikina T.Y., Khrenova M.G., Boyko K.M., Popov V.O., Bezsudnova E.Y. // Molecules. 2021. V. 26. P. 5053.
15. Bakunova A.K., Isaikina T.Y., Popov V.O., Bezsudnova E.Y. // Catalysts 2022. V. 12. P. 1551.
16. Bakunova A.K., Matyuta I.O., Minyaev M.E., Isaikina T.Y., Boyko K.M., Popov V.O., Bezsudnova E.Y. // Arch. Biochem. Biophys. 2024. V. 756. P. 110011.
17. Bakunova A.K., Matyuta I.O., Nikolaeva A.Y., Boyko K.M., Popov V.O., Bezsudnova E.Yu. // Biochem. 2023. V. 88. P. 687–697.
18. Winter G., Waterman D.G., Parkhurst J.M., Brewster A.S., Gildea R.J., Gerstel M., Fuentes-Montero L., Vollmar M., Michels-Clark T., Young I.D., et al. // Acta Crystallogr. Sect. D Struct. Biol. 2018. V. 74. P. 85–97.
19. Collaborative Computational Project, Number 4 // Acta Crystallogr. D. Biol. Crystallogr. 1994. V. 50. P. 760–763.
20. Vagin A., Teplyakov A. // J. Appl. Crystallogr. 1997. V. 30. P. 1022–1025.
21. Murshudov G.N., Skubák P., Lebedev A.A., Pannu N.S., Steiner R.A., Nicholls R.A., Winn M.D., Long F., Vagin A.A. // Acta Crystallogr. Sect. D Biol. Crystallogr. 2011. V. 67. P. 355–367.
22. Emsley P., Lohkamp B., Scott W.G., Cowtan K. // Acta Crystallogr. Sect. D Biol. Crystallogr. 2010. V. 66. P. 486–501.
23. Morozov V.Y. Vitamin B – pyridoxal phosphate. Part A. / Eds Dolphin D., Poulson R., Avramovic O. New York: John Wiley & Sons, 1986. P. 131–222.
24. Dirksen A., Dawson P.E. // Bioconjug. Chem. 2008. V. 19. P. 2543–2548.
25. Castro-Oropeza R., Pino-Ángeles A., Khomutov M.A., Urdiales J.L., Moya-García A.A., Vepsäläinen J., Persson L., Sarabia F., Khomutov A., Sánchez-Jiménez F. // Amino Acids. 2014. V. 46. P. 621–631.
26. Khomutov A.R., Gabibov A.G., Khurs E.N., Tolosa E.A., Shuster A.M., Goryachenkova E.V., Khomutov R.M. Biochemistry of Vitamin B6 / Eds Christen P., Korpela T. Basel: Birkhauser, 1987. P. 317–321.
27. Peisach D., Chipman D.M., van Ophem P.W., Manning J.M., Ringe D. // Biochemistry. 1998. V. 37. P. 4958–4967.
28. Shilova S.A., Khrenova M.G., Matyuta I.O., Nikolaeva A.Y., Rakitina T.V., Klyachko N.L., Minyaev M.E., Boyko K.M., Popov V.O., Bezsudnova E.Y. // Molecules. 2023. V. 28. P. 2109.
29. Bakunova A.K., Kostyukov A.A., Kuzmin V.A., Popov V.O., Bezsudnova E.Y. // Biochim. Biophys. Acta – Proteins Proteomics. 2023. V. 1871. P. 140886.
30. Hayashi H., Mizuguchi H., Miyahara I., Islam M.M., Ikushiro H., Nakajima Y., Hirotsu K., Kagamiyama H. // Biochim. Biophys. Acta – Proteins Proteomics. 2003. V. 1647. P. 103–109.

Specific Activation of the Expression of Growth Factor Genes in Expi293F Human Cells Using CRISPR/Cas9-SAM Technology Increases Their Proliferation

P. A. Bobrovsky[1,2*], E. N. Grafskaia[1], D. D. Kharlampieva[1], V. A. Manuvera[1,2], V. N. Lazarev[1,2]
[1]Lopukhin Federal Research and Clinical Center of Physical-Chemical Medicine of Federal Medical Biological Agency, Moscow, 119435 Russian Federation
[2]Moscow Institute of Physics and Technology, Moscow, 141701 Russian Federation
[*]E-mail: pbobrovskiy@gmail.com
Received April 18, 2024; in final form, August 02, 2024
DOI: 10.32607/actanaturae.27415

ABSTRACT **Human cell lines play an important role in biotechnology and pharmacology. For them to grow, they need complex nutrient media containing signaling proteins — growth factors. We have tested a new approach that reduces the need of cultured human cell lines for exogenous growth factors. This approach is based on the generation of a modified cell with a selectively activated gene expression of one of the endogenous growth factors: IGF-1, FGF-2, or EIF3I. We modified the Expi293F cell line, a HEK293 cell line variant widely used in the production of recombinant proteins. Gene expression of the selected growth factors in these cells was activated using the CRISPR/Cas9 technology with the synergistic activation mediators CRISPR/Cas9-SAM, which increased the expression of the selected genes at both the mRNA and protein levels. Upon culturing under standard conditions, the modified lines exhibited increased proliferation. A synergistic effect was observed in co-culture of the three modified lines. In our opinion, these results indicate that this approach is promising for efficient modification of cell lines used in biotechnology.**
KEYWORDS **CRISPR/Cas9-SAM, HEK293, proliferation, IGF-1, FGF-2, EIF3I.**
ABBREVIATIONS **FBS – fetal bovine serum; HEK293 – human embryonic kidney 293 cell line; IGF-1 – insulin-like growth factor 1; FGF-2 – fibroblast growth factor 2; EIF3I – eukaryotic translation initiation factor 3 subunit I; SAM – synergistic activation mediator; sgRNA – single-guide RNA.**

INTRODUCTION

Mammalian, in particular human, cell lines are of great importance in pharmacology, biotechnology, and basic research. Immortalized cell lines are cultured *in vitro* like microorganisms, but at the molecular level, they retain virtually all the features of the cells of the organism from which they are derived. However, unlike bacteria and yeast, mammalian cell lines are much more sensitive to culture conditions and nutrient medium composition. Apart from low-molecular compounds, these media should contain special signaling proteins that ensure cell proliferation, as a necessity. Upon routine culturing, these components are added to the medium, together with fetal bovine serum (FBS) that has variable composition and is expensive. Furthermore, the use of serum is unacceptable in the production of recombinant proteins for medical purposes, given the low replicability of the results obtained and the existing restrictions on the use of components of animal origin [1, 2]. In addition, FBS negatively affects suspension culture, which requires the introduction of additional components or transition to adhesion culture and increases the cost of production by orders of magnitude [3]. The proteins necessary for normal cell growth can be added to the nutrient medium or produced by the cells. Because the cost of media and growth factors constitutes the bulk of the costs when culturing eukaryotic cells, the transition to culture in basic media can significantly reduce the cost of producing recombi-

nant proteins suitable for biopharmaceutical applications. The second important point is a short half-life of growth factors in the medium, which significantly increases the cost of long-term culture in bioreactors [4]. Therefore, a pressing issue is how to modify cell lines to boost the expression of the genes of the key growth factors that help to maintain the normal proliferation of cells capable of growing and producing recombinant proteins in minimal nutrient media.

More than 70% of the recombinant proteins produced in eukaryotic expression systems are harvested in cultures of Chinese hamster ovary (CHO) cells [5]. Despite the fact that this cell line exhibits good proliferative activity and can produce recombinant proteins in large quantities, there are some limitations to its use. Some post-translational modifications of the proteins in CHO cells, such as the glycosylation pattern, are not typical of human proteins [6]. This circumstance may potentially render CHO-derived products immunogenic to humans [7]. One of the alternatives to CHO cells is the human HEK293 cell line. This line is better suited to the production of biotherapeutic drugs with post-translational modifications typical of human proteins. The HEK293 cell line, despite its epithelial origin and adhesive nature, has been adapted to suspension culture in serum-free or chemically defined media and is used to produce recombinant proteins both in laboratories and on an industrial scale [8]. Studies on the optimization of nutrient media have led to the development of several commercial formulations of chemically defined media and various additives in the form of animal-derived components, which have made possible the production of recombinant proteins in HEK293 cells in large quantities [9]. However, this cell line continues to lag behind the CHO line, which is a leader in the production of pharmaceutical recombinant proteins. HEK293 is inferior in proliferative activity, cultivation time, and product yield [10]. Activation of the expression of key growth factor genes in HEK293 cells may potentially increase their proliferative activity and productivity. The production of endogenous growth factors may help avoid the use of culture media containing components of animal origin and significantly reduce the cost of production compared to the use of commercial media containing purified growth factors. It should be noted that the use of recombinant growth factors as an additive to imitate the blood serum composition makes culture media very expensive, in particular due to the rapid degradation of the factors in the culture medium [11].

Given the abovementioned considerations, we set out to generate HEK293 cell lines with activated expression of one of three genes encoding the IGF-1, FGF-2, and EIF3I growth factors of cells. Positive effects of increased production of these growth factors on cell culture proliferation or the production of target recombinant proteins have been reported [12–15]. The Expi293F line, a suspension HEK293 variant adapted to efficient production of recombinant proteins, was selected for modifications [16]. Expression of growth factor genes was activated using the synergistic activation mediator technology (CRISPR/Cas9-SAM), which is a variant of the CRISPR/Cas9 genome editing system. This system enhances the expression of target genes [17]. The proposed approach, on the one hand, enables very effective achievement of high expression levels of the target genes [18], and, on the other hand, selection of several options for fine-tuning the expression of growth factor genes. In addition, the use of the CRISPR/Cas9-SAM technology enables rapid activation of the expression of other growth factors and an analysis of their impact on the ability of a culture to grow in a basic serum-free nutrient medium. We demonstrate an activation of the expression of selected genes in the produced cell lines at both the mRNA and protein levels. Activation of the expression of growth factor genes increased the proliferation of the modified cell lines. The results obtained confirm the efficiency of the chosen approach in the generation of new human cell lines that can be used in biopharmaceuticals.

EXPERIMENTAL

Bacterial strains and cell lines

The *E. coli* Top10 strain (Invitrogen, USA), the *F– mcrA Δ(mrr-hsdRMS-mcrBC) φ80lacZΔM15 ΔlacX74 nupG recA1 araD139 Δ(ara-leu)7697 galE15 galK16 rpsL(Str^R) endA1 λ$^-$* genotype, was used in the genetic engineering procedures.

The Expi293F™ (Gibco, USA) and Phoenix-AMPHO (ATCC CRL-3213) cell lines were used in this study.

Cell line cultivation

For manipulations, the Expi293F cells were placed in adhesive growth conditions. The cells were cultured in DMEM (HiMedia, India) supplemented with 10% FBS (Gibco) and 1.5 μg/mL gentamicin (Gibco) in a CO_2 incubator (Heraeus, Germany) at 37°C, relative humidity ⩾ 80%, and 5% CO_2.

Construction of plasmids for producing lentiviral particles

The CRISPR/Cas9-SAM expression activation system requires three lentiviral vectors that are produced using three plasmids: lenti_sgRNA(MS2)_

puro (Addgene #73795), lenti_MS2-P65-HSF1_Hygro (Addgene #61426), and lenti_dCAS-VP64_Blast (Addgene #61425) [17]. Two of these plasmids are used without further manipulation, and the lenti_sgRNA(MS2)_puro plasmid is designed to carry a short DNA fragment encoding a single-guide RNA (sgRNA) protospacer. Before protospacer sequences were selected, the DNA segments corresponding to the 5'-adjacent regions of the growth factor genes were validated by sequencing. Protospacer sequences were selected using the CHOPCHOP service (https://chopchop.cbu.uib.no/). Six protospacer sequences were selected for the promoter region of each growth factor gene (IGF-1, FGF-2, EIF3I). To produce a vector encoding chimeric sgRNA, the lenti_sgRNA(MS2)_puro vector was treated with the BsmBI restriction endonuclease (Thermo Fisher Scientific, USA) and then ligated with an oligonucleotide duplex corresponding to one of the protospacer sequences (Appendix 1, Appendix 2). Ligation products were cloned into the *E. coli* Top10 strain, and colonies carrying the target construct were selected. In total, we constructed 18 plasmid vectors based on lenti_sgRNA(MS2)_puro, which encoded sgRNAs targeting the promoter regions of the growth factor genes.

Lentivirus production and transduction

For lentivirus assembly, the culture medium of Phoenix-AMPHO cells was replaced with DMEM containing 25 μM chloroquine diphosphate (Sigma, USA) and incubated at 37°C and 5% CO_2 for 5 h. Phoenix-AMPHO cells were transfected simultaneously with four (lenti_dCAS-VP64_Blast/lenti_MS2-P65-HSF1_Hygro/lenti_sgRNA(MS2)_puro/LeGo_G2 (Addgene #25917) [19], pMD2.G (Addgene #12259), and pRSV-Rev, pMDL/pRRE [20]) plasmids using polyethyleneimine: PEI MAX 40K (1 mg/mL, Polysciences, USA) (DNA:PEI ratio = 1:3) according to the previously described technique [21]. After incubation at room temperature for 20 min, the DNA–PEI mixture was added dropwise to the cells and incubated for 6 h. The medium was then changed to Opti-MEM containing 2 mM sodium butyrate (Sigma). After 48 h, the medium containing lentiviruses was filtered through a 0.22-μm filter (TPP, Switzerland), added with 100 μg/mL protamine sulfate (Ellara, Russia), and immediately applied to Expi293F cells for infection. After incubation for 24 h, the medium was replaced with a fresh, complete DMEM medium. After lentiviral transduction, the cells were passaged at least 3 times with an appropriate antibiotic. For lenti_dCAS-VP64-Blast, lenti_MS2-P65-HSF1-Hygro, and lenti_gRNA-puro lentiviruses, we used blasticidin at a concentration of 7 μg/mL, hygromycin at a concentration of 300 μg/mL, and puromycin at a concentration of 2 μg/mL, respectively. To determine the transduction efficiency in the cells after three passages, the expression of the target gene was analyzed.

Quantitative PCR

Transduced cells were removed using 0.05% trypsin with EDTA (Gibco), centrifuged at 500 g for 5 min, and the supernatant was collected. Total RNA was isolated from samples containing approximately 10^6 cells using the Trizol reagent (Thermo Fisher Scientific). Total RNA was treated with 2 enzyme units of DNase I (Thermo Fisher Scientific) in the presence of 20 enzyme units of the ribonuclease inhibitor (Thermo Fisher Scientific). cDNA was synthesized using a RevertAid RT Reverse Transcription kit (ThermoFisher Scientific) with hexamer primers. Real-time PCR was performed on a CFX96 Touch amplifier (BioRad, USA) using a 5X qPCRmix-HS SYBR ready-to-use PCR mixture (Evrogen, Russia). Data were normalized to the *gapdh* reference gene level (Appendix 1).

Measurement of proliferative activity

To visualize an increase in modified cells, 2×10^4 cells were seeded per well of a six-well plate, cultured in DMEM containing 10% FBS in a carbon dioxide incubator at 37°C and 5% CO_2 for 24 h, then transferred to a Celena X High Content Imaging System (Logos Biosystems, Republic of Korea) for live cell imaging, and cultured in an isolated chamber at 37°C and 5% CO_2 for 190 h. As evaporation occurred, the wells were replenished with a nutrient medium. The cells in the GFP channel (470/530 nm) were imaged at 10× magnification every 8 h, 324 fields of view per well, with laser autofocus every 10 fields of view. The images were processed using the Celena EXPLORER software (Logos Biosystems).

To compare the growth of the modified cells in a basic medium free of FBS, we measured the electrical resistance (impedance) between electrodes located at the bottom of the plate wells using an xCELLigence RTCA DP biosensor cell analyzer (Agilent, USA). Changes in impedance depend on the contact area between the cells and an electrode; this parameter is used to automatically calculate the cell index that characterizes the status of the cell culture at a given time. Modified cells were seeded at 10^4 cells per well of a 16-well E-plate (Agilent). After 40 h, the medium was replaced with a fresh DMEM medium containing 1.5 μg/mL gentamicin, with/without 10% FBS. The plates were transferred to the cell

analyzer, and the cells were cultured at 37°C and 5% CO_2 for 120 h. Electrical resistance was measured every 30 min.

The effect of a conditioned medium on the growth of unmodified cells was compared using a colorimetric test with tetrazolium salt. Expi293F cells were seeded at 10^4 per well of a 96-well plate. After 24 h, 100 μL of the conditioned medium from the modified cells was added to each well. To produce the conditioned medium, a monolayer of modified cells was washed with PBS and incubated with the Opti-MEM medium (Gibco) for 48 h. The conditioned medium from Expi293F-dCas9-MS2 cells was used as a control. The medium was collected and concentrated 10-fold using a Microcon 3 kDa centrifugal filter (Millipore, USA). The conditioned medium was mixed with DMEM or the Opti-MEM basic medium containing 1.5 μg/mL gentamicin, an amino acid solution (Himedia), a vitamin solution for RPMI 1640 (Himedia) at a 1 : 10 ratio, and used in the experiments. After 96 h, the cells were added with an MTT solution to a final concentration of 5 μg/mL and the plate was incubated in an incubator for 4 h. A solubilizing solution was added, and absorbance was measured at 570/690 nm on a Multiscan Ascent microplate reader (Thermo Fisher Scientific).

Immunoblot

For Western blot hybridization, the proteins separated during electrophoresis were transferred to a 0.45 μm PVDF membrane (Amersham Biosciences, USA). The transfer was performed in a Hoefer TE77XP chamber (USA) at a current of 0.8 mA/cm^2 and a voltage limited to 30 V for 1 h. To detect IGF-1, the PAA050Hu06 antibody (CloudClone, USA) was used at a dilution of 1 : 1,000; for FGF-2, the PAA551Hu01 antibody (CloudClone) was used at a dilution of 1 : 400; and for EIF3I, the DF12393 antibody (Affinity Biosciences, China) was used at a dilution of 1 : 2,000.

Statistical analysis

The statistical analysis was performed using the Mann–Whitney U test and the Python programming language (version 3.12) (Python Software Foundation, USA).

RESULTS

Generation of an Expi293F intermediate cell line carrying the common components of the CRISPR/Cas9-SAM system

Three components are required to activate gene expression in the CRISPR/Cas9-SAM system. In this regard, lentiviral particles carrying an integration cassette encoding the dCas9-VP64 fusion protein gene, particles encoding the MS2-p65-HSF chimeric protein, and particles encoding sgRNA were produced in Phoenix-AMPHO cells. Expi293F cells were transduced with the lentiviral particles. Transduction using the MS2-P65-HSF1_Hygro vector resulted in the Expi-MS2 precursor line carrying a construct encoding the chimeric MS2-p65-HSF protein. After selection on a hygromycin-containing medium and cloning, a line with high expression of the recombinant *MS2-P65-HSF1* gene was selected using quantitative RT-PCR. Then, the Expi-MS2 line was transduced with dCas9-VP64 lentiviral particles to produce the Expi-dCas9-MS2 precursor line encoding the chimeric MS2-p65-HSF protein and the defective dCas9-VP64 nuclease. After cell transduction, selection was performed on a medium containing hygromycin and blasticidin. Expression of recombinant genes was confirmed by quantitative RT-PCR. Therefore, we succeeded in generating an Expi293F precursor line encoding two components of the CRISPR/Cas9-SAM system and suitable for transduction with lentiviral vectors encoding specific sgRNA.

Generation of cell lines with activated expression of growth factor genes

For the targeted activation of the expression of one of the four selected genes, Expi-dCas9-MS2 cells were transduced with lentiviral particles encoding sgRNA. As described above, we constructed six vectors for each of the selected growth factors and produced lentiviral particles. The vectors were named using the first letter of the gene name and the serial number of the protospacer sequence (Appendix 2). Next, we selected the most promising sgRNAs, which provided increased expression of genes of the IGF-1, FGF-2, and EIF3I growth factors. After transduction, the cells were cultured for 72 h. Transcriptional activation of growth factor genes was determined by quantitative RT-PCR (*Fig. 1*).

IGF-1 gene expression was observed for four out of six sgRNAs. Since *IGF-1* is not expressed in human embryonic kidney cells, it is impossible to assess any changes in its expression. In further study, we investigated the lines generated using i2 and i5 sgRNAs because analysis of these lines by real-time PCR revealed the lowest threshold cycle value (*Table 1*). Analysis of the *FGF-2* gene expression level showed that expression of all sgRNAs enhanced *FGF-2* expression 2- to 5-fold. f5 and f6 sgRNAs were selected for further work (*Table 1*). Also, expression of all six sgRNAs was shown to increase the expression of the EIF3I factor gene 44- to 81-fold. Then, we studied the lines produced using e1 and e6 sgRNAs (*Table 1*).

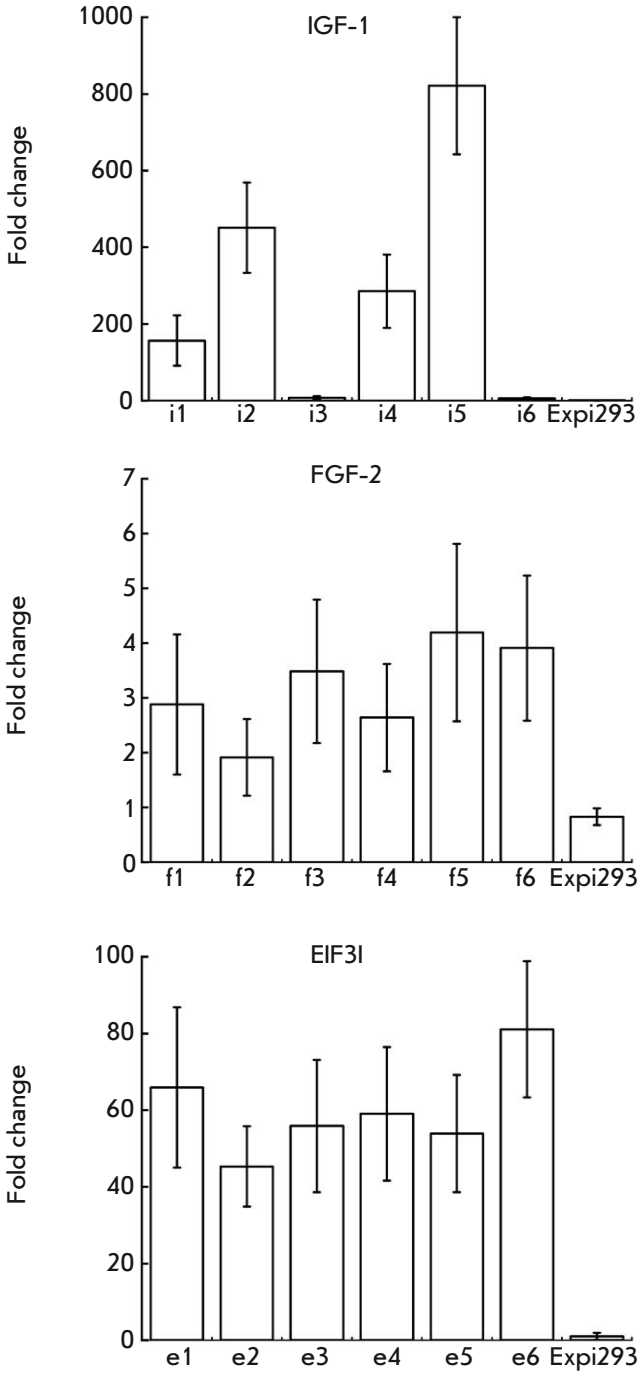

Fig. 1. Fold change of IGF1, FGF2, and EIF3I genes in Expi-dCas9-MS2 cell lines transduced with lentiviral vectors encoding sgRNAs targeting the promoter regions of the respective genes. Lentiviral vectors encoding i1–i6, f1–f6, and e1–e6 sgRNAs (Appendix 2) were used to activate *IGF1*, *FGF2*, and *EIF3I* gene expression. IGF1 expression is not typical of HEK cells; so, fold change was calculated relative to the lowest IGF1 expression in the modified cell line (Expi-dCas9-MS2-i6). FGF2 and EIF3I are expressed in human embryonic kidney cells; so, changes in the expression levels were evaluated relative to the Expi-dCas9-MS2 cell lines. Data are presented as a mean ± SEM

Table 1. Protospacer sequences of guide RNAs that ensure the highest level of target gene expression

Gene	Protospacer	Construct
IGF-1	AGGCATACAATGGAAATAGG	i2
IGF-1	GTGTTTTGTAGATAAATGTG	i5
FGF-2	GGCCGAACCGCCGAACTCAG	f5
FGF-2	CGCGCGACATCAGTCCGGCG	f6
EIF3I	AGGATCCTTCCAGGGCAAAG	e1
EIF3I	GAATGTCTTTCCTTGGAGGG	e6

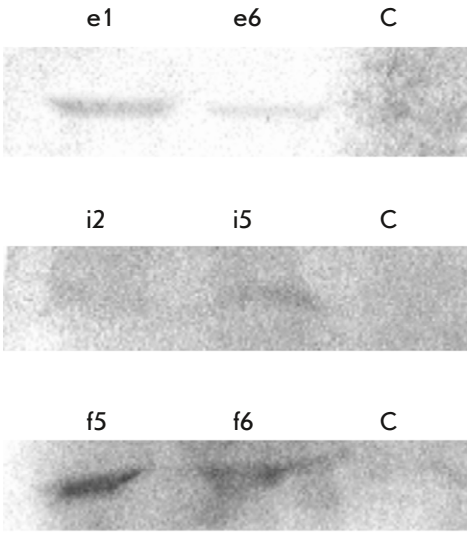

Fig. 2. Western blot analysis of culture medium samples from Expi293F cells with activated expression of growth factor genes. e1 and e6 samples are cells with activated expression of the *EIF3I* gene; f5 and f6 samples are cells with activated expression of the *FGF2* gene; i2 and i5 samples are cells with activated expression of the *IGF1* gene. C is Expi293F cells

Detection of induced accumulation of growth factors using immunoblotting

The expression products of the activated genes were detected by Western blot hybridization using antibodies specific to the growth factors under study. In the case of the secreted growth factors (IGF-1, FGF-2), we analyzed the culture medium; to detect the intracellular growth factor (EIF3I), we analyzed the cell lysates (*Fig. 2*).

The analysis revealed the EIF3, IGF1, and FGF2 factors in the culture medium of the cells transduced with lentiviral vectors encoding e1, e6, i2, i5, f5, and f6 sgRNAs (*Table 1*).

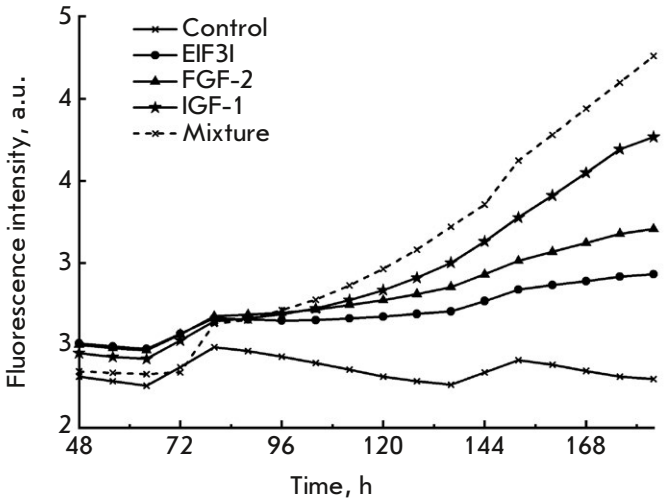

Fig. 3. Proliferative activity of modified cell lines. Expi293F-dCas9-MS2 (GFP) cells cultured in a DMEM medium containing 10% FBS were transduced with lentiviral vectors encoding sgRNAs to activate the expression of growth factor genes. The fluorescence intensity was measured using the Celena X High Content Imaging System. The total fluorescence intensity in each field of view was assessed using the FIJI software [22]. The control is Expi293F-dCas9-MS2 (GFP) cells. EIF3I, FGF-2, and IGF-1 are cells with increased expression of the corresponding growth factor genes, which were produced by transduction with lentiviral vectors encoding e6, f6, and i2 sgRNAs, respectively. The mixture is a co-culture of Expi-IGF1, Expi-FGF2, and Expi-EIF3I cells

Proliferation of modified cell lines

The proliferative activity of the cell lines was studied using the Celena X High Content Imaging System. To facilitate the visualization and subsequent data processing, the Expi293F-dCas9-MS2 cells were transduced with a lentiviral vector encoding the green fluorescent protein and then with the e1, e6, i2, i5, f5, and f6 lentiviral vectors to activate the expression of growth factor genes. Proliferation was assessed by analyzing changes in the fluorescence intensity of the cells due to the accumulation of the eGFP protein in them. In addition to cell lines expressing only one of the studied factors (*IGF-1*, *EIF3I*, and *FGF-2*), mixed culture of all three lines was also studied to assess the potential of a synergistic effect (*Fig. 3*).

As a result, we showed increased proliferative activity of both cells with elevated expression of each of the IGF-1, EIF3I, and FGF-2 factors (*Fig. 4*) and co-cultured cells. In this case, the proliferative activity was higher in co-cultured cells.

Cell proliferation in the basic serum-free medium was studied using the xCelligence RTCA DP cell analyzer, which enables to assess the viability of cell cultures in real time without additional markers and labels. The proliferative activity of co-cultured cells expressing IGF-1, EIF3I, and FGF-2 in a FBS-free DMEM medium was shown to be higher than that of unmodified cells (*Fig. 5A*), but lower than that of un-

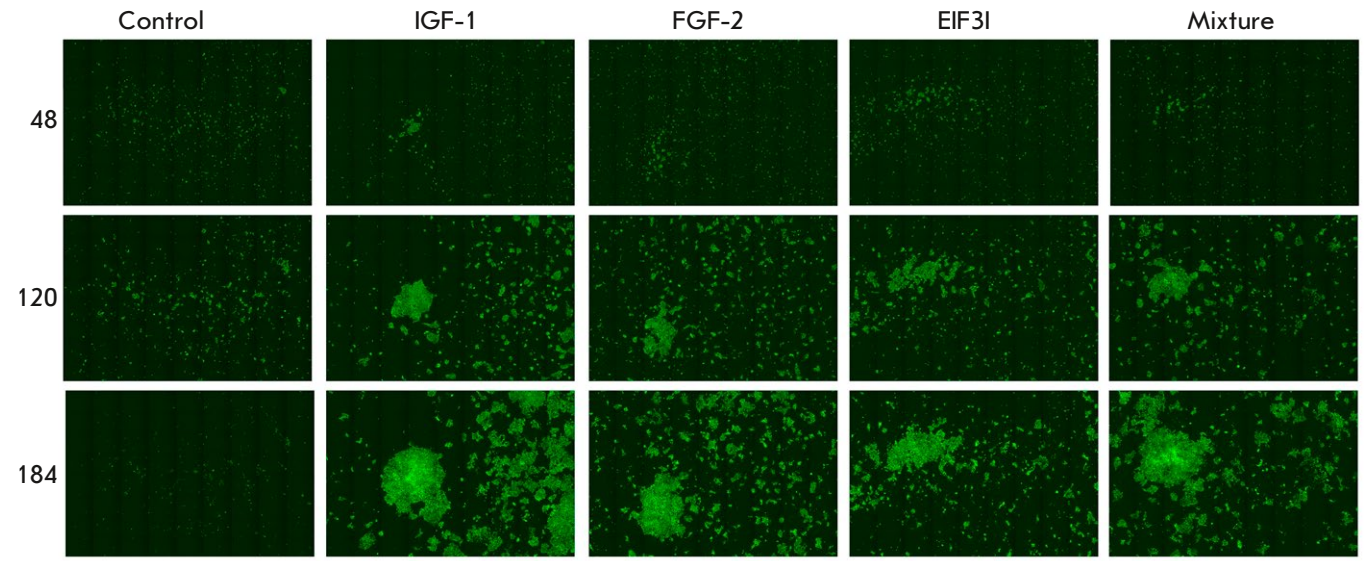

Fig. 4. Comparison of the growth of modified cells expressing IGF-1, FGF-2, and EIF3I growth factor genes. The control is Expi293F-dCas9-MS2 cells transduced with the LeGo-G2 lentiviral vector. IGF-1, FGF-2, and EIF3I are Expi293F-dCas9-MS2 cells transduced with the LeGo-G2 lentiviral vector and the i2, f6, and e6 vectors, respectively. The mixture is a co-culture of Expi-IGF1, Expi-FGF2, and Expi-EIF3I cells. The images were acquired using the Celena X High Content Imaging System. Each image contains 72 fields of view

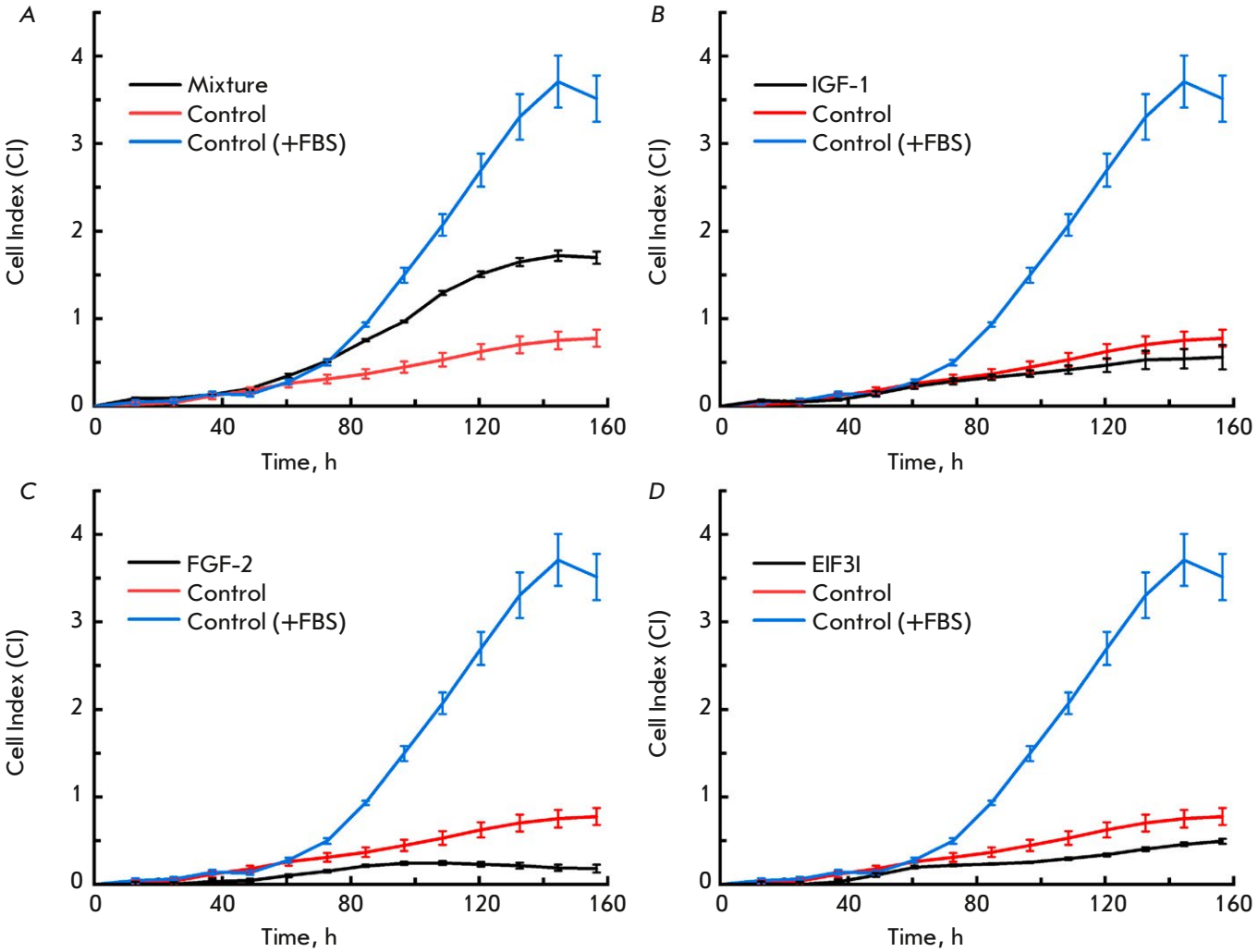

Fig. 5. Analysis of modified cell proliferation in a DMEM basic serum-free medium using real-time impedance measurements. The control is Expi293F-dCas9-MS2 cells cultured in a DMEM medium. The control (+FBS) is Expi293F-dCas9-MS2 cells cultured in a DMEM medium supplemented with 10% FBS. The mixture (*A*) is a co-culture of Expi-IGF1, Expi-FGF2, and Expi-EIF3I cells. IGF1 (*B*), FGF2 (C), and EIF3I (*D*) are Expi293F-dCas9-MS2 cells transduced with the i2, f6, and e6 lentiviral vectors, respectively. Data are presented as a mean ± SEM for $n = 4$

modified cells cultured in a medium containing 10% FBS. In cell cultures producing one of the studied factors, no increase in the proliferative activity was observed (*Fig. 5B–D*).

Thus, co-culture of modified cells expressing IGF-1, EIF3I, and FGF-2 in an FBS-free medium increased their proliferative activity compared with that in the control cells.

The effect of secreted growth factors on intact cell viability

To assess the effect of the secreted growth factors on the viability of intact cells, the conditioned medium was collected, filtered, and added to Expi293F cells. After 96 h, cell viability was measured using a colorimetric test (*Fig. 6*). The metabolic activity of the cells, in contrast to that of the control samples, was shown

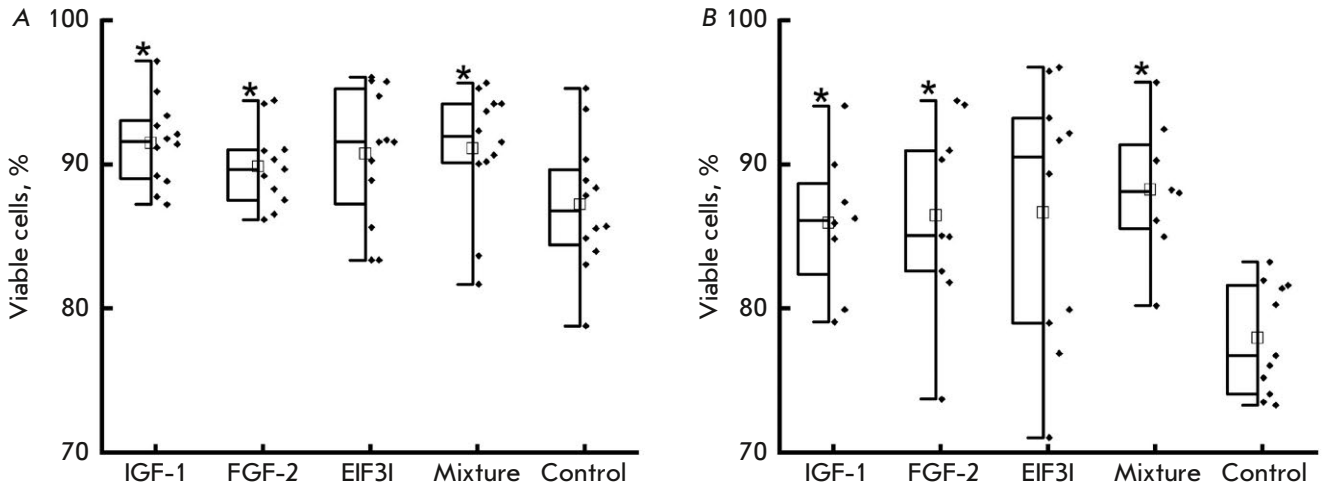

Fig. 6. Viability assay of cells cultured in a conditioned medium from modified cells. IGF1, FGF2, EIF3, Mixture, and Control are conditioned media from the corresponding Expi293F-dCas9-MS2 cell lines transduced with the i2, f6, and e6 lentiviral vectors, respectively. A culture medium from non-modified Expi293F-dCas9-MS2 cells was used as the control. Data are presented as box-and-whisker plots, with the box indicating the 25th and 75th percentiles, the whiskers representing the interquartile range, the black line within the boxes representing the median, the square representing the mean, and the asterisk (*) indicating significant differences from the control at $p < 0.05$. Dots are viability values for each replicate. (*A*) Conditioned medium mixed with a Opti-MEM medium; (*B*) conditioned medium mixed with a DMEM medium free of FBS

to increase after the addition of a conditioned medium from cells expressing individual factors (IGF-1, EIF3I, and FGF-2). The mixture of conditioned media also had a positive effect on the viability of intact cells. The difference in cell viability upon the use of Opti-MEM (*Fig. 6A*) or DMEM (*Fig. 6B*) was insignificant.

DISCUSSION

For an efficient production of recombinant proteins for medical purposes, it is desirable to use human cell cultures capable of undergoing suspension culture in liquid media of a composition that is as simple as possible, ideally free of animal-derived components. A human cell culture is capable of generating proteins whose processing is as close as possible to that in the human body. Suspension culture enables the use of bioreactors for culture growth and relatively easy scaling up of production. Simple medium composition ensures cost-effectiveness, and minimum use of animal-derived additives allows one to avoid contamination of the final product with undesirable impurities. In this study, we tested a fundamental approach that may produce such cell cultures for biotechnological purposes. Our approach is based on selective activation of the expression of endogenous genes encoding protein factors that enhance cell proliferation.

The HEK293 human embryonic kidney cell line is the human cell line most commonly used in biotechnology. We used an Expi293F cell line, a suspension variant of the HEK293 cell line, that was optimized for highly efficient production of recombinant proteins at high densities (the culture remains viable at a density of 5×10^6 cells/mL) and a doubling of time of about 24 h [16]. Expi293F requires a number of growth factors for proliferation [23]. Our approach aims to activate the expression of the corresponding genes in the cells rather than add growth factors to the culture medium. Currently, a powerful tool for selective gene activation is available – the synergistic activation mediator technology (CRISPR/Cas9-SAM), which is a variant of the CRISPR/Cas9 genome editing system. It uses sgRNA that complementarily

binds to a selected region of the promoter of the activated gene. As in genome editing, the Cas9 protein binds to the sgRNA. We used a mutant Cas9 protein lacking nuclease activity and fused with a VP64 tetramer, which enabled recruitment of transcription factors and activation of mRNA synthesis [24].

As the first target, we chose the genes of three factors: IGF-1, FGF-2, and EIF3I. Insulin is known to be necessary for cell proliferation in a serum-free medium [25] and is used in some modified basic media. Along with insulin, there are many insulin-like growth factors (IGFs) that also stimulate cell proliferation. IGF-1 and insulin belong to the same family and have similar tertiary structures. In addition, activation of *IGF-1* gene expression by genomic editing has a positive effect on cell proliferation [26]. Fibroblast growth factors (FGF-1 and FGF-2) are important components of any medium for culturing cells, especially for maintaining their ability to proliferate [12]. These proteins have been produced in *Escherichia coli* and eukaryotic cells. In this case, it has been shown that FGF-1 and FGF-2 are prone to proteolytic degradation and denaturation in the cellular environment, which results in a relatively short half-life of these factors, and the recommended concentrations (10–100 ng/mL) complicate their use as medium additives [27, 28]. Cell culture proliferation is regulated by slowing down or accelerating transitions between different phases of the cell cycle. An increase in the growth rate due to overexpression of genes that promote the G1/S transition, such as eukaryotic initiation factor 3 (EIF3), enhances the production of recombinant proteins. EIF3 is a large multidomain protein the individual subunits of which also exhibit functional activity [13]. EIF3I was earlier shown to be involved in an increasing proliferative activity of cells, as the expression of the gene for this factor was elevated and in decreasing activity in knockout was observed [29]. In addition, there is a report of an increase in the culture growth rate upon overexpression of genes, such as *eIF3I*, that promote the G1/S transition [30].

At the first step, we sequenced the promoter regions of the selected genes. Next, we generated a modified Expi293F cell line expressing the dCAS-VP64 and MS2-P65-HSF1 proteins required for the CRISPR/Cas9-SAM system to function [17]. Expression of the introduced genes at the RNA level was confirmed by quantitative RT-PCR. Then, we modified the produced Expi-dCas9-MS2 line by introducing one of the recombinant sgRNA-encoding genes into its genome. However, sgRNAs specific to different promoter regions may have different degrees of efficiency. Therefore, we selected six sequences of sgRNA protospacer regions for each target to compare their effect on expression activation. The comparison was performed using quantitative RT-PCR. Most likely, each of the growth factors has its own optimal expression level, but determining this level requires a separate, large study. Thus, we selected one sgRNA variant for each gene which provided the highest activation of transcription.

For a number of reasons, transcription activation does not always lead to the accumulation of the corresponding protein. The presence of one of the three proteins in each of the three selected modified cell lines was confirmed by immunoblotting. The presence of the target proteins, the EIF3, IGF-1, and FGF-2 factors, was demonstrated. At this stage of the study, the presence of growth factors was assessed only qualitatively.

At the first stage of the investigation of modified cell proliferation, we used a DMEM basic nutrient medium supplemented with 10% FBS and the Celena X High Content Imaging System. This system provides real-time micro-images of the culture plate surface. In this study, the Expi-IGF1, Expi-FGF2, and Expi-EIF3I cell lines were infected with lentiviral particles encoding the green fluorescent protein. Although the Celena X system enables one to conduct an analysis of cells in transmitted light, the use of fluorescent proteins facilitates the visualization of the cells under study and the total fluorescence intensity can be used as a quantitative indicator. We chose the lentiviral vector, because it ensures integration of the recombinant green fluorescent protein gene into the genomic DNA of the cell and its further transmission during cell division without the losses typical of transient transfection of plasmid DNA. All three modified cell lines turned out to grow faster than the control line (*Figs. 3, 4*). The most profound effect on proliferation was exerted by an increase in the expression of the IGF-1 factor gene. At the same time, co-culture of all three modified lines yielded a greater proliferative effect than that of each line taken individually. An increase in the proliferative activity of cells cultured in a basic serum-free medium was observed only upon co-culture of cells producing all three growth factors, but proliferation of these cells was lower than that upon culture in a medium containing FBS (*Fig. 5*). Enhanced cell growth in co-culture is quite expected, because the entire set of growth factors is required for cell proliferation in culture. Despite this, three factors are not enough to completely switch to the use of basic media free of FBS. In addition, without FBS, there is no increased proliferation in a culture of cells producing one of the factors (*Fig. 5B–D*). However, the contribution of individual factors is noticeable in the presence of FBS (*Figs. 3, 4*). FBS-based stimula-

tion of the proliferation of cell lines expressing the EIF3I factor was described earlier [30].

We also analyzed the effect of a conditioned medium from modified lines incubated in a Opti-MEM medium for 48 h on the viability of Expi293F cells. This medium was chosen for initial culture, because it ensures good culture growth and is free of FBS, which may cancel the effect of the factors under study. A conditioned medium from modified cell lines increases the metabolic activity of intact cells compared with that of the control. The observed effect was related to both media from cell lines expressing one of the factors and a mixture of conditioned media.

Our findings suggest that careful selection of activated genes and control of their activation level may be used to generate a human cell line that is either less dependent on exogenous signaling proteins or even completely independent of them. The development of such a line will significantly reduce the cost and simplify the production of recombinant proteins for medical purposes.

CONCLUSION

By using the CRISPR/Cas9-SAM synergistic activation mediator technology, we generated an Expi293F human cell line with enhanced expression of the genes encoding the IGF-1, FGF-2, and EIF3I factors. Then, we demonstrated the activation of target gene expression both at the mRNA and protein levels. The modified cell lines exhibited increased proliferative activity under standard culture conditions and in co-culture of three producer lines in a DMEM basic medium free of FBS. In our opinion, our findings indicate that there is a possibility to use the selected approach in biotechnology. We believe that activation of various endogenous growth factor genes enables the production of cell lines that possess increased productivity and can grow on simple and inexpensive nutrient media. ●

The study was supported by the Russian Science Foundation, grant No. 23-24-00012, https://rscf.ru/project/23-24-00012/.

REFERENCES

1. Minonzio G., Linetsky E. // CellR4. 2014. V. 2. № 6. P. 1–10.
2. Coecke S., Balls M., Bowe G., Davis J., Gstraunthaler G., Hartung T., Hay R., Merten O.W., Price A., Schechtman L., et al. // Altern. Lab. Anim. 2005. V. 33. № 3. P. 261–287.
3. Stout A.J., Mirliani A.B., Rittenberg M.L., Shub M., White E.C., Yuen J.S.K., Kaplan D.L. // Comm. Biol. 2022. V. 5. № 1. P. 1–13.
4. Ahmed S., Chauhan V.M., Ghaemmaghami A.M., Aylott J.W. // Biotechnol. Lett. 2018. V. 41. № 1. P. 1–25.
5. Li W., Fan Z., Lin Y., Wang T.Y. // Front. Bioeng. Biotechnol. 2021. V. 9. P. 1–11.
6. Croset A., Delafosse L., Gaudry J.P., Arod C., Glez L., Losberger C., Begue D., Krstanovic A., Robert F., Vilbois F., et al. // J. Biotechnol. 2012. V. 161. № 3. P. 336–348.
7. Jefferis R. // J. Immunol. Res. 2016. V. 2016. P. 1–15.
8. Tan E., Chin C.S.H., Lim Z.F.S., Ng S.K. // Front. Bioeng. Biotechnol. 2021. V. 9. P. 1–9.
9. Sun H., Wang S., Lu M., Tinberg C.E., Alba B.M. // PLoS One. 2023. V. 18. № 6. P. 1–25.
10. Kumar N., Gammell P., Clynes M. // Cytotechnology. 2007. V. 53. № 1–3. P. 33.
11. Guan N., Liu Z., Zhao Y., Li Q., Wang Y. // Drug Deliv. 2020. V. 27. № 1. P. 1438.
12. Mossahebi-Mohammadi M., Quan M., Zhang J.S., Li X. // Front. Cell Dev. Biol. 2020. V. 8. P. 1–10.
13. Roobol A., Roobol J., Smith M.E., Carden M.J., Hershey J.W.B., Willis A.E., Smales C.M. // Metab. Eng. 2020. V. 59. P. 98.
14. Voorhamme D., Yandell C.A. // Mol. Biotechnol. 2006. V. 34. № 2. P. 201–204.
15. Mendes J.M.F., Valverde L. de F., Vidal M.T.A., Paredes B.D., Coelho P., Allahdadi K.J., Coletta R. Della, Souza B.S. de F., Rocha C.A.G. // Int. J. Mol. Sci. 2020. V. 21. № 18. P. 1–20.
16. Fang X.T., Sehlin D., Lannfelt L., Syvänen S., Hultqvist G. // Biol. Proced. Online. 2017. V. 19. № 1. P. 1–9.
17. Joung J., Konermann S., Gootenberg J.S., Abudayyeh O.O., Platt R.J., Brigham M.D., Sanjana N.E., Zhang F. // Nat. Protocols 2017. V. 12. № 4. P. 828–863.
18. Bobrovsky P.A., Moroz V.D., Lavrenova V.N., Manuvera V.A., Lazarev V.N. // Biochemistry (Moscow). 2020. V. 85. № 11. P. 1310–1318.
19. Weber K., Bartsch U., Stocking C., Fehse B. // Mol. Ther. 2008. V. 16. № 4. P. 698–706.
20. Dull T., Zufferey R., Kelly M., Mandel R.J., Nguyen M., Trono D., Naldini L. // J. Virol. 1998. V. 72. № 11. P. 8463–8471.
21. Tiscornia G., Singer O., Verma I.M. // Nat. Protocols. 2006. V. 1. № 1. P. 241–245.
22. Schindelin J., Arganda-Carreras I., Frise E., Kaynig V., Longair M., Pietzsch T., Preibisch S., Rueden C., Saalfeld S., Schmid B., et al. // Nat. Methods. 2012. V. 9. № 7.

P. 676–682.
23. Abaandou L., Quan D., Shiloach J. // Cells. 2021. V. 10. № 7. P. 1–21.
24. Omachi K., Miner J.H. // PLoS One. 2022. V. 17. № 6. P. 1–13.
25. Soos M.A., Field C.E., Siddle K. // Biochem J. 1993. V. 290. № 2. P. 419–426.
26. Roberston M.J., Raghunathan S., Potaman V.N., Zhang F., Stewart M.D., McConnell B.K., Schwartz R.J. // FASEB J. 2020. V. 34. № 1. P. 555.
27. Yang Z., Xiong H.-R., Yang Z., Xiong H.-R. // Biomed. Tissue Culture. 2012. 250 p.
28. Sedlář A., Trávníčková M., Matějka R., Pražák Š., Mészáros Z., Bojarová P., Bačáková L., Křen V., Slámová K. // Internat. J. Mol. Sci. 2021. V. 22. P. 1843.
29. Yuan Y., Zhang Y., Yao S., Shi H., Huang X., Li Y., Wei Y., Lin S. // J. Biol. Chem. 2014. V. 289. № 41. P. 28310–28323.
30. Ahlemann M., Zeidler R., Lang S., Mack B., Münz M., Gires O. // Mol. Carcinog. 2006. V. 45. № 12. P. 957–967.

Appendix 1

Table 1. List of the oligonucleotides used in the study

Name	Sequence 5'>3'	Application
igf1_F	TGGGTTTTACAGCTCGGCAT	Sequencing
igf1_R	GGAAACAGCTGGGGGAACAT	Sequencing
fgf2_F	AAGCCTGCTCTGACACAGAC	Sequencing
fgf2_R	GTTCACGGATGGGTGTCTCC	Sequencing
eif3i_F	GGGATCCACACTGGTTGAGG	Sequencing
eif3i_R	TCACTCGTCTGCATTCAGGG	Sequencing
i1_F	CACCGTGTAGACAGGAAACAGCTGG	Constructing sgRNA(MS2)_puro-i1
i1_R	AAACCCAGCTGTTTCCTGTCTACAC	Constructing sgRNA(MS2)_puro-i1
i2_F	CACCGAGGCATACAATGGAAATAGG	Constructing sgRNA(MS2)_puro-i2
i2_R	AAACCCTATTTCCATTGTATGCCTC	Constructing sgRNA(MS2)_puro-i2
i3_F	CACCGTATTTCCAAGTGAGTGAGT	Constructing sgRNA(MS2)_puro-i3
i3_R	AAACACTCACTCACTTGGAAATACC	Constructing sgRNA(MS2)_puro-i3
i4_F	CACCGCACTAACACACATTCTTTTA	Constructing sgRNA(MS2)_puro-i4
i4_R	AAACTAAAAGAATGTGTGTTAGTGC	Constructing sgRNA(MS2)_puro-i4
i5_F	CACCGTGTTTTGTAGATAAATGTG	Constructing sgRNA(MS2)_puro-i5
i5_R	AAACCACATTTATCTACAAAACACC	Constructing sgRNA(MS2)_puro-i5
i6_F	CACCGCTCTAGTTTTAAAATGCAA	Constructing sgRNA(MS2)_puro-i6
i6_R	AAACTTGCATTTTAAAACTAGAGCC	Constructing sgRNA(MS2)_puro-i6
f1_F	CACCGATAAGGGGCGGTGGAGCCC	Constructing sgRNA(MS2)_puro-f1
f1_R	AAACGGGCTCCACCGCCCCTTATCC	Constructing sgRNA(MS2)_puro-f1
f2_F	CACCGGCAGGGCTTTGGCATTCCC	Constructing sgRNA(MS2)_puro-f2
f2_R	AAACGGGAATGCCAAAGCCCTGCCC	Constructing sgRNA(MS2)_puro-f2
f3_F	CACCGGGCCGGCCTCTGAGTTCGG	Constructing sgRNA(MS2)_puro-f3
f3_R	AAACCCGAACTCAGAGGCCGGCCCC	Constructing sgRNA(MS2)_puro-f3
f4_F	CACCGGAATGCCAAAGCCCTGCCG	Constructing sgRNA(MS2)_puro-f4
f4_R	AAACCGGCAGGGCTTTGGCATTCCC	Constructing sgRNA(MS2)_puro-f4
f5_F	CACCGGCCGAACCGCCGAACTCAG	Constructing sgRNA(MS2)_puro-f5
f5_R	AAACCTGAGTTCGGCGGTTCGGCCC	Constructing sgRNA(MS2)_puro-f5
f6_F	CACCGCGCGCGACATCAGTCCGGCG	Constructing sgRNA(MS2)_puro-f6
f6_R	AAACCGCCGGACTGATGTCGCGCGC	Constructing sgRNA(MS2)_puro-f6
e1_F	CACCGAGGATCCTTCCAGGGCAAAG	Constructing sgRNA(MS2)_puro-e1
e1_R	AAACCTTTGCCCTGGAAGGATCCTC	Constructing sgRNA(MS2)_puro-e1
e2_F	CACCGACATTTGTGAGCCTTTCCAG	Constructing sgRNA(MS2)_puro-e2
e2_R	AAACCTGGAAAGGCTCACAAATGTC	Constructing sgRNA(MS2)_puro-e2
e3_F	CACCGTGCAGGATGGGAACTAGCAG	Constructing sgRNA(MS2)_puro-e3
e3_R	AAACCTGCTAGTTCCCATCCTGCAC	Constructing sgRNA(MS2)_puro-e3
e4_F	CACCGATGAATTCGAGGCGAGGGTC	Constructing sgRNA(MS2)_puro-e4
e4_R	AAACGACCCTCGCCTCGAATTCATC	Constructing sgRNA(MS2)_puro-e4
e5_F	CACCGTGGGGTTGTAGCAGGGGTCG	Constructing sgRNA(MS2)_puro-e5
e5_R	AAACCGACCCCTGCTACAACCCCAC	Constructing sgRNA(MS2)_puro-e5
e6_F	CACCGAATGTCTTTCCTTGGAGGG	Constructing sgRNA(MS2)_puro-e6
e6_R	AAACCCCTCCAAGGAAAGACATTCC	Constructing sgRNA(MS2)_puro-e6
q_igf1_F	CTCTTCAGTTCGTGTGTGGAGAC	qPCR
q_igf1_R	CAGCCTCCTTAGATCACAGCTC	qPCR
q_fgf2_F	AGCGGCTGTACTGCAAAAACGG	qPCR
q_fgf2_R	CCTTTGATAGACACAACTCCTCTC	qPCR
q_eif3i_F	CAGAACGTCCTGTCAACTCAGC	qPCR
q_eif3i_R	CTTGCCAATCCTGGTGGAGGTT	qPCR
q_cas_F	AACCTATGCCCACCTGTTCG	qPCR
q_cas_R	AGGATTGTCTTGCCGGACTG	qPCR
q_ms2_F	CTGGGAGAGGGCTCCTACTT	qPCR
q_ms2_R	TCATGGTTGGGCCAGGATTC	qPCR
gapdhF	GTCTCCTCTGACTTCAACAGCG	qPCR
gapdhR	ACCACCCTGTTGCTGTAGCCAA	qPCR

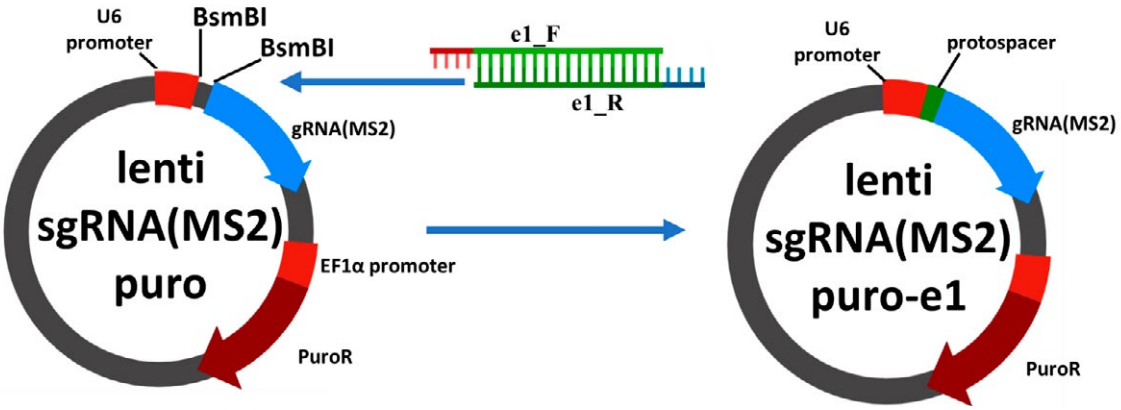

Fig. 1. Schematic cloning of lenti sgRNA(MS2)_puro series plasmids. To obtain a vector encoding chimeric guide RNA, the lenti sgRNA(MS2)_puro vector was treated with the BsmBI restriction endonuclease and ligated with an oligonucleotide duplex corresponding to one of the protospacer sequences (*Table 1*). Ligation products were cloned using the *E. coli* Top10 strain. The insertion structure was confirmed by sequencing

Appendix 2

Table 1. List of plasmids (with full and abbreviated names) for specific activation of the expression of growth factor genes

Plasmid full name	Duplex	Abbreviation	Gene
lenti sgRNA(MS2)_puro-e1	e1_F/e1_R	e1	EIF3I
lenti sgRNA(MS2)_puro-e2	e2_F/e2_R	e2	EIF3I
lenti sgRNA(MS2)_puro-e3	e3_F/e3_R	e3	EIF3I
lenti sgRNA(MS2)_puro-e4	e4_F/e4_R	e4	EIF3I
lenti sgRNA(MS2)_puro-e5	e5_F/e5_R	e5	EIF3I
lenti sgRNA(MS2)_puro-e6	e6_F/e6_R	e6	EIF3I
lenti sgRNA(MS2)_puro-f1	f1_F/f1_R	f1	FGF-2
lenti sgRNA(MS2)_puro-f2	f2_F/f2_R	f2	FGF-2
lenti sgRNA(MS2)_puro-f3	f3_F/f3_R	f3	FGF-2
lenti sgRNA(MS2)_puro-f4	f4_F/f4_R	f4	FGF-2
lenti sgRNA(MS2)_puro-f5	f5_F/f5_R	f5	FGF-2
lenti sgRNA(MS2)_puro-f6	f6_F/f6_R	f6	FGF-2
lenti sgRNA(MS2)_puro-i1	i1_F/i1_R	i1	IGF-1
lenti sgRNA(MS2)_puro-i2	i2_F/i2_R	i2	IGF-1
lenti sgRNA(MS2)_puro-i3	i3_F/i3_R	i3	IGF-1
lenti sgRNA(MS2)_puro-i4	i4_F/i4_R	i4	IGF-1
lenti sgRNA(MS2)_puro-i5	i5_F/i5_R	i5	IGF-1
lenti sgRNA(MS2)_puro-i6	i6_F/i6_R	i6	IGF-1

Plasmids for specific activation of the expression of growth factor genes were constructed based on the lenti sgRNA(MS2)_puro vector (Addgene #73795). To obtain a vector encoding chimeric guide RNA, the lenti sgRNA(MS2)_puro vector was treated with BsmBI restriction endonuclease and ligated with an oligonucleotide duplex (the primer sequences are provided in Appendix 1) corresponding to one of the protospacer sequences.

The Correlation Patterns of miRNA Expression with Targeted mRNA Transcripts in Glioma Patients with Wild-Type and Mutated Isocitrate Dehydrogenase (IDH) Genotypes

A. A. Bondarev[1], A. S. Evpak[1], A. L. Novoselov[1], A. A. Kudriaeva[1], A. A. Belogurov Jr.[1,2*]
[1]Shemyakin and Ovchinnikov Institute of Bioorganic Chemistry, Russian Academy of Sciences, Moscow, 117997 Russian Federation
[2]Russian University of Medicine, Department of Biological Chemistry, Ministry of Health of the Russian Federation, Moscow, 127473 Russian Federation
*E-mail: belogurov@mx.ibch.ru
Received December 28, 2023; in final form, July 01, 2024
DOI: 10.32607/actanaturae.27363

ABSTRACT **Low-grade gliomas are divided into two main genetic phenotypes based on the presence or absence of mutations in the isocitrate dehydrogenase (*IDH*) genes. The mutated IDH phenotype (IDHmut), in contrast to the wild-type phenotype (IDHwt), is characterized by a more positive response to pharmacological intervention and a significantly longer survival time. In this study, we analyzed the differential co-expression of 225,000 microRNA–mRNA pairs at the level of correlations between microRNA levels and their potential mRNA targets. Analysis of the associative relationships of individual representatives of the selected pairs revealed that the level of mRNAs encoded by the *ELN*, *ARL4C*, *C9orf64*, *PLAT*, and *FKBP9* genes associated with aggressive progression of glioma was increased in the IDHwt group. Meanwhile, the levels of miRNA-182, miRNA-455, and miRNA-891a associated with the negative prognosis in glioma were generally increased in the IDHmut group. Most (16/21) of the detected 21 microRNA–mRNA pairs with a significant difference in regulation between the IDHwt and IDHmut glioma samples had a weak or moderate positive correlation in IDHmut samples and a negative correlation in IDHwt samples. Therefore, our findings indicate that glioma samples from the IDHmut group with a positive prognosis potentially have a significantly less pronounced ability to microRNA-mediated regulation. We further suggest that such physiological disorders can lead to reduced tumor viability, resulting in an increased ability of the host to resist the spread of a malignant transformation of this genetic phenotype.**
KEYWORDS **LGG, low-grade gliomas, microRNA, differential expression.**
ABBREVIATIONS **LGG – low-grade gliomas; MN – malignant neoplasm; IDH – isocitrate dehydrogenase.**

INTRODUCTION

The incidence rate of glioma is ~ 6.6 per 100,000 population; glioblastoma is diagnosed in almost 50% of cases. The data on the incidence of malignant cerebral neoplasms in the Russian Federation are rather inconclusive. According to various estimates, the incidence rate of these malignant neoplasms (MNs) can be as high as 23 cases per 100,000 population; the incidence of glioma is 10–13 cases per 100,000 population [1]. The risk of developing this pathology increases abruptly with age: from 0.15 in childhood to 15 per 100,000 population in the elderly aged 75–84 years [2].

The reasons for the increasing incidence of glioma have yet to be fully elucidated. That is possibly related to the mass-scale introduction of high-tech methods for diagnosing malignant cerebral neoplasms, such as magnetic resonance imaging and positron emission tomography, into clinical practice [2]. Multiple external environmental factors have been considered as a reason for the emergence of glioma; however, the statis-

tically significant rise in the risk of glioma emergence is now believed to be associated exclusively with ionizing radiation [3–5].

MicroRNAs are small noncoding RNA molecules that regulate gene expression by binding to mRNA targets, thus causing their degradation or translation inhibition [6]. Numerous studies have revealed significant changes in microRNA expression during malignant transformation. Taking these results into account, microRNAs are currently being offered as potential diagnostic or prognostic biomarkers. Expression of microRNAs in humans with malignant neoplasms is disrupted via different mechanisms such as amplification or deletion of microRNA genes, abnormalities in microRNA transcription regulation, as well as epigenetic changes and defects in the mechanisms of microRNA processing. microRNAs can be classified as oncogenes or tumor suppressor genes.

The genetic features of gliomas are extensively used for tumor classification and selection of the optimal treatment strategy. Several attempts to characterize low-grade gliomas with wild-type and mutated isocitrate dehydrogenase (*IDH*) genes using microRNA signatures have been made [7–9]. In this study, we investigated the correlation patterns of microRNA co-expression with their potential targeted transcripts in patients with low-grade gliomas with wild-type and mutated *IDH* phenotypes.

EXPERIMENTAL

Data Sources

The TCGA-LGG cohort (https://portal.gdc.cancer.gov/projects/TCGA-LGG) containing the versatile genome sequencing data of individual patients with LGG, as well as data on gene and miRNA expression, was used as the source data to analyze low-grade gliomas.

Software

The analysis was conducted using standard tools for processing transcriptome data for the Python 3.10 programming language. The packages RNAnorm 2.1.0 and PyDESeq2 0.4.4 were used for data normalization and preprocessing. The correlation coefficients were calculated using the package SciPy v1.12.0. The survival curves were plotted using the package Lifelines 0.28.0.

Block diagram

Figure 1A shows the block diagram of the pipeline. Step sequence involves filtering according to the gene expression level, filtering across the TargetScan database with a certain confidence level (context++score threshold < -0.2), correlation analysis, and pair selection using the correlation coefficient level as a criterion.

RESULTS

It has been demonstrated earlier that the survival time of LGG patients correlates with the presence/absence of mutations in the *IDH* genes and presence/absence of a deletion in chromosomes 1p and 19q. Based on these data, it has been suggested that LGGs can be subdivided into three molecular subtypes: IDHwt – non-mutated *IDH* genes; IDHmut-no-codel – mutation in the *IDH* genes and absence of deletions in chromosomes 1p and 19q; and IDHmut-codel – mutations in the *IDH* genes and deletions in chromosomes 1p and 19q [10]. In this study, we settled upon two groups: the group with the wild-type *IDH* phenotype and the group carrying mutations in the *IDH* genes (IDHmut). We used data on the survival time of individual patients and previously published data on the molecular subtypes of LGG to analyze patient survival time in the cohorts. The recorded Kaplan–Meier curves agree well with the data published previously and demonstrate that survival time in patients with the wild-type *IDH* genotype was much shorter than that in patients with the mutated *IDH* phenotype (*Fig. 1B*).

The biological role of microRNA has been conventionally studied via differential gene expression analysis by isolating microRNAs characterized by significant intergroup differences in the average expression levels. However, these methods fail to capture changes in the cases when the average expression levels of regulatory and targeted RNAs remain unchanged. Differential co-expression analysis, which detects gene pairs or clusters whose co-expression changes between groups, can be used in this case [11]. These changes can attest to a loss of regulation between microRNA and its mRNA target due to mutations (e.g., in the binding site). Such parameters as parametric Pearson correlation or Spearman's rank correlation are used to quantify the co-expression level. By comparing these parameters in different groups, one can draw a conclusion that co-expression of a particular pair has been considerably changed. We searched for characteristic microRNAs whose regulatory function significantly changes in the IDHwt and IDHmut groups. Differential co-expression analysis revealed a difference in the regulation of the gene expression level by microRNAs potentially interacting with their transcripts depending on the presence/absence of mutations in the *IDH* genes.

There is intense clinical research under way into LGGs; however, comprehensive analysis of large-scale cohorts involving sequencing of tumor DNA and patients' DNA, as well as analysis of gene ex-

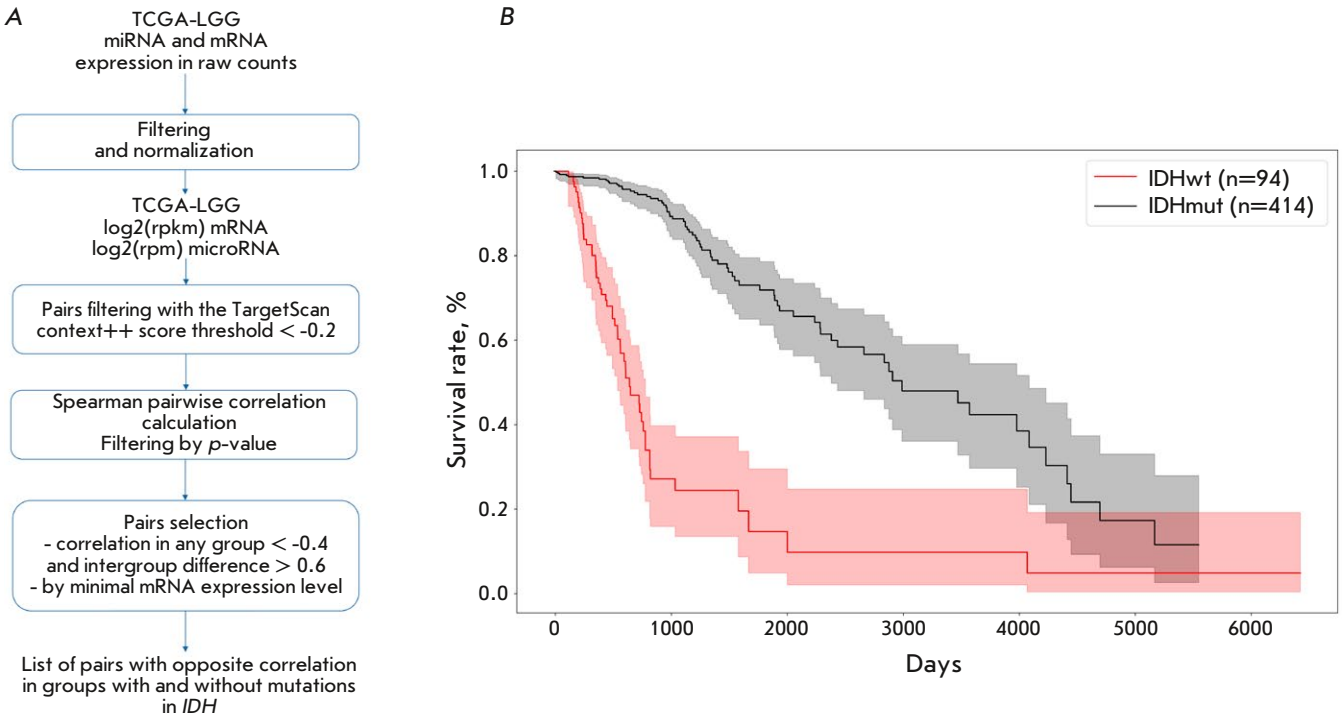

Fig. 1. (*A*) Block diagram of the bioinformatic pipeline. (*B*) The survival curve of TCGA-LGG patients divided into two molecular subtypes: IDHwt (a group carrying no mutations in the IDH genes) and IDHmut (a group carrying mutations in the IDH genes)

pression and DNA methylation, is virtually nonexistent. The only study of TGG samples collected from 530 patients has been deposited into the Cancer Genome Atlas (TCGA) (https://portal.gdc.cancer.gov/). We performed pre-filtering of all the possible pairs for microRNA–mRNA interactions obtained both experimentally and *in silico* across the existing databases. TargetScanHuman 8.0 (https://www.targetscan.org) for finding mRNA targets of microRNAs was used as the main database. At the second stage, we calculated the correlation of expression between protein-coding mRNAs and all the microRNAs. Pairs for which Spearman's correlation coefficient was < -0.4 in any of the groups (IDHwt or IDHmut), which corresponds to a strong negative correlation (namely, significant effect of this microRNA on gene expression), were considered significant. The absolute difference in intergroup correlation coefficients should be $\geqslant 0.6$.

The effort yielded 169 pairs (156 different mRNAs).

At the final stage, the pairs were filtered by the significance level of the correlation coefficient in each group ($p < 0.05$), by the mRNA expression level ($\geqslant 2$ in the $\log_2$ (RPKM) scale), and by the difference in correlation coefficients ($\geqslant 0.6$). *Figure 2* shows the data on dependence for 21 microRNA–mRNA target pairs that have passed through all the filtration stages. The expression levels for each microRNA–mRNA target pair in each sample are shown in a color corresponding to the IDHwt and IDHmut groups. For illustrative purposes, we provide linear regression for the IDHwt and IDHmut groups, where one can observe that their regulation patterns are differently directed. Color designation was used for the names of microRNA and mRNA: RNAs associated with a negative prognosis of LGG are shown in red; protective ones are shown in green. The data were obtained from earlier publications and are described in more detail in the Discussion section.

Figure 3 shows the expression levels in these pairs. The microRNA–mRNA pairs are clustered into three groups according to the prognosis of their effects on the disease course (in accordance with the published data); the color designation of names is similar to that used in *Fig. 2*. The expression levels of each pair in the samples collected from each patient, their median value for a group, and the level of significance of differential expression between the IDHwt and IDHmut groups calculated using the Mann–Whitney test are presented. Detailed analysis of the role of expression levels in the pairs provided in the Discussion section.

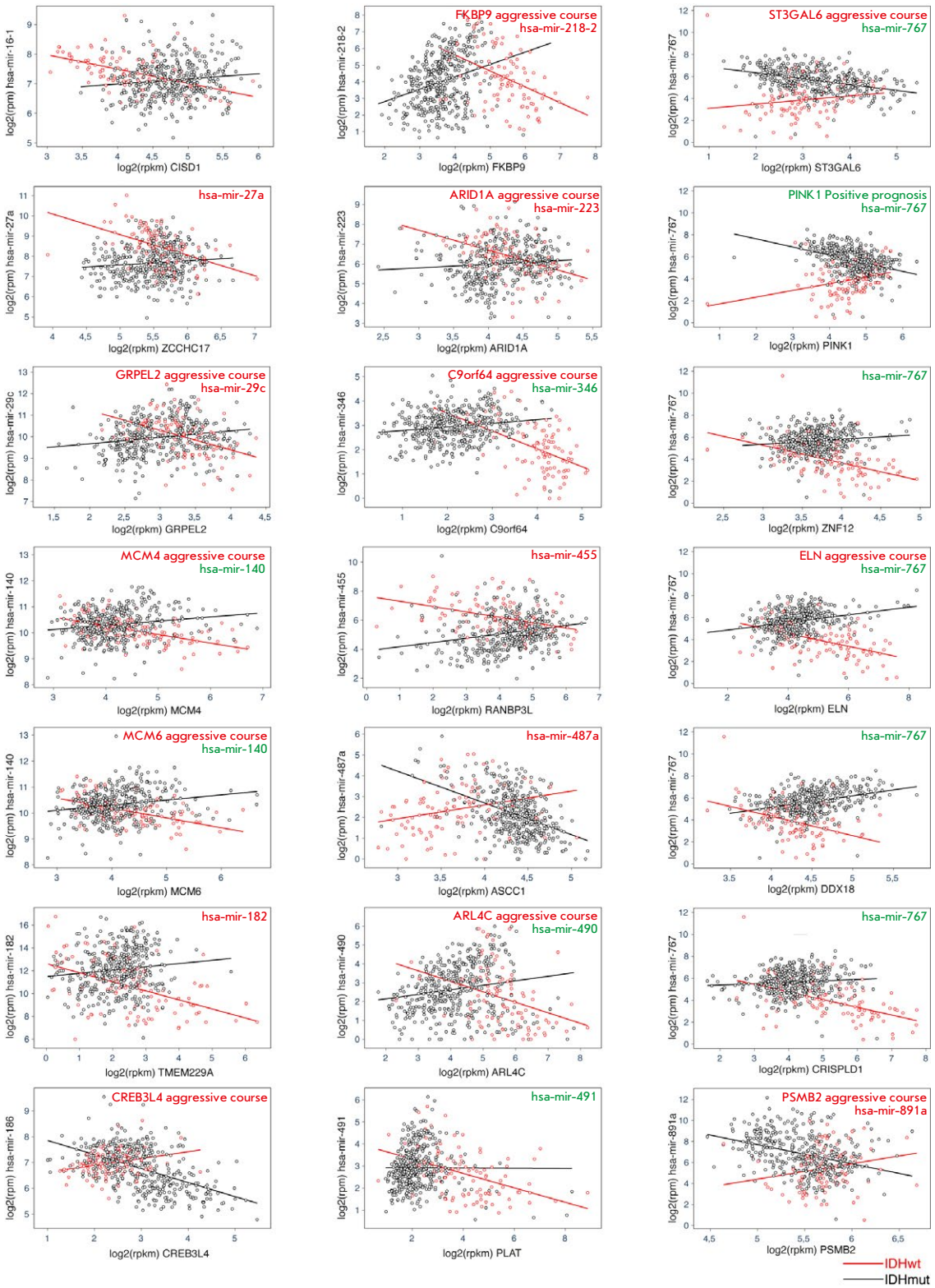

Fig. 2. Graphs of microRNA–mRNA correlations for 21 pairs. Black is the IDHmut group; red is the IDHwt group. Expression levels for each patient and linear regression for each group are shown. mRNAs and microRNAs associated with a negative prognosis of MN are marked in red; protective ones, in green. RPM – reads per million mapped reads; RPKM – reads per kilobase per million mapped reads

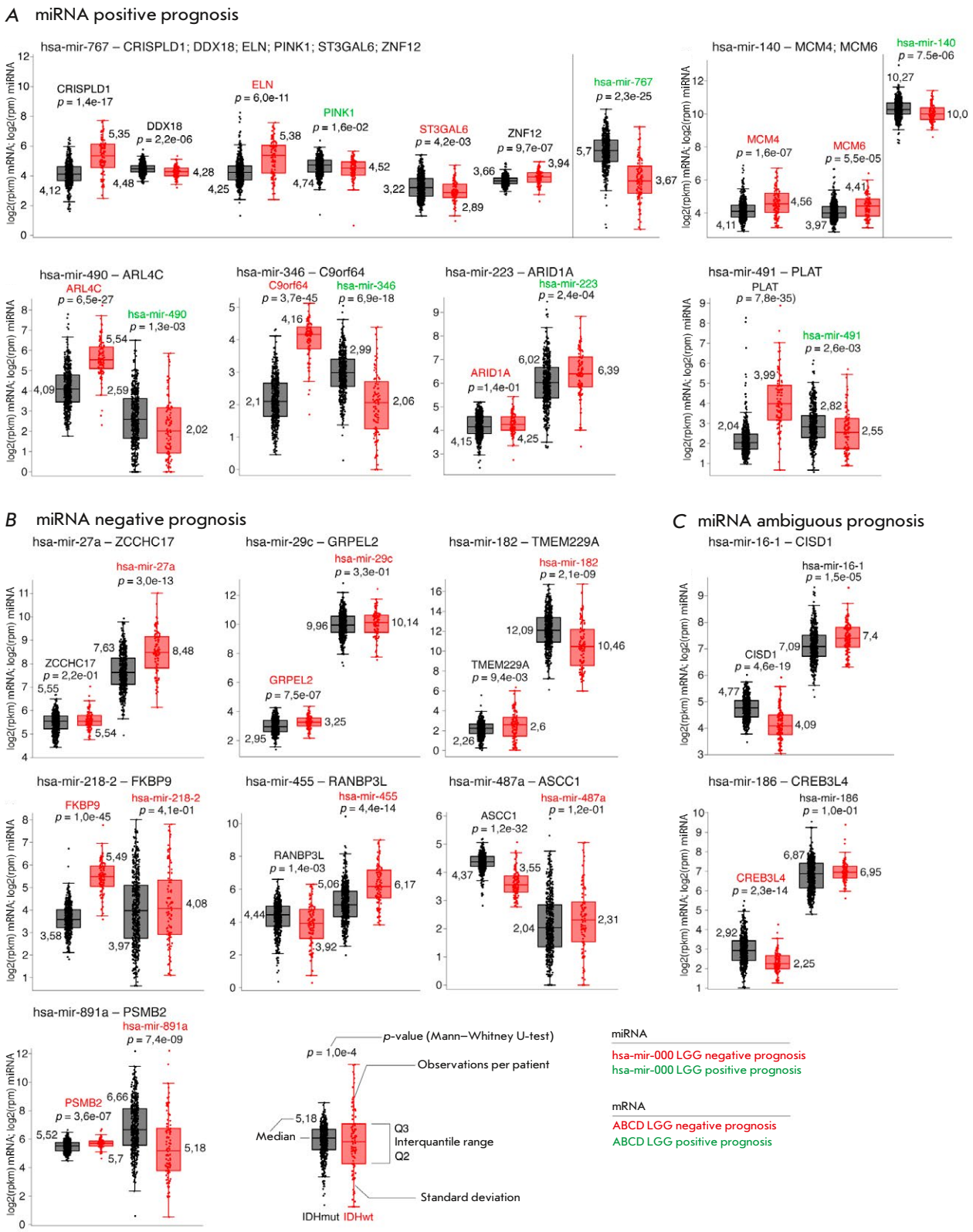

Fig. 3. Expression levels for 21 microRNA–mRNA pairs, grouped according to known data on the positive (*A*) and negative (*B*) effects of microRNAs on the disease course. mRNAs and microRNAs associated with a negative prognosis of MN are shown in red; protective ones, in green. The black diagrams are the IDHmut group; the red diagrams are the IDHwt group

Table 1. A list of miRNA–mRNA pairs filtered by the difference in correlation coefficients

mRNA	miRNA	Correlation (IDHmut)	Correlation (IDHwt)	Difference in correlation coefficients	TargetScan context++ score
DDX18	hsa-mir-767	0.365	-0.432	0.797	-0.325
PINK1	hsa-mir-767	-0.453	0.316	0.769	-0.239
ELN	hsa-mir-767	0.322	-0.442	0.764	-0.222
FKBP9	hsa-mir-218-2	0.319	-0.441	0.76	-0.243
CREB3L4	hsa-mir-186	-0.507	0.247	0.754	-0.25
ASCC1	hsa-mir-487a	-0.402	0.338	0.74	-0.217
ST3GAL6	hsa-mir-767	-0.406	0.308	0.714	-0.247
MCM6	hsa-mir-140	0.199	-0.508	0.707	-0.319
RANBP3L	hsa-mir-455	0.298	-0.405	0.703	-0.361
PSMB2	hsa-mir-891a	-0.405	0.297	0.702	-0.319
MCM4	hsa-mir-140	0.176	-0,512	0.688	-0.311
GRPEL2	hsa-mir-29c	0.208	-0.478	0.686	-0.306
ZNF12	hsa-mir-767	0.144	-0,521	0,665	-0.215
ARL4C	hsa-mir-490	0.237	-0.42	0.657	-0.241
ZCCHC17	hsa-mir-27a	0.111	-0.532	0.643	-0.221
PLAT	hsa-mir-491	0.195	-0.439	0.634	-0.252
CRISPLD1	hsa-mir-767	0.12	-0.51	0.63	-0.314
CISD1	hsa-mir-16-1	0.114	-0.51	0.624	-0.451
ARID1A	hsa-mir-223	0.147	-0.469	0,616	-0.232
C9orf64	hsa-mir-346	0.178	-0.438	0.616	-0.231
TMEM229A	hsa-mir-182	0.129	-0.474	0.603	-0.264

Interestingly, a strong negative correlation between protein-coding mRNAs and miRNAs is observed in the group without mutations in the *IDH* genes and either no correlation or a positive correlation is observed in the group of patients carrying a mutation in the *IDH* genes in the vast majority of cases, which potentially attests to the loss of a functional association between miRNA and mRNA targets.

Table 1 lists the numerical data for the obtained pairs.

DISCUSSION

MicroRNAs are small, single-stranded noncoding RNAs (20–23 nucleotides long) that are involved in oncogenesis, as well as progression and metastatic spread of various tumors as they regulate a large number of transcripts [12]. microRNA expression is altered in many brain tumors, including both low-grade gliomas and the most common and malignant subtypes of glioblastoma [13]. microRNAs are associated with the key processes in gliomas such as cell proliferation, apoptosis, and invasion [14].

Mutations in the *IDH* genes are the main genetic marker characterizing the aggressiveness of gliomas. Patients with the wild-type *IDH* phenotype have a negative prognosis, whereas mutations in the *IDH* genes are associated with increased survival time [15–17].

This study assessed potential dysregulation of the physiological function of miRNA in the IDHwt and IDHmut groups. Most of the 21 detected miRNA–mRNA pairs with differential co-expression (16/21) are characterized by either weak or moderate positive correlation between protein-coding mRNAs and miRNAs in IDHmut samples and by negative correlation in IDHwt samples.

In high-grade gliomas, expression of miRNA-767 (which is considered protective in glioma patients) is significantly lower compared to low-grade gliomas and healthy tissues [18, 19]. According to our data, the

miRNA-767 level is reduced in the IDHwt group compared to IDHmut and correlates negatively with the transcripts of such genes as *DDX18* (RNA helicase), *ELN* (connective tissue protein responsible for elasticity), *ZNF12* (transcriptional repressor), and *CRISPLD1* (extracellular vesicle protein), while positively correlating with mRNA of *PINK1* (kinase involved in mitochondrial protein phosphorylation) and *ST3GAL6* (sialyltransferase) in samples with the wild-type *IDH1* phenotype. Importantly, the upregulated expression of the *ELN* [20] and *ST3GAL6* genes [21] is associated with the more aggressive type of gliomas and, therefore, lower survival time. Meanwhile, gliomas characterized by downregulated expression of the protective *PINK1* gene correlate with a low survival time of patients who have undergone chemotherapy or radiation therapy [22]. Currently, no data are available on the role played by the *DDX18*, *ZNF12*, and *CRISPLD1* genes in patients with gliomas, and low-grade gliomas in particular.

According to the published data, expression of miRNA-218-2 [23], 487a [24], 891a [25], 29c [26], 27a [27], 182 [28], and 455 [29] is elevated in aggressive gliomas or is associated with a negative prognosis, while miRNA-140 [30], 490 [31], 346 [32], and 223 [33] facilitate the inhibition of tumor proliferation. The findings on miRNA-16-1 expression are rather inconclusive: its level is reduced in gliomas with the mutated *IDH1* phenotype compared to wild-type *IDH1* tissues; meanwhile, reduced expression of this miRNA contributes to tumor proliferation [34, 35]. No credible information about the role of miRNA-186 in patients with gliomas could be found. We observed a statistically significant difference between the studied IDHwt and IDHmut groups in terms of the expression of the aforementioned miRNAs for miRNA-182, miRNA-455, and miRNA-891a, whose levels were significantly reduced in glioma samples in the IDHwt group. Contrariwise, the miRNA-455 level was increased in the IDHwt group compared to IDHmut glioma samples.

Overexpression of the genes whose transcripts act as potential targets for dysregulated miRNAs in the IDHmut and IDHwt groups is observed in more aggressive glioma types: *FKBP9* [36] – *CREB3L4* [37], *MCM4*, *MCM6* [38], *PSMB2* [39], *ARID1A* [40], *ARL4C* [41], *GRPEL2* [42], and *C9orf64* [43]. No data on the involvement of such genes as *ASCC1*, *ZCCHC17* (participates in the biogenesis of ribosomal DNA), *PLAT*, *CISD1*, *TMEM229a* and *RANBP3L* in the development and spread of any glioma types have been found. The conducted analysis revealed significant elevation of the levels of mRNAs encoding the ELN, ARL4C, C9orf64, PLAT, and FKBP9 proteins in IDHwt samples compared to the IDHmut group.

CONCLUSIONS

Our study has demonstrated that differential co-expression analysis can be successfully used to search for physiologically significant miRNA–mRNA pairs in groups of patients with LGGs and different *IDH* mutational phenotypes. The revealed patterns demonstrate that the mRNA level is elevated in the IDHwt group, which is typical of an aggressive progression of gliomas. Meanwhile, the level of miRNAs associated with a negative prognosis in glioma patients is generally increased in the IDHmut group, which is characterized by much higher chances of survival, once again attesting to the intricate pattern of formation of transcriptional regulatory networks. Nonetheless, at the level of associative relationships, glioma samples from the IDHmut group with a positive prognosis have a much smaller regulation ability. These physiological disruptions may reduce tumor viability and, therefore, improve the ability of a host to resist the progression of malignant neoplasms. ●

This work was conducted under a subsidy from the Ministry of Education and Science of the Russian Federation (project No. 13.2251.21.0111 (075-15-2021-1033)).

REFERENCES

1. Pavlova G.V., Baklaushev V.P., Ivanova M.A., Goryainov S.A., Rybalkina E.Yu., Kopylov A.M., Chekhonin V.P., Potapov A.A., Konovalov A.N. // Burdenko's Journal of Neurosurgery. 2014. V. 78. № 6. P. 85–100. https://doi.org/10.17116/neiro201478685-100.
2. Weller M., Stupp R., Hegi M.E., van den Bent M., Tonn J.C., Sanson M., Wick W., Reifenberger G. // Neuro Oncol. 2012. V. 14. № 4. P. Iv100–108. https://doi.org/10.1093/neuonc/nos206.
3. Bondy M.L., Scheurer M.E., Malmer B., Barnholtz-Sloan J.S., Davis F.G., Il'yasova D., Kruchko C., McCarthy B.J., Rajaraman P., Schwartzbaum J.A., et al. // Cancer. 2008. V. 113. № 7. P. 1953–1968. https://doi.org/10.1002/cncr.23741.
4. Connelly J.M., Malkin M.G. // Curr. Neurol. Neurosci. Rep. 2007. V. 7. № 3. P. 208–214. https://doi.org/10.1007/s11910-007-0032-4.
5. Ostrom Q.T., Barnholtz-Sloan J.S. // Curr. Neurol. Neurosci. Rep. 2011. V. 11. № 3. P. 329–335. https://doi.org/10.1007/s11910-011-0189-8.
6. Kim V.N., Han J., Siomi M.C. // Nat. Rev. Mol. Cell Biol. 2009. V. 10. № 2. P. 126–139. https://doi.org/10.1038/nrm2632.
7. Zhang J.H., Hou R., Pan Y., Gao Y., Yang Y., Tian W.,

Zhu Y.B. // J. Cell. Mol. Med. 2020. V. 24. № 13. P. 7504–7514. https://doi.org/10.1111/jcmm.15377.
8. Cheng W., Ren X., Zhang C., Han S., Wu A. // J. Neurooncol. 2017. V. 132. № 2. P. 207–218. https://doi.org/10.1007/s11060-016-2368-6.
9. Qian Z., Li Y., Fan X., Zhang C., Wang Y., Jiang T., Liu X. // J. Neurooncol. 2018. V. 137. № 1. P. 127–137. https://doi.org/10.1007/s11060-017-2704-5.
10. Cancer Genome Atlas Research Network, Brat D.J., Verhaak R.G., Aldape K.D., Yung W.K., Salama S.R., Cooper L.A., Rheinbay E., Miller C.R., Vitucci M., et al. // N. Engl. J. Med. 2015. V. 372. № 26. P. 2481–2498. https://doi.org/10.1056/nejmoa1402121.
11. Zhiyanov A., Engibaryan N., Nersisyan S., Shkurnikov M., Tonevitsky A. // Bioinformatics. 2023. V. 39. № 2. https://doi.org/10.1093/bioinformatics/btad051.
12. Bartel D.P. // Cell. 2009. V. 136. № 2. P. 215–233. https://doi.org/10.1016/j.cell.2009.01.002.
13. Møller H.G., Rasmussen A.P., Andersen H.H., Johnsen K.B., Henriksen M., Duroux M. // Mol. Neurobiol. 2013. V. 47. № 1. P. 131–144. https://doi.org/10.1007/s12035-012-8349-7.
14. Zhou Q., Liu J., Quan J., Liu W., Tan H., Li W. // Cancer Sci. 2018. V. 109. № 9. P. 2651–2659. https://doi.org/10.1111/cas.13714.
15. Jiao Y., Killela P.J., Reitman Z.J., Rasheed A.B., Heaphy C.M., de Wilde R.F., Rodriguez F.J., Rosemberg S., Oba-Shinjo S.M., Nagahashi Marie S.K., et al. // Oncotarget. 2021. V. 3. № 7. P. 709–722. https://doi.org/10.18632/oncotarget.588.
16. Parsons D.W., Jones S., Zhang X., Lin J.C., Leary R.J., Angenendt P., Mankoo P., Carter H., Siu I.M., Gallia G.L., et al. // Science. 2008. V. 321. № 5897. P. 1807–1812. https://doi.org/10.1126/science.1164382.
17. Yan H., Parsons D.W., Jin G., McLendon R., Rasheed B.A., Yuan W., Kos I., Batinic-Haberle I., Jones S., Riggins G.J., et al. // N. Engl. J. Med. 2009. V. 360. № 8. P. 765–773. https://doi.org/10.1056/nejmoa0808710.
18. Zhang J., Xu S., Xu J., Li Y., Zhang J., Zhang J., Lu X. // Oncol. Rep. 2019. V. 42. № 1. P. 55–66. https://doi.org/10.3892/or.2019.7156.
19. Piwecka M., Rolle K., Belter A., Barciszewska A.M., Żywicki M., Michalak M., Nowak S., Naskręt-Barciszewska M.Z., Barciszewski J. // Mol. Oncol. 2015. V. 9. № 7. P. 1324–1340. https://doi.org/10.1016/j.molonc.2015.03.007.
20. Kocatürk B. // Cancer Med. 2023. V. 12. № 3. P. 3830–3844. https://doi.org/10.1002/cam4.5169.
21. Schildhauer P., Selke P., Staege M.S., Harder A., Scheller C., Strauss C., Horstkorte R., Scheer M., Leisz S. // Cells. 2023. V. 12. № 23. P. 2758. https://doi.org/10.3390/cells12232758.
22. Agnihotri S., Golbourn B., Huang X., Remke M., Younger S., Cairns R.A., Chalil A., Smith C.A., Krumholtz S.L., Mackenzie D., et al. // Cancer Res. 2022. V. 82. № 24. P. 4695. https://doi.org/10.1158/0008-5472.can-22-3445.
23. Liu Y., Yan W., Zhang W., Chen L., You G., Bao Z., Wang Y., Wang H., Kang C., Jiang T. // Oncol. Rep. 2012. V. 28. № 3. P. 1013–1021. https://doi.org/10.3892/or.2012.1902.
24. Kumar A., Nayak S., Pathak P., Purkait S., Malgulawar P.B., Sharma M.C., Suri V., Mukhopadhyay A., Suri A., Sarkar C. // J. Neurooncol. 2018. V. 139. № 1. P. 23–31. https://doi.org/10.1007/s11060-018-2840-6.
25. Zakrzewska M., Gruszka R., Stawiski K., Fendler W., Kordacka J., Grajkowska W., Daszkiewicz P., Liberski P.P., Zakrzewski K. // BMC cancer. 2019. V. 19. № 1. P. 544. https://doi.org/10.1186/s12885-019-5739-5.
26. Wu J., Li L., Jiang C. // Mol. Neurobiol. 2015. V. 52. № 3. P. 1540–1546. https://doi.org/10.1007/s12035-014-8937-9.
27. Ge Y.F., Sun J., Jin C.J., Cao B.Q., Jiang Z.F., Shao J.F. // Asian Pac. J. Cancer Prev. 2013. V. 14. № 2. P. 963–968. https://doi.org/10.7314/apjcp.2013.14.2.963.
28. Jiang L., Mao P., Song L., Wu J., Huang J., Lin C., Yuan J., Qu L., Cheng S.Y., Li J. // Am. J. Pathol. 2010. V. 177. № 1. P. 29–38. https://doi.org/10.2353/ajpath.2010.090812.
29. Wang W., Mu S., Zhao Q., Xue L., Wang S. // Oncol. Lett. 2019. V. 18. № 6. P. 6150–6156. https://doi.org/10.3892/ol.2019.10927.
30. Yang H.L., Gao Y.M., Zhao J.A. // Mol. Med. Rep. 2017. V. 16. № 3. P. 3634–3640. https://doi.org/10.3892/mmr.2017.6951.
31. Zhao L., Tang X., Luo R., Duan J., Wang Y., Yang B. // Curr. Neurovasc. Res. 2018. V. 15. № 3. P. 246–255. https://doi.org/10.2174/1567202615666180813130143.
32. Li Y., Xu J., Zhang J., Zhang J., Zhang J., Lu X. // Cancer Cell Int. 2019. V. 19. P. 294. https://doi.org/10.1186/s12935-019-1017-5.
33. Ding Q., Shen L., Nie X., Lu B., Pan X., Su Z., Yan A., Yan R., Zhou Y., Li L., Xu J. // Pathol. Res. Pract. 2018. V. 214. № 9. P. 1330–1339. https://doi.org/10.1016/j.prp.2018.05.012.
34. Krell A., Wolter M., Stojcheva N., Hertler C., Liesenberg F., Zapatka M., Weller M., Malzkorn B., Reifenberger G. // Neuropathol. Appl. Neurobiol. 2019. V. 45. № 5. P. 441–458. https://doi.org/10.1111/nan.12532.
35. Hong L., Qing O., Ji Z., Chengqu Z., Ying C., Hao C., Minhui X., Lunshan X. // Sci. Rep. 2017. V. 7. № 1. P. 13470. https://doi.org/10.1038/s41598-017-14035-2.
36. Xu H., Liu P., Yan Y., Fang K., Liang D., Hou X., Zhang X., Wu S., Ma J., Wang R., Li T., Piao H., Meng S. // J. Exp. Clin. Cancer Res. 2020. V. 39. № 1. P. 44. https://doi.org/10.1186/s13046-020-1541-0.
37. Hu Y., Chu L., Liu J., Yu L., Song S. B., Yang H., Han F. // Aging (Albany NY). 2019. V. 11. № 19. P. 8156–8168. https://doi.org/10.18632/aging.102310.
38. Cai H. Q., Cheng Z.J., Zhang H.P., Wang P.F., Zhang Y., Hao J.J., Wang M.R., Wan J.H. // Hum. Pathol. 2018. V. 78. P. 182–187. https://doi.org/10.1016/j.humpath.2018.04.024.
39. He W., Zhang Z., Tan Z., Liu X., Wang Z., Xiong B., Shen X., Zhu X. // Res. Sq. 2023. https://doi.org/10.21203/rs.3.rs-2751848/v1.
40. Lin W.W., Ou G.Y., Zhao W.J. // J. Cell. Mol. Med. 2021. V. 25. № 21. P. 10111–10125. https://doi.org/10.1111/jcmm.16947.
41. Chen Q., Fu W.J., Tang X.P., Wang L., Niu Q., Wang S., Lin Y., Cao M.F., Hu R., Wen H.Y., et al. // J. Cancer. 2021. V. 12. № 3. P. 818–826. https://doi.org/10.7150/jca.45052.
42. Tang C.T., Li Y.F., Chou C.H., Huang L.C., Huang S.M., Hueng D.Y., Tsai C.K., Chen Y.H. // Int. J. Mol. Sci. 2021. V. 22. № 23. P. 12705. https://doi.org/10.3390/ijms222312705.
43. Xu W., Han L., Zhu P., Cheng Y., Chen X. // Aging. 2023. V. 15. № 24. P. 15578–15598. https://doi.org/10.18632/aging.205422.

Reconstruction of the Reaction of Andalusicin Lantibiotic Modification by Lanthionine Synthetase AncKC in a Heterologous *Escherichia coli* System

N. Z. Mirzoeva[1], S. O. Pipiya[1], Yu. A. Mokrushina[1,2], M. V. Serebryakova[3], A. A. Grigoreva[4,5], S. A. Dubiley[4,5], S. S. Terekhov[1], I. V. Smirnov[1,2*]

[1]Shemyakin–Ovchinnikov Institute of Bioorganic Chemistry of the Russian Academy of Sciences, Moscow, 117997 Russian Federation

[2]Department of Chemistry, Lomonosov Moscow State University, Moscow, 119991 Russian Federation

[3]A.N. Belozersky Institute of Physicochemical Biology, Moscow, 119991 Russian Federation

[4]Center of Life Sciences, Skolkovo Institute of Science and Technology, Moscow, 121205 Russian Federation

[5]Institute of Gene Biology, Russian Academy of Sciences, Moscow, 119334 Russian Federation

*E-mail: ivansmr@inbox.ru

Received December 11, 2023; in final form, September 13, 2024

DOI: 10.32607/actanaturae.27347

ABSTRACT **The increasing resistance of microorganisms to antibiotics makes it a necessity that we search for new antimicrobial agents. Due to their genetically encoded nature, peptides are promising candidates for new antimicrobial drugs. Lantipeptide andalusicin exhibits significant antimicrobial activity against Gram-positive bacteria, making it a promising scaffold for the development of DNA-encoded libraries of lantibiotics. In this study, the modification reaction of andalusicin by class III lanthionine synthetase AncKC was reconstructed in a heterologous *Escherichia coli* system. The results obtained open possibilities for creating novel peptide-based antimicrobial agents.**

KEYWORS **lanthipeptides, posttranslational modifications, antimicrobial peptides.**

INTRODUCTION

Searching for novel antimicrobial agents is among the most pressing challenges faced by researchers in the 21st century. The rapid spread of multidrug-resistant bacterial strains represents a huge risk to public health and needs particular attention. Peptides are attractive candidates for use as new antibiotics because of their genetically encoded nature, making it possible to generate a diverse group of potential artificial antimicrobial agents [1, 2].

Lantipeptides are a group of peptides that are produced by Gram-positive bacteria on ribosomes and undergo post-translational modifications. Post-translational modifications of lantipeptides involve dehydration of Ser and Thr residues to dehydroalanine (Dha) and dehydrobutyrine (Dhb), followed by cyclization via the formation of intramolecular thioether bonds through the Cys residue, giving rise to the non-canonical amino acids lanthionine (Lan) and methyllanthionine (MeLan) [3]. Lantipeptides are synthesized as a prepeptide comprising the C-terminal sequence that undergoes post-translational modifications and the N-terminal leader peptide that is recognized by modifying enzymes and is then proteolytically removed [4]. Lantipeptides exhibiting antimicrobial activity, commonly referred to as lantibiotics, are of the greatest interest [5]. Classification of lantipeptides is based on the differences in the structures and mechanisms of action of the enzymes involved in the post-translational modification of lantipeptides. Four classes of lantipeptides have been recognized until recently; however, the latest findings suggest that a new, fifth class, can exist [6].

Lantipeptide andalusicin was isolated from the bacterium *Bacillus thuringiensis SV andalusiensis* B23193 (*Fig. 1*) [7]. The andalusicin biosynthesitic gene cluster contains genes encoding class III lanthionine synthetase AncKC involved in post-translational modification of lantipeptides, methyltransferase performing methylation, and ABC transporters export-

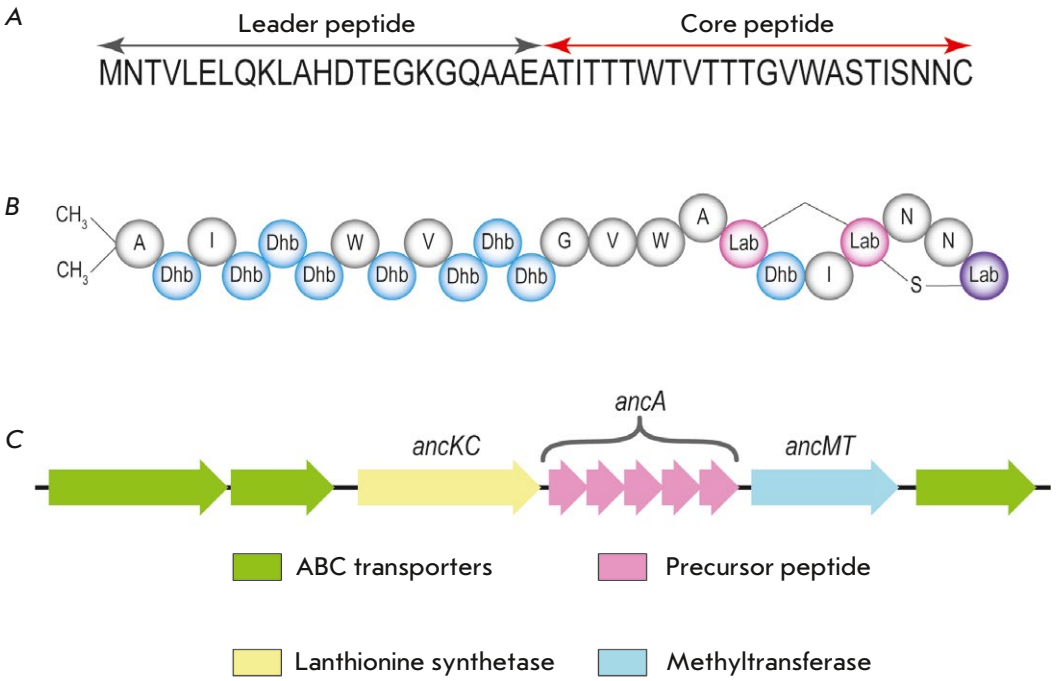

Fig. 1. The structure of lantibiotic andalusicin: (*A*) the primary structure of andalusicin; (*B*) the structure of mature andalusicin; and (*C*) schematic representation of the andalusicin biosynthetic gene cluster

ing lantipeptides into the extracellular environment. Mature dimethylated andalusicin exhibits a strong antimicrobial activity against numerous bacterial species belonging to the genus *Bacillus*, including *B. cereus*, which cause severe toxicoinfectious diseases in humans. The labionin ring, which is characteristic exclusively of class III lantipeptides and present in the structure makes andalusicin an especially interesting target for designing an artificial variety of antimicrobial peptides and peptide molecules with improved properties.

MATERIALS AND METHODS

Plasmid construction and transformation of bacterial cells

The *ancKC* and *ancA* genes were produced by chemical synthesis, treated with restriction endonucleases, and ligated into the pIvI-His-TEV vector (*Fig. 2*).

E. coli BL21 (DE3) cells were selected as a producer strain. The resulting genetic construct was used for chemical transformation of bacteria. Expression of the genes within the construct ensured co-expression of prepeptide and lanthionine synthetase AncKC, thus resulting in *in vivo* post-translational modifications. The transformed clones were transferred into Petri dishes with a 2xYt agar-based growth medium (16 g/L tryptone, 10 g/L yeast extract, and 5 g/L NaCl) supplemented with ampicillin to a concentration of 100 μg/mL.

Production of modified andalusicin

A solitary colony of the producer strain was selected for cultivation in 10 mL of the liquid 2xYT growth medium at 37°C overnight. The overnight bacterial culture (1 mL) was inoculated in 100 mL of liquid 2xYT growth medium. The cells were cultured at 37°C under shaking until OD_{600} = 0.4–0.6; IPTG was then added to a final concentration of 1 mM, and the cells were incubated at 18°C for 18 h under constant stirring. Upon expression completion, the cell mass was sedimented by centrifugation.

Purification of recombinant modified andalusicin

The cell mass was disintegrated ultrasonically and centrifuged at 12,000 rpm for 20 min. The following lysis buffer was used: 20 mM Tris-HCl pH 8.0, 500 mM NaCl. Andalusicin was purified by metal-chelate affinity chromatography using the Ni-NTA sorbent (Qiagen, Germany). An application buffer (20 mM Tris-HCl pH 8.0, 500 mM NaCl, 10 mM imidazole) and elution buffer (20 mM Tris-HCl pH 8.0, 500 mM NaCl, 300 mM imidazole) were used for chromatographic purification of the peptide. The samples after chromatographic purification were analyzed using denaturing Tricine–polyacrylamide gel electrophoresis under denaturing conditions [8].

Mass spectrometry analysis

To conduct mass spectrometry analysis, the samples were treated with iodoacetamide and subjected to

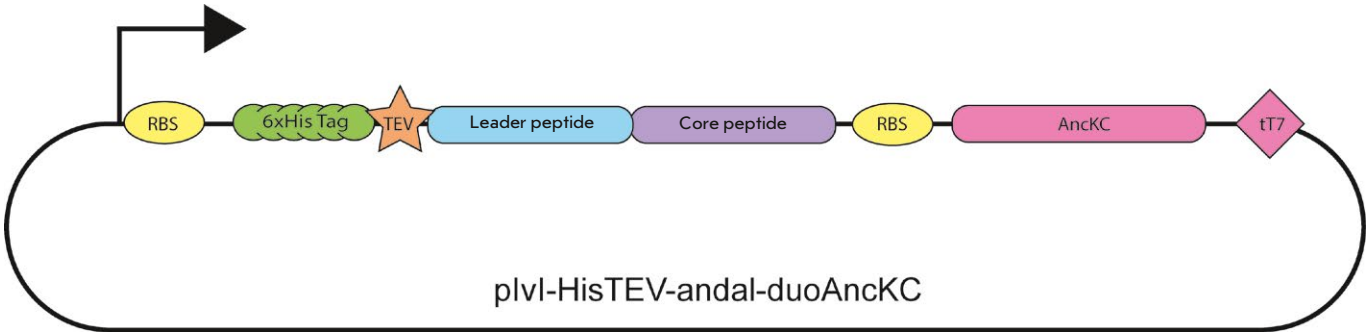

Fig. 2. Schematic representation of the genetic construct containing the transcription unit for andalusicin biosynthesis

trypsinolysis (Promega, USA). Next, 0.5 μL of the sample was mixed with 0.5 μL of a 2,5-dihydroxybenzoic acid solution (40 mg/mL in 30% acetonitrile, 0.5 TFA, Sigma Aldrich) on a target and dried.

The mass spectra were recorded on a MALDI-TOF mass spectrometer (Bruker Daltonics, Germany) in the positive ion mode. The spectra of proteolytic peptides were recorded using a reflectron; the accuracy of monoisotopic masses of singly charged protonated ions was ~ 0.005% (50 ppm). Tandem mass spectrometry fragmentation spectra were recorded with an accuracy in the measuring of fragmented ions ⩾ 1 Da. Peptides were identified based on the combined peptide fingerprinting data and fragmentation spectra of individual peptides using the FlexAnalysis 3.3 and Biotools 3.3 software (Bruker Daltonics). The Mascot 2.3.02 software was used to search across the in-house database where the sequences of putative proteins had been preliminarily deposited, with allowance for the potential oxidation of Met residues with atmospheric air, potential modification of Cys residues with iodoacetamide or β-mercaptoethanol, potential dehydrogenation of Ser and Thr residues, and potential phosphorylation of Ser and Thr residues. Candidate proteins with score > 56 were considered to have been confidently identified ($p < 0.05$). The spectra were additionally marked manually.

Analysis of antimicrobial activity

Antimicrobial activity was analyzed using the agar diffusion technique in Petri dishes containing a 2xYT agar growth medium without the antibiotic. *B. cereus* ATCC 4342 colony was cultured in 10 mL of the liquid 2xYT growth medium at 37°C overnight. Bacterial lawn on the agar medium surface was produced using a cotton wool pad moistened with the overnight culture of the bacterium under study.

The sample of modified andalusicin precursor was treated with Glu-C protease (NEB, USA) to remove the leader sequence. The resulting reaction mixture was applied dropwise onto Petri dishes preliminarily divided into equal segments so that droplets contained 8, 4, 2, 1, and 0.5 μg of the core peptide of modified andalusicin. The Petri dishes were incubated at 37°C overnight, and zones of bacterial growth inhibition were detected.

RESULTS AND DISCUSSION

Andalusicin, a class III lantipeptide, consists of 23 amino acid residues and carries the labionin ring, which is formed via post-translational modification of the precursor peptide by lanthionine synthetase AncKC. Andalusicin exhibits a strong antimicrobial activity against *B. cereus* ATCC 4342; thus, it is an interesting target for further research.

A genetic construct co-expressing the genes of andalusicin prepeptide and lanthionine synthetase AncKC in a single reading frame was obtained in this study. Chemical transformation of *E. coli* BL21 (DE3) cells resulted in the strain producing modified andalusicin prepeptide.

The modification profile of the produced andalusicin prepeptide was analyzed to prove successful reconstruction of the modification reaction. The purest product fractions were used to conduct a mass spectrometry analysis.

The mass spectrometry analysis detected molecular ions with m/z 3,606.74 and 2,755.28 Da (*Fig. 3B*). The ions with m/z = 3,606.74 and 2,755.28 Da corresponded to the modified polypeptide trypsinolytically cleaved at the Lys31 (the B+C fragment) and Lys39 positions (fragment C), respectively. Fragmentation of fragment C ion (*Fig. 3C*) was used to further study the structure of andalusicin.

An analysis of the fragmentation spectrum of this molecular ion allowed us to determine the amino acid sequence of the modified peptide and identify 11 dehydroamino acid residues. The presence of Δm/z

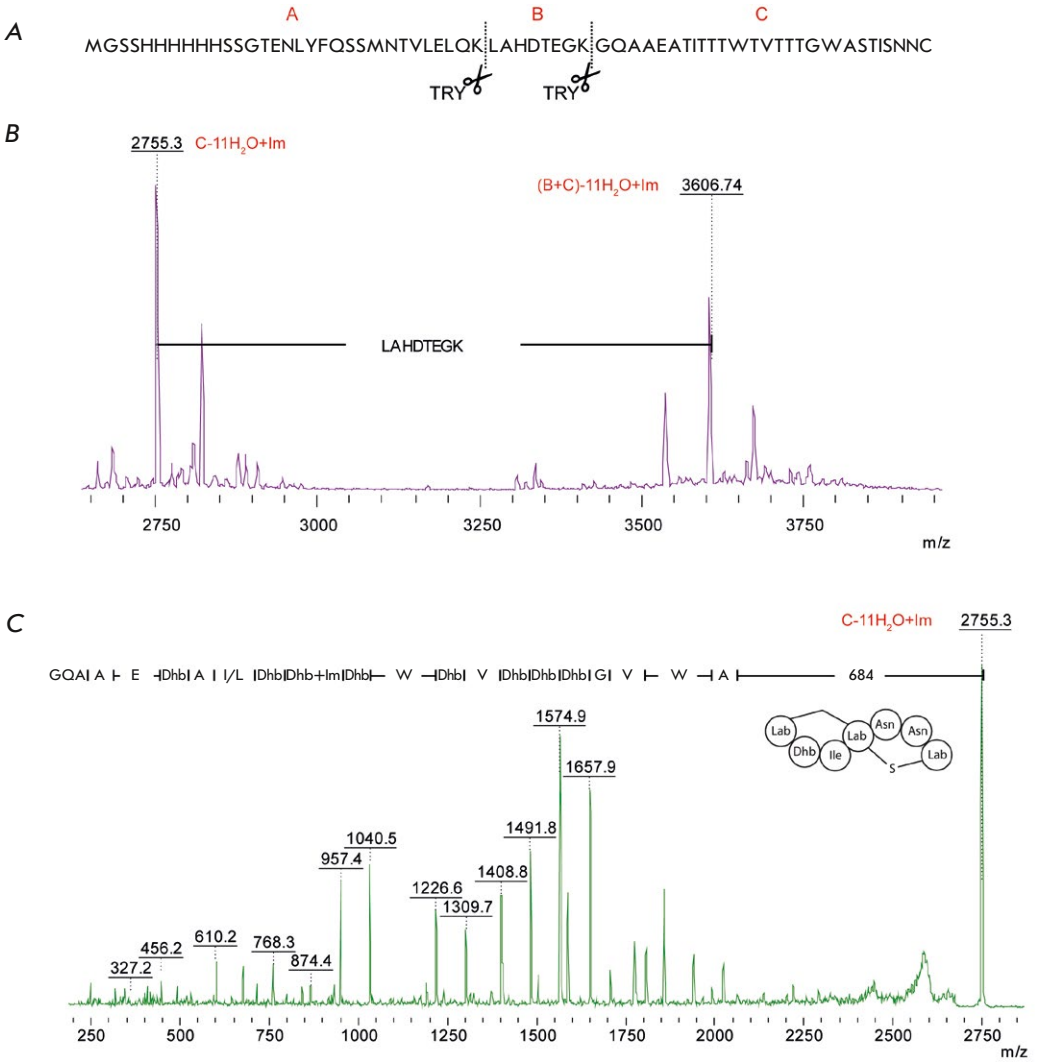

Fig. 3. Mass spectrometric analysis of recombinant prepeptide andalusicin: (*A*) the structure of prepeptide andalusicin with indicated proteolysis sites; (*B*) the mass spectrum of prepeptide andalusicin after trypsin digestion; and (*C*) the fragmentation spectrum of the 2755.3 Da ion

683.84 Da in the fragmentation spectrum between the molecular ion and the first fragmented ion corresponds to the labionin ring at the C-terminus of andalusicin. The absence of fragmentation in this spectral region attests to the conformational rigidity of the structure.

The antimicrobial activity of an andalusicin analog was analyzed using the diffusion technique. The *B. cereus* ATCC 4342 strain was used as the model organism. The findings demonstrate that the antimicrobial activity is 20 ± 10-fold lower than that of mature wild-type andalusicin, which is possibly due to the fact that the andalusicin analog does not carry two methyl groups at the N-terminus of the core peptide (*Fig. 4*).

Hence, it has been demonstrated that AncKC introduces post-translational modifications into the andalusicin precursor corresponding to similar modifications to the wild-type peptide, which are caused by a

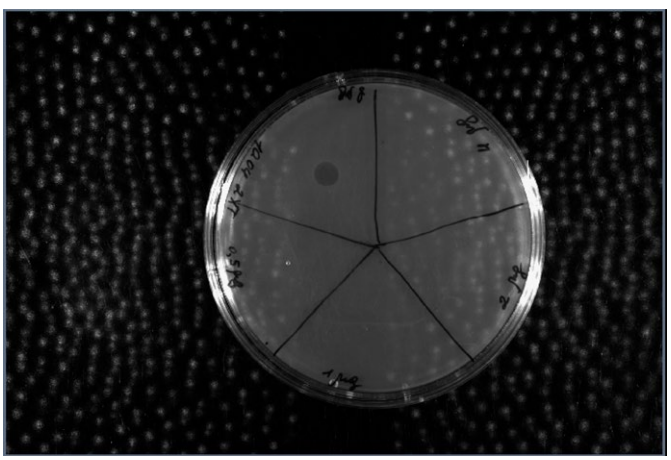

Fig. 4. Results of the activity test of the obtained andalusicin analog using the agar diffusion method. The bacterial strain *B. cereus* ATCC 4342 was used as the model organism

successful reconstruction of this reaction in the heterologous *E. coli* system. The minimal antimicrobial activity is also indicative of successful modification of the andalusicin analog. The presence of dehydroamino acids within the structure, in combination with the labionin ring at the C-terminus of the lantipeptide, ensures binding to lipid II, one of the key participants in the bacterial cell wall biosynthesis.

The results of this study deepen our understanding of class III lantipeptides and open up new avenues for the targeted modification of recombinant antimicrobial peptides.

CONCLUSIONS

Designing novel antimicrobial agents is among the top priorities of our time. Peptides are promising candidates for use as new antibiotics. In particular, some members of the lantipeptide family exhibit a strong antimicrobial activity; along with unique post-translational modifications, it makes them interesting study objects. We have generated a genetic construct co-expressing the genes of class III lanthionine synthetase AncKC and lantipeptide andalusicin, which enables simultaneous production and modification of the peptide in the heterologous protein producer *E. coli* BL21 (DE3). A mass spectrometry analysis of the recombinant andalusicin prepeptide verified that post-translational modifications corresponding to those in wild-type andalusicin were introduced. These findings broaden the scope of opportunity in using lantipeptides to search for and design novel antibiotics. ●

This work was supported by the Russian Science Foundation (grant No. 19-14-00331).

REFERENCES

1. Hudson G.A., Mitchell D.A. // Curr. Opin. Microbiol. 2018. V. 45. P. 61–69.
2. Wang L., Wang N., Zhang W., Cheng X., Yan Z., Shao G., Wang X., Wang R., Fu C. // Signal Transduct. Target Ther. 2022. V. 7. № 1. P. 48.
3. Repka L.M., Chekan J.R., Nair S.K., van der Donk W.A. // Chem. Rev. 2017. V. 117. № 8. P. 5457–5520.
4. Zhang Q., Yang X., Wang H., van der Donk W.A. // ACS Chem Biol. 2014. V. 9. № 11. P. 2686–2694.
5. Schnell N., Entian K.D., Schneider U., Götz F., Zähner H., Kellner R., Jung G. // Nature. 1988. V. 333. № 6170. P. 276–278.
6. Ortiz-López F.J., Carretero-Molina D., Sánchez-Hidalgo M., Martín J., González I., Román-Hurtado F., de la Cruz M., García-Fernández S., Reyes F., Deisinger J.P., et al. // Angew. Chem. Int. Ed. Engl. 2020. V. 59. № 31. P. 12654–12658.
7. Grigoreva A., Andreeva J., Bikmetov D., Rusanova A., Serebryakova M., Garcia A.H., Slonova D., Nair S.K., Lippens G., Severinov K., et al. // iScience. 2021. V. 24. № 5. P. 102480.
8. Schägger H. // Nat Protoc. 2006. V. 1. № 1. P. 16–22.

Cannula Implantation Reduces the Severity of the Beta Amyloid Effect on Peroxidized Lipids and Glutathione Levels in the Brain of BALB/c Mice

K. A. Mukhina[1], V. A. Mitkevich[1], I. Yu. Popova[1,2*]
[1]Engelhardt Institute of Molecular Biology, Russian Academy of Sciences, Moscow, 119991 Russian Federation
[2]Institute of Theoretical and Experimental Biophysics, Russian Academy of Sciences, Pushchino, 142290 Russian Federation
*E-mail: I-Yu-Popova@yandex.ru
Received May 31, 2024; in final form, September 06, 2024
DOI: 10.32607/actanaturae.27439

ABSTRACT **Sporadic Alzheimer's disease (sAD) is the most common of neurodegenerative disorders. The lack of effective therapy indicates that the mechanisms of sAD development remain poorly understood. To investigate this pathology in animals, intracerebroventricular injection of β-amyloid peptide (Aβ) using a Hamilton syringe, either during stereotactic surgery or through a pre-implanted cannula, is used. In this study, we analyzed the effect of chronic cannula implantation on the severity of Aβ effects at the behavioral, histological, and biochemical levels. The results showed that the local damage to neural tissue caused by cannulation has no bearing on the effect of Aβ on animal behavior and the microglial parameters of the unilateral hippocampus two weeks after the Aβ administration. However, cannula implantation fundamentally modifies some biochemical markers of the oxidative stress that occurs in the brain tissue in response to Aβ administration. Thus, the presence of a cannula reduces the severity of the Aβ impact on the levels of peroxidized lipids and glutathione two- and 10-fold, respectively. It is important to note that the detected changes are chronic and systemic. This is known because the homogenate of the entire contralateral (in relation to the cannula implantation site) hemisphere was analyzed, and the analysis was performed two weeks after implantation. At the same time, cannulation does not affect the rate of reactive oxygen species production. The obtained data indicate that chronic implantation of a cannula into the brain of experimental animals fundamentally distorts some parameters of oxidative stress in the neural tissue, which are widely used to assess the severity of experimental Alzheimer's-type diseases.**
KEYWORDS **amyloid toxicity, immunohistochemistry, microglia, reactive oxygen species, glutathione, lipid peroxides.**
ABBREVIATIONS **Aβ – β-amyloid; DG – dentate gyrus; ROS – reactive oxygen species; AD – Alzheimer's disease; sAD – sporadic Alzheimer's disease; group C – control group; group C-C – control group with cannula implantation; group AD – group with modeled Alzheimer's disease; group AD-C – group with modeled Alzheimer's disease and cannula implantation.**

INTRODUCTION

One of the central problems in modern neurobiology is developing an effective therapy for sporadic (non-hereditary) Alzheimer's disease (sAD). To date, sAD, which accounts for up to 95% of all diagnosed Alzheimer's disease (AD) cases, is the third most common cause of death after cerebrovascular diseases and cancer [1]. On current estimates, the number of people diagnosed with sAD will double every 20 years, reaching 66×10^6 and 115×10^6 people by 2030 and 2050, respectively [2]. However, these estimates have not taken into consideration the COVID-19 pandemic outcomes, which might add significantly to the increase in the number of AD patients [3, 4]. It is believed that sAD is caused by a combination of genetic and environmental risk factors without a confirmed

medical history of AD [5]. Many hypotheses on sAD etiology currently exist. The disease is associated with β-amyloid (Aβ) deposition [6], tau protein hyperphosphorylation [7], oxidative stress [8, 9], glucose hypometabolism [10], neuroinflammation [11], degeneration of cholinergic neurons [12], disruptions in the intestinal microbiota [13, 14], disruptions in the lipid metabolism [15], autophagy dysfunction [16], insulin resistance [17, 18], synaptic dysfunction [8, 19], etc. However, the lack of effective treatments indicates our insufficient understanding of sAD mechanisms. One of the common approaches used to study the mechanisms of sAD development is a single Aβ injection into the brain of sAD model animals [20–22]. Beta-amyloid is usually injected unilaterally, in the lateral ventricle using a Hamilton syringe during stereotaxic surgery or through a pre-implanted guide cannula. The cannula implant allows for direct, lengthy administration of various substances into the brain, including potential therapeutic drugs; however, this at the same time leads to additional damage to tissue, triggering a local inflammatory response [23]. This initial inflammatory response is mainly due to microglia activation, with the release of interleukin-1β [24, 25]. As shown in the control animals, the acute inflammatory response lasts less than one week [26]; past two weeks, glia alignment along the implanted object is observed [23]. Meanwhile, Aβ is known as a direct microglia activator [27, 28]. Thus, both chronic cannulation and Aβ act in the same direction. As a result, tissue response to cannula implantation may enhance or, conversely, mask the effect of Aβ. However, there is no experimental evidence in the literature to prove this. Yet it is obvious that distortions in the effects of Aβ in the study of sAD development mechanisms or the testing of potential therapeutic drugs may lead to false conclusions.

The aim of the current work was to study the effect of neural tissue damage resulting from cannula implantation on the formation of amyloid toxicity following intracerebroventricular (ICV) administration of Aβ to BALB/c mice. The presence and severity of the synergism of these effects was assessed at the systemic level using behavioral tests and at the cellular and subcellular levels using immunohistochemical and biochemical methods two weeks after Aβ administration.

EXPERIMENTAL

Experiments were conducted in male BALB/c mice weighing 25–33 g. Mice were received from the Stolbovaya Breeding Nursery (https://www.pitst.ru/, Moscow Region, Chekhov District, Stolbovaya settlement). The animals were housed in individual cages with a 12-hour light/dark cycle and access to food and water *ad libitum* in a room with controlled temperature (22°C). All studies were conducted in accordance with the Ethical Principles for Biomedical Research of the 1964 Helsinki Declaration and approved by the Biosafety and Bioethics Committee of the Institute of Theoretical and Experimental Biophysics of the Russian Academy of Sciences (Pushchino), protocol No. 40/2023 dated February 15, 2023.

The experimental scheme is presented in *Fig. 1A*. Two series of experiments were conducted. The animals in the first series underwent neurosurgery. During the surgery, they were injected either 1 μl

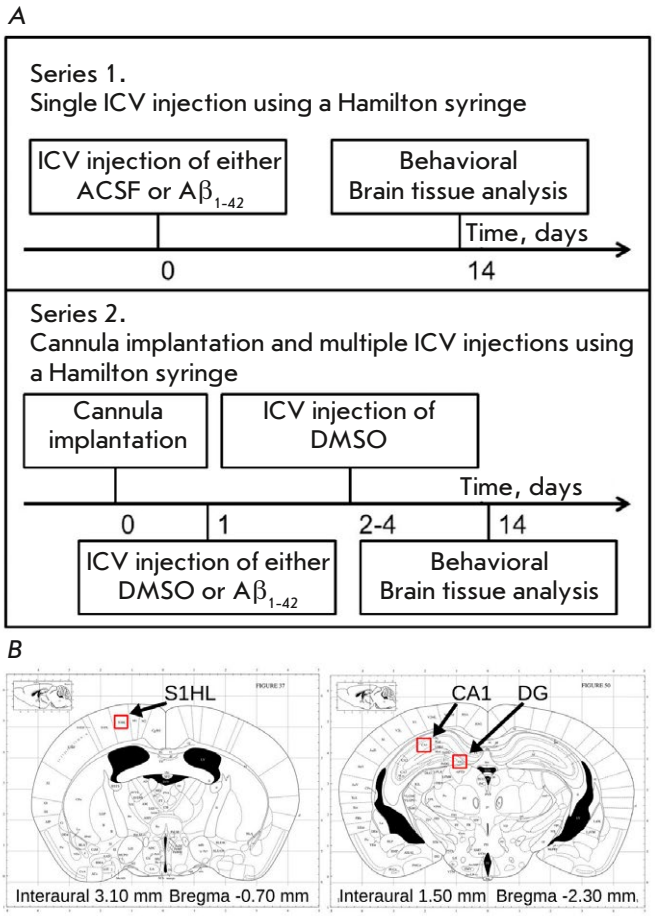

Fig. 1. (*A*) Schematic representation of the experiment. (*B*) Atlas image of the frontal section of the mouse brain [29] with indication of the site of a guide cannula implantation (left) and CA1 and dentate gyrus areas for microglia cell quantification (right)

of an artificial cerebrospinal fluid (ACSF) (group C) or 1 μl of $A\beta_{1-42}$ to model sAD (group AD) in the left lateral ventricle of the animal brain using a Hamilton syringe. The animals in the second group underwent neurosurgery with implantation of a guide cannula for drug administration. The drugs were administered through the cannula using a Hamilton syringe 24 h after the surgery. Since the cannula is implanted for repeated drug administration, and the drugs are often dissolved in DMSO, we replaced the ACSF solution with DMSO in this experimental series. On the first day of administration, the first group of animals received 1 μl of DMSO (group C-C) and the other group received 1 μl of $A\beta_{1-42}$+DMSO (group AD-C). All animals continued to receive DMSO for the following 3 days.

The behavioral open field test was performed 14 days after $A\beta_{1-42}$ administration. Next, the mice were anesthetized with isoflurane. The brain was removed. Half of the brain was fixed in paraformaldehyde for a immunohistochemical analysis, and the other half was analyzed biochemically.

Stereotaxic surgeries were performed under general gaseous anesthesia using isoflurane (1–4%; oxygen partial pressure, 0.8). The coordinates for Hamilton syringe implantation (G29) were identical for all the groups of animals: AP = -0.7; L = 1.4; h = 2.2 [29]. The guide cannula (stainless steel; size G21) for microinjections was positioned above the left lateral ventricle at the following coordinates: AP = -0.7; L = 1.4; h = 1.5 [29] (*Fig. 1B*).

Drug microinjections

The control animals received either ACSF (NaCl 0.9% + PBS + 5 mM glucose) or DMSO (Sigma-Aldrich, USA). The AD groups were injected with $A\beta_{1-42}$ (Sigma-Aldrich). Oligomeric $A\beta_{1-42}$ (1 mg, Sigma-Aldrich) was dissolved in 1 ml of a 1.0% NH_4OH solution in saline and sonicated for 1 min. Aliquots were stored at –80°C. Prior to the experiments, the $A\beta_{1-42}$ solution was fibrillized for 24 h at 36°C and sonicated for 1 min. Solutions were injected at a rate of 1 μl/min in a volume of 1 μl.

Behavior

To assess the general condition of the animals, we used the Open Field test. The test represents a brightly illuminated open black circular arena 60 cm in diameter and with a wall height of 50 cm. The behavior of each animal was recorded individually for 3 min using a video camera. The EthoVision software (Noldus Information Technology, the Netherlands) was used for video recording and analysis. Behavior was analyzed in two zones: in the center (d = 20 cm) and along the walls. The following parameters were assessed: time spent in each zone, movement/immobility ratio in each zone, frequency in entering the central zone, the latency period before the first entrance in the zone along the walls, the total distance traveled, and the average speed of movement. The Open Field setup was sanitized with a 10% alcohol solution for each animal.

Histology

The brain's left hemisphere was placed in cold paraformaldehyde for fixation and storage. Sections were made onto a Leica VT 1200 S vibratome (Leica, Germany). Frontal 35-μm sections were obtained, and microglia were stained with primary rabbit anti-Iba-1 antibodies (1 : 1 000; Wako, Japan) according to the manufacturer's instructions. Next, secondary goat anti-rabbit antibodies (1 : 1 000; Alexa Fluor 488, ThermoFisher, USA) were used. After staining, the sections were mounted on slides and microglia fluorescence was analyzed on a Nikon E200 microscope at ×40 magnification. The number and total area of Iba-1+ cells in 300 × 300 μm squares were calculated. The analysis was performed in the CA1 area and the dentate gyrus (DG) of the hippocampus (*Fig. 1B*) using ImageJ software (NIH, USA); six sections from each brain were analyzed. Any change in the number of microglial cells in the hippocampus depending on the distance from the implanted cannula (1,200 μm in the caudal direction) was also assessed.

Biochemistry

The right hemisphere was placed in an ice-cold buffer containing 220 mM mannitol, 70 mM sucrose, 10 mM Hepes, and 1 mM EGTA (pH 7.35) immediately after rapid extraction from the skull (20–40 s). The brain tissue was cut into small pieces and placed in a homogenizer (Duran, Wheaton) with 4 ml of the buffer and homogenized manually for 1.5 min. The brain homogenate was fractionated by centrifugation at different rates. The homogenate was centrifuged at 4,000 *g* for 10 min at 4°C. The pellet was resuspended in 3 ml of a potassium phosphate buffer containing 125 mM KCl and 8 mM KH_2PO_4 (pH 7.4) to obtain a membrane-enriched fraction 1. The supernatant was centrifuged at 12,000 *g* for 15 min at 4°C. The cytosol-enriched supernatant constituted fraction 2. The resulting pellet was resuspended in 0.5 ml of the EGTA-free isolation medium to obtain mitochondria-enriched fraction 3. All the fractions were kept on ice during the experiment. Oxidative stress markers were determined in the three fractions obtained; hereinafter they are referred to as the membrane,

cytoplasmic, and mitochondrial fractions. Evaluations were performed for half an hour using a CLARIOstar microplate reader (BMGlabtech, Germany).

Changes in reactive oxygen species (ROS) formation were determined by fluorimetry using the Amplex Red dye (30 μM, Thermo Fisher Scientific). The concentration of reduced sulfhydryl groups was measured using the Ellman photometric method with 1.3 mM 5,5'-dithiobis-(2-nitrobenzoic acid) (DTNB, ThermoFisher, USA). The optical density was measured at a wavelength of 415 nm using the cysteine calibration curve. Peroxidized lipids were determined by fluorimetry of the products of the reaction with 7.5 mM thiobarbituric acid (TBARS assay, Sigma-Aldrich, USA). Fluorescence was measured with excitation at 530 nm, absorption at 554 nm, and a calibration curve of 1,1,3,3-tetraethoxypropane (Sigma-Aldrich, St. Louis, MO, USA). The protein content in fractions for biochemical normalization was determined using the Bradford method and Coomassie Brilliant Blue R-250. The optical density was measured at 595 nm using a calibration curve of bovine serum albumin. Since the cytoplasmic fraction had a higher protein content compared to the membrane and mitochondrial fractions, it had lower normalized values.

Statistical analysis

The statistical analysis was performed using the Mann–Whitney criterion and single-factor ANOVA method. Data were presented as mean ± SD, $p \leqslant 0.05$ (*), $p \leqslant 0.01$ (**), $p \leqslant 0.001$ (***).

RESULTS

The experiments were performed in four animal groups: 1 – A control group that received a single dose of ACSF through a Hamilton syringe during neurosurgery (group C, $n = 6$); 2 – A group that received a single injection of $A\beta_{1-42}$ through a Hamilton syringe during neurosurgery (group AD, $n = 6$); 3 – A control group with DMSO administration through an implanted cannula for 3 days (group C-C, $n = 6$); and 4 – animals that received a single injection of $A\beta_{1-42}$ with subsequent administration of DMSO through an implanted cannula for 3 days (group AD-C, $n = 7$).

Behavioral Open Field test

To assess the general condition of the mice, their motor activity and anxiety level in the new environment – the open field test – was carried out. The analysis of three parameters (distance traveled, speed of movement, and time spent in the central square) did not reveal any significant differences between the four study groups (*Fig. 2A,B,C*). Evaluation of relative changes between the two groups without cannulas (C and AD) and the two groups with cannulas (C-C and AD-C) showed that the presence of an implanted cannula changes the direction of behavioral reactions in the animals (*Fig. 2A,B,C*).

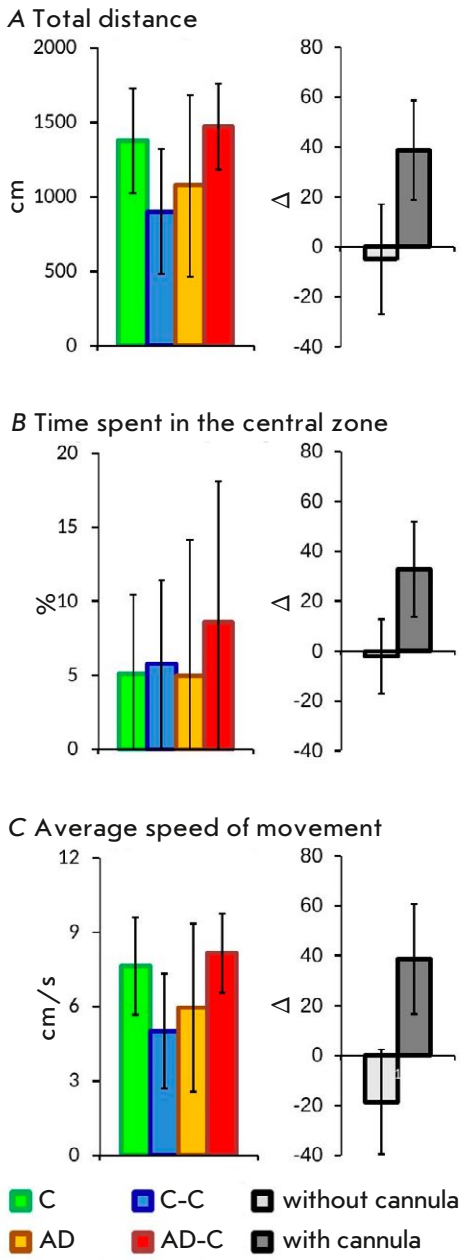

Fig. 2. Behavioral analysis in experimental animals using the Open Field test. (*A*) Total distance traveled. (*B*) Total time spent in the central zone. (*C*) Average speed of movement. Data for each group of experimental animals are presented on the left; pairwise comparisons of control groups and groups receiving $A\beta_{1-42}$ (C/AD and C-C/AD-C) are presented on the right. Data are presented as mean values + standard deviation

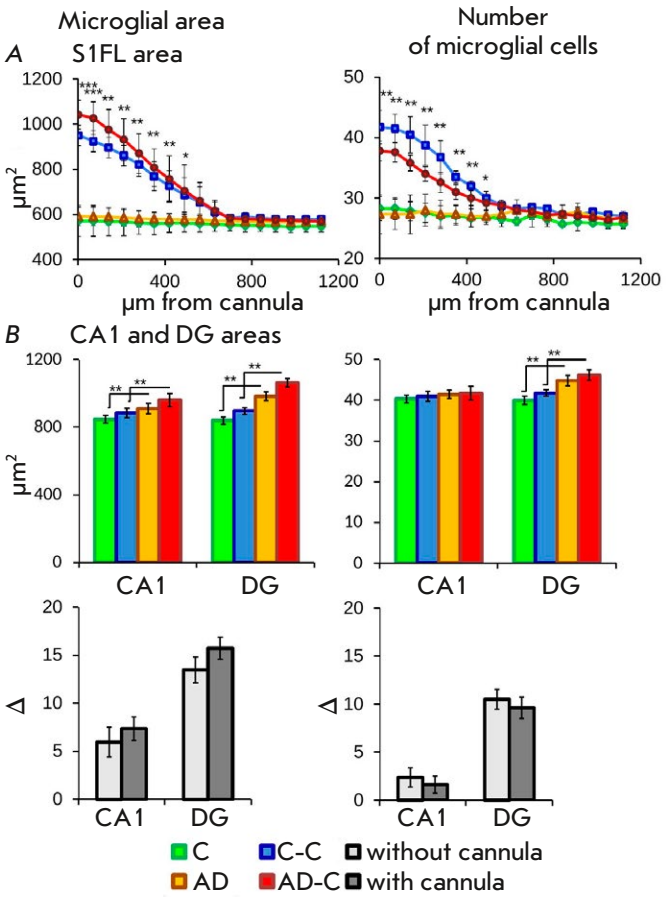

Fig. 3. Immunohistochemical analysis of microglial cells. (*A*) Changes in the number and area size of microglial cells at a distance from the cannula implantation site to the occipital part of the brain. (*B*) Effect of cannulation and $A\beta_{1-42}$ administration on microglia in the CA1 and DG fields of the hippocampus. Data for each group of experimental animals are presented at the top; pairwise comparisons of control groups and groups receiving $A\beta_{1-42}$ (C/AD and C-C/AD-C) are presented at the bottom. Data are presented as mean values + standard deviation. Significance: $p \le 0.05$ (*), $p \le 0.01$ (**), $p \le 0.001$ (***)

Hippocampal microglia

Since any intervention in the brain leads to tissue damage to some extent and, as a result, microglia activation, the first goal was to evaluate the damage to the area around the implanted guide cannula by analyzing microglia. Two weeks after neurosurgery, sequential analysis of sections with increasing distance from the cannula was performed. Microglia activation caused by cannula implantation was noted at a distance of ~600 μm from the cannula (*Fig. 3A*). Cannula implantation increased the total area of microglial cells by 423.7 ± 74.1 μm² in the control animals and by 449.9 ± 85.5 μm² in AD animals. Meanwhile, the total cell number was increased by 13.5 ± 4.6 and 10.5 ± 3.8 in the control and AD animals, respectively.

Immunohistochemical analysis of microglia in the CA1 field and the hilus of the hippocampal DG revealed an increase in the cell area in the mouse AD model compared to the control group: by 63.3 ± 28.4 and 143 ± 42.4 μm² in the animals without a cannula (AD-C) and by 143.1 ± 37.9 and 167.2 ± 29.6 μm² in those with a cannula (AD-C – C-C), respectively. The cell number was increased only in the DG region (*Fig. 3B*).

A comparative pairwise analysis of the animals with and without cannula implantation revealed no significant differences between the groups in neither cell area nor cell number (*Fig. 3B*). This data indicates that implantation has no negative effect on microglial cell parameters (number and area) at a distance of >600 μm from the cannula.

Biochemistry

We performed a biochemical analysis of oxidative stress markers in the brain's right hemisphere (contralateral to the cannula implantation site) in the experimental animals.

Peroxidized lipids

Analysis of the level of peroxidized lipids in the brain homogenate from the experimental animals demonstrated that cannula implantation results in a more than twofold increase in the level of peroxidized lipids in the first fraction, which mostly contains cell membranes (comparison of groups C and C-C, $p < 0.01$, *Fig. 4A, Table 1*). The fact that the cannula was implanted in the left half of the brain while the biochemical parameters were analyzed in the homogenate of the right half of the brain indicates that there was a significant effect of the damaged tissue on the overall level of peroxidized lipids in the brain.

In the animals without cannula implantation, Aβ administration resulted in a significant increase in the level of peroxidized lipids. In the first brain homogenate fraction, the level of peroxidized lipids was 6 × 104 ± 0.2 × 104 and 13 × 104 ± 2 × 104 μM/mg of protein in the C and AD groups, respectively. Amyloid injection through a cannula (AD-C group) resulted in an additional increase in the level of peroxidized lipids to 16 × 104 ± 0.9 × 104 μM/mg of protein. This dependence was observed in all three fractions (*Fig. 4A*). Furthermore, the level of peroxidized lipids in the C-C group was similar to that in the AD group (13 × 104 ± 2 × 104 and 12.6 × 104 ± 0.5 × 104 μM/mg of protein in the first

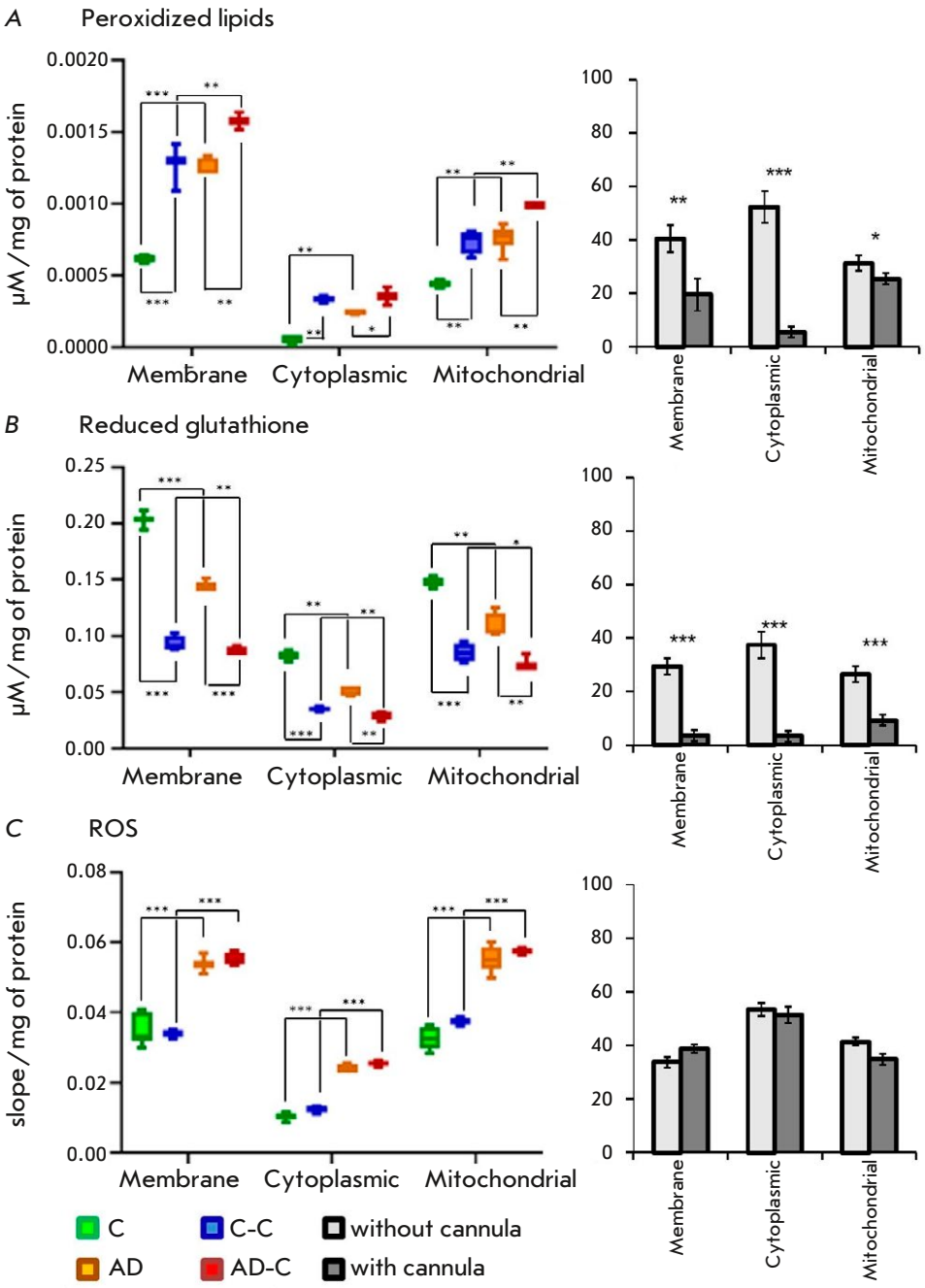

Fig. 4. Biochemical analysis for oxidative stress markers. (*A*) Level of peroxidized lipids. (*B*) Reduced glutathione level. (*C*) ROS level. Data for each group of experimental animals are presented on the left; pairwise comparisons of the control groups and groups receiving $A\beta_{1-42}$ (C/AD and C-C/AD-C) are presented on the right. Data are presented as mean values + standard deviation.
Significance: $p \le 0.05$ (*), $p \le 0.01$ (**), $p \le 0.001$ (***)

fraction, respectively). This is indication of a chronic increase in free-radical oxidation in the contralateral hemisphere of the brain relative to the implantation site in the experimental animals.

Pairwise comparison of the groups with and without a cannula (*Fig. 4A*) showed Aβ administration resulting in a twofold increase of the oxidized lipids level in the first fraction in the animals without a cannula (comparison between the C and AD groups) compared to the animals with an implanted cannula (comparison between the C-C and AD-C groups).

Glutathione

Glutathione, an important factor determining the cell Red/Ox potential, is mainly located in the cytosol. Analysis of the glutathione level in a brain homogenate from the experimental animals showed that cannula implantation leads to a 2.4-fold decrease in the glutathione level in the second fraction, which mainly contains cytosol (comparison of groups C and C-C, $p < 0.01$, *Fig. 4B*, *Table 1*). This dependence was observed in all three fractions. This fact is indication of a significant impact of the

Table 1. Level of oxidative stress markers in the brain homogenate fractions from experimental animals. Values are presented in % relative to the membrane fraction of the C-group and standard deviations

Oxidative stress marker	Fraction	C	C-C	AD	AD-C
Lipid peroxides	membrane	100 ± 4	204 ± 27	202 ± 9	253 ± 14
	cytoplasmic	9 ± 5	54 ± 4	39 ± 2	57 ± 14
	mitochondrial	71 ± 4	119 ± 13	121 ± 14	159 ± 1
Glutathione	membrane	100 ± 3	46 ± 3	70 ± 2	45 ± 1
	cytoplasmic	41 ± 2	17 ± 1	25 ± 2	16 ± 1
	mitochondrial	73±2	42 ± 4	54 ± 5	35 ± 1
ROS	membrane	100 ± 12	97 ± 3	154± 5	159 ± 5
	cytoplasmic	30 ± 3	36 ± 3	69 ± 3	73 ±2
	mitochondrial	91 ± 9	108 ± 3	159 ± 11	165 ± 3

implanted cannula on the overall glutathione level in the brain.

Amyloid administration resulted in a decrease in glutathione levels in all experiments. However, the changes in the animals without a cannula were 75% more pronounced compared to those in the animals with a cannula (AD/C groups – 40% and AD-C/C-C groups – 5%, *Fig. 4B*).

Interestingly, the glutathione level in the C-C group was lower than that in the AD group (0.035 ± 0.002 and 0.052 ± 0.004 μM/mg of protein in fraction 2, respectively). This indicates a chronic decrease in the regenerative capacity of the neural tissue due to the presence of the cannula in the brain of the experimental animals.

Reactive oxygen species

Cannula implantation did not affect the rate of ROS production: the values did not differ significantly between the C and C-C groups (*Fig. 4B, Table 1*).

Amyloid administration resulted in a similar increase of approximately 75% in the ROS production rate in all three homogenate fractions, regardless of the presence of a cannula (*Fig. 4B, Table 1*). Pairwise comparison of the groups (with and without a cannula) revealed no significant differences between them (*Fig. 4B*).

DISCUSSION

In this work, we endeavored to study the effect of the guide cannula on the state of brain neural tissue in a mouse sAD model. Animal behavior was assessed at the systemic level; a immunohistochemical analysis of microglia and a biochemical analysis of brain oxidative stress markers were performed to assess the cellular and subcellular aspects of the impact. The analysis was undertaken two weeks after neurosurgery and $A\beta_{1-42}$ administration, since an acute response to damage would have receded by this time, and changes in the parameters can be considered as signs of the initial stage of the chronic pathology.

Behavioral studies in an AD animal model, especially at early stages of the disease, are of interest, since they can be used to identify such psychoneurological disorders as hyperexcitability and anxiety. It has been shown that psychoneurological symptoms are an early manifestation of cognitive impairment in humans [30]. However, due to the fact that it is impossible to establish the moment of disease onset in humans, the specific stage of the onset of neurodegeneration in psychoneurological disorders remains unknown. In this regard, animal behavioral tests at different stages of AD are of particular interest. In the present study, the experimental animals were tested using the Open Field test. The Open Field test did not reveal substantive differences between the experimental groups two weeks after $A\beta_{1-42}$ injection. However, pairwise comparison of the animals with and without a cannula showed that the implanted cannula changes the direction of the behavioral responses. A tendency towards decreased/increased motor activity was noted in mice without/with implanted cannula, respectively. This suggests a need to develop new behavioral tests that can detect

early psychoneurological disorders in experimental AD model animals.

Since implantation of the guide cannula results in mechanical damage to brain tissue, it is important to distinguish between the effect of this damage and that of drugs injected chronically through the cannula. To achieve that, it is important to determine the area of mechanical damage around the cannula. Activated microglial cells, i.e. brain-resident macrophages, are one of the most commonly used biomarkers of neural tissue damage [31]. In our study, a comparative analysis of the parameters of the microglial cells and neural tissue around the cannula using a thin Hamilton syringe for injections showed that the number of activated microglial cells and their total area around the cannula increased by an average of 30 and 40%, respectively. The number of activated microglia gradually decreased with an increase in the distance from the cannula and reached the control level at a distance of 560 μm. For this reason, the effect of amyloid on hippocampal microglia in the animals with implanted cannulas was analyzed at a distance of >600 μm from the implantation site. In contrast to the use of a cannula, a single injection using a 0.33-mm Hamilton syringe had not increase the number and area of microglial cells two weeks after stereotactic surgery.

Administration of $A\beta_{1-42}$ to animals treated both with and without the use of a cannula resulted in the activation of hippocampal microglia, which manifested itself in an increased cell area. Interestingly, the increase in the DG cell area was accompanied by growth in the cell number. At the same time, in the CA1 field, the number of microglial cells was unchanged. A comparative pairwise analysis of hippocampal microglia in the animals with and without a cannula showed that, although the level of microglia activation in the animals with a cannula was slightly higher, the presence of a cannula did not fundamentally affect the effect of $A\beta_{1-42}$. Thus, our data demonstrate that local damage to neural tissue caused by a cannula implantation does not alter the effect of Aβ on the hippocampal tissues located at a sufficient distance (600 μm) from the cannula.

Since numerous studies have shown that oligomeric Aβ induces oxidative stress in neural tissue [32, 33], we analyzed oxidative stress markers in the right hemisphere (contralateral to the cannula implantation site) in the experimental animals. A comparative analysis of the two control groups (C and C-C) showed that cannula implantation had significantly increased the level of peroxidized lipids and drastically decreased the glutathione level in all three fractions (see *Table 1*). This suggests the development of chronic oxidative stress because of cannula implantation. At the same time, the ROS level did not differ between the groups.

The published data indicate that the decrease in glutathione level after cannula implantation may be associated with increased glutamate expression and excitotoxicity, which lead to enhanced oxidative stress, microglia activation, and zinc release, resulting in neuronal death. This manifests itself on the second day after mechanical injury to the neural tissue [34]. In addition, reactive activation of astrocytes takes place upon injury; these cells act as the main source of restored glutathione in the brain, which also results in a decreased glutathione level [35].

Amyloid administration in control animals (the AD group) led to an increased level of peroxidized lipids (by 100% in the membrane fraction) to the values in the C-C group. The decrease in glutathione level was significant (a 40% change in the cytoplasmic fraction when comparing the C and AD groups) but less pronounced than that caused by cannula implantation (a 60% change in the cytoplasmic fraction when comparing the C and C-C groups). The total ROS level changed by the same amount in the groups with and without implanted cannula.

Pairwise comparison of groups with cannula (C-C and AD-C) and without cannula (C and AD) demonstrated that cannula implantation, by triggering oxidative stress through mechanical damage to tissue, fundamentally reduces the severity of the effect of Aβ on peroxidized lipids and glutathione levels (two- and 10-fold, respectively). At the same time, it does not affect the ROS production rate. These data show that the total ROS level is an adequate and reliable proxy of disease development. At the same time, cannula implantation fundamentally distorts the effect of Aβ on the glutathione level in neural tissue, which can lead to false conclusions when interpreting experimental data on the mechanisms of sAD development and testing potential therapeutic drugs.

The data obtained here indicate that it is important to take into account the effect of the mechanical damage to tissue caused by an implanted cannula when analyzing the biochemical parameters of oxidative stress, which are widely used to assess the severity of experimental Alzheimer's disease-type pathology.

CONCLUSION

The study of the development the amyloid pathology with intracerebral administration of Aβ to BALB/c mice showed that the damage to neural tissue caused by a cannula implantation does not affect the behavioral and histological aspects of the Aβ effect. However,

cannula implantation had a fundamental impact on (masked) the severity of the Aβ effect on the peroxidized lipids and glutathione levels in neural tissue. The ROS production rate did not depend on the presence of the cannula, thus confirming that this parameter is an adequate and reliable marker of pathology development. These facts indicate that cannula implantation unequally affects the biochemical markers of oxidative stress in response to amyloid injection. This is especially important to take into account in animal studies of the neural tissue redox state. ●

This work was supported by the State Assignment No. 075-01025-23-01 and the Russian Science Foundation grant No. 19-74-30007.

REFERENCES

1. Takizawa C., Thompson P.L., van Walsem A., Faure C., Maier W.C. // J. Alzheimers Dis. 2015. V. 43. № 4. P. 1271–1284.
2. Batsch N.L., Mittelman M.S. // World Alzheimer Report. 2012. P. 1–80.
3. Gonzalez-Fernandez E., Huang J. // Curr. Neurol. Neurosci. Rep. 2023. V. 23. № 9. 531–538.
4. Li W., Sun L., Yue L., Xiao S. // Front. Immunol. 2023. V. 14. P. 1120495.
5. Mattsson N., Zetterberg H. // Expert. Rev. Neurother. 2014. V. 14. № 6. P. 621–630.
6. Paroni G., Bisceglia P., Seripa D. // J. Alzheimers Dis. 2019. V. 68. № 2. P. 493–510.
7. Wu X.L., Pina-Crespo J., Zhang Y.W., Chen X.C., Xu H.X. // Chin. Med. J. 2017. V. 130. № 24. P. 2978–2990.
8. Tönnies E., Trushina E. // J. Alzheimers Dis. 2017. V. 57(4). P. 1105–1121.
9. Wang X., Wang W., Li L., Perry G., Lee H.G., Zhu X. // Biochim. Biophys. Acta. 2014. V. 1842. № 8. P. 1240–1247.
10. Zilberter Y., Zilberter M. // J. Neurosci. Res. 2017. V. 95. № 11. P. 2217–2235.
11. Kaur D., Sharma V., Deshmukh R. // Inflammopharmacology. 2019. V. 27. № 4. P. 663–677.
12. Ferreira-Vieira T.H., Guimaraes I.M., Silva F.R., Ribeiro F.M. // Curr. Neuropharmacol. 2016. V. 14. № 1. P. 101–115.
13. Kowalski K., Mulak A. // J. Neurogastroenterol. Motil. 2019. V. 25. № 1. P. 48–60.
14. Junges V.M., Closs V.E., Nogueira G.M., Gottlieb M.G.V. // Curr. Alzheimer Res. 2018. V. 15. № 13. P. 1179–1190.
15. Zarrouk A., Debbabi M., Bezine M., Karym E.M., Badreddine A., Rouaud O., Moreau T., Cherkaoui-Malki M., yeb M., Nasser B., et al. // Curr. Alzheimer Res. 2018. V. 15. № 4. P. 303–312.
16. Li Q., Liu Y., Sun M. // Cell. Mol. Neurobiol. 2017. V. 37. № 3. P. 377–388.
17. Rhea E.M., Leclerc M., Yassine H.N., Capuano A.W., Tong H., Petyuk V.A., Macauley S.L., Fioramonti X., Carmichael O., Calon F., Arvanitakis Z. // Aging Dis. 2024. V. 15. № 4. P. 1688–1725.
18. Alves S.S., Servilha-Menezes G., Rossi L., da Silva Junior R.M.P., Garcia-Cairasco N. // Neurosci. Biobehav. Rev. 2023. V. 152. P. 105326.
19. Chen Y., Fu A.K.Y., Ip N.Y. // Pharmacol. Ther. 2019. V. 195. P. 186–198.
20. Balducci C., Forloni G. // Curr. Pharm. Des. 2014. V. 20. № 15. P. 2491–2505.
21. Puzzo D., Gulisano W., Palmeri A., Arancio O. // Expert. Opin. Drug Discov. 2015. V. 10. № 7. P. 703–711.
22. Zhang L., Chen C., Mak M.S., Lu J., Wu Z., Chen Q., Han Y., Li Y., Pi R. // Med. Res. Rev. 2020. V. 40. № 1. P. 431–458.
23. Holguin A., Frank M.G., Biedenkapp J.C., Nelson K., Lippert D., Watkins L.R., Rudy J.W., Maier S.F. // J. Neurosci. Methods. 2007. V. 161. № 2. P. 265–272.
24. Schultz R.L., Willey T.J. // J. Neurocytol. 1976. V. 5. № 6. P. 621–642.
25. Vincent V.A., van Dam A.M., Persoons J.H., Schotanus K., Steinbusch H.W., Schoffelmeer A.N., Berkenbosch F. // Glia. 1996. V. 17. № 2. P. 94–102.
26. Turner J.N., Shain W., Szarowski D.H., Andersen M., Martins S., Isaacson M., Craighead H. // Exp. Neurol. 1999. V. 156. № 1. P. 33–49.
27. Heppner F.L., Ransohoff R.M., Becher B. // Nat. Rev. Neurosci. 2015. V. 16. № 6. P. 358–372.
28. Manocha G.D., Floden A.M., Rausch K., Kulas J.A., McGregor B.A., Rojanathammanee L., Puig K.R., Puig K.L., Karki S., Nichols M.R., et al. // J. Neurosci. 2016. V. 36. № 32. P. 8471–8486.
29. Paxinos G., Franklin K.B.J. The Mouse Brain in Stereotaxic Coordinates. 2nd Edition. San Diego: Acad. Press, 2001. 133 c.
30. Deardorff W.J., Grossberg G.T. // Handb. Clin. Neurol. 2019. V. 165. P. 5–32.
31. Morganti-Kossmann M.C., Rancan M., Otto V.I., Stahel P.F., Kossmann T. // Shock. 2001. V. 16. № 3. P. 165–177.
32. Butterfield D.A., Halliwell B. // Nat. Rev. Neurosci. 2019. V. 20. P. 148–160.
33. Cheignon C., Tomas M., Bonnefont-Rousselot D., Faller P., Hureau C., Collin F. // Redox Biol. 2018. V. 14. P. 450–464.
34. Hinzman J.M., Thomas T.C., Quintero J.E., Gerhardt G.A., Lifshitz J. // J. Neurotrauma. 2012. V. 29. № 6. P. 1197–1208.
35. Dringen R., Hirrlinger J. // Biol. Chem. 2003. V. 384. № 4. P. 505–516.

5'-Noraristeromycin Repurposing: Well-known S-Adenosyl-L-homocysteine Hydrolase Inhibitor As a Potential Drug Against Leukemia

O. N. Novikova[1], E. S. Matyugina[2], A. V. Gorshenin[1], Yu. I. Velikorodnaya[1], M. D. Krengauz[2,3], V. O. Vedernikova[2,3], P. V. Spirin[2,4], V. S. Prassolov[2,4], S. N. Kochetkov[2], A. L. Khandazhinskaya[2*]

[1]Research Institute of Hygiene, Toxicology and Occupational Pathology, Federal Medical and Biological Agency, Volgograd, 400048 Russian Federation

[2]Engelhardt Institute of Molecular Biology, Russian Academy of Sciences, Moscow, 119991 Russian Federation

[3]Moscow Institute of Physics and Technology (National Research University), Dolgoprudny, 141701 Russian Federation

[4]Center for High-Precision Editing and Genetic Technologies for Biomedicine, Institute of Molecular Biology. V.A. Engelhardt, Russian Academy of Sciences, Moscow, 119991 Russian Federation

*E-mail: khandazhinskaya@bk.ru

Received June 03, 2024; in final form, July 15, 2024

DOI: 10.32607/actanaturae.27443

ABSTRACT **5′-Noraristeromycin as a racemic mixture of enantiomers was found to exhibit a pronounced cytotoxic effect on leukemia cells; IC_{50} for the Jurkat, K562, and THP-1 cell lines was 7.3, 1.3, and 3.7 μM, respectively. The general toxicity of 5'-noraristeromycin was studied in experiments on white mice upon single-dose intragastric administration; toxicometric parameters were determined, and the clinical and pathomorphological presentation of acute intoxication was studied. LD_{50} of the substance was shown to be 63.2 (52.7÷75.8) mg/kg; LD_{16}, 44.7 mg/kg, and LD_{84}, 89.4 mg/kg. Administration of the substance at a dose within the studied dose range is accompanied by systemic damage to the internal organs and tissues of the experimental animals.**

KEYWORDS **5'-noraristeromycin, leukemia, cytotoxicity, acute toxicity, toxicometric parameters.**

ABBREVIATIONS **DMSO – dimethyl sulfoxide; IC_{50} – half-maximal inhibitory concentration; LD_{16}, LD_{50}, and LD_{84} – doses causing death in 16, 50, and 84% of experimental animals upon intragastric administration on day 14 of observation, mg/kg; PBS – phosphate-buffered saline.**

INTRODUCTION

Drug repurposing for cancer therapy implies the search for compounds exhibiting an antitumor activity among substances used in the therapy of other diseases. This approach significantly reduces the cost of designing new drugs, since the substances have been well-studied and their manufacturing technologies have already been developed.

S-Adenosylhomocysteine hydrolase (SAH hydrolase) catalyzes the hydrolysis of SAH to adenosine and *L*-homocysteine, resulting in the accumulation of SAH, a natural inhibitor of S-adenosylmethionine-dependent methyltransferases in the cell. SAH hydrolase inhibitors exhibit a strong antiviral activity, which is described using the terms of inhibiting maturation of viral mRNA (5'-capping) [1]. The SAH hydrolase gene is often amplified in malignant human neoplasms, including cervical and colon cancer [2, 3], indicating that SAH hydrolase can be used as a therapeutic target. Accumulation of SAH in eukaryotic cells treated with SAH hydrolase inhibitors, as well as altering the SAM/SAH ratio, was found to have numerous implications. First, it disrupts DNA methylation, which is a factor responsible for the epigen-

etic regulation of eukaryotic gene expression. DNA methylation disruption is revealed in cancer patients: while the overall genome is hypomethylated, the promoter regions of tumor suppressor genes are locally hypermethylated [4]. Second, it disturbs the function of PRC2 (Polycomb repressive complex 2), the conserved protein complex needed to maintain gene repression. The catalytic subunit of PRC2, the EZH2 protein, ensures the mono-, di-, and trimethylation of histone H3 (Lys27). A number of human tumors have been shown to be characterized by overexpression of PRC2 subunits and to carry mutations that enhance the catalytic activity of EZH2.

The antitumor activity of a number of SAH hydrolase inhibitors (e.g., neplanocin A, 3-deazaneplanocin, 3-deazaadenosine, aristeromycin, etc.) has been demonstrated on different tumor cell lines and even *in vivo* [5–9]. Aristeromycin was first isolated from a *Streptomyces citricolor* culture in 1967 [10]; synthesis of its derivative, 5'-norasteromycin, from 5-amino-4,6-dichloropyrimidine, was reported in 1992 [11]. In *in vitro* experiments, this compound exhibited a pronounced antiviral activity against cowpox, smallpox, and vesicular stomatitis viruses, parainfluenza virus type 3, reovirus type 1, human cytomegalovirus, as well as hepatitis B, measles, and influenza B viruses [12–14]. The antiviral properties of 5'-norasteromycin are based on the inhibition of S-adenosyl-*L*-homocysteine hydrolase activity [12, 14]. This compound was found to highly selectively suppress, along with S-adenosyl-*L*-homocysteine hydrolase, the activity of alpha subunit IκB kinase, the key kinase involved in the nuclear factor kappa B activation cascade [15]. The pharmacokinetic parameters of 5'-norariste romycin administered orally at a dose of 10 mg/kg were determined in the same study; its prophylactic and therapeutic effects associated with the inhibition of tumor necrosis factor α at a dose of 1 mg/kg were revealed using a rheumatoid arthritis model. Based on computer simulation data, Singh et al. [16] hypothesized that this compound may be hepatotoxic. The earliest data on the cytostatic properties of 5'-norariste romycin were published 30 years ago [12]; at concentrations of 0.39–0.50 μg/mL it inhibited proliferation in cultures of L1210/0 mouse leukemia cells as well as human lymphocytes Molt4 and CEM/0. However, comprehensive studies of the substance's cytotoxicity have not been conducted yet and we were unable to find any publications that assess the degree of acute toxicity of this substance to animals.

The objective of this study was to evaluate the antitumor activity of 5'-norariste romycin in cell cultures, followed by an investigation of the characteristics of its toxicity in homeothermic animals and assessment of its main toxicometric parameters.

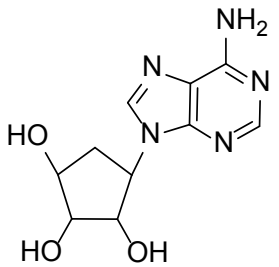

The structure of 5'-norariste romycin

EXPERIMENTAL

Materials and Methods

5′-Norariste romycin as a racemic mixture of enantiomers was synthesized according to the procedure described in [13].

Cell lines

The Jurkat, K562, and THP-1 cells were cultured using RPMI 1640 medium (Gibco, USA) supplemented with 10% fetal bovine serum (FBS), 100 μg/mL penicillin, 100 μg/mL streptomycin, 1 mM sodium pyruvate, and 2 mM *L*-glutamine. The cell cultures were incubated at 37°C in the presence of 5% CO_2.

Cytotoxicity of 5′-norariste romycin against Jurkat, K562, and THP-1 leukemia cells

To assess the cytotoxic activity of 5′-norariste romycin on the THP-1, Jurkat, and K562 leukemia cells, they were seeded into the wells of a 96-well plate (2,500, 2,000, and 2,500 cells per well, respectively). The cells were then treated with the drug within a broad range of concentrations (0.86–50 μM). DMSO at a concentration of 0.25% per well (corresponding to the percentage of DMSO when administering the drug at maximum concentration) was used as the control. The total volume of the well was 100 μL. The cells were incubated for 72 h. Cell survival was evaluated using a Resazurin Cytotoxicity Assay Kit (CEL-04-4-30 ML) (Abisense, Russia). Resazurin was added to PBS at a 1 : 100 ratio (volume, 100 μL) and incubated at +37°C in the presence of 5% CO_2 for 4 h. Absorbance was then measured (absorbance at 570 nm; reference wavelength, 620 nm) using an Multiskan FC microplate photometer (ThermoScientific, USA). The average signal for the wells containing the medium only was subtracted from the value recorded for each well. Next, the data obtained regarding the concentration were normalized to the control and the IC_{50} value

(half-maximal inhibitory concentration) was calculated using nonlinear regression. At least three replicates were made for each concentration. The IC_{50} value was calculated, and diagrams showing the dependence of living cells on drug concentration were plotted using the GraphPad Prism software v.8.4.3 (GraphPad Software, San Diego, USA).

Toxicity of 5′-noraristeromycin for white outbred mice

The toxicity of the compound was studied in compliance with the Guidelines for Conducting Preclinical Studies of Drugs [17].

Male and female white outbred mice weighing 25–30 g were used as biomodels. The animals were procured from the nursery at the Research Institute of Hygiene, Toxicology and Occupational Pathology, Federal Medical and Biological Agency of the Russian Federation.

The experimental and control groups consisted of four animals; the number of male and female animals in the batches was identical. The mice were randomly assigned to groups taking into account the absence of external signs of diseases and homogeneity of body weight (± 10%).

Doses within the range from 40 to 1 000 mg/kg were tested. The substance was administered intragastrically using a metal probe (0.05 mL per 10 g body weight). The control animals received an identical amount of the solvent (99% DMSO of compendial grade, JSC "Tatchempharmpreparaty", Russia) via the same route.

After administration of the substance, the animals were followed up for 14 days; data on clinical manifestations of intoxication and deaths were documented. The lethal doses of the substance were calculated by probit analysis according to the procedure proposed by D.J. Finney using the Microsoft Excel 2013 software on day 14 post-administration [18].

The necropsy of the animals that had not survived was conducted shortly after their death; the macroscopic signs of the impact of the studied substances were documented. Internal organs (heart, lungs, liver, spleen, pancreas, kidneys, stomach, small and large intestine) were removed [19, 20] and subjected to a histological examination. The biomaterial was fixed in 10% neutral formalin for 4 days. Next, the samples were dehydrated using ascending alcohol series, bleached using chloroform in a Cytadel 2000 tissue processor (Shendon), and embedded into a Histomix paraffin medium (Biovitrum, Russia). Paraffin sections 4–5 μm thick were prepared using a Microm HM340E rotary microtome and mounted onto glass slides. For survey studies, the sections were subjected to hematoxylin and eosin staining using the conventional procedure [20].

The microsections were studied and photographed using an AxioScope A1 microscope (Carl Zeiss, Germany) equipped with an AxioCam MRc5 high-resolution digital camera. The recorded images were analyzed using the ZENpro 2012 software (Carl Zeiss).

RESULTS AND DISCUSSION

The cytotoxic activity of 5′-noraristeromycin was assessed in continuous Jurkat, THP-1, and K562 human leukemia cells. The drug was shown to exhibit a pronounced cytotoxic activity against all three cell lines. Significant cytotoxicity was observed for 5′-noraristeromycin concentrations < 1 μM. The half-maximal inhibitory concentrations (IC_{50}) of the drug calculated using linear regression were as follows: ~7.3 μM for Jurkat cells, ~1.7 μM for K562 cells, and ~3.7 μM for THP-1 cells (*Fig. 1*). These values indicate that the drug is also potentially effective in models of laboratory animals, and it would be interesting to further study the mechanisms of its action against malignant leukemia cells.

Monitoring of the evolution of the clinical picture of intoxication caused by 5′-noraristeromycin demonstrated that 5 min after administration of the drug at doses of 200 and 1 000 mg/kg, mice developed sudden agitation and hind limb dysfunction. The animals died within the first 24 h post-administration. No clinical signs were observed during the first hour after administration of 50 and 80 mg/kg 5′-noraristeromycin; the mice subsequently exhibited sluggish behavior and developed lethargy. Administration of the drug at a dose of 40 mg/kg was accompanied by neither clinical signs of intoxication nor animal death.

Table 1 summarizes the determined lethal doses of 5′-noraristeromycin administered intragastrically as a single dose.

Macroscopic assessment of the organs of nonsurviving animals showed that the main changes in them were those related to the gastrointestinal tract. At a dose ranging from 80 to 1 000 mg/kg, the drug caused hemorrhage into the gastric mucosa and the first part of the small intestine, resulting in thinning of their walls, sluggishness, and a yellowish-brown mucoid content in the small intestine. Sluggish small intestine with distended regions and yellowish-brown mucoid intestinal content were observed after the necropsy of the only nonsurviving animal that had received 50 mg/kg 5′-noraristeromycin.

Administration of 5′-noraristeromycin at a dose of 80 mg/kg, which is close to the median lethal dose, to the animals induced pronounced changes in the histoarchitectonics of the analyzed organs and tissues.

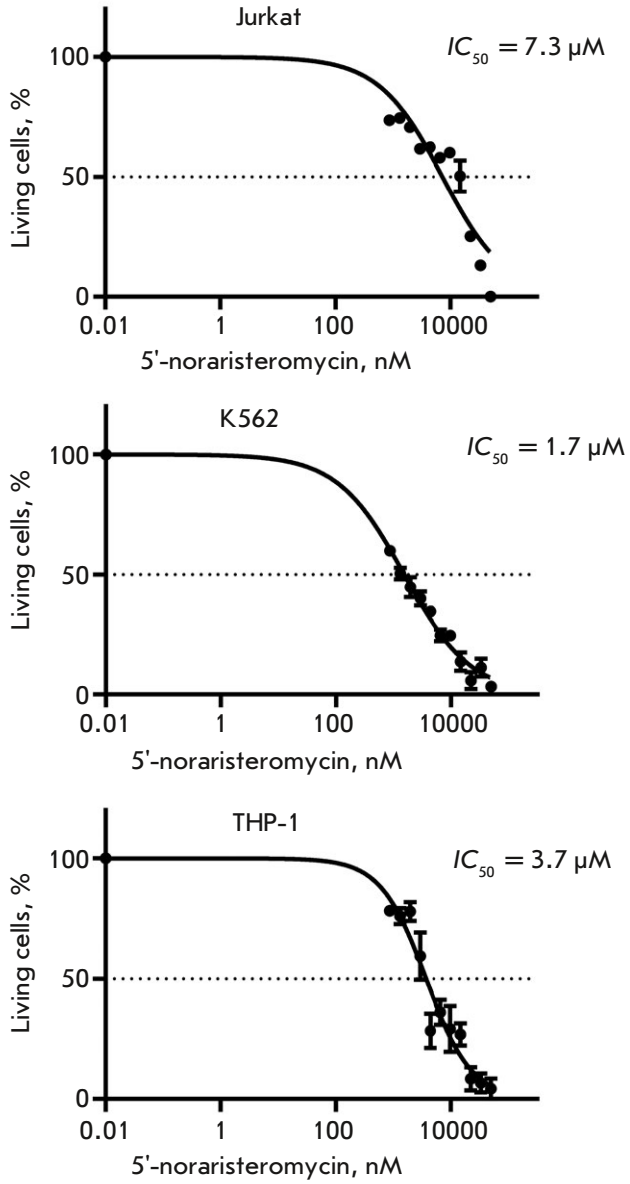

Fig. 1. Survival of leukemia cells after treatment with 5'-noraristeromycin. Curves showing the percentage (%) of living Jurkat, K562, and THP-1 cells in wells treated with the drug at a concentration of 0.86–50 μM are shown. The IC_{50} values were calculated using nonlinear regression and are shown to the right of the graphs for each of the three cell lines

Hence, microscopic examination of the gastric wall revealed an activation of chief cells and mucoid cells, accompanied by gland dilation and accumulation of mucoid contents in them (*Fig. 2A*). Death and desquamation of numerous mucosal epithelial cells into the intestinal lumen was found when examining a small intestine fragment. The remaining villi became more flattened; their apical surface contained no fringe of microvilli. Thinning of the submucosa and partial reduction of the muscle and serous membranes were also observed (*Fig. 2B*).

Total discomplexation of hepatic plates, severe periportal steatosis in combination with hepatocyte death in the centrilobular regions was observed in the liver tissue (*Fig. 3A*). Morphological examination revealed signs of apoptosis related to the death of some hepatocytes, while other cells had undergone necrotic changes (*Fig. 3B*). Either nuclear pyknosis or chromatin redistribution into the submembrane space was observed in relatively intact hepatocytes.

Death of multiple lymphoid cells at the periphery of white pulp follicles was detected in the spleens of the experimental animals (*Fig. 4*).

Erythrocyte stasis and sludging in glomerular capillaries and the intertubular space were observed in the kidneys of an experimental mouse. The lumens of numerous convoluted tubules had narrowed, because of the hypertrophy of the epithelial cells lining them; the cytoplasm contained multiple vacuoles (*Fig. 5A*). Infiltration of the interstitial lung tissue by polymorphonuclear neutrophils was observed in the lung tissue of one experimental mouse. Alveolar septal thickening and edema, as well as erythrocyte diapedesis into interalveolar septa, were also detected (*Fig. 5B*).

Therefore, having studied the toxic properties of 5′-noraristeromycin, we determined that the median lethal dose of the compound administered orally to outbred mice was 63.2 mg/kg. The main intoxication symptoms within the first several minutes were

Table 1. 5'-Noraristeromycin doses lethal to outbred mice after single-dose intragastric administration

Dose, mg/kg	Number of animals per group/number of nonsurviving animals	Calculated lethal doses, mg/kg		
		LD_{16}	LD_{50} with confidence intervals	LD_{84}
40 50 80 200 1000	4/0 4/1 4/3 4/4 4/4	44.7	63.2 (52.7...75.8)	89.4

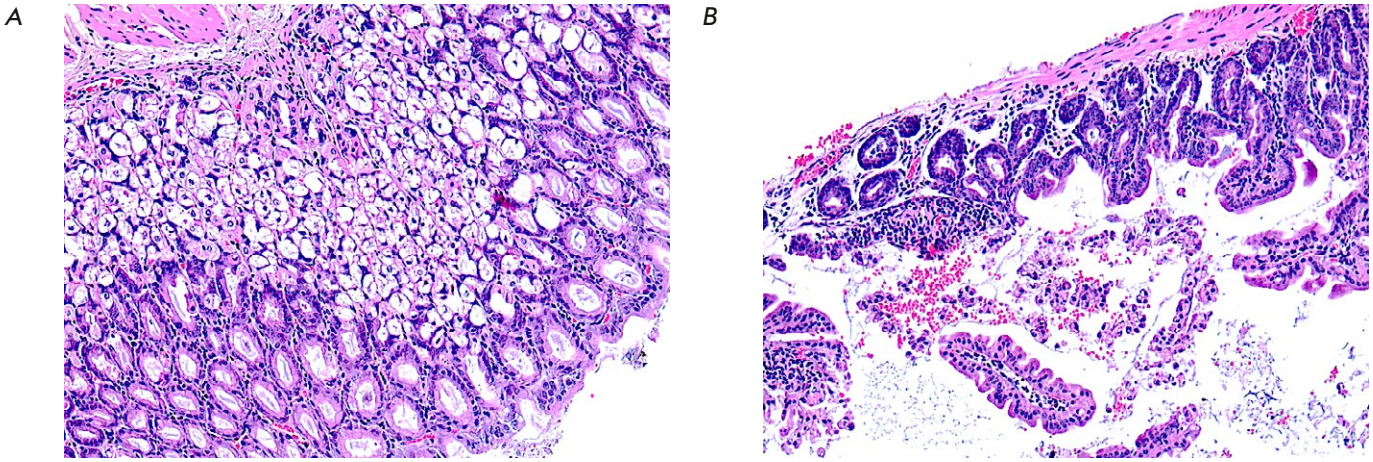

Fig. 2. A fragment of the mucous membrane of the wall of the stomach (*A*) and small intestine (*B*) in an experimental mouse after administration of 80 mg/kg 5'-noraristeromycin. Hematoxylin–eosin staining. 200× magnification

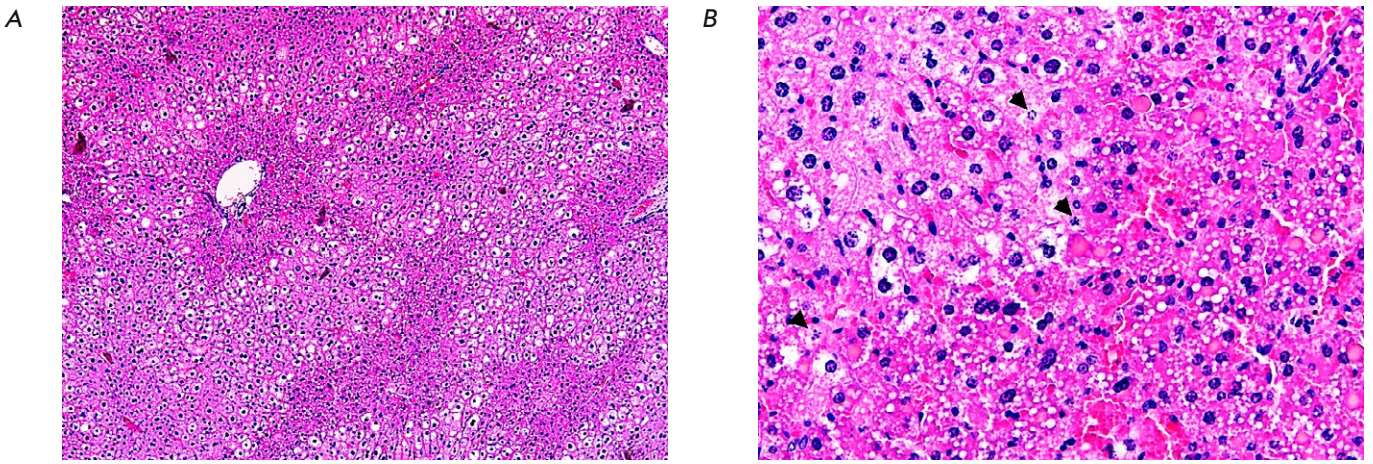

Fig. 3. A fragment of liver tissue from an experimental mouse after administration of 80 mg/kg 5'-noraristeromycin. The hepatocytes with a fragmented nucleus are apoptotic cells (shown with an arrow); round cells with homogeneous cytoplasm are necrotic cells. Hematoxylin–eosin staining. Magnification ×100 (*A*); ×400 (*B*)

neurological abnormalities (sudden agitation and hind limb dysfunction); the later symptoms (during the period between 2 h post-administration until death) involved severe hypodynamia.

Clinical manifestations and the results of the pathomorphological study demonstrated that administration of 5′-noraristeromycin at doses ⩾ 50 mg/kg causes systemic damage to the internal organs and tissues of experimental animals. The negative effect was primarily noted in the organs of the gastrointestinal tract (stomach, small intestine, and liver) and the immune system (spleen).

Intragastric administration of 40 mg/kg 5′-noraristeromycin caused neither clinical signs of intoxication nor death of the experimental animals during the entire observation period.

CONCLUSIONS

Comprehensive analysis of the study results revealed a high *in vitro* cytostatic activity of the newly synthe-

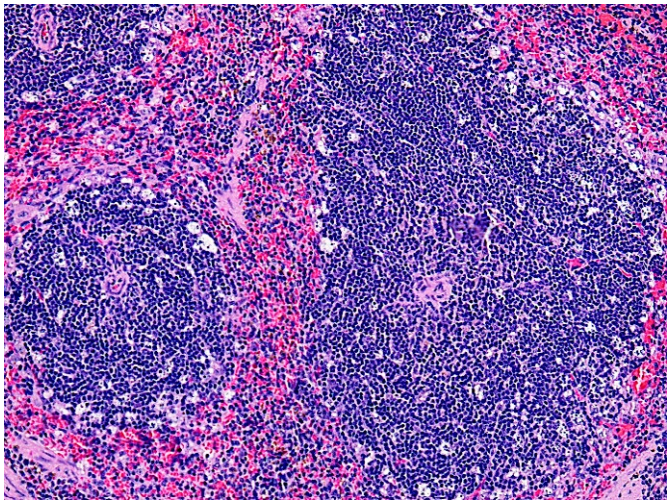

Fig. 4. A fragment of the spleen of an experimental mouse after administration of 80 mg/kg 5'-noraristeromycin. Hematoxylin–eosin staining. 200× magnification

sized chemical compound, 5′-noraristeromycin, against Jurkat, K562, and THP-1 leukemia cells. Cytotoxic activity of the compound against leukemia cells was observed at concentrations as low as 1–10 μM. This compound had no toxic effect when administered intragastrically at a dose < 50 mg/kg. It is noteworthy that some drugs widely used in the therapy of malignant hematologic diseases have similar toxicometric parameters. An example is etoposide: according to different estimates, the range of half-maximal effective concentrations of this drug added to continuous leukemia cell lines is ~ 10–100 μM [21, 22]. Meanwhile, the nonlethal doses used in mouse model studies are ~ 50 mg/kg [23, 24].

In the experiments involving laboratory animals, a number of features of the general toxicity of the compound have been revealed in the range of lethal doses. 5′-Noraristeromycin will further require preclinical investigation and an assessment of specific antitumor activity in *in vivo* models to potentially develop a novel drug.

The data on the cytotoxic potential of the tested compound against leukemia cells obtained in preliminary studies, as well as the results of a study of general toxicity in laboratory animals, provide grounds to consider 5′-noraristeromycin as a promising antitumor agent. The mechanism of its cytotoxic activity against malignant cells and its suitability as a component in combination therapy along with the commonly used chemotherapeutics need more thorough study. ●

This work was supported by the Russian Science Foundation (grant No. 23-64-10018, https://rscf.ru/project/23-64-10018/). Half-maximal effective concentrations of the drug against leukemia cells were determined under support from the Ministry of Science and Higher Education of the Russian Federation (grant No. 075-15-2019-1660).

A

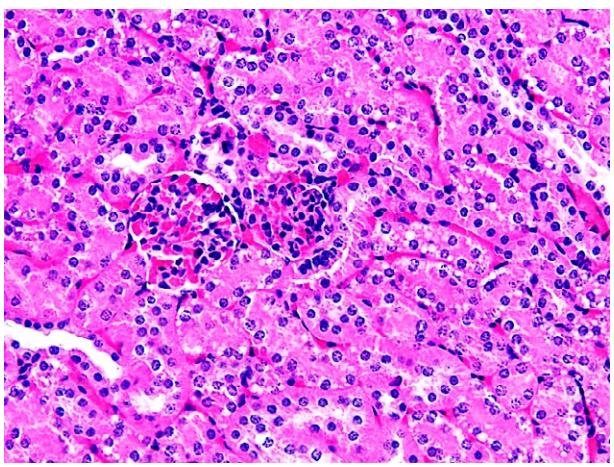

B

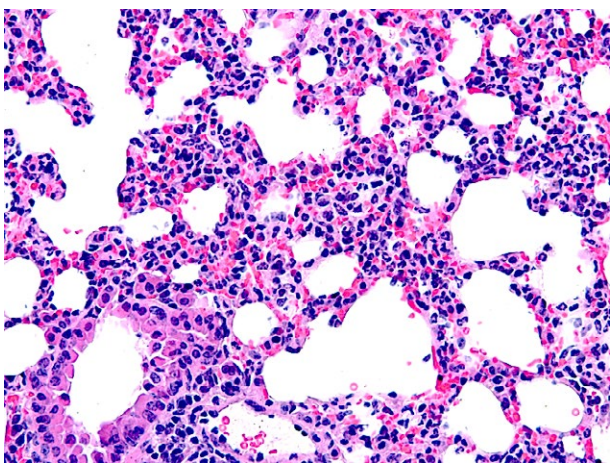

Fig. 5. A fragment of kidney (*A*) and lung (*B*) tissue from an experimental mouse after administration of 80 mg/kg 5'-noraristeromycin. Hematoxylin–eosin staining. 400× magnification

REFERENCES
1. De Clercq E. // Med. Res. Rev. 2009. V. 29. P. 611–645.
2. Scotto L., Narayan G., Nandula S.V., Arias-Pulido H., Subramaniyam S., Schneider A., Kaufmann A.M., Wright J.D., Pothuri B., Mansukhani M., et al. // Genes Chromosomes Cancer. 2008. V. 47. P. 755–765.
3. Loo L.W., Tiirikainen M., Cheng I., Lum-Jones A., Seifried A., Church J.M., Gryfe R., Weisenberger D.J., Lindor N.M., Gallinger S., et al. // Genes Chromosomes Cancer. 2013. V. 52. P. 450–466.
4. Gros C., Fahy J., Halby L., Dufau I., Erdmann A., Gregoire J.M., Ausseil F., Vispe S., Arimondo P.B. // Biochimie. 2012. V. 94. P. 2280–2296.
5. Aury-Landas J., Girard N., Lhuissier E., Adouane D., Delepee R., Boumediene K., Bauge C. // Cell Physiol. Biochem. 2019. V. 53. P. 731–745.
6. Hayden A., Johnson P.W., Packham G., Crabb S.J. // Breast Cancer Res. Treat. 2011. V. 127. P. 109–119.
7. Uchiyama N., Dougan D.R., Lawson J.D., Kimura H., Matsumoto S.I., Tanaka Y., Kawamoto T. // Biochem. Biophys. Res. Commun. 2017. V. 491. P. 1–7.
8. Uchiyama N., Tanaka Y., Kawamoto T. // Eur. J. Pharmacol. 2017. V. 812. P. 138–146.
9. Wu G., Wang N., Luo Y., Zhang Y., Wang P., Zhu Z., Gao Y., Du Z., Yang B. // Tumour Biol. 2017. V. 39. P. 1010428317699117.
10. Kusaka A., Yamamoto H., Shibata M., Muroi M., Kishi T., Mizuno K. // J. Antibiotics. 1968. V. 21. Is. 4. P. 255–263.
11. Patil S.D., Schneller S.W., Hosoya M., Snoeck R., Andrei G., Balzarini J., De Clercq E. // J. Med. Chem. 1992. V. 35. № 18. P. 3372–3377.
12. Siddiqi S.M., Chen X., Schneller S.W., Ikeda S., Snoeck R., Andrei G., Balzarini J., De Clercq E. // J. Med. Chem. 1994. V. 37. P. 551–554.
13. Khandazhinskaya A.A., Shirokova E.A., Shipitsin A.V., Karpenko I.L., Belanov E.F., Kukhanova M.K., Yasko M.V. // Coll. Czechoslovak Chem. Commun. 2006. V. 71. P. 1107–1121.
14. De Clercq E. // Nucleosides, Nucleotides. Nucl. Acids. 1998. V. 17. № 1. P. 625–634.
15. Ito M., Hamano T., Komatsu T., Asamitsu K., Yamakawa T., Okamoto T. // Modern Rheumatol. 2014. V. 24. № 5. P. 775–780.
16. Singh D.B., Gupta M.K., Singh D.V., Singh S.K., Misra K. // Interdisciplinary Sci.-Comput. Life Sci. 2013. V. 5. № 1. P. 1–12.
17. Guidelines for conducting preclinical studies of drugs. Part 1. M.: Grif & K, 2012. 944 p.
18. Finney D.J. Probit analysis. A statistical treatment of the sigmoid response curve. Cambridge: Cambridge Univ. Press, 1947. 272 p.
19. Merkulov G.A. Pathological technique course. 5th ed., rev. and additional L.: Medicine. Leningr. department, 1969. 423 p.
20. Microscopic technology: manual / ed. D.S. Sarkisov, Yu.L. Perov. M: Medicine, 1996. 544 p.
21. Husaini R., Ahmad M., Zakaria Z. // Exp. Ther. Med. 2017. V. 13. № 6. P. 3209–3216.
22. Zhou Z., Zwelling L.A., Ganapathi R., Kleinerman E.S. // Br. J. Cancer. 2001. V. 85. № 5. P. 747–751.
23. Slater L.M., Stupecky M., Sweet P., Osann K., Eklof A., Arquilla E.R. // Cancer Chemother. Pharmacol. 2001. V. 48. № 4. P. 327–332.
24. Kluska M., Woźniak K. // Internat. J. Mol. Sci. 2021. V. 22. № 12. P. 6602.

Abundance of Tumor-Infiltrating B Cells in Human Epithelial Malignancies

E. A. Petrov[1], D. M. Malabuiok[1], H. Zheng[2], Yu. A. Mokrushina[1,3], V. A. Abrikosova[1], Yu. B. Kuzmin[4], P. V. Tzarapaev[4], S. O. Kochkina[4], I. V. Eltsov[4], V. D. Knorre[1], I. V. Smirnov[1,3,5*], S. S. Terekhov[1], Z. Mamedli[4], N. E. Kushlinskii[4], D. V. Rogozhin[4], V. B. Matveev[4], P. V. Kononets[4], I. S. Stilidi[4], H. Zhang[2], A. G. Gabibov[1,3]

[1]Shemyakin–Ovchinnikov Institute of Bioorganic Chemistry, Moscow, 117997 Russian Federation
[2]State Key Laboratory of Medicinal Chemical Biology and College of Life Sciences, Nankai University, 94 Weijin Road, Tianjin, 300071 China
[3]Department of Chemistry, Lomonosov Moscow State University, Moscow, 119991 Russian Federation
[4]Blokhin National Medical Research Center of Oncology, Moscow, 115522 Russian Federation
[5]Endocrinology Research Center, Moscow, 117036 Russian Federation
*E-mail: ivansmr@inbox.ru

Received December 13, 2023; in final form, July 28, 2024
DOI: 10.32607/actanaturae.27353

ABSTRACT **Cancer is a major global health problem. The type of malignant neoplasm and the potency of the immune response against tumors are two of the key factors influencing the outcome of the disease. The degree of tumor infiltration by lymphocytes plays an important role in antitumor response development, generally correlating with a favorable prognosis of treatment for certain cancers. We analyzed the abundance of tumor-infiltrating B cells (TIBs) in solid tumors of different cancers. TIBs were shown to be more abundant in colon and sigmoid colon cancer samples compared with cecal, rectal, and kidney cancer samples. The median and interquartile range of the TIB fraction were 11.5% and 4–20% in colon cancer, 6% and 3–11% in sigmoid colon cancer, 2.7% and 0.7–3.7% in cecal cancer, 2.5% and 0.9–3.6% in rectal cancer, 1.4% and 1.0–2.3% in kidney cancer, and 3.0% and 1.8–12% in lung cancer, respectively. However, there were no significant differences in the abundance of TIBs among samples at different stages of the cancer. Hence, investigation of the B cell response in colon cancer is of particular interest, since increased quantities of TIBs may indicate the existence of immunogenic tumor markers or the cell-cell interactions involved in disease progression. We believe that studying the diversity of TIBs in colon cancer will increaseour understanding of the mechanisms of the disease, contributing to the identification of new molecular targets for targeted oncotherapy.**

KEYWORDS **tumor-infiltrating B cells, colorectal cancer, solid tumors.**

ABBREVIATIONS **CRC – colorectal cancer; NSCLC – non-small cell lung cancer; CCRCC – clear cell renal cell carcinoma; TIBs – tumor-infiltrating B cells.**

INTRODUCTION

Malignant neoplasms are among the most challenging medical and social problems. According to the WHO, the incidence of cancers continues to increase. The most common oncological diseases are breast, lung, colorectal, and prostate cancers. Despite improvements in the treatment. as well as new therapies, the mortality rate from some types of tumors, such as lung, colorectal, and liver cancers, remains very high [1].

Tumor-infiltrating immune cells play a key role in the development of the body's immune response to the tumor; they are capable of exhibiting both pro-tumor and anti-tumor activity. Tumor-infiltrating immune cells are a heterogeneous set that includes T cells, B cells, natural killer (NK) cells, macrophages, neutrophils, and dendritic cells. The subset composition and percentage of tumor-infiltrating immune cells can vary depending on the type and stage of a cancer, as well as from patient to patient [2]. Tumor-infiltrating lymphocytes (TILs) involve T and B cells that have moved from the bloodstream and migrated into the tumor. The presence of TILs in a tumor may be a prognostic marker of a favorable course of the disease and the efficacy of therapy [3].

Investigation of adaptive immunity in oncoimmunology is largely focused on CD8+ cytotoxic T lym-

phocytes (CTLs). CTLs are considered to be the main effectors of the antitumor immune response; they directly destroy transformed cells. High levels of tumor infiltration by CTLs correlate with a favorable prognosis for the course of the disease and increased overall survival chances in patients with different cancers [4]. CD4+ T cells are an integral part of adaptive immunity, but their role in the immune response to a tumor remains unsettled [5]. Along with CD8+ T cells, there are tumor-specific CD4+ T helper (Th) cells that can recognize tumor antigens and effectively slow tumor growth in animal models in the absence of CTLs [6]. However, the bulk of the antitumor effect of CD4+ Th cells is the Th-mediated activation of CTLs to recognize and destroy tumor cells or activate other immune cells, in particular the B cell component of the immune response [7]. On the contrary, the subset of CD4+ T regulatory (Treg) lymphocytes is known to exert an immunosuppressive effect, mainly due to the production of cytokines (IL-10 and TGFβ), and suppress the antitumor function of the effector cells of the tumor microenvironment, contributing thus to malignant growth and an unfavorable outcome [8].

Less is known about B cells that infiltrate the tumor and often co-localize with T cells, sometimes forming organized lymphoid structures [9]. Tumor-infiltrating B cells (TIBs) affect malignancies through two opposing mechanisms and can both promote and suppress tumors [10]. The antitumor effects of B cells are mediated through various pathways. Upon humoral responses to tumor neoantigens, B cells differentiate into plasma cells and secrete tumor-specific antibodies that mediate antibody-dependent cellular cytotoxicity (ADCC), complement-dependent cytotoxicity (CDC), or antibody-dependent cellular phagocytosis (ADCP). In addition to antibody production, B cells can secrete a variety of cytokines, thus influencing the function of other immune cells in the tumor microenvironment in multiple directions. For example, secretion of IL-12 by B cells mediates the proliferation and antitumor action of T and NK cells and secretion of IL-10 by regulatory B cells (Breg), through suppression of the autoimmune response, has a protumor effect [11]. Also, B cells can act as antigen-presenting cells (APCs); when Th2 cells are activated by the CD40 ligand, B cells express chemokines and costimulatory factors and induce a T cell antitumor immune response [12]. Thus, TIBs have a broad potential for tumor cell destruction and exert a significant impact on the balance of activation or suppression of other immune cells in the tumor's microenvironment.

TIBs have been studied particularly widely in breast cancer, where they are found in 25% of cases and account for up to 40% of the tumor-infiltrating lymphocyte population. In breast cancer, the prognosis of patient survival and the choice of therapy depend on the abundance of TIBs [13]. At present, the abundance of TIBs is known to positively correlate with a favorable clinical outcome of melanoma [14], ovarian cancer, non-small cell lung cancer [15], and squamous cell cervical cancer [16, 17].

The aim of this study was to assess the abundance of B lymphocytes in various nosological forms of oncological diseases and to assess the association between the B lymphocyte content and the clinical and morphological characteristics of these diseases.

EXPERIMENTAL

The study included 50 patients undergoing surgical treatment at the Blokhin National Medical Research Center of Oncology of the Ministry of Health of the Russian Federation. The malignant nature of the tumors in all the patients was clinically verified upon routine pathomorphological examination. The study included donors who had not undergone chemotherapy before surgery. All patients gave informed consent to participate in the study. The study was conducted in compliance with current legal and ethical standards.

Tumor cell isolation

A ~0.5–2 cm^3 tumor fragment was placed in a 50 mL tube with phosphate-buffered saline (PBS) immediately after tumor resection; further manipulations with the material were started within 1.5–3 h after surgery. Biological material was transported to the laboratory at room temperature. A sample was precipitated in a benchtop centrifuge (Eppendorf, Germany) for 5 min (100 g, 24°C). The supernatant was decanted, and 5 mL of the handling medium (a 1 : 1 mixture of DMEM F12 and RPMI 1640 (PanEco, Russia), 10% HyClone bovine fetal serum (Cytiva, USA), and an antibiotic–antimycotic solution (Thermo Fisher Scientific, USA) to a final concentration of 1%) were added. The tumor fragment was transferred to a 60 mm Petri dish (SPL, South Korea) and mechanically minced using a #10 medical scalpel (Apexmed, India) into ~1–3 mm^3 pieces. The resulting suspension was transferred to a 15 mL test tube and precipitated in a benchtop centrifuge (Eppendorf) for 5 min (100 g, 24°C). The supernatant was decanted, followed by addition of 2 mL of a warm handling medium containing a mixture of enzymes: 0.5 mg DNase I (Sigma, USA), collagenase types I and IV (Merck, USA) 1 mg of each, and 2 mg hyaluronidase (Microgen, Russia). The tube with the tissue fragments was placed on a rotating platform (Biosan, Latvia) and incubated at 7 rpm in a CO_2 incubator at 37°C and 8% CO_2 for 40 min. After incuba-

tion, the solution with cells was gently mixed 25–50 times using a serological pipette to break up aggregates until a homogeneous suspension was obtained. The cell suspension was successively filtered through cell sieves with pore sizes of 100, 70, and 40 μm, with the used sieve being additionally washed each time with 2 mL of the handling medium. The cells were precipitated in a benchtop centrifuge (Eppendorf) for 15 min (300 g, 24°C). The cell pellet was treated with 1 mL of ACK buffer (150 mM ammonium chloride; 10 mM potassium bicarbonate; 0.1 mM EDTA-Na_2) for 1 min to lyse erythrocytes, when necessary. The reaction was stopped with 2 mL of the handling medium. The cells were pelleted in a benchtop centrifuge (Eppendorf) for 7 min (300 g, 24°C). The supernatant was decanted; the cell pellet was resuspended in 2 mL of the culture medium (DMEM advanced 90% (Thermo Fisher Scientific), 10% HyClone bovine fetal serum (Cytiva, USA), L-alanyl-L-glutamine (Yeasen, USA) up to 2 mM, antibiotic–antimycotic (Thermo Fisher Scientific) up to 1%); and the number of viable cells was estimated by the trypan blue dye exclusion method using a CellDrop FL automated cell counter (DeNovix, USA). An aliquot of the prepared cells was stained, followed by cytometric analysis. The remaining cells were cryopreserved in the CryoMed-M medium (PanEco) according to the manufacturer's instruction.

Quantification of B lymphocytes by flow cytofluorometry

Dissociated tumor cells (2×10^6) were precipitated in a benchtop centrifuge (Eppendorf) for 5 min (350 g, 4°C). The medium was decanted, and the cell pellet was resuspended in 100 μL of phosphate-buffered saline containing 0.5% BSA and 2 mM EDTA. Staining was performed using a mouse monoclonal (clone 2D1) anti-human common leukocyte antigen CD45 antibody conjugated with APC-Cy7 (Sony, USA) at a 1 : 300 dilution and a mouse monoclonal (clone HIB19) anti-human B lymphocyte antigen CD19 antibody conjugated with PE-Cy7 (BioLegend, USA) at a 1 : 1,000 dilution. Incubation with antibodies was performed in the dark at 4°C for 30 min. To identify dead cells, a SYTOX Green dye (BioLegend, USA) was added at a 1 : 3,000 dilution and incubated in the dark at 4°C for more than 15 min. The sample was then washed three times with 500 μL of phosphate-buffered saline containing 2 mM EDTA and resuspended in 100 μL for staining analysis on an ACEA Novocyte flow cytometer (ACEA Biosciences, USA). Statistical data processing was performed using Python tools (seaborn, pandas). The median was estimated in each study group; the decision on the reliability of the differences between analyzed samples was made based on the nonparametric Mann–Whitney U-test.

RESULTS AND DISCUSSION

The study included 50 patients with malignancies of various nosologies: CRC (n = 31), NSCLC (n = 13), and CCRCC (n = 6). Cells were isolated from tumor material according to the protocol in [18] with some modifications. The final workflow for preparing a homogeneous cell suspension included mechanical mincing of the sample, dissociation of tissue fragments with a mixture of enzymes, and three successive stages of filtration through cell sieves with pore sizes of 100, 70, and 40 μm (*Fig. 1*).

Mechanical dissociation involves mincing of a tumor fragment into small pieces with a medical scalpel to increase the area of tissue contact with enzymes at the next stage. Enzymatic dissociation by enzymes possessing collagenase, hyaluronidase, and DNase activities is used to destroy the extracellular matrix and prepare a tumor cell suspension. The type of enzymes used for dissociation can significantly affect the quantitative yield and viability of the resulting cells. In the course of the study, we selected an optimal enzyme combination involving hyaluronidase, DNase I, collagenase types 1 and 4 (1.0, 0.25, 0.5, and 0.5 mg/mL, respectively; see Experimental section), the use of which provided effective destruction of cell contacts. This combination reduced the duration of the enzymatic dissociation stage to 30–40 min and increased the yield of viable cells to 80% or more. Filtration of the resulting suspension is necessary for further disaggregation of the cell sample. In this case, the use of a 100 μm cell sieve enabled effective removal of the large cell conglomerates and fat fraction and facilitated further filtration of the sample through 70 and 40 μm sieves to produce a homogeneous cell suspension. Thus, the use of a combination of mechanical and enzymatic dissociation of tumor tissue yielded a homogeneous cell suspension with a high viability level of 88%, on average.

To identify and quantify the B cell population, reflecting the degree of tumor tissue infiltration, all samples were analyzed by flow cytometry (*Fig. 2*). Staining was performed using monoclonal anti-human common leukocyte antigen CD45 antibodies conjugated with APC-Cy7 (CD45 APC-Cy7) and anti-human B lymphocyte antigen CD19 antibodies conjugated with PE-Cy7 (CD19 PE-Cy7). At the first step, a tumor cell population was identified in the forward scatter (FSC) versus side scatter (SSC) dot plot (*Fig. 2A*). Then, single cells were separated from cell aggregates that could be the source of redundant fluorescence signals in further quantification of B cells (*Fig. 2B*).

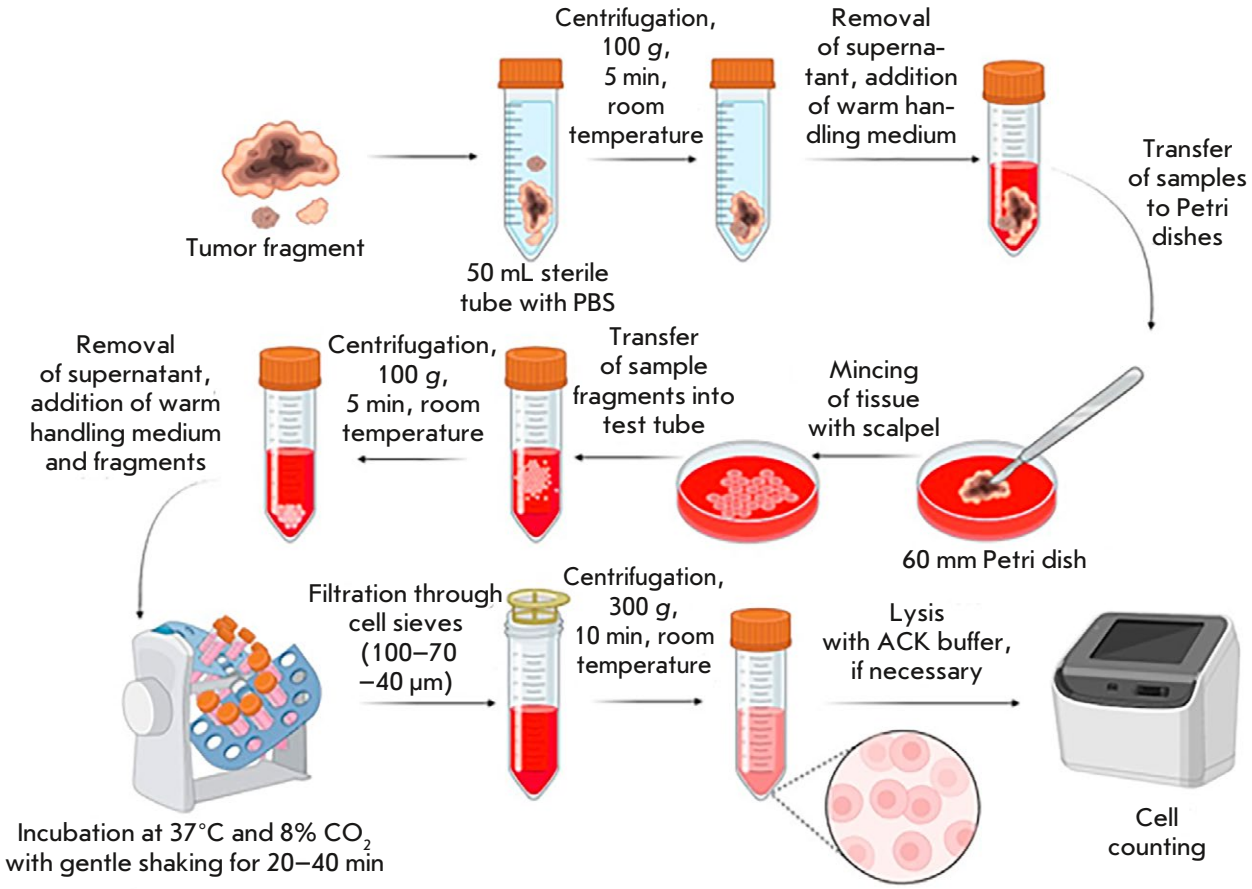

Fig. 1. Tumor tissue dissociation workflow

At the second stage, living cells were gated among single cells (*Fig. 2C*) by staining with a fluorescent dye, SytoxGreen, that has high affinity for nucleic acids. The dye penetrates only into cells with damaged plasma membranes, so it is used to assess cell viability. Then, four subsets were identified among the living cells based on staining with specific antibodies to the surface antigens CD45 and CD19, where the gate with double positive staining corresponded to B cells (*Fig. 2D*).

The cell samples of all studied nosologies were analyzed in the same way. The content of CD19+ B cells varied significantly, from 0.4 to 40% (*Fig. 3A*).

The highest percentage of TIBs was observed in patients with colon and sigmoid colon cancer; the group median was 11.5 and 6%, respectively ($p < 0.05$). In the other groups (cecal and rectal cancer, lung cancer), the median B cell fraction was about 3%. The lowest B cell fraction was observed in kidney cancer, with the median amounting to 1%.

The interquartile range of the TIB fraction was 4–20% for colon cancer, 3–11% for sigmoid colon cancer, 0.7–3.7% for cecal cancer, 0.9–3.6% for rectal cancer, 1.0–2.3% for kidney cancer, and 1.8–12% for lung cancer.

The abundance of TIBs in colon cancer samples was analyzed based on the disease stage (*Fig. 3B*).

Our findings did not reveal statistically significant differences in the percentage of TIBs at different stages of the tumors.

A generalized analysis of the B lymphocyte content in CRC and the clinical and morphological characteristics of the disease are presented in *Table 1*.

There is a direct correlation between the B cell content and the tumor size; namely, larger tumors are characterized by a higher content of B cells. It is also worth noting that poorly differentiated tumors are characterized by high B cell contents, but that these results do not reach statistical significance.

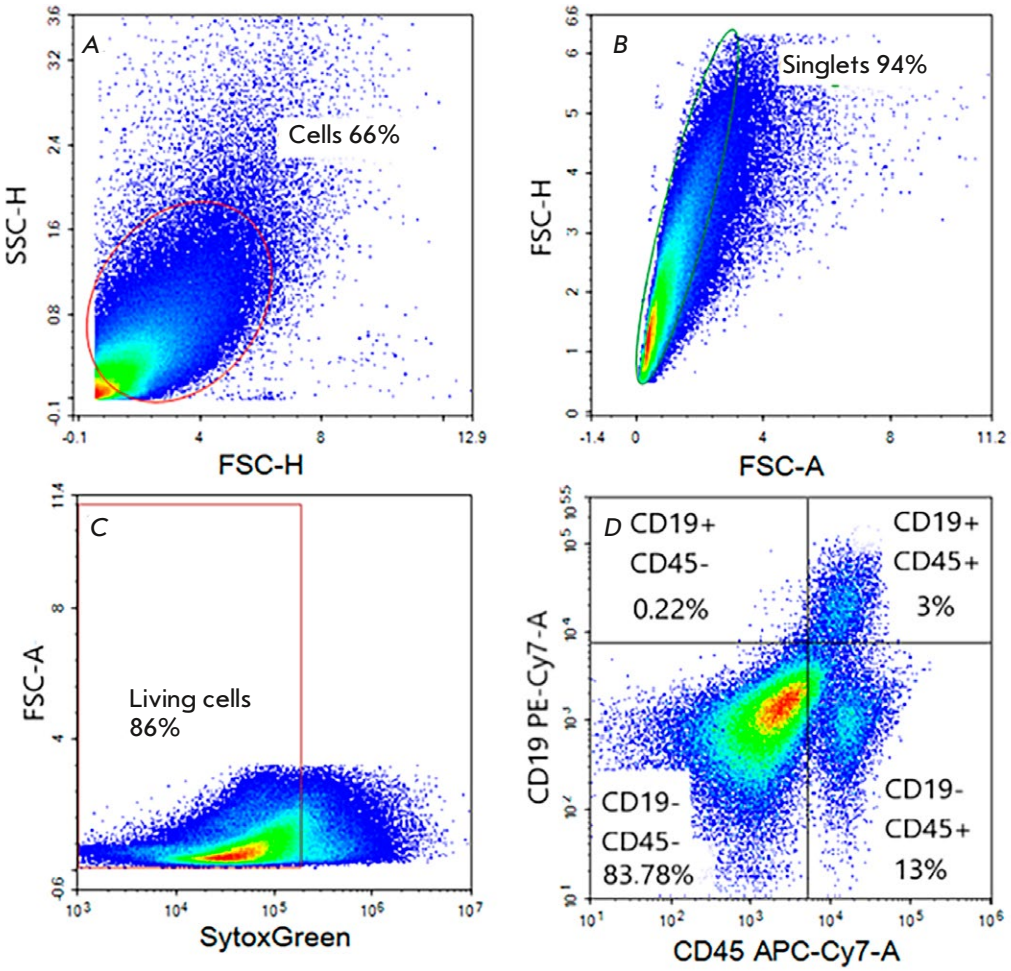

Fig. 2. Sequential gating strategy for assessing the fraction of tumor-infiltrating B cells. (*A*) The oval area denotes cells assigned to the tumor cell population based on lateral and forward light scattering data. (*B*) The oval area highlights single cells. (*C*) The rectangular area denotes the living cell population. (*D*) The image is divided into quadrants that are related to the CD45–/CD19–, CD45–/CD19+, CD45+/CD19–, and CD45+/CD19+ cell subsets. The CD45+/CD19+ cell subset corresponds to B cells

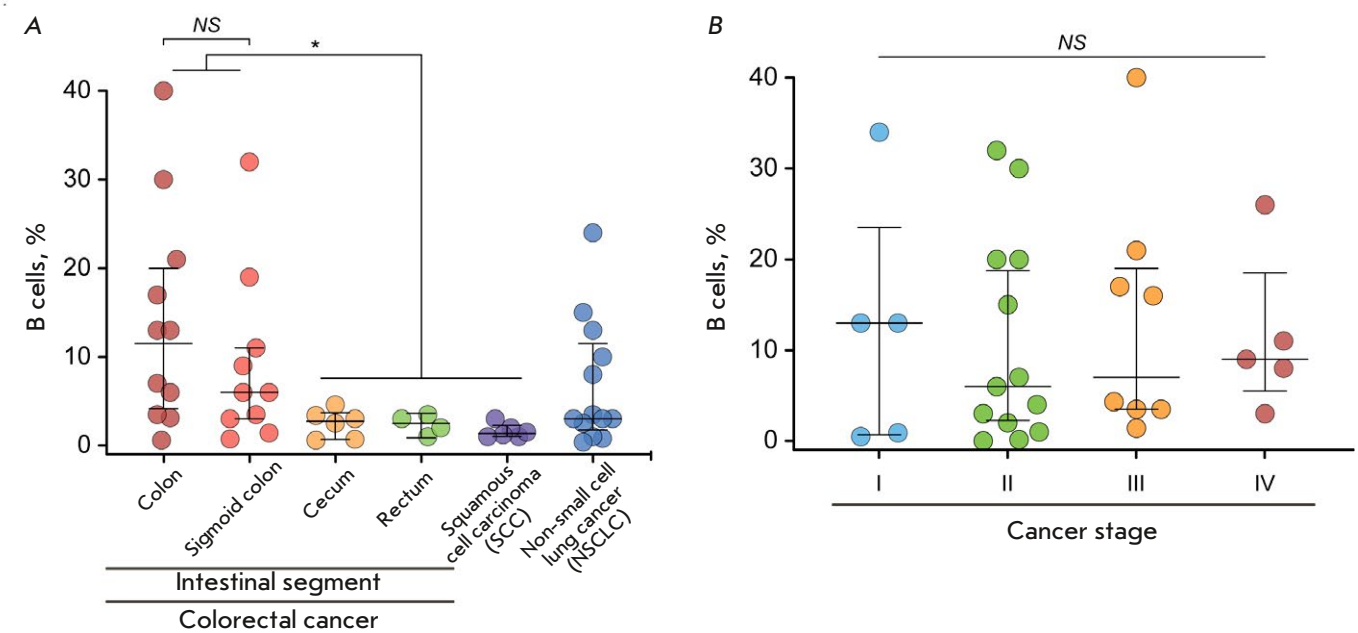

Fig. 3. (*A*) Quantification of tumor-infiltrating B cells in tumor material of various nosologies. (*B*) Abundance of tumor-infiltrating B cells in colon cancer samples, depending on the stage. Statistical analysis was performed using the nonparametric Mann–Whitney U test. $^{*}P < 0.05$; NS – no significant difference

Table 1. Association between B cell content and clinical and morphological parameters in colorectal cancer

Parameter	*n*	CD19+ B cells, %		
		Median	Quartiles 25–75%	*p*
Age ⩽63 >63	 15 16	 7.0 3.3	 3.5–15.0 2.1–14.5	0.428
Gender Male Female	 14 17	 7.0 3.5	 3.5–20.0 2.3–8.5	0.135
Stage I–II III–IV	 18 13	 6.0 3.5	 1.8–16.3 2.8–12.0	0.805
Grade (G) G1 G2–G3	 4 27	 3.8 15.0	 2.1–9.5 6.0–20.0	0.175
Tumor size (T) T1–T2 T3–T4	 20 11	 1.9 6.0	 0.2–3.1 3.0–16.0	0.019*
Nodal status (N) N0 N1	 29 2	 5.15 4.0	 2.0–13.8 3.0–16.0	0.707
Metastasis (M) M0 M1	 28 3	 4.3 6.0	 2.3–15.5 4.0–8.0	0.727
Location Large intestine Rectum	 27 4	 6.0 3.25	 2.5–16.0 2.3–3.9	0.255
Large intestine segment Left Right	 14 13	 5.15 8.0	 1.7–9.3 2.8–18.5	0.296

CONCLUSION

According to 2020 data, some 1.9 million new cases of colorectal cancer were recorded around the world. Some estimates show that the annual increase in Russia stands at about 50,000 new cases. Colorectal cancer is detected quite late, so the mortality rate attendant to it is rather high and can reach 40% within a year from the time of tumor diagnosis [19], and, according to the World Health Organization, it is the second leading cause of cancer death in the world [20]. Given this, the search for therapeutically significant tumor-specific antigens and/or therapeutic antibodies to these types of cancers is a critical undertaking.

The data obtained in this study deepen our knowledge about the abundance of TIBs in various nosological forms of cancer. We have found that colon cancer is characterized by the highest percentage of TIBs. The material for investigation can be collected regardless of the disease stage, because we have not identified reliable differences in the abundance of B cells at different stages of tumor progression. However, there are conflicting data to the effect that the content of TIBs in colorectal cancer depends on the stage of tumor development [21]. The number of intratumoral B cells is also known to inversely correlate with the stage of lung cancer [22].

From a fundamental point of view, profound profiling of TIBs adds to our knowledge of immune response patterns to cancer cells and will open up new opportunities in the search for potential markers of malignant transformation. From a practical point of view, tumor-infiltrating B cells may be used to create antibody libraries for further development of CAR-T therapy and other personalized therapy approaches. ●

This study was supported by a joint grant by the Russian Science Foundation No. 23-44-00043 and a grant by the National Natural Science Foundation of China 82261138553.

REFERENCES

1. World Health Organization. Official WHO website. Available at: https://www.who.int/.
2. Kim S., Kim A., Shin J.Y., Seo J.S. // Sci. Rep. 2020. V. 10. № 1. P. 9536.
3. Brummel K., Eerkens A.L., de Bruyn M., Nijman H.W. // Br. J. Cancer. 2023. V. 128. № 3. P. 451–458.
4. Yu P., Fu Y.X. // Lab. Investig. J. Tech. Methods Pathol. 2006. V. 86. № 3. P. 231–245.
5. Tay R.E., Richardson E.K., Toh H.C. // Cancer Gene Ther. 2021. V. 28. № 1–2. P. 5–17.
6. Perez-Diez A., Joncker N.T., Choi K., Chan W.F., Anderson C.C., Lantz O., Matzinger P. // Blood. 2007. V. 109. № 12. P. 5346–5354.
7. Fearon E.R., Pardoll D.M., Itaya T., Golumbek P., Levitsky H.I., Simons J.W., Karasuyama H., Vogelstein B., Frost P. // Cell. 1990. V. 60. № 3. P. 397–403.
8. Pati S., Chowdhury A., Mukherjee S., Guin A., Mukherjee S., Sa G. // Appl. Cancer Res. 2020. V. 40. № 1. P. 7.
9. Sharonov G.V., Serebrovskaya E.O., Yuzhakova D.V., Britanova O.V., Chudakov D.M. // Nat. Rev. Immunol. 2020. V. 20. № 5. P. 294–307.
10. Zhang E., Ding C., Li S., Zhou X., Aikemu B., Fan X., Sun J., Zheng M., Yang X. // Biomark. Res. 2023. V. 11. № 1. P. 28.
11. Li Q., Teitz-Tennenbaum S., Donald E.J., Li M., Chang A.E. // J. Immunol. 2009. V. 183. № 5. P. 3195–3203.
12. Guo F.F., Cui J.W. // J. Oncol. 2019. V. 2019. P. 2592419.
13. Marsigliante S., Biscozzo L., Marra A., Nicolardi G., Leo G., Lobreglio G.B., Storelli C. // Cancer Lett. 1999. V. 139. № 1. P. 33–41.
14. Willsmore Z.N., Harris R.J., Crescioli S., Hussein K., Kakkassery H., Thapa D., Cheung A., Chauhan J., Bax H.J., Chenoweth A., et al. // Front. Immunol. 2021. V. 11. P. 622442.
15. Federico L., McGrail D.J., Bentebibel S.E., Haymaker C., Ravelli A., Forget M.A., Karpinets T., Jiang P., Reuben A., Negrao M.V., et al. // Ann. Oncol. Off J. Eur. Soc. Med. Oncol. 2022. V. 33. № 1. P. 42–56.
16. Reuschenbach M., von Knebel Doeberitz M., Wentzensen N. // Cancer Immunol. Immunother. 2009. V. 58. № 10. P. 1535–1544.
17. Coronella-Wood J.A., Hersh E.M. // Cancer Immunol. Immunother. 2003. V. 52. № 12. P. 715–738.
18. Leelatian N., Doxie D.B., Greenplate A.R., Sinnaeve J., Ihrie R.A., Irish J.M. // Curr. Protoc. Mol. Biol. 2017. V. 118. P. 25C.1.1–25C.1.23.
19. Avksentyeva M. // Eur. J. Health Econ. HEPAC Health Econ. Prev Care. 2010. V. 10. Suppl 1. P. S91–98.
20. World Health Organization. Official WHO website. Available at: https://www.who.int/ru/news-room/fact-sheets/detail/colorectal-cancer.
21. Bindea G., Mlecnik B., Tosolini M. // Immunity. 2013. V. 39. № 4. P. 782–795.
22. Gottlin E.B., Bentley R.C., Campa M.J., Pisetsky D.S., Herndon J.E., Patz E.F. // J. Thorac. Oncol. Off Publ. Int. Assoc. 2011. V. 6. № 10. P. 1687–1690.

Synthetic Lesions with a Fluorescein Carbamoyl Group As Analogs of Bulky Lesions Removable by Nucleotide Excision Repair: A Comparative Study on Properties

A. A. Popov, V. M. Golyshev, L. S. Koroleva, K. D. Nazarov, R. O. Anarbaev, I. O. Petruseva*
Institute of Chemical Biology and Fundamental Medicine, Siberian Branch of Russian Academy of Sciences, Novosibirsk, 630090 Russian Federation
*E-mail: irapetru@niboch.nsc.ru
Received May 03, 2024; in final form, July 05, 2024
DOI: 10.32607/actanaturae.27419

ABSTRACT **Mammalian nucleotide excision repair (NER), known for its broad substrate specificity, is responsible for removal of bulky lesions from DNA. Over 30 proteins are involved in NER, which includes two distinct pathways: global genome NER and transcription-coupled repair. The complexity of these processes, the use of extended DNA substrates, and the presence of bulky DNA lesions induced by chemotherapy have driven researchers to seek more effective methods by which to assess NER activity, as well as to develop model DNAs that serve as efficient substrates for studying lesion removal. In this work, we conducted a comparative analysis of model DNAs containing bulky lesions. One of these lesions, N-[6-{5(6)-fluoresceinylcarbamoyl}hexanoyl]-3-amino-1,2-propanediol (nFluL), is known to be efficiently recognized and excised by NER. The second lesion, N-[6-{5(6)-fluoresceinylcarbamoyl}]-3-amino-1,2-propanediol (nFluS), has not previously been tested as a substrate for NER. To evaluate the efficiency of lesion excision, a 3'-terminal labeling method was employed to analyze the excision products. The results showed that nFluS is removed approximately twice as efficiently as nFluL. Comparative analyses of the effects of nFluL and nFluS on the geometry and thermal stability of DNA duplexes — combined with spectrophotometric and spectrofluorimetric titrations of these DNAs with complementary strands — were performed next. They revealed that the absence of an extended flexible linker in nFluS alters the interaction of the bulky fluorescein moiety with neighboring nitrogenous bases in double-stranded DNA. This absence is associated with the enhanced efficiency of excision of nFluS, making it a more effective synthetic analog for studying bulky-lesion removal in model DNA substrates.**

KEYWORDS **nucleotide excision repair, bulky lesion, spectrometric titration.**

ABBREVIATIONS **NER – nucleotide excision repair; GG-NER – global genome NER; nFluL – N-[6-{5(6)-fluoresceinylcarbamoyl}hexanoyl]-3-amino-1,2-propanediol; nFluS – N-[6-{5(6)-fluoresceinylcarbamoyl}]-3-amino-1,2-propanediol; ODN – oligodeoxyribonucleotide.**

INTRODUCTION

The integrity and stability of the genome are maintained by DNA repair mechanisms. One such mechanism is nucleotide excision repair (NER), which is responsible for the removal of bulky lesions. These lesions are typically covalent adducts that introduce significant changes into the regular structure of DNA. NER is a multistep process during which proteins sequentially assemble multisubunit complexes of variable composition at a site of DNA damage. The damage is then recognized and excised, along with a surrounding segment of DNA, typically 24 to 32 nucleotides in length. The original DNA sequence is restored by repair polymerases and ligases, using the intact strand as a template. There are two branches of NER: global genome NER (GG-NER), which operates independently of the transcriptional activity of the genome, and transcription-coupled repair [1, 2].

The NER system is characterized by broad substrate specificity and is capable of removing a va-

riety of DNA lesions. These include damage caused by UV and ionizing radiation or by chemically active environmental substances like polycyclic aromatic hydrocarbons and their reactive metabolites (e.g., diol epoxides). The mechanism of action of many chemotherapeutic drugs also involves the formation of bulky DNA adducts. Numerous studies have been conducted to investigate the NER mechanism. The major proteins involved in NER have been identified, along with their roles, interactions, and key stages of the repair performed by them [1, 3]. Nonetheless, many details of the NER mechanism, including the specific roles of certain proteins, remain unclear and are still being explored at the level of protein–nucleic-acid complexes [4–7]. A key area of interest, both in basic and applied research, is the comparative assessment of NER activity *in vitro*. In such studies, GG-NER activity is typically evaluated using model substrates: linear DNA duplexes at least 120 base pairs (bp) long, with a bulky lesion introduced into one strand at an internal position [8–11]. Similar DNA duplexes of various lengths are also utilized to study the interactions of damaged DNA with the recombinant proteins involved in both NER branches [7, 12], as well as to examine NER activity in the context of nucleosomes [4].

Model DNAs are frequently constructed using synthetic analogs of lesions, introduced into DNA via automated synthesis. This process imposes specific requirements on the properties of the modified nucleotide incorporated into a DNA strand [13]. Finding synthetic analogs of bulky DNA lesions that can be i) effectively removed by the NER system and ii) stably and efficiently incorporated into model DNAs remains an important pursuit in this field. These model DNAs can be used to assess NER activity, including practical applications such as determining the resistance of cells to chemotherapy-induced or spontaneous DNA damage. These DNAs also serve as valuable tools for studying in detail the mechanisms of NER.

In this work, we conducted a comparative analysis of model DNA duplexes containing one of two synthetic bulky lesions that differ in the way the N-[6-{5(6)-fluoresceinylcarbamoyl}] group is attached to a propanediol moiety. By means of DNA containing N-[6-{5(6)-fluoresceinylcarbamoyl}hexanoyl]-3-amino-1,2-propanediol (nFluL), which is effectively removed by NER proteins, we earlier performed comparative analyses of NER activity in cell extracts from various mammals [14–17]. N-[6-{5(6)-fluoresceinylcarbamoyl}]-3-amino-1,2-propanediol (nFluS) as a model lesion has not been researched previously (*Fig. 1*).

The structure of the nFluS lesion, which lacks a hexanoyl linker, was selected based on our studies on the efficiency of initial recognition of lesion-containing DNA regions by XPC protein complexes. This recognition involves detecting a bulky lesion in the destabilized double-stranded DNA (dsDNA) region by ATP-dependent 5'→3' helicase XPD, a subunit of the TFIIH complex. By analyzing several model DNAs containing lesions that are excised at various efficiency rates by the NER system, we previously demonstrated that XPD exhibits the strongest affinity for an nFlu-containing model DNA [18]. Molecular dynamics simulations indicate that the presence of an extended flexible linker allows the fluorescein moiety to shift its position and interact with multiple regions of dsDNA surrounding the lesion, including the 3' side, thereby leading to the destabilization of the DNA structure in this region [17, 18]. XPC binding to this destabilized DNA region results in the formation of repair-unproductive XPC–DNA complexes, because the TFIIH verification complex, which binds to the 3' side of the lesion and moves in the 5'→3' direction, fails to encounter the lesion and dissociates from the DNA [19, 20]. Although NMR methods afford us the most detailed elucidation of the structure and interactions of bulky DNA lesions, these techniques require milligram quantities of DNA samples containing a lesion.

Here, in addition to the comparative evaluation of the efficiency of excision of nFluS and nFluL by proteins from a NER-competent HeLa cell extract, we also assessed the influence of nFluS or nFluL at an internal position of one strand of a 16 bp DNA duplex on dsDNA geometry and thermal stability. This was done by thermal denaturation assays with optical

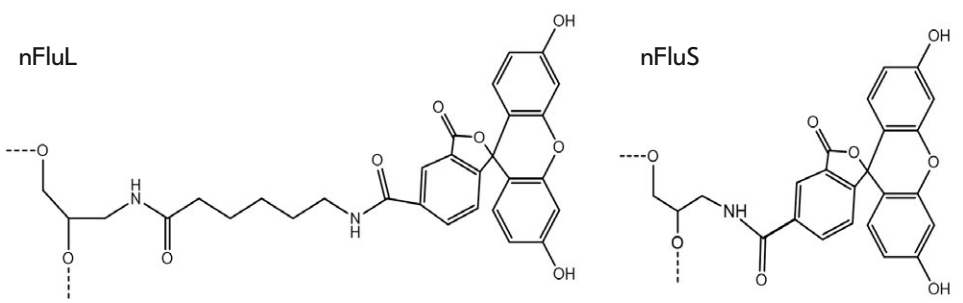

Fig. 1. Synthetic analogs of the lesions used in this work. nFluL – N-[6-{5(6)-fluoresceinylcarbamoyl}-hexanoyl]-3-amino-1,2-propanediol; nFluS – N-[6-{5(6)-fluoresceinylcarbamoyl}]-3-amino-1,2-propanediol

Table 1. Oligodeoxyribonucleotides (ODNs) used in this work

No.	Sequence	Length, nt.	Description
1	P-5′-atccagggcgacggtg	16	Unmodified strand (middle link)
2	P-5′-atccagggmSgacggtg	16	ODN with a non-nucleotide unit carrying a fluorescein residue (nFluS) for incorporation into the upper strand (middle unit, ODN-2)
3	P-5′-atccagggmLgacggtg	16	ODN with a non-nucleotide unit carrying a fluorescein residue and with a linker based on aminohexanoic acid (nFluL), for incorporation into the upper strand (middle unit of the upper strand, ODN-3)
4	P-5′-caccgtcgccctggat	16	A lower strand without a modification
5	5′-tggacgatatcccgcaagaggcccggcagtaccggcataac-caagcctatgcctacagc	59	A 5′ component of the top strand (the left arm of the top strand)
6	P-5′-ccgaggatgacgatgagcgcattgttagatttcatacacg-gtgcctgactgcgttagcaatt	62	A 3′ component for the top strand (the right arm of the top strand)
7	5′-catcctcggcaccgtcgccctggatgctgtaggcatag	38	A complementary strand for ligation of three fragments of the upper strand of the base sequence
8	5′- tgcgctcatcgtcatcctcggcaccgtcgccctggatgctgtagg-cataggctt	54	A lower unmodified strand (middle link for the lower strand, ODN-7)
9	5′-gggggcgtaccttgtgagcaatcgtgttcatcat-P	34	A template for elongation (completion) of excision products [α-^{32}P]dCMP
10	5′-P-ggttatgccggtactgccgggcctcttgcgggatatcgtcca	42	A 3′ component for the lower strand (the right arm of the lower strand)
11	5′-cgatgagcgcattgttagatttc	23	The complementary strand for ligation of ODN-7 and the left arm of the lower strand
12	5′-agtaccggcataaccaagcctatgcc	26	The complementary strand for ligation of ODN-7 and the right arm of the lower strand

signal detection. Spectrometric titration experiments were also conducted, yielding data on the interaction of the polycyclic moieties of the bulky lesions with neighboring nitrogenous bases in DNA [21].

EXPERIMENTAL

Materials

An NER-competent extract from HeLa cells was prepared by a standard protocol [22]. T4 polynucleotide kinase, T4 DNA ligase, and Taq DNA polymerase were acquired from Biosan (Russia), whereas proteinase K, EDTA, Tris, HEPES, and dithiothreitol (DTT) came from Sigma (USA). ODNs were synthesized in the Laboratory of Biomedical Chemistry, Institute of Chemical Biology and Fundamental Medicine, SB RAS. The amidophosphites used in the synthesis were provided by NanoTech-S (Russia). [γ-^{32}P]ATP (3000 Ci/mmol) and [α-^{32}P]dCTP (3000 Ci/mmol) were obtained from the Institute of Chemical Biology and Fundamental Medicine, SB RAS. The following materials were also employed: DEAE filters DE-81 (Whatman, UK), urea, N,N′-methylenebisacrylamide (Amresco, USA), acrylamide (Applichem, Germany), and TEMED (Helicon, Russia). Other chemicals used included PSA, $MgCl_2$, NaCl, H_3BO_3, NaOH, sodium cacodylate, $LiClO_4$, $(NH_4)_2SO_4$, HCl, and acetone.

The nucleotide sequences of all the ODNs utilized in this work are listed in *Table 1*.

Synthesis of extended model DNAs

Long model DNAs (137 bp) were constructed from ODNs 1–3 and 5–12 with the help of T4 DNA ligase, as previously described. The sequences of the ODNs and the extended model DNAs were identical to those used in our earlier studies [14].

Evaluation of the substrate properties of model DNA duplexes containing fluorescein adducts

For a comparative analysis of specific excision efficiency, the 3'-end–labeling method for excision products was employed [14]. The reaction mixture (30 μl), which contained 16 nM DNA substrate, 1.6 mg/ml NER-competent cell extract, and 0.5 μM template ODN-9 for hybridization of excision products in a buffer (25 mM Tris-HCl pH 7.8, 45 mM NaCl, 4.4 mM $MgCl_2$, 0.1 mM EDTA, and 4 mM ATP), was incubated at 30°C for 10–40 min. The reaction was inactivated by heating the mixture to 95°C, followed by cooling to room temperature. After the addition of 3 μl of a mix-

ture containing 100 μM dATP, dGTP, and dTTP, 5 units of Taq DNA polymerase, and 500–750 Bq [α-^{32}P]dCTP, the reaction was incubated at 37°C for 5 min. Next, 0.5 μl of 50 μM dCTP was added and the reaction was incubated for an additional 15 min. The reaction was terminated by the addition of solutions of proteinase K (4 μg/ml) and 10% SDS (1 μl each), followed by incubation for 30 min at 37°C. The reaction products were precipitated with 96% ethanol, centrifuged at 12,000´ *g* (4°C), and washed with 70% ethanol, and the resulting pellet was dissolved in water. The reaction products were separated by denaturing polyacrylamide gel electrophoresis (PAGE). Gels containing radioactively labeled DNA samples were analyzed using an Imaging Screen-K radioluminescent screen (Kodak, USA), followed by scanning on a GE Typhoon FLA 9500 instrument. Quantitative analysis of the results was performed in the Quantity One software.

Determination the bending angle of DNA duplexes

This angle was calculated from the electrophoretic mobility data obtained under nondenaturing conditions (10% polyacrylamide gel, 1× TBE, 4°C) via the formula:

$$\alpha = \pi - \arccos\sqrt{\frac{\mu_{mod}}{\mu_{unmod}}},$$

where μ_{mod} and μ_{unmod} are the electrophoretic mobility rates of duplexes during separation in a nondenaturing gel.

Evaluation of the DNA duplexes' thermal stability by thermal denaturation with optical signal recording

The thermal stability of the DNA duplexes was evaluated on a Cary 300-Bio spectrophotometer (Varian, Australia) equipped with a six-section Peltier element for temperature variation and quartz cuvettes with a 0.2 cm optical path length. The temperature range was set between 5°C and 95°C. Sample temperatures in each cuvette were calibrated using Temperature Probes Series II thermocouples (Varian, Australia). Measurements were taken at wavelengths of 260, 270, and 300 nm (baseline; slit width: 1 nm, signal averaging time: 1 s, temperature change rate: 0.5°C/min). All thermal denaturation samples were dissolved in Mili-Q deionized water and 10 mM cacodylate buffer [$(CH_3)_2AsO_2Na$] pH 7.2 containing 0.1 M NaCl. Thermodynamic parameters were calculated via analysis of changes in the optical density during heating and cooling at wavelengths of 260 and 270 nm, with theoretical curve fitting based on a two-state model in the Simplex software. Data characterizing the DNA thermal stability were stored in Microsoft Excel.

Spectrometric titration

This procedure was performed using 16-mer ODNs (*Table 1*). Two series of samples containing ODN-2 (nFluS-ODN) or ODN-3 (nFluL-ODN) at a constant concentration (5.4 μM) and a complementary strand (ODN-4) at various concentrations, from 1.25 to 5.4 μM, were prepared in 20 mM Tris-HCl buffer pH 8.0, containing 50 mM NaCl. The control samples contained only an ODN carrying a modification. Samples were incubated for 5 min at 95°C in 1× TE buffer, followed by cooling at 1°C/min to room temperature to enable duplex formation. Spectra were recorded on a CLARIOstar plate reader spectrofluorimeter (BMG Labtech, Germany) in Corning 3635 UV-transparent plates. The standard deviation of the data was calculated via the formula:

$$s = \sqrt{\frac{1}{n-1}\sum_{i=1}^{n}\left(xi - \bar{x}\right)^2},$$

where n is the sample size, xi is the ith element, and $\bar{x}$ is the sample mean. The error bars in all figures represent standard deviations based on at least three independent experiments.

RESULTS AND DISCUSSION

Comparative evaluation of the efficiency of nFluL and nFluS removal from model DNAs in the specific excision reaction

The effect of the structural differences between nFluL and nFluS on the efficiency of their removal from DNA substrates was assessed by the end-labeling method for excision products [14] (*Fig. 2A*). Extended DNA duplexes (137 bp) containing a non-nucleotide unit, either nFluL or nFluS, at an internal position (68th) of one strand were used as substrates for NER. Model DNA substrates were incubated at 30°C for 0–40 min with the HeLa cell extract (containing NER proteins). After the reaction was stopped, specific excision products (24–32-nucleotide-long DNA fragments containing the lesion) were hybridized with the template (*Table 1*, ODN-9), which is complementary to the damaged DNA region (*Fig. 2A*). The specific excision products hybridized to the template were extended with Taq DNA polymerase. The specific excision products that hybridized to the template were extended with Taq DNA polymerase and a mixture of dNTPs with [α-^{32}P]dCTP, resulting in the labeling of the excision products. The extended excision products were predominantly

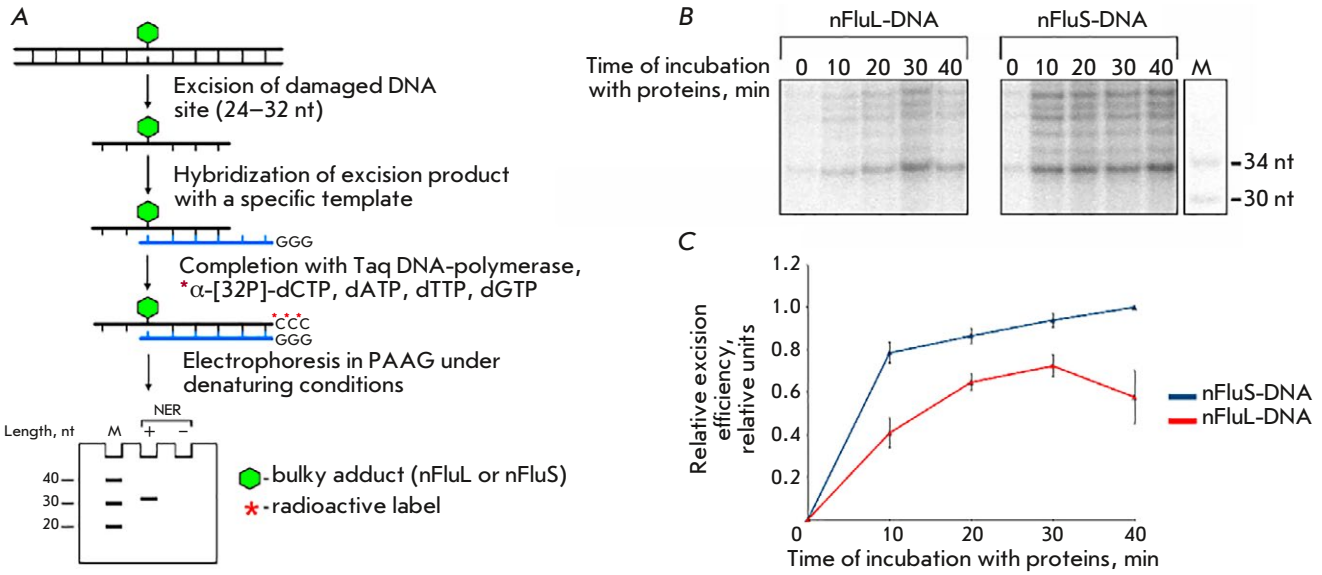

Fig 2. Comparative evaluation of the efficiency of removal of nFluL or nFluS from model DNA in a specific excision reaction catalyzed by the proteins of the HeLa cell extract. (*A*) is a schematic representation of the procedure for evaluating the excision activity of NER *in vitro* by the method of end labeling of specific excision products, adapted from [14, 23]; (*B*) is a radioautograph of the gel after the separation of excision reaction products; (*C*) is a graph of the dependence of the relative efficiency in the excision of the damaged DNA site on the incubation time with NER proteins. The values for the curves were calculated taking into account the signal intensity of products with a length of 34 nt

34 nucleotides long. Separation of the excision products was performed by denaturing PAGE (*Fig. 2B*). Based on the intensity of the 34-nucleotide bands, graphs of relative excision efficiency were plotted as a function of the incubation time of nFluS-DNA or nFluL-DNA with NER proteins (*Fig. 2C*).

As the results indicate, nFluS was removed from the model DNA 1.5–2 times more efficiently than nFluL during the entire experiment. Additional experiments allowed us to compare the changes — in dsDNA geometry and stability — induced by these bulky lesions; these changes influence the efficiency of DNA damage removal by the NER system.

Geometrical Features of Model DNAs Containing the Bulky Modification nFluL or nFluS

One of the irregularities — in the regular dsDNA structure — recognized at the initial stage of damage recognition is a bending of the sugar-phosphate backbone at the lesion site. The bend magnitude depends on the type of lesion and the surrounding sequence [24]. Decreased compactness of the curved structure hinders DNA migration through polyacrylamide gel pores. The greater the backbone bend caused by a bulky modification, the lower the mobility of the duplex during nondenaturing PAGE. Accordingly, the geometrical features of 16-mer DNA duplexes carrying the nFluL or nFluS modification in one strand were determined based on their electrophoretic mobility in nondenaturing gels. A typical autoradiograph of the gel illustrating these experiments is shown in *Fig. 3*.

Judging from the calculated bending angles (see "Determination of the bending angle of DNA duplexes"), the nFluL-containing DNA duplex had suffered a stronger bend, with a bending angle of 165.40 ± 0.95°, consistent with earlier data [17, 25]. In contrast, the bending angle in nFluS-dsDNA was 170.64 ± 0.83°. These differences in backbone bending between the two substrates may be a result of dissimilar interactions of the fluorescein group with neighboring nucleotide bases. Molecular dynamics simulations suggest that the nFluL moiety is predominantly located outside the duplex, whereas substantial mobility in the damaged region results in frequent appearance/disappearance of a bend (~135°) [17]. Conversely, nFluS appears less prone to eversion, likely owing to the fluorescein group's location within the duplex. Despite the smaller bending angle in nFluS-DNA, it was excised more efficiently by HeLa cell extract proteins. As shown previously [11], however, the efficiency of bulky-adduct repair does not always correlate with the degree of DNA helix bend.

The comparison of the thermal stability of duplexes

The thermal stability and thermodynamic characteristics of the 16 bp DNA duplexes were determined by thermal denaturation with optical signal recording. Analysis of the denaturation curves revealed

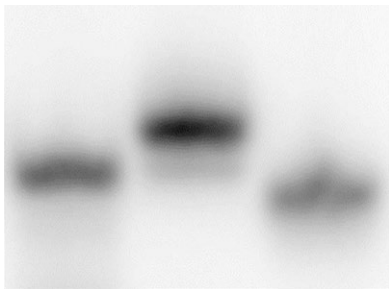

Fig. 3. A comparison of electrophoretic mobility among 16-mer DNA duplexes. An autoradiograph of a polyacrylamide gel after electrophoresis under nondenaturing conditions. Lane *1* – nFluS-dsDNA, lane *2* – nFluL-dsDNA, and lane *3* – NM-dsDNA

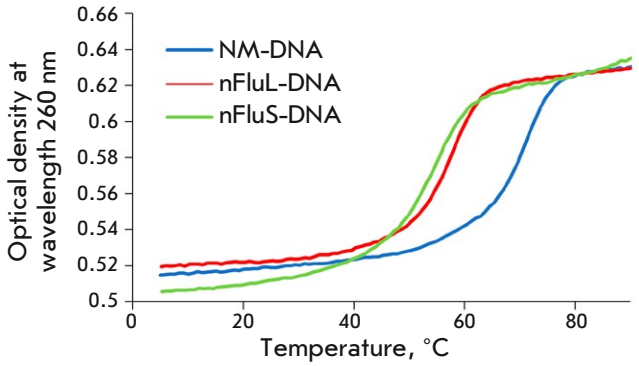

Fig. 4. The dependence of the optical density of DNA duplexes at 260 nm on temperature

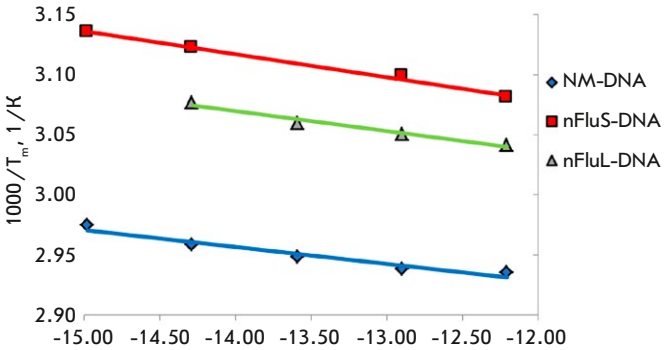

Fig. 5. A linear van 't Hoff plot for the unmodified DNA duplex and duplexes containing an nFlu lesion (nFluL or nFluS)

that the hypochromic effect in the unmodified duplex was more pronounced as compared to duplexes containing a non-nucleotide linker. In particular, the hypochromic effect was 14.75% for NM-DNA, 13.5% for nFluL-DNA, and 14.3% for nFluS-DNA. Normalized graphs of optical density vs. temperature illustrate the differences in thermal stability among the duplexes (*Fig. 4*).

The unmodified DNA duplex was found to be the most thermally stable (T_m = 67.6 ± 0.3°C), while the nFluL duplex manifested T_m of 55.6 ± 0.3°C; and nFluS, the lowest thermal stability (T_m = 51.5 ± 0.3°C). Thus, nFluL and nFluS destabilize the duplex structure more than does another bulky lesion, nAnt (T_m for nAnt DNA = 59.6 ± 0.2°C) [16], with nFluS inducing the greatest destabilization. Other molecular modeling studies suggest that fluorescein groups (Flu-dU and nFluL) linked to the sugar-phosphate backbone by extended linkers disturb and destabilize the regular dsDNA structure through interactions with neighboring nucleotide bases. Molecular dynamics simulations have revealed that the fluorescein group of nFluL can frequently get everted from a duplex [17, 25].

Our data suggest that the much-reduced thermal stability of nFluS-containing duplexes, compared to nFluL, may be due to the preferential positioning of the nFluS fluorescein group within the duplex, where it distorts the DNA structure and interacts with nearby nucleotide bases [26].

Through minimization of the sum of squares of the deviations between the experimental and theoretical thermal denaturation curves, the thermodynamic parameters of melting were calculated next. ΔS° and ΔH° were determined by linearization of the expression in coordinates $1000/T_m$ and $\ln(C_t/4)$ (van 't Hoff coordinates) and construction of a linear dependence of the reciprocal of the melting temperature on the logarithm of the concentration $\ln(C_t/4)$ by the least-squares method. The graphs are presented in *Fig. 5*. The results of the calculations of the thermodynamic parameters in *Table 2* also indicate an enhanced ability of nFluS to destabilize the double-stranded structure of surrounding DNA as compared to nFluL.

Table 2. Thermodynamic data and the melting temperatures of the DNA duplexes

DNA duplex	ΔS°, cal/(mol×K)	ΔH°, kcal/mol	$\Delta G°_{37}$, kcal/mol	T_m (20 μM), °C
NM-DNA	-382 ± 167	-140.0 ± 56.7	-20.2 ± 4.8	67.6 ± 0.3**
nFluL-DNA	-339 ± 187	-119.4 ± 61.2	-14.3 ± 3.2	55.6 ± 0.3**
nFluS-DNA	-295 ± 104	-103.5 ± 33.5	-12.0 ± 1.2	51.5 ± 0.3**

**Standard deviation for temperature takes into account the error of the measuring instrument.

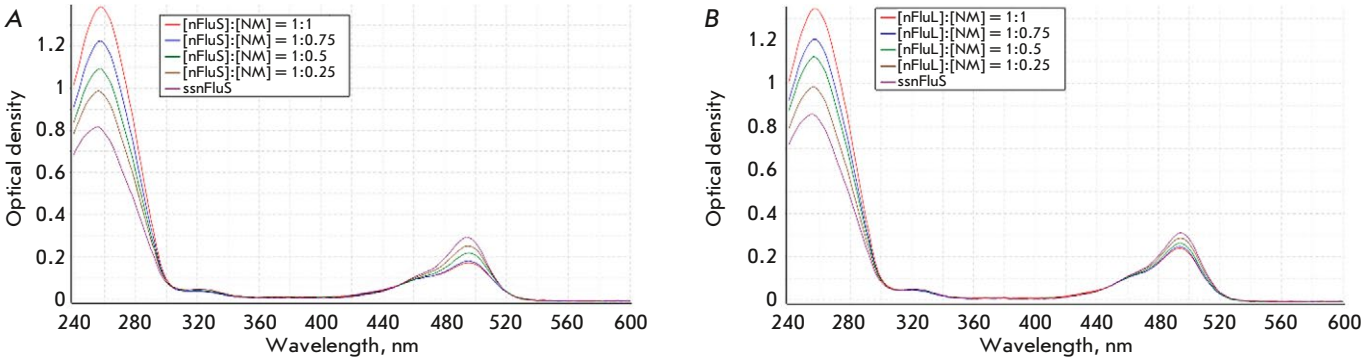

Fig. 6. Optical absorption spectra of samples containing nFluS-DNA (*A*) or nFluL-DNA (*B*) at a constant concentration of 5.4 μM. Concentration ratios are shown for samples containing modified (nFluS- or nFluL) and unmodified (nm) strands that form duplexes

Spectrometric titration

The spectrometric titration method, in combination with other approaches, allows one to draw conclusions about the presence of a number of interactions involving (or not involving) a fluorescent group on the basis of data on the changes in the spectral characteristics caused by duplex formation. The most noticeable differences between the two lesions containing a bulky carboxyfluorescein moiety were revealed in a comparative analysis of DNA duplexes containing the bulky modification nFluL or nFluS by spectrometric titration. The samples contained a modified nFluS or nFluL strand at a fixed concentration of 5.4 μM; the concentration of complementary DNA varied. The control samples in each series contained only the modified strand. The measurements were carried out after hybridization of the strands. The optical absorption spectra are given in *Fig. 6*.

At 260 nm, a gradual increase in the optical density of both series of samples was observed, the result of an increase in the total concentration of DNA in the mixture. By contrast, at 495 nm (the maximum absorption of fluorescein), the nature of the change in the optical density of the samples containing nFluS-DNA or nFluL-DNA changed as the concentration of the complementary strand in the samples went up, and, consequently, the amount of double-stranded structures rose too.

A comparison of optical absorption between nFluS-DNA and nFluL-DNA via titration of unmodified DNA was performed next. It showed that in the region of maximum nucleotide absorption (260 nm) in both DNA series, along with an increase in the optical density, an identical hypochromic effect was present, all due to the formation of duplexes (*Fig. 6*). The nature of the changes in the optical density near the maximum fluorescein absorption (495 nm) differed: in the case of DNA duplexes containing nFluS, the hypochromic effect, which appeared at the maximum concentration of the intact strand, amounted to 40%, whereas in DNA duplexes containing nFluL, it did not exceed 20% (*Fig. 6*).

Elsewhere, using the absorption spectra of DNA duplexes containing *cis*- and *trans*-B[α]P-N2-dG lesions as an example, it has been demonstrated that the formation of duplexes in which the benzo[α]pyrene (B[α]P) adduct forms strong intercalation complexes is accompanied by a hypochromic effect manifesting itself in the absorption region of the pyrenyl rings of B[α]P [27]. Thus, the results of our spectrophotometric titration showed that the presence of a lesion containing a longer spacer moiety leads to a level of local DNA destabilization sufficient for the efficient recognition and removal of nFluL by NER proteins; however, its fluoresceinylcarbamoyl group does not form stable sandwich structures or any other complexes the formation of which causes noticeable changes in the spectrum. These findings are in agreement with recently-performed molecular dynamics simulations of nFuL-containing DNA trajectories [17].

The most illustrative results, allowing us to determine the reasons for the differences in properties between the two fluorescein-based lesions, were obtained in a comparison of fluorescence spectra between the two series of samples containing nFluS-DNA or nFluL-DNA and the unmodified DNA strand at the same ratios as in the analyses of changes in the optical spectra. The resultant excitation and emission spectra of DNA duplexes containing the nFluS or nFluL lesion are shown in *Figs. 7* and *8*, respectively. The fluorescence excitation spectra were recorded at a fixed emission wavelength of 548 nm; the excitation wavelength was varied in the range of 420–520 nm with a step of 1 nm (*Fig. 7A,B*, respectively). Emission spectra — representing the dependence of the light emission intensity of the fluorophore (Flu) on the wave-

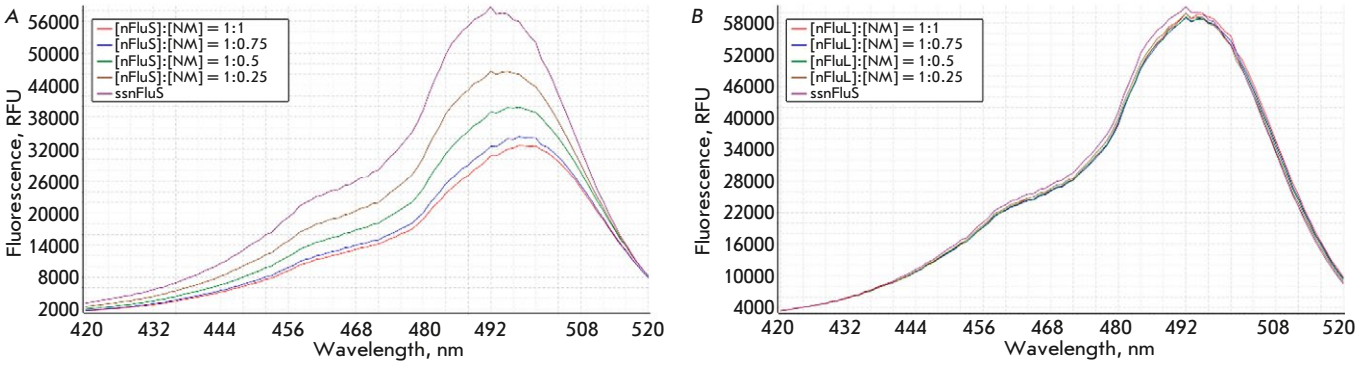

Fig. 7. Fluorescence excitation spectra in the range of 420–520 nm in a series of samples containing nFluS-DNA (*A*) or nFluL-DNA (*B*) at a concentration of 5.4 μM and a complementary strand without modifications (nm)

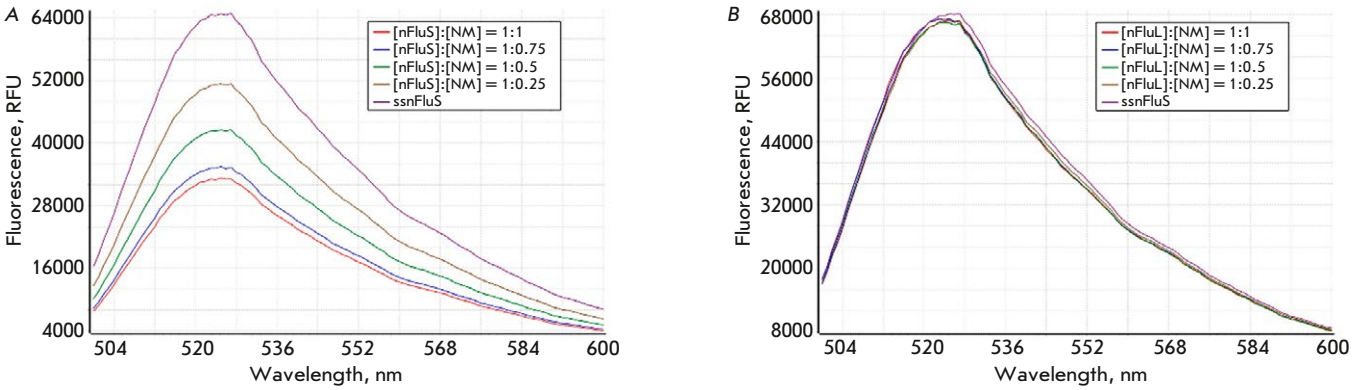

Fig. 8. Fluorescence emission spectra of the series of samples containing nFluS (*A*) or nFluL (*B*) at 5.4 μM and the complementary strand without modifications (nm)

length of the excitation light — were recorded in the range of 500–600 nm with a measurement step of 1 nm at a fixed excitation wavelength of 533 nm (*Fig. 8A,B*). The fluorescence intensities of the samples containing nFluS-DNA noticeably and steadily decreased with an increase in the concentration of the complementary strand, whereas in the case of samples containing nFluL-DNA, which has an extended linker, the fluorescence intensity remained virtually unchanged (*Figs. 7A* and *8A*).

Thus, the results of a spectrometric titration enable us to state with a high degree of confidence that, during duplex formation, the fluoresceinylcarbamoyl moiety of the nFluS lesion is located inside the duplex and remains capable of interacting with the guanosines of the DNA nucleotides closest to the lesion, similarly to the descriptions of some types of fluorescein positioning in DNA duplexes [26].

CONCLUSION

We hypothesized that nFluS (N-[6-{5(6)-fluoresceinylcarbamoyl}]-3-amino-1,2-propanediol) represents an analog of a bulky lesion whose efficiency of specific excision from model DNA is higher than that of nFluL (N-[6-{5(6)-fluoresceinyl carbamoyl}hexanoyl]-3-amino-1,2-propanediol). The hypothesis was proven successfully. Comparative analyses of the geometrical features, thermodynamic characteristics, optical absorption spectra, and fluorescence spectra of model DNA duplexes containing nFluS or nFluL showed that the higher efficiency in the specific excision of nFluS compared to nFluL is explained by the additional destabilization of the dsDNA structure under the influence of the interaction of the fluoresceinylcarbamoyl moiety with neighboring nitrogenous bases of dsDNA. A given localization of the destabilized region in nFluS-containing dsDNAs probably promotes the formation of productive XPC–DNA complexes, thereby improving the substrate properties of nFluS-DNA in a specific excision reaction. Molecular modeling experiments are required to prove this interpretation right. ●

The work was carried out with financial support from the Russian Science Foundation (project No. 19-74-10056P).

REFERENCES
1. Schärer O.D. // Cold Spring Harb. Perspect. Biol. 2013. V. 5. № 10. P. a012609.
2. Sugasawa K. // Enzymes. 2019. V. 45. P. 99–138.
3. Krasikova Y., Rechkunova N., Lavrik O. // Int. J. Mol. Sci. 2021. V. 22. № 12. P. 6220.
4. Shafirovich V., Kolbanovskiy M., Kropachev K., Liu Z., Cai Y., Terzidis M.A., Masi A., Chatgilialoglu C., Amin S., Dadali A., et al. // Biochemistry. 2019. V. 58. № 6. P. 561–574.
5. Fu I., Mu H., Geacintov N.E., Broyde S. // Nucl. Acids Res. 2022. V. 50. № 12. P. 6837–6853.
6. Fu I., Geacintov N.E., Broyde S. // Nucl. Acids Res. 2023. V. 51. № 22. P. 12261–12274.
7. Kim J., Li C.L., Chen X., Cui Y., Golebiowski F.M., Wang H., Hanaoka F., Sugasawa K., Yang W. // Nature. 2023. V. 617. № 7959. P. 170–175.
8. Huang J.C., Sancar A. // J. Biol. Chem. 1994. V. 269. P. 19034–19040.
9. Reardon J.T., Sancar A. // Proc. Natl. Acad. Sci. USA. 2006. V. 103. № 11. P. 4056–4061.
10. Kropachev K., Kolbanovskii M., Cai Y., Rodríguez F., Kolbanovskii A., Liu Y., Zhang L., Amin S., Patel D., Broyde S., et al. // J. Mol. Biol. 2009. V. 386. № 5. P. 1193–1203.
11. Lukyanchikova N.V., Petruseva I.O., Evdokimov A.N., Silnikov V.N., Lavrik O.I. // Biochemistry (Mosc.). 2016. V. 81. № 3. P. 386–400.
12. Li C.L., Golebiowski F.M., Onishi Y., Samara N.L., Sugasawa K., Yang W. // Mol. Cell. 2015. V. 59. № 6. P. 1025–1034.
13. Gillet L.C., Alzeer J., Schärer O.D. // Nucl. Acids Res. 2005. V. 33. № 6. P. 1961–1969.
14. Evdokimov A., Petruseva I., Tsidulko A., Koroleva L., Serpokrylova I., Silnikov V., Lavrik O. // Nucl. Acids Res. 2013. V. 41. № 12. e123.
15. Evdokimov A., Kutuzov M., Petruseva I., Lukjanchikova N., Kashina E., Kolova E., Zemerova T., Romanenko S., Perelman P., Prokopov D., et al. // Aging (Albany NY). 2018. V. 10. № 6. P. 1454–1473.
16. Lukyanchikova N.V., Petruseva I.O., Evdokimov A.N., Silnikov V.N., Lavrik O.I. // Biochemistry (Mosc). 2016. V. 81. № 3. P. 263–274.
17. Naumenko N.V., Petruseva I.O., Lomzov A.A., Lavrik O.I. // DNA Repair (Amst.). 2021. V. 108. P. 1–11.
18. Petruseva I., Naumenko N., Kuper J., Anarbaev R., Kappenberger J., Kisker C., Lavrik O. // Front. Cell Dev. Biol. 2021. V. 9. P. 617160.
19. Sugasawa K., Akagi J., Nishi R., Iwai S., Hanaoka F. // Mol. Cell. 2009. V. 36. № 4. P. 642–653.
20. Cheon N.Y., Kim H.S., Yeo J.E., Schärer O.D., Lee J.Y. // Nucl. Acids Res. 2019. V. 47. № 16. P. 8337–8347.
21. Liu Z., Ding S., Kropachev K., Jia L., Amin S., Broyde S., Geacintov N.E. // PLoS One. 2015. V. 10. № 9. P. e0137124.
22. Reardon J.T., Sancar A. // Methods Enzymol. 2006. V. 408. P. 189–213.
23. Popov A.A., Petruseva I.O., Naumenko N.V., Lavrik O.I. // Biochemistry (Mosc). 2023. V. 88. № 11. P. 1844–1856.
24. Reeves D.A., Mu H., Kropachev K., Cai Y., Ding S., Kolbanovskiy A., Kolbanovskiy M., Chen Y., Krzeminski J., Amin S., et al. // Nucl. Acids Res. 2011. V. 39. № 20. P. 8752–8764.
25. Evdokimov A.N., Tsidulko A.Y., Popov A.V., Vorobiev Y.N., Lomzov A.A., Koroleva L.S., Silnikov V.N., Petruseva I.O., Lavrik O.I. // DNA Repair (Amst.). 2018. V. 61. P. 86–98.
26. Nazarenko I., Pires R., Lowe B., Obaidy M., Rashtchian A. // Nucl. Acids Res. 2002. V. 30. № 9. P. 2089–2195.
27. Huang W., Amin S., Geacintov N.E. // Chem. Res. Toxicol. 2002. V. 15. № 2. P. 118–126.

Investigating the Structure of the Components of the PolyADP-Ribosylation System in *Fusarium* Fungi and Evaluating the Expression Dynamics of Its Key Genes

A. A. Stakheev*, R. R. Kutukov, M. E. Taliansky, S. K. Zavriev
Shemyakin–Ovchinnikov Institute of Bioorganic Chemistry, Moscow, 117997 Russian Federation
*E-mail: stakheev.aa@gmail.com
Received: June 17, 2024; in final form, July 18, 2024
DOI: 10.32607/actanaturae.27450

ABSTRACT **Poly(ADP-ribose) polymerase (PARP) is the key enzyme in polyADP-ribosylation, one of the main post-translational modifications. This enzyme is abundant in eukaryotic organisms. However, information on the PARP structure and its functions in members of the Fungi kingdom is very limited. In this study, we performed a bioinformatic search for homologs of PARP and its antagonist, PARG, in the genomes of four *Fusarium* strains using their whole-genome sequences annotated and deposited in databases. The *F. graminearum* PH-1, *F. proliferatum* ET-1, and *F. oxysporum* Fo47 strains were shown to possess a single homolog of both PARP and PARG. In addition, the *F. oxysporum* f. sp. *lycopersici* strain 4287 contained four additional proteins comprising PARP catalytic domains whose structure was different from that of the remaining identified homologs. Partial nucleotide sequences encoding the catalytic domains of the PARP and PARG homologs were determined in 11 strains of 9 *Fusarium* species deposited in all-Russian collections, and the phylogenetic properties of the analyzed genes were evaluated. In the toxigenic *F. graminearum* strain, we demonstrated up-regulation of the gene encoding the PARP homolog upon culturing under conditions stimulating the production of the DON mycotoxin, as well as up-regulation of the gene encoding PARG at later stages of growth. These findings indirectly indicate involvement of the polyADP-ribosylation system in the regulation of the genes responsible for DON biosynthesis.**
KEYWORDS ***Fusarium*, parylation, PARP, PARG, transcription regulation, mycotoxin, expression.**
ABBREVIATIONS **PARP – poly(ADP-ribose) polymerase; PARG – poly(ADP-ribose) glycohydrolase; PCR – polymerase chain reaction; DON – deoxynivalenol; bp – base pair; aa – amino acid.**

INTRODUCTION

Plant diseases that are caused by phytopathogenic fungi are a significant problem for agriculture and the economy in all regions of the world [1, 2]. Members of some taxonomic groups of the Fungi kingdom, in particular the *Fusarium* genus, are able not only to infect agricultural crops, but also to produce toxic secondary metabolites – mycotoxins [3] – that inhibit protein synthesis, induce apoptotic processes, and exert hepatotoxic and immunosuppressive effects on mammals [4–7]. The ability to synthesize trichothecene mycotoxins is a factor of fungal aggressiveness to host plants: mutant *F. graminearum* strains which had not produced deoxynivalenol (DON) were shown to be able to infect a plant, but the infection did not spread to other parts of the plant [8].

The biosynthesis of the main mycotoxin groups occurs in a similar manner: the key genes responsible for its various stages are grouped in clusters under the control of one or more regulatory factors [9, 10]. In turn, global transcription factors are mediators that regulate the expression of specific genes, depending on various environmental factors, such as temperature, humidity, pH, and nutrient availability [11, 12].

The key regulatory processes include histone protein modifications; in particular, poly(ADP-ribosyl)ation or parylation.

Parylation involves the transfer of several ADP-ribose residues from the NAD+ cofactor molecule to the target amino acid or nucleic acid, which changes the structure, function, and stability of the target molecule [13, 14]. The key enzyme responsible for the parylation reaction is poly(ADP-ribose) polymerase (PARP), which belongs to the poly(ADP-ribosyl) transferase family [15]. According to current concepts, enzymes of this family are structurally and functionally similar to the exotoxins of pathogenic bacteria, such as the diphtheria and cholera toxins [16, 17]. PARP is a fairly conservative enzyme; it is found in all eukaryotes, except yeast. The best characterized to date is human PARP1, which is a 116 kDa protein consisting of three main domains: the N-terminal DNA-binding domain comprising zinc finger structures, the central regulatory (BRCT) domain, and the C-terminal catalytic domain, which is the most conservative and characteristic domain of the proteins of the poly(ADP-ribosyl) transferase family [18, 19]. In addition, PARP1 homologs can contain the WGR (Trp–Gly–Arg) domain, transmembrane structures, and various regulatory sequences [20]. The spectrum of PARP-regulated processes is quite wide: DNA repair, apoptosis, cell cycle regulation, gene transcription control, etc. [21–24]. It is currently known that some eukaryotes contain several PARP copies; e.g., human cells contain, apart from PARP1, the homolog proteins PARP2 and PARP3, which are functionally similar to PARP1. In general, the human genome contains 17 genes encoding PARP family proteins [15, 25]. It should also be noted that parylation is a reversible modification: poly(ADP-ribose) glycohydrolase (PARG), a PARP antagonist, is responsible for the hydrolysis of ribose–ribose bonds and the cleavage of polymer chains [26, 27]. In the canonical version (human), PARG consists of a C-terminal catalytic macrodomain and an N-terminal regulatory part, although its structure may differ in other organisms [28].

It should be noted that, despite their versatility and high conservatism, information about the functions of the parylation system enzymes in Fungi, in particular *Ascomycota*, is quite limited. There are a number of studies indicating the involvement of PARP in apoptosis [29, 30], replicative aging [31], and the formation of asexual reproduction structures [32]. In this case, almost nothing is known about a potential role for PARP in the pathogenesis and biosynthesis of mycotoxins.

The aim of this study was to identify possible PARP and PARG homologs in members of the *Fusarium* genus using a bioinformatic search in open access databases and sequencing of *PARP* and *PARG* gene fragments in the strains of 9 *Fusarium* species common in Russia and neighboring countries. In addition, we compared the expression profiles of the PARP and PARG homologs in the *F. graminearum* strain capable of mycotoxin biosynthesis when grown on different media.

EXPERIMENTAL

Bioinformatic analysis

To search for the PARP and PARG homologs, we selected four strains of *Fusarium* fungi whose whole genome structures have been annotated and deposited in online GenBank NCBI (https://www.ncbi.nlm.nih.gov/genbank/) and Fusarium oxysporum pangenome databases (http://www.fopgdb.site/): *F. graminearum* PH-1, *F. proliferatum* ET-1, *F. oxysporum* Fo47, and *F. oxysporum* f. sp. *lycopersici* 4287. Amino acid sequences of the human PARP1 and PARG proteins and the *Aspergillus nidulans* PARP homolog (PrpA) and the nucleotide sequences of the corresponding genes were used as references. The homologs were searched using the BLAST algorithm [33]. Functional domains in the identified protein sequences were modeled using the InterPro online service (https://www.ebi.ac.uk/interpro/).

Fungal strains

In this study, we used 11 strains of 9 species of the *Fusarium* genus from the collections of the Federal Research Center of Nutrition and Biotechnology (FRCNB), the All-Russian Research Institute of Plant Protection (VIZR), and the Pushchino Scientific Center for Biological Research (All-Russian Collection of Microorganisms, VKM). The list of strains, with their geographical origin, host plant species, collection years, and collection affiliation, is provided in *Table 1*. The cultures were grown on potato sucrose agar at 25°C for 7 days.

Isolation of nucleic acids

DNA was isolated according to the previously reported technique [34]. RNA was isolated from liquid cultures of the *F. graminearum* MFG 58918 fungus using a RNeasy Plant Mini Kit (Qiagen, Germany) according to the manufacturer's protocol. The concentration and quality of the nucleic acids were assessed using a NanoVue spectrophotometer (GE HealthCare, USA), a Qubit fluorometer (Thermo Scientific, USA), and electrophoresis in 1% agarose gel.

Table 1. Fungal strains used in the study

Strain	Species	Collection	Source of isolation	Geographical origin	Year
MFG 58918	*F. graminearum*	VIZR	Wheat grain	Krasnodar Region	2016
ION-17-9/8	*F. graminearum*	FRCNB	Wheat grain	Moscow Region	2017
MFG 96801	*F. oxysporum*	VIZR	Wheat grain	North Ossetia	2007
F-840	*F. oxysporum*	VKM	Unknown	Germany	Unknown
MFG 58242	*F. venenatum*	VIZR	Unknown	Germany	2008
ION-3/4	*F. coffeatum*	FRCNB	Wheat grain	Tula Region	2014
F-3495	*F. redolens*	VKM	Barley grain	Moscow Region	Unknown
F-206	*F. verticillioides*	VKM	Tobacco plant	Krasnodar Region	Unknown
F-446	*F. fujikuroi*	VKM	Rice grain	Japan	Unknown
MFG 61701	*F. poae*	VIZR	Wheat grain	Saratov Region	2010
F-3951	*F. solani*	VKM	Soil	Moscow Region	Unknown

Primer design, PCR, and sequencing of amplification products

The primers for PCR and sequencing were designed using the ClustalW algorithm [35]. The physicochemical properties of the primers were assessed using the Oligo 6.71 software.

The structures of the primers and probes used to assess the relative expression of the reference gene *TEF1α* and the trichodiene synthase gene *TRI5* had been published previously [36].

PCR was performed on a Tertsik thermal cycler (DNA-Technology, Russia) using the following amplification programs:

Program 1 (PARPF-R primers): 93°C, 90 s (1 cycle); 93°C, 1 s; 55°C, 5 s; 72°C, 5 s (40 cycles).

Program 2 (PARGF-R primers): 93°C, 90 s (1 cycle); 93°C, 10 s; 60°C, 15 s; 72°C, 10 s (40 cycles).

Quantitative PCR for assessing relative transcript abundances was performed on a DT-96 detecting thermal cycler (DNA-Technology) using Program 2. Transcript accumulation was assessed using the QGene software [37].

The PCR products were cloned using a Quick-TA kit (Eurogen, Russia) according to the manufacturer's protocol. DNA fragments were sequenced by the Sanger technique at Evrogen JSC using an ABI PRISM BigDye Terminator v. 3.1 reagent kit, followed by analysis of the reaction products on an ABI PRISM 3730 Applied Biosystems automatic sequencer.

The resulting nucleotide sequences were deposited in the NCBI GenBank database (accession numbers PQ040409–PQ040429).

Phylogenetic analysis

Multiple alignment and the phylogenetic analysis of the amino acid and nucleotide sequences, as well as assessment of their phylogenetic properties, were performed using the MEGA7 software package [38]. Phylogenetic trees were constructed using the maximum likelihood (ML) method and the Jones–Taylor–Thornton (for amino acids, [39]) and GTR+G (for nucleotides, [40]) models. The robustness of the phylogenetic tree topologies was confirmed by bootstrap analysis (1,000 replicates).

Evaluation of the accumulation of the DON mycotoxin produced by *F. graminearum* in the liquid culture

To evaluate the accumulation of mycotoxin deoxynivalenol (DON), the *F. graminearum* MFG 58918 strain

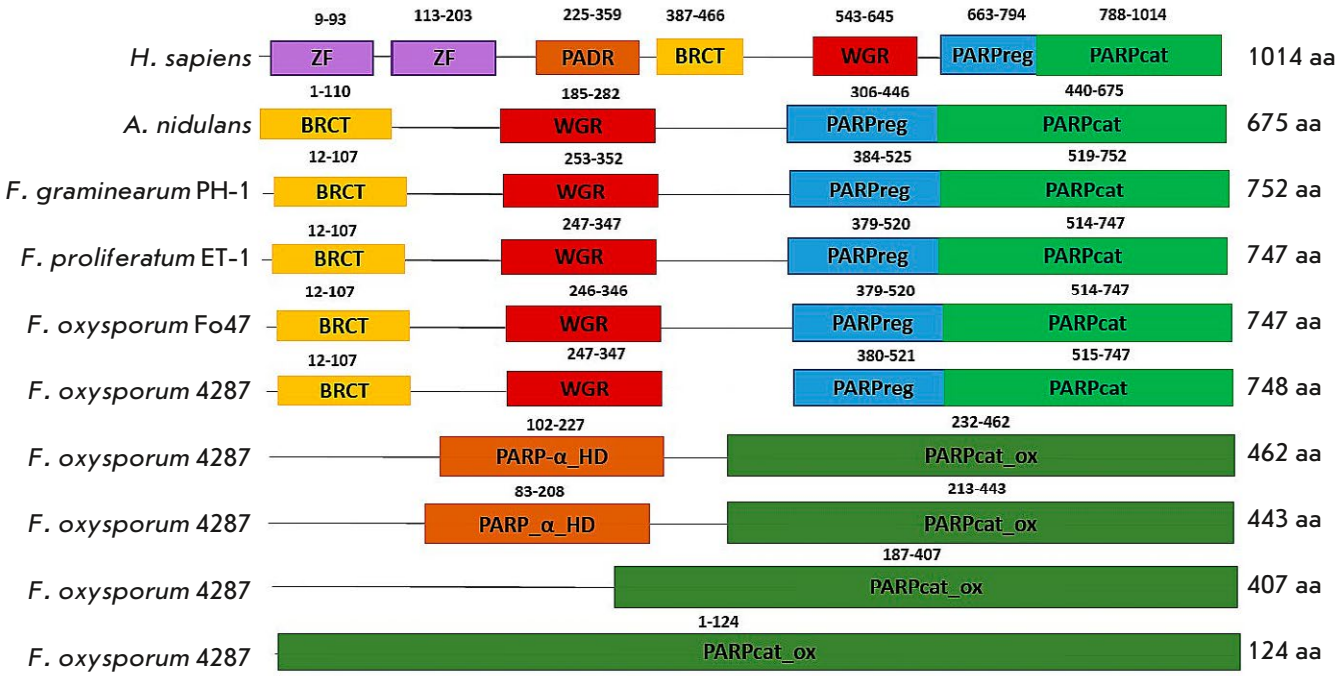

Fig. 1. Schematic representation of the main functional domains of human PARP1, the *A. nidulans* PrpA, and PARP homologs of four *Fusarium* strains. The range of amino acids in each domain is indicated above the corresponding domain. ZF is a 'zinc finger' structure

was cultured in two media of different compositions: a potato sucrose broth and the MYRO medium [41]. For this purpose, the liquid media (10 mL) were inoculated with 100 μL of a *F. graminearum* MFG 58918 conidium suspension and incubated at 25°C for 7 days. Material for the analysis of the relative expression of the target genes was collected every 24 h, from days 2 to 7. Samples for the analysis of mycotoxin levels were collected on days 4 and 6 of culture.

The mycotoxin content in the media was analyzed by an immunochemical express method using DONSENSOR test kits (Unisensor, Belgium) according to the manufacturer's protocol.

RESULTS

Search for PARP and PARG homologs

A search performed using the BLASTp algorithm revealed that the genomes of *F. graminearum* PH-1, *F. proliferatum* ET-1, and the *F. oxysporum* Fo47 and 4287 strains contained one open reading frame, and that their translation products were presumably human PARP1 and *A. nidulans* PrpA homologs. The identified proteins consisted of 747–752 amino acid residues and contained four putative domains: BRCT, WGR, regulatory, and catalytic. Unlike human PARP1, they lacked the N-terminal domain, which contains zinc finger structural motifs, and the pADR subdomain (*Fig. 1*). In general, the structure of the identified homologs corresponded to that of the previously characterized PrpA from *A. nidulans* [32]. Analysis of amino acid sequence similarities revealed that the most conserved part of all analyzed proteins was the catalytic domain: for example, the identity of the catalytic domain sequences of human PAPR1 and its homolog in *F. graminearum* PH-1 was 43.9% and the identity of the sequences of the four analyzed *Fusarium* strains was 85.1%. Meanwhile, comparison of the whole PARP sequences showed a degree of identity of 24.5% between the humans and *F. graminearum* and 76.6% among the *Fusarium* strains. Also, an amino acid motif – histi-

dine–tyrosine–glutamic acid (H–Y–E, *Fig. 2*) – was revealed in the homolog structures, which is, according to current concepts, key for the catalytic function of PARP.

In addition, a search for PARP homologs using only the amino acid sequences of the PARP1 and PrpA catalytic domains as a query revealed four more open reading frames in the genome of the *F. oxysporum* f. sp. *lycopersici* 4287 strain, whose translation products contained PARP catalytic domains (*Fig. 1*). Two of them were the 443 aa (FoxPARP443, GenBank accession number XP_018253699) and 462 aa (FoxPARP462, XP_018251710) proteins containing alpha-helical (PARP αHD) subdomains at the N-terminus of their catalytic domains. Another predicted 407 aa homolog (FoxPARP407, XP_018251711) contained only the catalytic domain, without the αHD subdomain. The fourth homolog was a short 124 aa protein (FoxPARP124, XP_018251751) the entire structure of which was characterized as a catalytic domain. It is interesting to note that the genes encoding the four "additional" PARPs are located on different chromosomes (chromosome 3: FoxPARP462, FoxPARP407, and FoxPARP124; chromosome 6: FoxPARP443; the gene encoding the "main" PARP is located on chromosome 4). The structures of these homologs differed significantly from each other and from the "main" PARP homologs of *F. oxysporum* and other species. The degrees of identity of the catalytic domain structures of FoxPARP443 and FoxPARP407, FoxPARP443 and FoxPARP124, FoxPARP443 and "main" PARP of *F. oxysporum* f. sp. *lycopersici*, and FoxPARP443 and human PARP1 were 67%, 52.8%, 57.2%, and 31.2%, respectively. These results were confirmed by data from a phylogenetic analysis of the amino acid sequences of the catalytic domains (*Fig. 3*). The dendrogram shows two clusters supported by bootstrap values of 92 and 100%: the first included the "main" domains of the four analyzed strains, and the second included the catalytic domains of the FoxPARP462, FoxPARP443, and FoxPARP407 proteins. The FoxPARP124 protein domain formed a separate branch in an intermediate position between the two clusters. In addition, neither the catalytic H–Y–E motif nor any other arginine–serine–glutamic acid (R–S–E) motif typical of the family of poly(ADP-ribosyl) transferases was revealed in the structure of the catalytic domains of the "additional" PARPs.

PARG homologs were searched using human PARG as a reference. One open reading frame was identified in each of the analyzed genomes. The translated proteins consisted of 443–476 aa and had a common structure, including an N-terminal α-helical and a C-terminal catalytic domain. In all the structures of

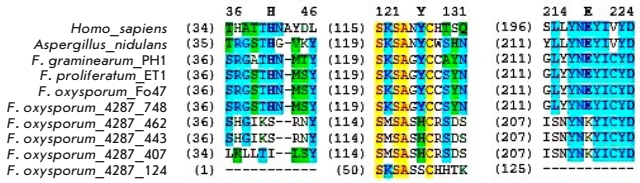

Fig. 2. Fragments of amino acid sequence alignment of human PARP1, the *A. nidulans* PrpA, and PARP homologs of four *Fusarium* strains, which contain amino acid residues constituting the H–Y–E motif. Key amino acids are shown in bold

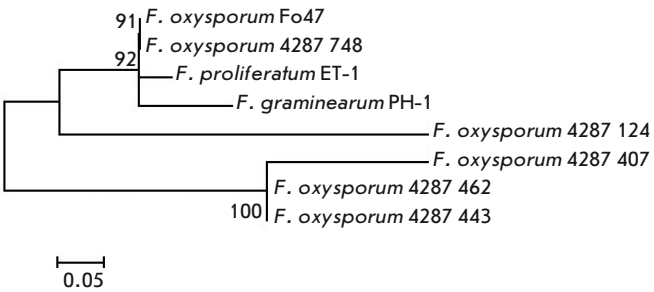

Fig. 3. The phylogenetic tree constructed based on alignment of the amino acid sequences of the catalytic domains of the PARP homologs identified in the genomes of four *Fusarium* strains using the maximum likelihood method. Bootstrap values of >50% (1,000 replicates) are shown

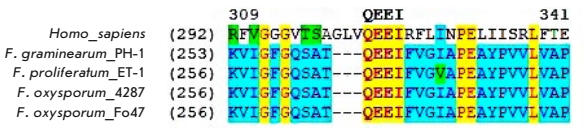

Fig. 4. A fragment of amino acid sequence alignment of the human PARG and PARG homologs of four *Fusarium* strains, which contains the Q–E–E–I motif (shown in bold)

the discovered homologs, a glutamine–glutamic acid–glutamic acid–isoleucine (Q–E–E–I) motif was identified, which is considered essential for the functional activity of the enzyme (*Fig. 4*). In this case, the analysis of amino acid sequence similarities revealed that PARG was a less conservative protein than PARP: the level of identity of PARG from the four analyzed *Fusarium* strains was 60.5%, and that of the *Fusarium* and human PARG homologs was only 17.6%.

Primer design, sequencing, and phylogenetic analysis of the fragments of the genes encoding the PARP and PARG homologs

On the basis of alignment of the nucleotide sequences of the genes encoding the PARP and PARG homologs identified in the bioinformatic analysis, we constructed universal primers for the sequencing of their fragments. The sequence encoding the PARP catalytic domain, the *PARG* gene fragment encoding the C-terminus of the α-helical domain, the N-terminus of the catalytic domain, and the region connecting them were selected as targets. The structures of the developed primers were as follows: PARP: forward primer PARPF (5'-ATCCTCTYGATCGHCARTT-3'), reverse primer PARPR (5'-GHAGSAGRTAVCGBAGCTTG-3'); PARG: forward primer PARGF (5'-GGYAAAATHCCATTYTGGCC-3'), reverse primer PARGR (5'-AGACVACGACDGCHCCTCCTT-3'). We found that the pair of PARPF–R primers amplified the DNA fragments of all the 11 strains selected for the study (*Table 1*) and that the pair of PARGF–R primers amplified all, except for the DNA of the *F. solani* F-3951 strain. The sizes of the amplified fragments were 611 bp for PARP and 596–611 bp for PARG. Analysis of the phylogenetic characteristics of the sequenced fragments confirmed the suggestion that PARG was less conservative than PARP: the fragment of the gene encoding the PARP homolog contained 58.7% conservative, 41.3% variable, and 25.8% parsimony informative positions, whereas the fragment of the gene encoding the PARG homolog contained 42.8% conservative, 57.1% variable, and 42.4% parsimony informative positions. The phylogenetic tree constructed based on the analysis of the fragments of the gene encoding the PARP homolog (*Fig. 5A*) contained two main clusters, one of which contained species capable of synthesizing trichothecene toxins (*F. graminearum*, *F. poae*, *F. venenatum*, *F. coffeatum*; bootstrap support, 69%), and the other that included species producing other groups of toxins (*F. fujikuroi*, *F. verticillioides*, *F. oxysporum*, *F. redolens*; bootstrap support, 96%). The *F. solani* F-3951 strain formed a separate branch; it should be noted that the entire group of *Fusarium* strains formed a single, large cluster with a bootstrap support value of 100%. A similar picture was observed in the analysis of the phylogenetic tree constructed based on a comparison of fragments of the gene encoding the PARG homolog (*Fig. 5B*), with the difference being that the bootstrap support value for clusters containing trichothecene-producing and non-producing species was higher (94 and 99%, respectively). In addition, there were topological differences related to the fact that *F. venenatum* and *F. coffeatum* formed a separate subcluster with a bootstrap support value of 100%.

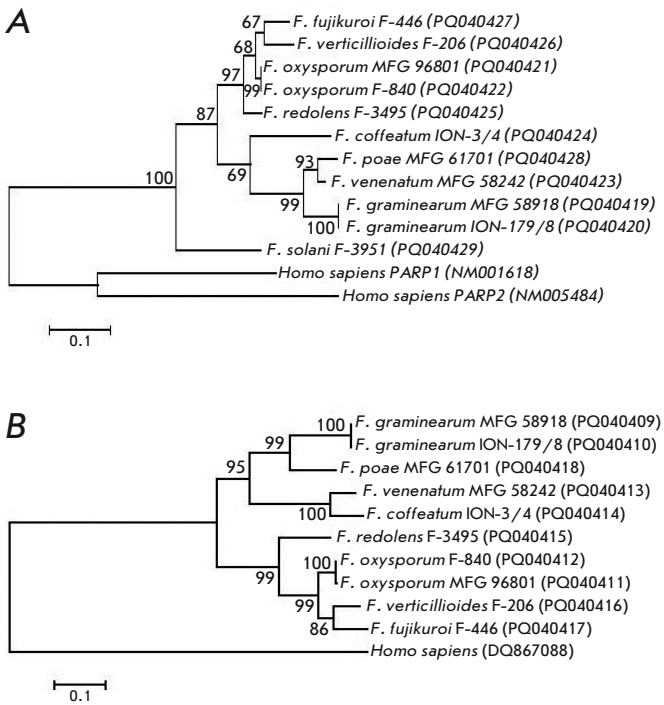

Fig. 5. Phylogenetic trees constructed based on nucleotide sequence alignments of PARP (*A*) and PARG (*B*) of eleven *Fusarium* strains from all-Russian collections using the maximum likelihood method. Bootstrap values of >50% (1,000 replicates) are shown. The GenBank accession number of each strain studied is shown in brackets

Analysis of DON mycotoxin accumulation and the expression dynamics of genes encoding the PARP and PARG homologs during fungal growth on different media

To compare toxin formation levels, the *F. graminearum* MFG 58918 strain was cultured on a potato sucrose broth (PSB), which is considered favorable for the growth of fungal biomass, and a MYRO medium, which stimulates mycotoxin biosynthesis (in particular DON). Analysis of DON accumulation in the MYRO medium showed that its concentration was 30.6 mg/L of the medium on day 4 and 39.9 mg/L of the medium on day 6. In this case, in cultures grown on PSB, DON was not detected at any of those time points. In addition to the genes encoding the PARP (*FgPARP*) and PARG (*FgPARG*) homologs, analysis of the relative expression dynamics also included the *TRI5* gene encoding trichodiene synthetase, a key enzyme in the biosynthesis of trichothecene toxins.

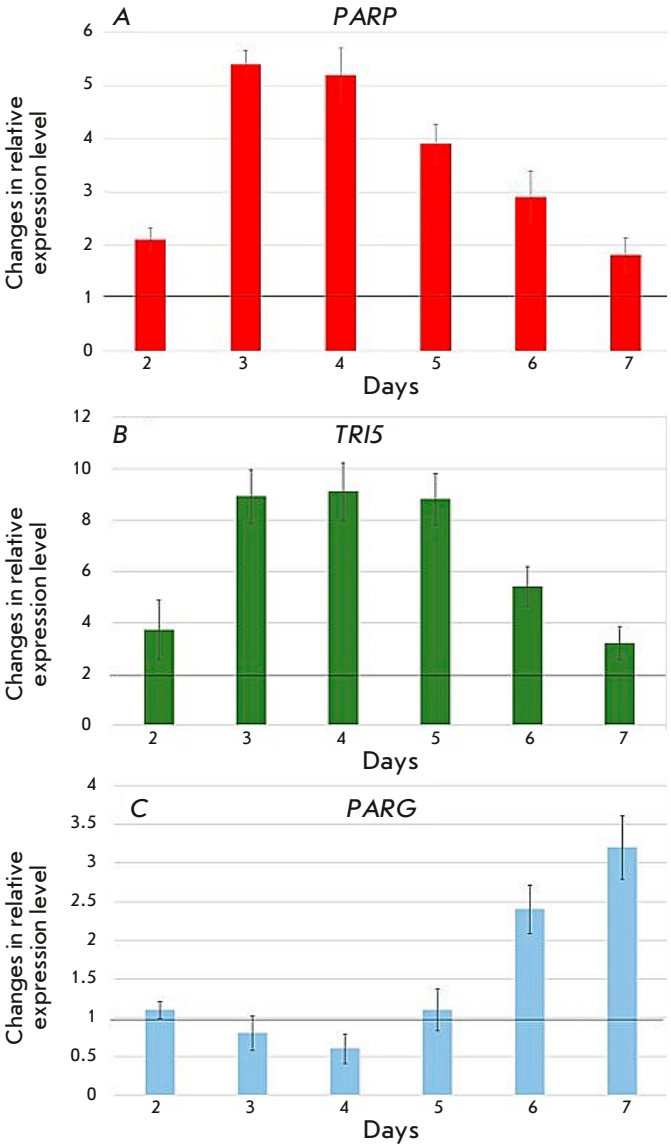

Fig. 6. Estimation of the relative expression levels of the *FgPARP* (*A*), *TRI5* (*B*), and *FgPARG* (*C*) genes on days 2 to 7 of culture on the MYRO medium compared to the control (PSB, set as 1 unit)

We found that the relative expression of both *TRI5* and *FgPARP* upon growth on the MYRO medium exceeded that in the control (PSB) at each time point. The relative expression of the *FgPARP* gene was maximal on day 3 of growth (5.4-fold higher than in the control, *Fig. 6A*), and that of the *TRI5* gene was maximal on day 4 (8.6-fold higher than in the control, *Fig. 6B*). However, the relative expression levels of both genes decreased on days 6 to 7. Relative expression of the *FgPARG* gene on days 2–5 of growth on the MYRO medium was virtually identical to that in the control culture, but it increased on days 6 to 7 (2.3- and 3.2-fold higher, respectively, than in the control, *Fig. 6B*).

DISCUSSION

PARP is an enzyme that is involved in many important cellular processes and is found in organisms from different taxonomic groups. The importance of studying PARP and the parylation system is generally determined by its possible practical significance, in particular the use of this enzyme as a target for drugs and agents against pathogens, including those causing plant diseases [42–46]. However, information on the structure and functions of parylation system components in fungi is currently extremely scarce. There is data indicating that *Saccharomyces cerevisiae* and *Schizosaccharomyces pombe* yeasts lack PARP homologs [47]. On the other hand, the toxigenic fungus *A. nidulans* contains a human PARP1 homolog (PrpA) that is involved in DNA repair and asexual development [32]. It has been shown that a PARP homolog from *F. pseudograminearum* participates in apoptosis [30], and that treatment of *F. oxysporum* with an inhibitor of the biosynthesis of NAD+, the main PARP substrate, reduces the growth and pathogenicity of the fungus [48]. In this case, one of the most interesting questions is the potential involvement of PARP and its homologs in the regulation of mycotoxin biosynthesis, in particular fusariotoxins. Currently, histone modifications and chromatin structure changes are considered to be some of the main factors influencing the activity of genes and biosynthetic clusters in general [49, 50], but the role of parylation in these processes in fungi is unknown.

In the present work, we searched for homologs of PARP and its antagonist PARG using databases containing whole genome structures of fungi of the *Fusarium* genus with predicted translation products. In each of the four studied genomes, we found approximately 750 aa PARP1 and PrpA homologs possessing a universal structure: BRCT and WGR domains at the N-terminus and regulatory and catalytic domains at the C-terminus. Unlike human PARP1, the fungal enzymes lacked a N-terminal regulatory domain containing the zinc finger motifs responsible for the search for and recognition of DNA damage and PARP binding to it, which may be an indication of their greater relation to human PARP2, which also lacks these structures [15], than to PARP1. In this regard, the question of how fungal PARPs bind to DNA and perform repair remains open. Possible alternatives to zinc fingers may be involvement of the WGR domain [20] or the use of an intermediary protein in

the binding process. One of the most interesting results of the study was the identification, in addition to the "main" PARP homolog, of four proteins containing the catalytic domain, but lacking the WGR and BRCT domains in the *F. oxysporum* f. sp. *lycopersici* 4287 strain. Further search in the database using the BLASTp algorithm revealed that proteins containing the catalytic domain and structurally similar to the "additional" PARPs found in strain 4287 were also present in other *Fusarium* strains, primarily in *F. oxysporum*. This species is very plastic; in addition to the main (core) chromosomes, its genome can also contain additional chromosomes that often carry genes associated with pathogenicity and specificity to specific host plants [51, 52]. Probably, fungi have acquired "additional" proteins containing PARP catalytic domains independently of the "main" ones through horizontal gene transfer, whose indirect indication may be the presence of similar proteins in some plants, such as alfalfa or wheat. However, "additional" PARPs cannot completely duplicate the functions of the "main" ones due to the lack of a number of functionally significant domains in their structure. However, this does not equate to a functional inferiority of these proteins because what causes changes in the chromatin structure and nucleosome rearrangements may not be associated with the enzymatic activity of PARP [53].

The functional activity of the identified PARP1 homologs was indirectly confirmed by a search for amino acid motifs, which are believed to play a key role in the catalytic action of enzymes. This result is important from an evolutionary point of view: according to current concepts, bacterial exotoxins, such as the diphtheria and cholera toxins, are precursors of parylation system enzymes in eukaryotes. They are able to attach monoADP-ribose residues (mono(ADP-ribosyl)ation or marylation) to the proteins of the host organism, thereby exerting a negative effect on physiological and biochemical processes [17, 42]. The key catalytic motif of the diphtheria toxin is H–Y–E, and that of the cholera toxin is R–S–E. Accordingly, the families of eukaryotic poly(ADP-ribosyl) transferases derived from these two toxins differ in the presence of one of these motifs [54]. In this study, we showed that the catalytic centers of PARP homologs in *Fusarium* fungi contain the catalytic motif H–Y–E and, thus, may be attributed to the family of enzymes derived from the diphtheria toxin. In this case, the "additional" PARPs of strain 4287 did not contain any of these catalytic motifs, which also indicates the independent nature of their origin. Also, we found that each of the studied *Fusarium* strains contained one PARG homolog of the classical structure with the key catalytic motif Q–E–E–I.

Another objective of the study was to augment available information on the structure and polymorphism of genes encoding the PARP and PARG homologs in *Fusarium* genus fungi. At present, databases contain only single records of nucleotide sequences characterized as genes encoding components of the parylation system. Universal primers were developed, and sequencing and phylogenetic analysis of fragments of the corresponding genes were performed in strains of nine species of the *Fusarium* genus available in all-Russian collections. The fragment encoding the catalytic domain of the PARP homolog was shown to be more conserved than the gene fragment encoding the PARG homolog. Interestingly, the topologies of phylogenetic trees constructed based on a comparison of the structures of these two genes also differed slightly. According to the results of the analysis of PARG homologs, the *F. coffeatum* and *F. venenatum* species form a separate subcluster supported by a bootstrap value of 100%. This result looks unusual because, despite the similarity of the toxin profiles (the ability to synthesize type A trichothecene toxins), these two species belong to different species complexes (*F. coffeatum* belongs to the Fusarium incarnatum-equiseti species complex, and *F. venenatum* belongs to the F. sambucinum species complex). In this case, the topology of the phylogenetic tree constructed based on a comparison of the nucleotide sequences of the gene fragment encoding the PARP homolog had a more classical appearance: *F. venenatum* formed a subcluster with a closely related *F. poae*, and *F. coffeatum* formed a separate branch.

In this study, we assessed for the first time the expression dynamics of genes encoding the PARP and PARG homologs in toxigenic *F. graminearum* under conditions favorable for toxin synthesis and on a medium where the toxin was not produced. An increase in the relative expression level of *FgPARP* was shown to correlate with toxin accumulation and increased expression of *TRI5*, a key gene of the biosynthetic cascade. At later stages of culture (days 6 to 7), we observed an increase in the expression level of the *FgPARG* gene, which is probably associated with deparylation and a decrease in toxin biosynthesis. It should be noted that these results only indirectly suggest a relationship between the activity of genes encoding the proteins of the parylation system and toxin biosynthesis. For more reliable data proving these facts, further research is needed: in particular, the production of mutant strains and/or suppression of the expression of target genes using other approaches without genetic transformation; e.g., RNA interference.

CONCLUSION

Based on the results of this study, we have significantly expanded and systematized the amount of information about the presence of components of the parylation system in phytopathogenic fungi of the *Fusarium* genus, as well as the structure, polymorphism, and activity of the corresponding genes. Our findings form the basis for further research into the role played by parylation in the vital activity of fungi, as well as the possible development of new approaches to combating these pathogens. ●

This study was supported by the Russian Science Foundation (grant No. 22-14-00049).

REFERENCES

1. Almeida F., Rodriguez M.L., Coelho C. // Front. Microbiol. 2019. V. 10. P. 214.
2. Fones H.N., Bebber D.P., Chaloner T.M., Kay W.T., Steinberg G., Gurr S.J. // Nat. Food. 2020. V. 1. № 6. P. 332–342.
3. Latham R.L., Boyle J.T., Barbano A., Loveman W.G., Brown N.A. // Essays Biochem. 2023. V. 67. № 5. P. 797–809.
4. Woloshuk C.P., Shim W.-B. // FEMS Microbiol. Rev. 2013. V. 37. № 1. P. 94–109.
5. Escrivá L., Font G., Manyes L. // Food Chem. Toxicol. 2015. V. 78. P. 185–206.
6. Kamle M., Mahato D.K., Gupta A., Pandhi S., Sharma B., Dhawan K., Vasundhara Mishra S., Kumar M., Tripathi A.D., et al. // Microbiol. Res. 2022. V. 13. № 2. P. 292–314.
7. Jansen C., von Wettstein D., Schafer W., Kogel K.H., Felk A., Maier F.J. // Proc. Natl. Acad. Sci. USA. 2005. V. 102. № 46. P. 16892–16897.
8. Maier F.J., Miedaner T., Hadeler B., Felk A., Salomon S., Lemmens M., Kassner H., Schäfer W. // Mol. Plant. Pathol. 2006. V. 7. № 6. P. 449–461.
9. Alexander N.J., Proctor R.H., McCormick S.P. // Toxin Rev. 2009. V. 28. P. 198–215.
10. Wang W., Liang X., Li Y., Wang P., Keller N.P. // J. Fungi. 2023. V. 9. № 1. P. 21.
11. Keller N. // Nat. Rev. Microbiol. 2019. V. 17. № 3. P. 167–180.
12. Gallo A., Perrone G. // Int. J. Mol. Sci. 2021. V. 22. № 15. P. 7878.
13. Bellocchi D., Costantino G., Pellicciari R., Re N., Marrone A., Coletti C. // ChemMedCem. 2006. V. 1. № 5. P. 533–539.
14. Gibson B.A., Kraus W.L. // Nat. Rev. Mol. Cell Biol. 2012. V. 13. № 7. P. 411–424.
15. Amé J.C., Spenlehauer C., de Murcia G. // BioEssays. 2004. V. 26. № 8. P. 882–893.
16. Alemasova E.E., Lavrik O.I. // Nucl. Acids Res. 2019. V. 47. № 8. P. 3811–3827.
17. Mikolčević P., Hloušek-Kasun A., Ahel I., Mikoč A. // Comput. Struct. Biotechnol. J. 2021. V. 19. P. 2366–2383.
18. Kim M.Y., Zhang T., Kraus W.L. // Genes Dev. 2005. V. 19. P. 1951–1967.
19. Thomas C., Ji Y., Wu C., Datz H., Boyle C., MacLeod B., Patel S., Ampofo M., Currie M., Harbin J., et al. // Proc. Natl. Acad. Sci. USA. 2019. V. 116. № 20. P. 9941–9946.
20. Suskiewicz M.J., Munnur D., Strømland Ø., Yang J.-C., Easton L.E., Chartin C., Zhu K., Baretić D., Goffinont S., Schuller M., et al. // Nucl. Acids Res. 2023. V. 51. № 15. P. 8217–8236.
21. Caldecott K.W. // Nat. Rev. Genet. 2008. V. 9. № 8. P. 619–631.
22. Chaudhuri A.R., Nussenzweig A. // Nat. Rev. Mol. Cell Biol. 2017. V. 18. № 10. P. 610–621.
23. Spechenkova N., Kalinina N.O., Zavriev S.K., Love A.J., Taliansky M. // Viruses. 2023. V. 15. № 1. P. 241.
24. Matveeva E., Maiorano J., Zhang Q., Eteleeb A.M., Convertini P., Chen J., Infantino V., Stamm S., Wang J., Rouchka E.C., et al. // Cell Discov. 2016. V. 2. P. 15046.
25. Sousa F.G., Matuo R., Soares D.G., Escargueil A.E., Henriques J.A.P., Larsen A.K., Saffi J. // Carcinogenesis. 2012. V. 33. № 8. P. 1433–1440.
26. Slade D., Dunstan M.S., Barkauskaite E., Weston R., Lafite P., Dixon N., Ahel M., Leys D., Ahel I. // Nature. 2012. V. 477. № 7366. P. 616–620.
27. Kamaletdinova T., Fanaei-Kahrani Z., Wang Z.-Q. // Cells. 2019. V. 8. № 12. P. 1625.
28. Dunstan M.S., Barkauskaite E., Lafite P., Knezevic C.E., Brassington A., Ahel M., Hergenrother P.J., Leys D., Ahel I. // Nat. Commun. 2012. V. 6. № 3. P. 878.
29. Sharon A., Finkelstein A., Shlezinger N., Hatam I. // FEMS Microbiol. Rev. 2009. V. 33. № 5. P. 833–854.
30. Chen L., Ma Y., Peng M., Chen W., Xia H., Zhao J., Zhang Y., Fan Z., Xing X., Li H. // mSphere. 2021. V. 6. № 1. P. e01140–20.
31. Kothe G.O., Kitamura M., Masutani M., Selker E.U., Inoue H. // Fungal Genet. Biol. 2010. V. 47. № 4. P. 297–309.
32. Semighini C.P., Savoldi M., Goldman G.H., Harris S.D. // Genetics. 2006. V. 173. № 1. P. 87–98.
33. Altschul S.F., Gish W., Miller W., Myers E.W., Lipman D.J. // J. Mol. Biol. 1990. V. 215. № 3. P. 403–410.
34. Stakheev A.A., Khairulina D.R., Zavriev S.K. // Int. J. Food Microbiol. 2016. V. 225. P. 27–37.
35. Thompson J.D., Higgins D.G., Gibson T.J. // Nucl. Acids Res. 1994. V. 22. P. 4673–4680.
36. Stakheev A.A., Erokhin D.V., Meleshchuk E.A., Mikityuk O.D., Statsyuk N.V. // Microorganisms. 2022. V. 10. № 7. P. 1347.
37. Simon P. // Bioinformatics. 2003. V. 19. № 11. P. 1439–1440.
38. Kumar S., Stecher G., Tamura K. // Mol. Biol. Evol. 2016. V. 33. № 7. P. 1870–1874.
39. Jones D.T., Taylor W.R., Thornton J.M. // Comput. Appl. Biosci. 1992. V. 8. № 3. P. 275–282.
40. Nei M., Kumar S. Molecular Evolution and Phylogenetics. New York: Oxford Univ. Press, 2000. 352 p.
41. Farber J.M., Sanders G.W. // Appl. Environ. Microbiol. 1986. V. 51. № 2. P. 381–384.
42. Holbourn K.P., Shone C.C., Acharya K.R. // FEBS J. 2006. V. 273. № 20. P. 4579–4593.

43. Della Corte L., Foreste V., Di Filippo C., Giampaolino P., Bifulco G. // Expert. Opin. Investig. Drugs. 2021. V. 30. № 5. P. 543–554.
44. Keller K.M., Koetsier J., Schild L., Amo-Addae V., Eising S., van den Handel K., Ober K., Koopmans B., Essing A., van den Boogaard M.L., et al. // BMC Cancer. 2023. V. 23. № 1. P. 310.
45. Rissel D., Peiter E. // Int. J. Mol. Sci. 2019. V. 20. № 7. P. 1638.
46. Feng B., Liu C., Shan L., He P. // PLoS Pathog. V. 12. № 12. P. e1005941.
47. Citarelli M., Teotia S., Lamb R.S. // BMC Evol. Biol. 2010. V. 13. № 10. P. 308.
48. Anand G., Waiger D., Vital N., Maman J., Ma L.J., Covo S. // Front. Microbiol. 2019. V. 10. P. 329.
49. Soukup A.A., Chiang Y.-M., Bok J.W., Reyes-Dominguez Y., Oakley B.R., Wang C.C.C., Strauss J., Kellep N.P. // Mol. Microbiol. 2012. V. 86. № 2. P. 314–330.
50. Reyes-Dominguez Y., Boedi S., Sulyok M., Wiesenberger G., Stoppacher N., Krska R., Strauss J. // Fungal Genet. Biol. 2012. V. 49. № 1. P. 39–47.
51. Delulio G.A., Guo L., Zhang Y., Goldberg J.M., Kistler H.C., Ma L.-J. // mSphere. 2018. V. 3. № 3. P. e00231–18.
52. Yang H., Yu H., Ma L.-J. // Phytopathology. 2020. V. 110. № 9. P. 1488–1496.
53. Malyuchenko N.V., Kotova E.Yu., Kirpichnikov M.P., Studitsky V.M., Feofanov A.V. // Herald of Moscow University. Series 16. Biology. 2019. V. 74. № 3. 158–162.
54. Cohen M.S., Chang P. // Nat. Chem. Biol. 2018. V. 14. № 3. 236–243.

The Features of Beta-Amyloid Phosphorylation in Alzheimer's Disease

P. A. Strelnikova[1,2#], A. E. Bugrova[1,2#], N. V. Zakharova[1,2], K. V. Danichkina[1], M. I. Indeykina[1,2], M. S. Gavrish[3], V. G. Krut'[4], A. A. Babaev[3], A. Yu. Morozova[5,6], A. S. Kononikhin[1,7*], V. A. Mitkevich[8*], A. A. Makarov[8], E. N. Nikolaev[1]

[1]Skolkovo Institute of Science and Technology, Moscow, 121205 Russian Federation
[2]Emanuel Institute of Biochemical Physics, Russian Academy of Science, Moscow, 119334 Russian Federation
[3]Institute of Neuroscience, Lobachevsky State University of Nizhny Novgorod, Nizhny Novgorod, 603022 Russian Federation
[4]Pirogov Russian National Research Medical University, Moscow, 117997 Russian Federation
[5]V. Serbsky National Medical Research Center of Psychiatry and Narcology, Moscow, 119034 Russian Federation
[6]Mental Health Clinic No. 1 named after N.A. Alekseev, Moscow Healthcare Department, Moscow, 117152 Russian Federation
[7]V.L. Talrose Institute for Energy Problems of Chemical Physics, N.N. Semenov Federal Research Center for Chemical Physics, Russian Academy of Sciences, Moscow, 119334 Russian Federation
[8]Engelhardt Institute of Molecular Biology, Russian Academy of Sciences, Moscow, 119991 Russian Federation
[#] Equal contribution
[*]E-mail: a.kononikhin@skoltech.ru; mitkevich@gmail.com

Received July 09, 2024; in final form, August 16, 2024
DOI: 10.32607/actanaturae.27456

ABSTRACT **Accumulation of neurotoxic aggregates of beta-amyloid peptides (Aβ) is a hallmark of Alzheimer's disease (AD) progression. Post-translational modifications (PTMs) increase Aβ aggregation and cytotoxicity, and the content of specific Aβ proteoforms is elevated in senile plaques of AD patients. The pathophysiological mechanisms of aggregate formation and the role of Aβ proteoforms need thorough study both to understand the role played by specific processes in the initiation of neuronal degradation and to find effective preventive means of therapeutic action. The present work investigates the dynamics of accumulation of phosphorylated serine-8 proteoform Aβ (pSer8-Aβ) using the 5xFAD mouse amyloid model. Aβ samples from human cerebrospinal fluid (CSF) and brain were also investigated. Western blot studies using 1E4E11 and 4G8 antibodies showed that accumulation of pSer8-Aβ in mouse brain starts as early as at the age of 3 months and reaches a maximum by the age of 14–17 months, which is generally similar to the dynamics of accumulation of the total pool of Aβ peptides. The pSer8-Aβ level in human CSF in AD patients can reach ~ 1–10% of the total amount of Aβ. Mass spectrometric analysis showed that Aβ phosphorylation by the Ser8, Tyr10, and Ser26 residues in brain tissues, as well as phosphorylation of the APP by Thr719 residue, is possible. These findings support the assumption that pSer8-Aβ proteoforms are involved in amyloidosis in AD.**

KEYWORDS **Beta-amyloid, mass spectrometry, Alzheimer's disease, phosphorylation.**

ABBREVIATIONS **AD – Alzheimer's disease; Aβ – beta-amyloid peptides; $Aβ_{1-42}$ – 42 amino acid long peptide; PTM – post-translational modifications; pSer8-Aβ – phosphorylated serine-8 proteoform of Aβ; CSF – cerebrospinal fluid; APP – amyloid precursor protein; SPE – solid-phase extraction; FA – formic acid; IP – immunoprecipitation; PSA – ammonium persulfate; BSA – bovine serum albumin; HPLC–MS – high-performance liquid chromatography, mass spectrometry; PASEF – parallel accumulation-serial fragmentation.**

INTRODUCTION

Alzheimer's disease (AD) accounts for 60–80% of all dementia cases, the risk of developing the condition being particularly high amongst the elderly [1]. The number of AD patients continues to increase significantly with every passing year and may reach 115 million by 2050 [2]. The pathogenesis of AD is closely related to the homeostasis of the beta-amyloid peptides

(Aβ) in the brain [3], and amyloid deposits are recognized markers of AD. Despite the more than 30 years of research history into this condition [4, 5], the need to elucidate detailed aspects of the molecular mechanisms of amyloidosis remains relevant, since influencing amyloidosis seems to be the most obvious strategy in the search for effective therapeutic agents for AD [6–8].

The full-length forms of Aβ peptides (Aβ1-40 and Aβ1-42) have important physiological functions that may vary in different tissues of the body, where these peptides take form from different isoforms of the amyloid precursor protein (APP), with the participation of β- and γ-secretases [9, 10]. These peptides play an important role in the regulation of angio- and neuro-genesis, as well as the reduction of the permeability of the blood–brain barrier (BBB). They also promote post-traumatic brain recovery [11]. An ability to aggregate to form cross-β structures is an important feature of Aβ peptides [12]. A lack of balance between the formation of full-length Aβ forms and their timely degradation can contribute to the formation of the modified proteoforms that form neurotoxic oligomers and aggregates [3, 13]. In particular, delayed degradation of full-length Aβ-peptides leads to the accumulation of truncated proteoforms [14–17] and emergence of post-translational modifications (PTMs), which stabilize Aβ aggregates and promote their further growth. It is noteworthy that most of the aforementioned modifications are located in the zinc-binding domain and refer to six polar amino acid residues in the N-terminal region 1–11 [17]; the presence of characteristic peptides truncated at the N-terminus in brain amyloid plaques is consistent with the increased modification rate in this region [15].

In general, pyro-Glu3, pyro-Glu11, isoAsp1, and isoAsp7 are the most abundant PTMs of Aβ peptides [14, 18–23], a fact that may contribute to their increased aggregation and the stabilization of senile plaques in AD. In particular, the assessment of the dynamics of accumulation of different PTMs in the amyloid deposits in the brains of 5xFAD mice used as AD models showed that the accumulation of pyro-Glu3-Aβ in these mice starts at a very early age and reaches a plateau by 8 months of age, whereas isomerization of Asp7 at 7 months of age amounts to only 8% and reaches its maximum (~30%) by the end of the life cycle, but never reaching saturation [24].

Ser8 phosphorylation is another PTM of the N-terminal Aβ site that may play an important role in AD pathogenesis. In particular, the formation of pSer8-Aβ, which occurs with participation of the protein kinases in the extracellular space and on the surface of brain cells [25], correlates with the manifestation of AD symptoms and impedes the Aβ degradation involving insulin-degrading and angiotensin-converting enzymes [26]. The immunohistochemical analysis of neocortex samples revealed the existence of a relationship between the phosphorylation of Aβ by Ser8 and its aggregation into dispersible oligomers, protofibrils and fibrils in symptomatic AD, but not at the preclinical stage [27]. Using synthetic full-length pSer8-$Aβ_{1-42}$ peptides, rapid formation of stable fibrillar aggregates and neurotoxic oligomers was observed in the absence of zinc ions [28, 29]. In addition, the possibility of formation of aggregates exhibiting increased neurotoxicity due to the interaction of pSer8-$Aβ_{1-42}$ with unmodified $Aβ_{1-42}$ was established [30]. The structural NMR analysis additionally revealed the higher amyloid amplification efficiency and increased thermodynamic stability of pSer8-$Aβ_{1-40}$ fibrils compared to the fibrils of the unphosphorylated peptide [31]. On the other hand, both full-length pSer8-$Aβ_{1-42}$ and its zinc-binding fragment pSer8-$Aβ_{1-16}$ significantly reduce the *in vitro* Aβ aggregation induced by zinc ions [32–34] and injections of pSer8-$Aβ_{1-42}$ reduce the formation of amyloid plaques in the mouse hippocampus [34]. Apparently, both scenarios are possible, when pSer8-Aβ triggers fibril formation or, on the contrary, supresses metal-dependent aggregation. The realization of each scenario depends on external factors such as the presence and concentration of zinc ions, Aβ partner proteins, etc. In this regard, studying the dynamics of pSer8-Aβ accumulation may help reaseachers clarify its role in the formation of amyloid deposits.

The optimization of approaches, including mass spectrometric (MS) ones, to the analysis of phosphorylated forms of amyloid remains a pressing task [17, 35, 36]. Aβ includes three potential phosphorylation sites (Ser8, Ser26, and Tyr10), as well as potential sites in the APP regions adjacent to Aβ. Evidence has been obtained of the *in vivo* presence of phosphorylated Aβ proteoforms with modified Ser8 and Ser26 [17, 24]. Further MS studies of these proteoforms may lead to the uncovering of important information on the role of phosphorylation pathways in amyloidosis, as well as to our understanding of the role played by phosphorylation in the pathogenesis of AD. In this work, we investigated the specificity of Aβ phosphorylation by Ser8 (pSer8-Aβ) using mass spectrometry and Western blotting in 5xFAD model mice, as well as in an AD patient.

EXPERIMENTAL

Reagents and Aβ-peptides

All the chemicals and solvents used in this study were of HPLC grade. Synthetic Aβ peptides ($Aβ_{1-16}$,

pSer8-$A\beta_{1-16}$, $A\beta_{1-42}$ and pSer8-$A\beta_{1-42}$) prepared by solid-phase synthesis and purified to > 99.5% purity using HPLC (BioPeptide Inc., USA) were dissolved in 10% acetonitrile to a concentration of 0.5 mg/mL, divided into 50 μL aliquots, and stored at -80°C. The synthetic peptides at known concentrations were used as standards and control samples ("spikes"). For the control samples, human blood plasma diluted with phosphate buffered saline (pH 7.4) at a 1 : 50 ratio was used as a template.

5xFAD mice

The 5xFAD transgenic mouse line (Jackson Laboratory, USA, stock number 006554) was used in this work [37]. Mice of this line have five severe AD-related inherited mutations in the human amyloid precursor protein (APP) (SweK670N, M671L, LonV717I and FloI716V) and the presenilin 1 (PSEN1) (M146L and L286V) genes expressed under the control of the mouse Thy1 promoter. These mice express transgenic human Aβ at significantly higher levels than native mouse Aβ, resulting in an accelerated deterioration of the cognitive brain function. The earliest behavioral impairments manifest themselves at an age of ~ 6 months and become maximally pronounced by 9 months of age [38].

Mouse brain samples were provided by the Center for Genetic Collections of Laboratory Animals (Lobachevsky Institute of Biology and Biomedicine, NNGU). The cohort consisted of six items aged 3, 8, 12, 12, 14, 17, and 23 months. The animals were kept in a colony with free access to food and water in a room with controlled temperature +20 ± 2°C and 40–60% humidity with a 12-hour light/dark cycle. The experiments on mice were performed according to the guidelines approved by the Local Ethics Committee and animal control authorities (Guidelines for Housing and Care of Animals. Environment, Housing and Management, 2016).

All the 5xFAD mice were genotyped to confirm the presence of all mutations. For this purpose, DNA was extracted from part of the tail, placed in 300 μL of lysis buffer (10 mM Tris-HCl, pH 8.0, 100 mM NaCl) with proteinase K, incubated at +55°C for 16–20 h with rotation at 650 rpm, mixed, and centrifuged at room temperature (5 min, 14 000 rpm). The upper fraction containing DNA was additionally washed once with isopropanol and twice with 80% ethanol, followed by centrifugation at +4°C (15 min, 14 000 rpm). The presence of the human *PSEN1* and *APP* genes was verified by polymerase chain reaction (PCR) using the insert-specific primers 5′-AAT AGA GAA GAA CGG CAG GAG CA-3′ and 5′-GCC AT G AGG GCACT AAT CAT-3′ for *PSEN1* and 5′-AGG ACT GAC CACT CG ACC AG-3′ and 5′-CGG GGGTCTAGTTCTTCTGCAT-3′ for *APP* [39]. The control primers were 5′-CT A GGC CAC AGAATTGAAAGATCT-3′ and 5′-GTAGGTGTGGA AAT T CT AGC ATC C-3′.

Human CSF and brain samples

A human brain tissue sample was obtained from an 82-year-old sporadic AD patient at autopsy (post-mortem interval (PMI), 15 h). Samples from the temporal lobe and hippocampus were frozen in liquid nitrogen for further MS analysis and fixed in 10% buffered formalin (BioVitrum, Russia) for histological analysis. To verify the diagnosis, 4–5 μm thick histological sections of brain tissue were made and stained with Congo red (BioVitrum, Russia). Anti-tau-protein and anti-Aβ antibodies were used for immunohistochemical (IHC) staining.

A CSF sample was obtained by diagnostic lumbar puncture with a sterile needle from a 79-year-old man diagnosed with Alzheimer's. The volume of cerebrospinal fluid was 1 mL. The sample was centrifuged (1 500 rpm, 15 min) within 1 h of collection, and the supernatant was collected. The samples were stored at -80°C.

All the procedures related to the obtention of human biological material were performed in accordance with the recommendations of the Declaration of Helsinki and after securing the approval of the Ethics Committee (Protocol No. 1 of January 25, 2022 of the Ethics Committee of the Mental Health Clinical Hospital No. 1 named after N.A. Alekseev, Moscow City Health Department). Written informed consent was obtained from the patients.

Extraction of Aβ-peptides from the brain tissue

For Aβ-peptide extraction, brain samples were homogenized on ice using a Potter glass homogenizer with the addition of four volumes of lysing buffer (20 mM Tris, 2.5 mM EDTA, 137 mM NaCl, pH 7.6) containing a mixture of protease inhibitors (Roche, France). After formic acid (FA) had been added up to 70% (by volume), the samples were sonicated (10 min × 2), shaken, and centrifuged (30 000 g, 1 h, +4°C). Evaporation of FA from the supernatant was achieved using a vacuum concentrator (Eppendorf, Germany). The obtained acidic extracts were stored at -80°C. Aβ was further isolated by solid-phase extraction (SPE) using Oasis MCX cartridges (Waters, USA) according to the manufacturer's protocol [40], with the following modifications: the acidic extracts were dissolved in a 8 M/2 M urea/thiourea mixture, and H_3PO_4 was added up to 2%. SPE cartridges were preconditioned with 1 mL of methanol and equilibrated with 1 mL

of 4% H_3PO_4. The sample (2 mL) was loaded into the SPE cartridge and washed with 2 mL of 4% H_3PO_4 and 10% acetonitrile (ACN). The Aβ-enriched fraction was eluted with 1 mL of a 75 : 15 : 10 (vol.) ACN/H_2O/NH_4OH solution, and the samples were evaporated to 100 μL using a vacuum concentrator (Eppendorf, Germany).

Aβ-peptide isolation from human CSF

Aβ-peptides were isolated from CSF and the control samples ("spikes") by immunoprecipitation (IP) using the monoclonal antibody 1E4E11 highly specific to pSer8-Aβ (Merck KGaA, Germany), as well as the antibodies 6E10 and 1E8 (three orders of magnitude more sensitive to unmodified Aβ) and 4G8 (with equal specificity to both forms of Aβ). IP was performed for 3 h at +4°C with the antibodies immobilized on Dynabeads magnetic particles (Thermo Scientific) in the presence of protease inhibitors. Aβ was eluted using 70% ACN supplemented with 10 mM HCl or double-denaturing buffer for samples for the subsequent peptide electrophoresis and Western blotting.

Peptide electrophoresis and Western blotting

The samples obtained after SPE enriched with the Aβ fraction were mixed at a 1 : 1 ratio with 2× sample buffer for peptide electrophoresis (100 mM Tris-HCl pH 8.8, 1% SDS, 4% beta-mercaptoethanol, 24% glycerol, 0.02% Coomassie brilliant blue) and denatured for 5 min at ~ +90°C [41]. Peptide electrophoresis was performed in Mini-PROTEAN cells (Bio-Rad, USA) using a Tris-tricine buffer system (25 mM Tris, 25 mM Tricine, 0.05% SDS) in 12% polyacrylamide gel. Four mL of a 30% acrylamide/bis-acrylamide solution (AA/BA, 29/1), 5 mL of 2.5 M Tris-HCl pH 8.8, 6 μL of TEMED, and 100 μL of 10% ammonium persulfate (PSA)) were added per 10 mL of separating gel. To prepare 5 mL of a 4% concentrating gel, 0.66 mL of AA/BA, 0.76 mL of 2.5 M Tris-HCl pH 8.8, 5 μL of TEMED, and 150 μL of PSA were added. Electrophoresis was performed for 1.5–2 h at 60 mA with sufficient cooling until the dye front started to emerge from the gel. Semi-dry transfer to a 0.2 μm pore size nitrocellulose membrane was performed for 1 h at 50 mA using a buffer containing 47.9 mM Tris, 38.6 mM glycine, 0.0385% SDS, and 20% methanol.

For Western blotting, the membrane was blocked for 30 min in a 2.5% milk solution in 0.01 M PBS and 0.1% Tween-20 supplemented with 10 mg/mL BSA and incubated with primary antibodies overnight. The 1E4E11 antibody (1 : 4,000, Merck KGaA, Germany), highly specific to this PTM, was used to detect pSer8-Aβ. Unmodified Aβ was detected using 6E10 antibodies (1 : 8 000, epitope 3–8, Biolegend, USA), as well as 4G8 antibodies (1 : 4 000, epitope 18–23, Biolegend, USA) capable of detecting both monomeric and oligomeric forms [42]. Incubation with secondary antibodies (1 : 5 000, horseradish peroxidase-conjugated IgG, Hy-test) was performed for 1 h. The results were visualized using enhanced chemiluminescence (ECL) with SuperSignal reagents (Thermo Fisher Scientific, USA). Images were acquired using the SYNGENE G:Box gel documentation system (Syngene, UK) and processed using the GeneTools software.

Chromatography-mass spectrometry (HPLC-MS) analysis

All the samples meant for HPLC-MS analysis were hydrolyzed by Lys-C protease (Promega, USA) to yield hydrophilic fragments of Aβ1-16. Samples after SPE (20 μl) were mixed (1 : 1) with 100 mM ammonium bicarbonate and 0.4 μg Lys-C, and then incubated at 37°C for 4 h.

Non-targeted HPLC-MS analysis of hydrolysate (Lys-C) samples was performed on a Dionex Ultimate 3000 HPLC system (Thermo Fisher Scientific) coupled to a TIMS TOF Pro high-resolution time-of-flight mass spectrometer (Bruker Daltonics, USA) using the parallel accumulation and sequential fragmentation (PASEF) data acquisition method in the DDA mode. The electrospray ionization (ESI) source settings were as follows: capillary voltage, 4500 V; end plate bias potential, 500 V; and dry gas flow rate, 3.0 L/min at 180°C. Measurements were carried out in the mass/charge (m/z) range of 100 to 1,700. The ion mobility range included values from 0.60 to 1.60 V·s/cm^2 ($1/k_0$, where k_0 is the ion mobility). The total cycle time was set to 1.16 s, and the number of PASEF MS/MS scans was set to 10. For small amounts of samples, the total cycle time was set to 1.88 s.

For HPLC, the loaded sample volume was 1 μL per injection. HPLC was performed using an Ion Optics emitter column (C18, 25 cm × 75 μm, 1.6 μm; Parkville, Australia) by gradient elution. Mobile phase A contained 0.1% formic acid in water; mobile phase B contained 0.1% FA in acetonitrile. Separation was performed at a flow rate of 400 nL/min using a 40-min gradient from 4 to 90% of phase B.

Data from non-target HPLC-MS were analyzed using the PEAKS Studio 8.5 software (parameters: parent ion mass measurement error, 20 ppm; fragment mass error, 0.03 Da). Methionine oxidation was identified as a possible variable modification. The search was performed using the Swissprot database of hu-

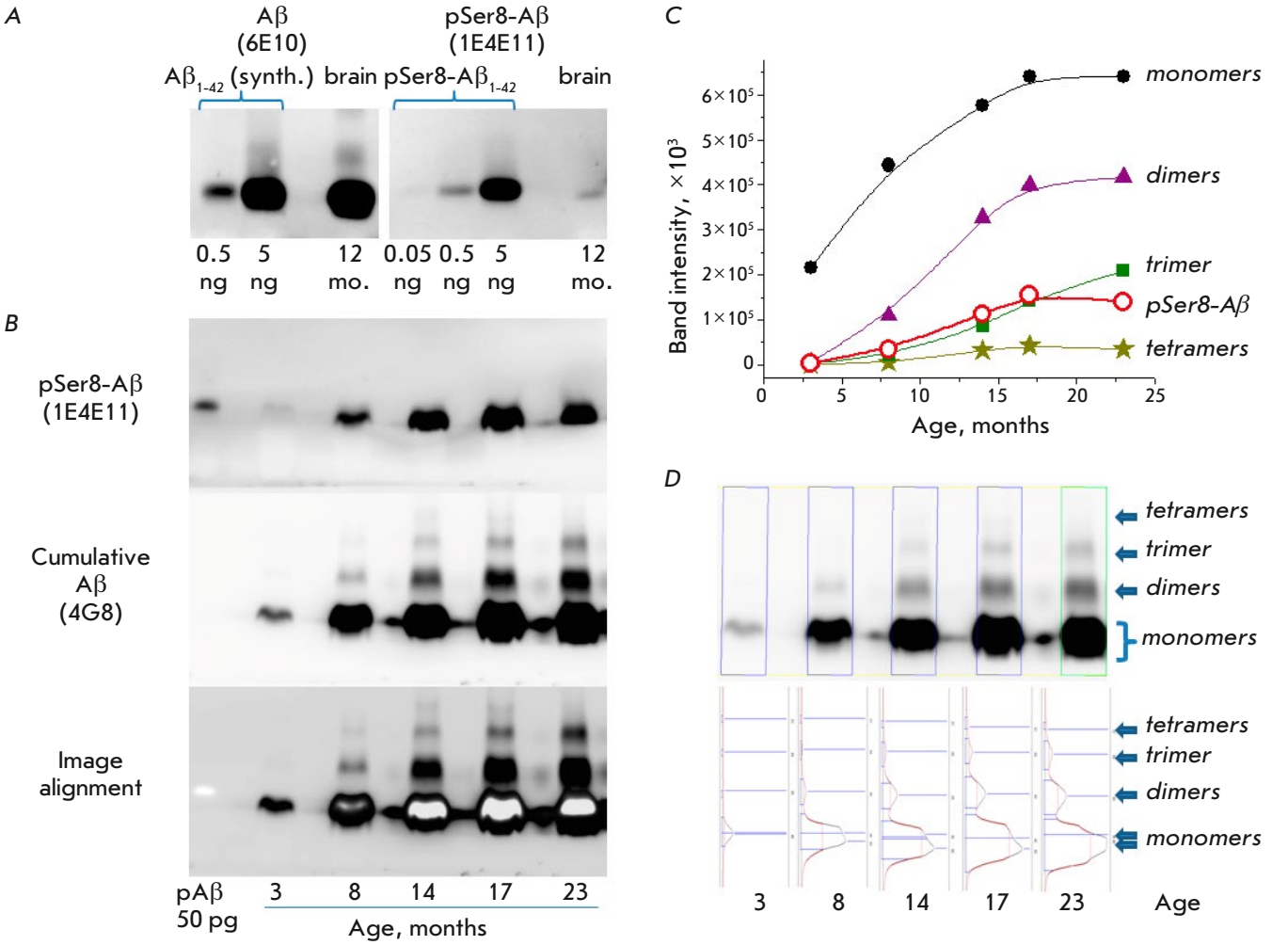

Fig. 1. Analysis of the dynamics of pSer8-Aβ accumulation against the total pool of Aβ peptides by Western blot in the brains of 5xFAD mice. (*A*) Accumulation of unmodified and pSer8 monomeric forms of Aβ in a 12-month-old mouse brain; the amount of sample applied corresponds to 0.3 mg of brain tissue for Aβ and 1 mg of tissue for pSer8-Aβ. (*B*) Comparative analysis of the accumulation of the total pool of peptide Aβ and pSer8-Aβ forms in the brain of mice of different ages; the amount of the applied sample corresponds to 3 mg of brain tissue. (*C*) Graphs showing the dynamics of accumulation of monomeric and oligomeric forms of Aβ based on the results of image processing in the GeneTools software. (*D*) GeneTools analysis of the staining intensity distribution of bands in each lane

man proteins. The FDR threshold for all the steps was set at 1% or lower.

RESULTS AND DISCUSSION

Dynamics of pSer8-Aβ accumulation in the brains of 5xFAD mice

The formation of fibrillar Aβ structures can be detected in the brains of 5xFAD mice as young as two months- old [37]. The dynamics of accumulation of some Aβ proteoforms studied previously showed that, in general, the accumulation of Aβ proteoforms correlates with the formation of amyloid deposits [24]. We performed a series of experiments to evaluate the dynamics of pSer8-Aβ accumulation by Western blotting.

The proportion of phosphorylated Aβ in a middle-aged mouse (12 months of age) was roughly estimated beforehand. For that purpose, we compared the peptide content in identical tissue weights from the same animal with a line of the corresponding synthetic standards $Aβ_{1-42}$ and pSer8-$Aβ_{1-42}$ (*Fig. 1A*). 6E10 antibodies, which are used to detect predominantly monomeric peptides (epitope 3–8), were used to identify unmodified Aβ; highly specific 1E4E11 antibodies were used to identify pSer8. The results indicate that

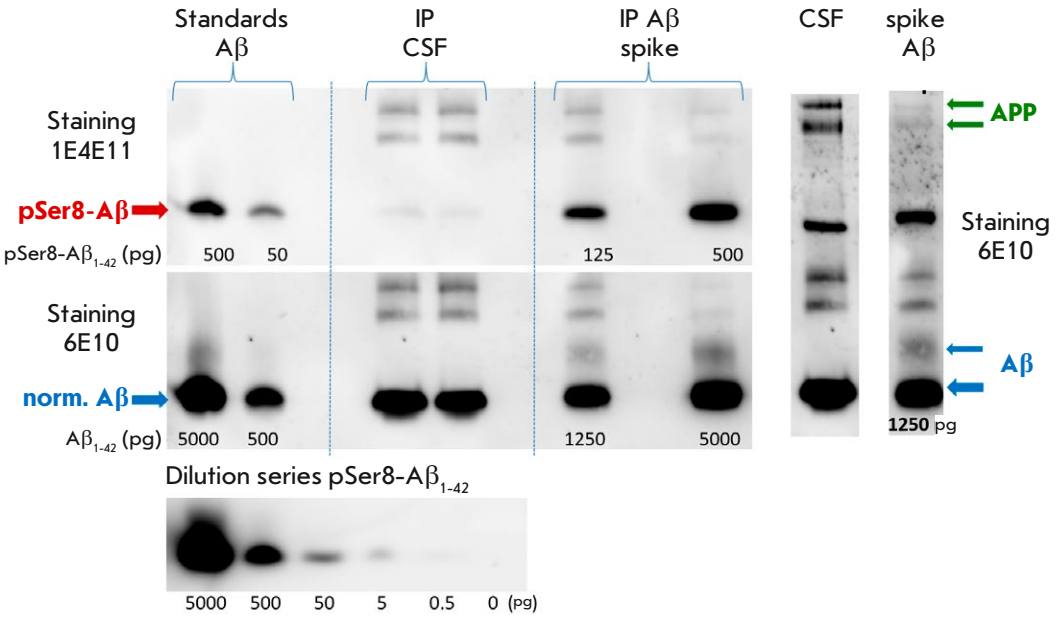

Fig. 2. Evaluation of pSer8-Aβ content in the cerebrospinal fluid (CSF) of a patient with AD by Western blot. Immunoprecipitation (IP) was performed in the patient's CSF, as well as the control samples of Aβ (spikes). The green arrows indicate the precursor protein (APP); the blue ones, monomer and dimer Aβ

the total amount of monomeric Ser8-unmodified Aβ proteoforms can be as high as 2 ng per mg of brain tissue by the age of 12 months, while the proportion of monomeric pSer8-Aβ can be 10–100 times smaller. It should be noted that Western blotting still does not belong to what is known as quantitative methods and allows only approximate relative quantification. In addition, both the total amount of Aβ and the amount of its modified forms can vary in different animals [24].

The dynamics of accumulation of total and modified Aβ were assessed using extracts obtained from the brain preparations of 3-, 8-, 14-, 17-, and 23-month-old mice (*Fig. 1B–D*). To minimize technical errors and, given that a preliminary experiment had confirmed that pSer8-Aβ could be present in significantly lower amounts with respect to unmodified Aβ, the same membrane was sequentially manifested first with antibodies to pSer8-Aβ (1E4E11) and only after with 4G8 antibodies, which, unlike 6E10, do not compete at all for the epitope with 1E4E11 and manifest all forms of Aβ that have no modifications in site 18–23 (including pSer8-Aβ), including their oligomers [42]. Visual evaluation of the Western blotting results (*Fig. 1B*) suggests that pSer8-Aβ peptides are already detectable at the age of 3 months and, in monomeric form, may peak by the age of 14 months. The results of additional evaluation of band intensity in the recorded images (*Fig. 1B*) demonstrate the similarity of the dynamics of pSer8-Aβ accumulation and the total pool of monomeric and dimeric forms of Aβ, which may be indirect indication of a relationship between Ser8 phosphorylation and oligomerization stimulation. Nevertheless, the result does not allow us to draw any direct conclusions about the possible presence of pSer8-Aβ in oligomeric forms: similar to 6E10 antibodies, the overlapping epitope in the N-terminus of the 1E4E11 antibodies may also poorly identify dimeric and oligomeric forms due to the reduced availability of the specific site.

Additional analysis of the distribution of the band staining intensity in each sample (*Fig. 1D*) further emphasized the presence of Aβ dimers, trimers, and tetramers in individual samples, and also revealed heterogeneity and the presence of at least two peaks in the stains corresponding to monomeric forms starting at the age of 8 months. This may indicate the presence of truncated monomers, along with full-length peptides. Notably, when the images in *Fig. 1B* are combined, the location of the phosphorylated proteoforms can rather be confined to the upper part of the monomeric spot and, in general, the spots corresponding to pSer8-Aβ have clearer boundaries compared to the overall spot.

Hence, it can be inferred that the lower part of the total spot may contain peptides truncated at the N-terminus and lacking a Ser8 site. This may be indication that Ser8 phosphorylation may facilitate cleavage of the corresponding N-terminal fragment.

Analysis of pSer8-Aβ in CSF

Western blot analysis of Aβ from the CSF of a patient with AD revealed the presence of significant amounts of pSer8-Aβ (*Fig. 2*). Sequential staining of the membrane with highly specific antibodies to pSer8-Aβ and

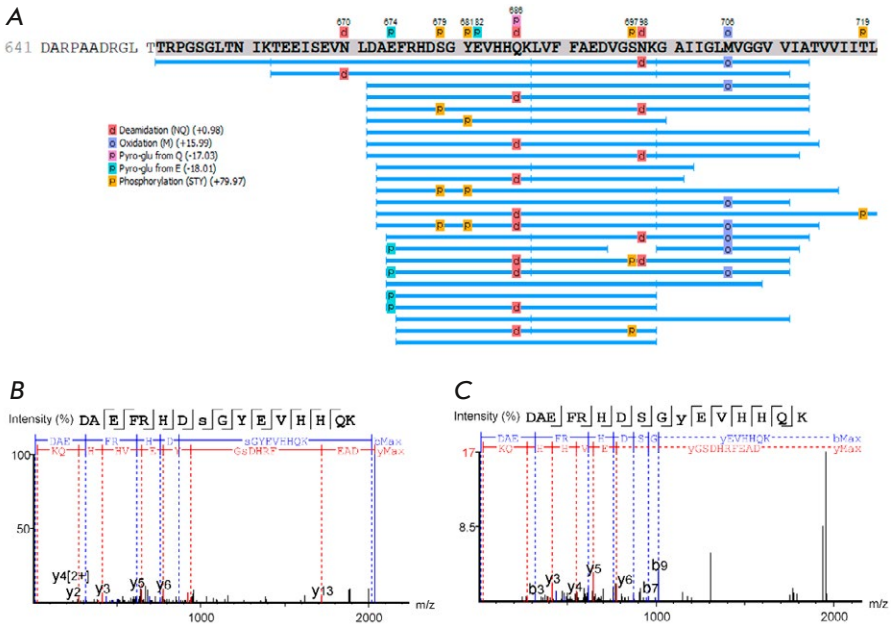

Fig. 3. Coverage of sequences of Aβ proteoforms (marked in gray) isolated from the brains of 5xFAD mice with localization of possible post-translational modifications including phosphorylation (Ser (S), Thr(T) and Tyr (Y)) – (*A*). Fragmentation mass spectra for phosphorylated Aβ16 peptide with different localization of phospho groups (the characteristic –y –b series of peptide fragment ions are noted): spectrum for Ser8(s) – (*B*); spectrum for Tyr10(y) – (*C*)

antibodies to the unmodified forms allowed us to establish that the proportion of pSer8-Aβ forms in the CSF may amount to ~ 1–10% of the unmodified full-length forms of the peptide. This value agrees well with the results of a quantitative determination of the fraction of phosphorylated amyloid monomers obtained using the electrochemical approach [43].

In addition, in the CSF sample, antibodies against the unmodified form of Aβ identify two high-molecular-weight bands corresponding to the ARP protein (*Fig. 2*); probably its glycosylated and non-glycosylated forms.

Mass spectrometric analysis of phosphorylated Aβ proteoforms from the brain tissue

Phosphorylation of Aβ had not previously been confirmed through mass spectrometry methods. In the present study, phosphorylation of Ser, Thr, and Tyr was examined by HPLC-MS analysis of sample fractions of Aβ from the brain tissue of 5xFAD mice (*Fig. 3*). Aβ peptides phosphorylated at the Ser8 and Tyr10 residues were identified; however, close observation of fragmentation spectra did not allow us to unambiguously determine the position of PTMs. In addition, a peptide with double phosphorylation was detected. This circumstance indicates the feasibility of the phosphorylation not only of the serine (Ser8), but also of the tyrosine (Tyr10) within amyloid. Phosphorylation of Tyr10 has been shown by neither MS nor any other method. Although it has been found that nitration and dityrosine formation can occur at this position, phosphorylation could be an intermediate reaction that is difficult to detect. In addition to Ser8 and Tyr10, some fragmentation spectra indicated the possibility of Ser26 phosphorylation. Nevertheless, the overall quality of the spectra recorded for Ser8, Tyr10, and Ser26 cannot be recognized as sufficient to draw any confident conclusions: so, this issue requires further research.

In addition, according to a HPLC-MS analysis of Aβ peptides from the human brain, phosphosite Thr (T719) was detected, whose phosphorylation was close to 100% and raised no doubt. This site is present only in elongated forms of Aβ (X- T48), which are most likely to be the products of alternative processing of APP or its degradation, unrelated to amyloidosis. Other possible phosphorylation positions in the APP — 729, 730, and 743 — had no reliable coverage in the MS analysis, making it impossible to draw any inference. The Tyr757 site had good coverage, but its phosphorylation was not detected.

In general, although the results of the MS analysis indicate the presence of certain phosphorylation sites in Aβ and adjacent APP regions, the need for further MS studies of phosphorylated Aβ proteoforms remains present. The solution to this problem may hinge to a significant extent on an optimization of the procedure for isolating phosphorylated Aβ proteoforms, since the frequently used FA solubilization readily hydrolyzes esterified phosphate groups [20, 22]. In addition, some hope is associated with the recent advances in the research into synthetic phos-

phorylated Aβ proteoforms by MALDI-TOF and with the use of matrix additives that minimize the loss of phosphate groups during ionization and enhance the ionization of phosphopeptides specifically [35, 36].

CONCLUSIONS

According to the results obtained in this study, accumulation of pSer8-Aβ-peptides in the brains of 5xFAD mice follows a similar dynamics as that in the accumulation of monomeric and dimeric forms of the total pool of Aβ peptides. By the end of the life cycle, the total amount of accumulated Aβ peptides can reach ~10 ng per mg of brain tissue and the proportion of pSer8-Aβ could attain 1–10%.

It is also shown that the proportion of pSer8-Aβ-forms in human CSF may reach ~ 1–10% of unmodified full-length Aβ forms. Using high-resolution mass spectrometry, we obtained indications of the possibility of Aβ phosphorylation by the Ser8 and Ser26 residues, as well as APP phosphorylation by the Thr719 residue. Indications that Tyr10 phosphorylation might be possible have been obtained by us for the first time. Further optimization of MS techniques for the efficient analysis of phosphorylated Aβ proteoforms remains highly potent. ●

This work was supported by the Russian Science Foundation (grant No. 19-74-30007).

REFERENCES

1. Alzheimer`s Association// Alzheimer's Dement. 2021. V. 17. № 3. P. 327–406.
2. Prince M., Bryce R., Albanese E., Wimo A., Ribeiro W., Ferri C.P. // Alzheimer's Dement. 2013. V. 9. № 1. P. 63–75.
3. Wang J., Gu B.J., Masters C.L., Wang Y.J. // Nat. Rev. Neurol. 2017. V. 13. № 10. P. 612–623.
4. Hardy J.A., Higgins G.A. // Science. 1992. V. 256. № 5054. P. 184–185.
5. Roher A.E., Lowenson J.D., Clarke S., Woods A.S., Cotter R.J., Gowing E., Ball M.J. // Proc. Natl. Acad. Sci. USA. 1993. V. 90. № 22. P. 10836–10840.
6. Klein W.L., Krafft G.A., Finch C.E. // Trends Neurosci. 2001. V. 24. № 4. P. 219–224.
7. Selkoe D.J., Hardy J. // EMBO Mol. Med. 2016. V. 8. № 6. P. 595–608.
8. Lee S.J.C., Nam E., Lee H.J., Savelieff M.G., Lim M.H. // Chem. Soc. Rev. 2017. V. 46. № 2. P. 310–323.
9. Evin G., Zhu A., Holsinger R.M.D., Masters C.L., Li Q.X. // J. Neurosci. Res. 2003. V. 74. № 3. P. 386–392.
10. Galozzi S., Marcus K., Barkovits K. // Expert Rev. Proteomics. 2015. V. 12. № 4. P. 343–354.
11. Kent S.A., Spires-Jones T.L., Durrant C.S. // Acta Neuropathol. 2020. V. 140. № 4. P. 417–447.
12. Gallardo R., Ranson N.A., Radford S.E. // Curr. Opin. Struct. Biol. 2020. V. 60. P. 7–16.
13. Rogers J., Strohmeyer R., Kovelowski C.J., Li R. // Glia. 2002. V. 40. № 2. P. 260–269.
14. Portelius E., Bogdanovic N., Gustavsson M.K., Volkmann I., Brinkmalm G., Zetterberg H., Winblad B., Blennow K. // Acta Neuropathol. 2010. V. 120. № 2. P. 185–193.
15. Wildburger N.C., Esparza T.J., Leduc R.D., Fellers R.T., Thomas P.M., Cairns N.J., Kelleher N.L., Bateman R.J., Brody D.L. // Sci. Rep. 2017. V. 7. № 1. P. 1–9.
16. Zakharova N. V., Bugrova A.E., Kononikhin A.S., Indeykina M.I., Popov I.A., Nikolaev E.N. // Expert Rev. Proteomics. 2018. V. 15. № 10. P. 773–775.
17. Zakharova N.V., Kononikhin A.S., Indeykina M.I., Bugrova A.E., Strelnikova P., Pekov S., Kozin S.A., Popov I.A., Mitkevich V., Makarov A.A., et al. // Mass Spectrom. Rev. 2022. V. 28. P. e21775.
18. Kummer M.P., Heneka M.T. // Alzheimer's Res. Ther. 2014. V. 6. № 3. P. 28.
19. Brinkmalm G., Portelius E., Öhrfelt A., Mattsson N., Persson R., Gustavsson M.K., Vite C.H., Gobom J., Månsson J.E., Nilsson J., et al. // J. Mass Spectrom. 2012. V. 47. № 5. P. 591–603.
20. Mukherjee S., Perez K.A., Lago L.C., Klatt S., McLean C.A., Birchall I.E., Barnham K.J., Masters C.L., Roberts B.R. // Brain Commun. 2021. V. 3. № 2. fcab028.
21. Inoue K., Hosaka D., Mochizuki N., Akatsu H., Tsutsumiuchi K., Hashizume Y., Matsukawa N., Yamamoto T., Toyo'Oka T. // Anal. Chem. 2014. V. 86. № 1. P. 797–804.
22. Roher A.E., Kokjohn T.A., Clarke S.G., Sierks M.R., Maarouf C.L., Serrano G.E., Sabbagh M.S., Beach T.G. // Neurochem. Int. 2017. V. 110. P. 1–13.
23. Moro M.L., Phillips A.S., Gaimster K., Paul C., Mudher A., Nicoll J.A.R., Boche D. // Acta Neuropathol. Commun. 2018. V. 6. № 1. P. 3.
24. Bugrova A.E., Strelnikova P.A., Indeykina M.I., Kononikhin A.S., Zakharova N.V., Brzhozovskiy A.G., Barykin E.P., Pekov S.I., Gavrish M.S., Babaev A.A., et al. // Int. J. Mol. Sci. 2021. V. 2022. P. 27.
25. Kumar S., Rezaei-Ghaleh N., Terwel D., Thal D.R., Richard M., Hoch M., Mc Donald J.M., Wüllner U., Glebov K., Heneka M.T., et al. // EMBO J. 2011. V. 30. № 11. P. 2255–2265.
26. Kumar S., Singh S., Hinze D., Josten M., Sahl H.G., Siepmann M., Walter J. // J. Biol. Chem. 2012. V. 287. № 11. P. 8641–8651.
27. Rijal Upadhaya A., Kosterin I., Kumar S., von Arnim C.A.F., Yamaguchi H., Fändrich M., Walter J., Thal D.R. // Brain. 2014. V. 137. № 3. P. 887–903.
28. Rezaei-Ghaleh N., Amininasab M., Kumar S., Walter J., Zweckstetter M. // Nat. Commun. 2016. V. 7. P. 11359.
29. Jamasbi E., Separovic F., Hossain M.A., Ciccotosto G.D. // Mol. Biosyst. 2017. V. 13. № 8. P. 1545–1551.
30. Hu Z.W., Au D.F., Cruceta L., Vugmeyster L., Qiang W. // ACS Chem. Neurosci. 2020. V. 11. № 14. P. 2058–2065.
31. Hu Z.W., Vugmeyster L., Au D.F., Ostrovsky D., Sun Y., Qiang W. // Proc. Natl. Acad. Sci. USA. 2019. V. 166. № 23. P. 11253–11258.
32. Kulikova A.A., Tsvetkov P.O., Indeykina M.I., Popov I.A., Zhokhov S.S., Golovin A. V., Polshakov V.I., Kozin S.A., Nudler E., Makarov A.A. // Mol. Biosyst. 2014. V. 10. № 10. P. 2590–2596.

33. Istrate A.N., Kozin S.A., Zhokhov S.S., Mantsyzov A.B., Kechko O.I., Pastore A., Makarov A.A., Polshakov V.I. // Sci. Rep. 2016. V. 6. P. 21734.
34. Barykin E.P., Petrushanko I.Y., Kozin S.A., Telegin G.B., Chernov A.S., Lopina O.D., Radko S.P., Mitkevich V.A., Makarov A.A. // Front. Mol. Neurosci. 2018. V. 11. P. 302.
35. Liepold T., Klafki H.W., Kumar S., Walter J., Wirths O., Wiltfang J., Jahn O. // J. Am. Soc. Mass Spectrom. 2023. V. 34. № 3. P. 505–512.
36. Kuzin A.A., Stupnikova G.S., Strelnikova P.A., Danichkina K.V., Indeykina M.I., Pekov S.I., Popov I.A. // Molecules. 2022. V. 27. № 23. P. 8406.
37. Oakley H., Cole S.L., Logan S., Maus E., Shao P., Craft J., Guillozet-Bongaarts A., Ohno M., Disterhoft J., van Eldik L., et al. // J. Neurosci. 2006. V. 26. № 40. P. 10129–10140.
38. Schneider F., Baldauf K., Wetzel W., Reymann K.G. // Pharmacol. Biochem. Behav. 2015. V. 128. P. 68–77.
39. Popugaeva E., Chernyuk D., Zhang H., Postnikova T.Y., Pats K., Fedorova E., Poroikov V., Zaitsev A.V., Bezprozvanny I. // Mol. Pharmacol. 2019. V. 95. № 4. P. 337–348.
40. Lame M.E., Chambers E.E., Blatnik M. // Anal. Biochem. 2011. V. 419. № 2. P. 133–139.
41. Haider S.R., Reid H.J., Sharp B.L. // Methods Mol. Biol. 2012. V. 869. P. 81–91.
42. Hatami A., Monjazeb S., Milton S., Glabe C.G. // J. Biol. Chem. 2017. V. 50. № 2. P. 517–525.
43. Yin Z., Wang S., Shen B., Deng C., Tu Q., Jin Y., Shen L., Jiao B., Xiang J. // Anal. Chem. 2019. V. 91. № 5. P. 3539–3545.

Genome Characterization of Two Novel *Lactococcus lactis* Phages vL_296 and vL_20A

T. A. Chuksina[1], A. A. Fatkulin[1], N. P. Sorokina[2], I. T. Smykov[2], E. V. Kuraeva[2], E. S. Masagnaya[2], K. A. Smagina[2], M. Yu. Shkurnikov[1*]

[1]Department of Biology and Biotechnology, HSE University, Moscow, 101000 Russian Federation

[2]V.M. Gorbatov Federal Research Center for Food Systems, Moscow, 109316 Russian Federation

*E-mail: mshkurnikov@hse.ru

Received July 29, 2024; in final form, September 15, 2024

DOI: 10.32607/actanaturae.27468

ABSTRACT **Fermented dairy products are produced using starter cultures. They ferment milk to create products with a certain texture, aroma, and taste. However, the lactic acid bacteria used in this production are prone to bacteriophage infection. We examined the genomes of two newly discovered bacteriophage species that were isolated from cheese whey during the cheesemaking process. We have determined the species and the lytic spectrum of these bacteriophages. Phages vL_20A and vL_296 were isolated using lactococcal indicator cultures. They have unique lytic spectra: of the 21 possible identified host bacteria, only four are shared amongst them. The vL_20A and vL_296 genomes comprise linear double-stranded DNA lengths with 21,909 and 22,667 nucleotide pairs, respectively.** *Lactococcus phage bIL67* **(ANI 93.3 and 92.6, respectively) is the closest to the phages vL_20A and vL_296. The analysis of the CRISPR spacers in the genomes of starter cultures did not reveal any phage-specific vL_20A or vL_296 among them. This study highlights the biodiversity of** *L. lactis* **phages, their widespread presence in dairy products, and their virulence. However, the virulence of phages is balanced by the presence of a significant number of bacterial strains with different sensitivities to phages in the starter cultures due to the bacterial immune system.**

KEYWORDS **bacteriophage, CRISPR-Cas, cheese making, starter cultures, One Health.**

ABBREVIATIONS **R-M – restriction-modification system; Abi – phage infection abortion system.**

INTRODUCTION

The production of fermented dairy products such as cheeses and yogurts is based on the use of starter cultures. They ferment milk, creating a product with a certain texture, aroma, and taste [1]. However, the lactic acid bacteria used in production are susceptible to bacteriophage infection [2]. Dairy factories represent a specific, isolated ecological niche for the bacteriophages of lactic acid bacteria, because lactobacilli are naturally present in raw milk and artificially introduced into pasteurized milk via bacterial starter cultures [3].

High levels of lactic acid fermentation prevent the development of extraneous and pathogenic microorganisms in milk, which are inactivated during pasteurization or trapped in milk after pasteurization, and also determine the population characteristics of the microbiome of dairy products by increasing acidity and specific antagonism against non-lactic acid bacteria. Phage infection can adversely affect the fermentation and growth of bacterial cultures [1]. If phages attack the starter culture, the fermentation process may slow down or even stop altogether. As a result, there is a risk of developing pathogenic microflora and the emergence of deviations in taste, aroma, and texture [4].

The composition of starter cultures for many fermented dairy products and cheeses includes *Lactococci* (*Lactococcus lactis* sps., *L. cremoris*). Therefore, bacteriophages lysing *Lactococci* are widely used in the dairy industry. Cheesemaking is the most vulnerable from the point of view of phage attacks. This is due to the fact that the mildest milk pasteurization mode is used in cheese production (temperature 72–76°C with exposure of 20–25 s), and part of the bacteriophage population of raw milk is

not destroyed. In addition, the serum formed during production almost always contains significant amounts of virions and is a significant source of bacteriophage spread in dairy factories, which are found in various objects, including production leaven, equipment, sanitary clothing, and exposed body parts of workers [5]. After the report on lactococcal bacteriophages in the 1930s [6] and the following numerous studies of this phenomenon, phagolysis is now considered a constant nuisance that is difficult to eliminate in the dairy industry.

Phage-resistant strains of lactic acid bacteria are selected to protect lactic acid bacteria from bacteriophages, and batches of starter cultures are systematically rotated [7], which points to the pressing need to study the phage resistance and the phagotype of lactococcal collection cultures. The effectiveness in selecting phage-resistant lactococcal cultures largely depends on the composition of the set of phages used and the spectrum of their lytic action. This indicates that systematic research into the phage background of dairy factories is needed. The phage–host interactions in cheese production are also a subject of interest from the perspective of the One Health paradigm, which implies a comprehensive, unified approach aimed at sustainable balance and optimization of human, animal, and their shared environmental health, including the ecosystem of dairy factories.

Bacteriophages are the most common viruses found on Earth. Most free-living bacteria are infected by phages. This is evidenced by the presence of prophages in most bacterial genomes [8, 9]. Bacteria have developed many mechanisms for anti-bacteriophage defense, which can be referred to as the "prokaryotic immune system" [10]. These mechanisms can be further separated into the innate and adaptive "prokaryotic immune systems" [11]. Classic examples of innate immunity include the restriction modification (R-M) [12] and phage infection abortion (Abi) systems [13]. However, many additional innate immune mechanisms have recently been discovered, highlighting the strong selective pressure exerted by phages on microbial communities [14,15].

The CRISPR-Cas system is the only "adaptive" prokaryotic immune system there is. It allows bacteria to incorporate short DNA sequences from phages into a special CRISPR cassette. Upon meeting a phage, transcribed spacers bind to the DNA of the phage and direct its degradation using Cas proteins [16].

In this study, we examined the genomes of two new bacteriophage species isolated during cheese production. We determined the species and the lytic spectra of the phages and analyzed their possible virulence mechanisms and sensitivity to the CRISPR-Cas system in the main starter cultures.

EXPERIMENTAL

Phage isolation and purification

Bacterial strains from the Collection of lactic acid bacteria for cheesemaking and phages were used in this study (All-Russia Research Institute of the Cheese and Butter Industries, V.M. Gorbatov Research Center for Food Systems, Russian Academy of Sciences).

Bacteriophages were isolated from cheese whey samples. The bacteriophage vL_20A was isolated from whey obtained during the manufacturing of semi-hard cheese at the Pereslavl Cheese Factory (Yaroslavl Region, Russia) on January 6, 1985, and spread on a sensitive culture of *L. lactis* subsp. *lactis* 393-8. The bacteriophage vL_296 was isolated from whey obtained during the manufacturing of semi-hard cheese at the Yugovsky Dairy Products Plant (Perm Krai, Russia) on July 6, 2022, and spread on a sensitive culture of *L. lactis* subsp. *lactis* 345-8.

The sensitive culture was grown on a M17 medium containing lactose (HiMedia, India). Serum samples were filtered through a sterile filter with a pore size of 0.45 μm.

The surface seeding method was used to isolate the bacteriophages: 0.1 mL of the *L. lactis* subsp. *lactis* culture was applied on Petri dishes containing the dried solid medium M17 (1.5% agar) in the phase of logarithmic growth, rubbed in with a glass spatula, and left for 10–15 min to absorb moisture into the agar. A drop of filtered serum was then applied on the Petri dish, covered with a lid, and left to rest for 10–15 min at room temperature. Next, the Petri dishes were flipped over and thermostated for 16–18 h at a temperature of 30 ± 1°C. In the presence of lysis zones at the site where serum was applied, a piece of agar from the lysis zone was placed in a test tube containing 3 mL of the M17 medium, thoroughly shaken, and kept for 24 h at 4 ± 2°C to ensure a more complete release of phage particles from the agar. Next, a drop of the medium from the test tube was applied on a fresh lawn of the culture and thermostated for 16–18 h. To obtain a pure bacteriophage, isolated mixtures of bacteriophages were titrated using a two-layer agar method: 0.1 mL of the culture and 0.1 mL of 10-fold dilutions of the phage mixture were introduced into test tubes containing 3 cm^3 of semi-liquid M17 agar (0.6% agar); the suspension was poured into a dish containing a dense medium and incubated for 18–24 h at 30 ± 1°C. Pieces of agar from individual negative colonies (plaques) were used to accumulate phages in a liquid medium contain-

ing a sensitive culture. The cultured bacteriophages were filtered through a sterile filter with a pore size of 0.22 μm and stored at 4 ± 2°C.

Phage host range

The lytic activity of the phages against 35 strains of *L. lactis* subsp. *lactis*, 35 strains of *L. cremoris*, and 35 strains of *L. lactis* subsp. *lactis* biovar. diacetylactis was determined by cultivation on a double-layer agar in culture plates [17]. The sensitivity of lactococci to phages was determined by the presence of a plaque at that spot. The results were divided into two categories: with plaque (+) and without plaque (−).

Transmission electron microscopy

Phage samples were fixed in a 1.5% glutaraldehyde solution in 0.1 M Sorenson phosphate buffer (pH 7.2) for 20 min at room temperature. Subsequently, 5 μL of the fixed sample was transferred to a supporting copper mesh (mesh-400) coated with a nitrocellulose (parlodium) film and kept for 2 min to deposit dispersed particles on the film surface. The contrast in a sample was increased by negative contrast [18, 19]. To achieve this, a drop (2 μL) of a 2% uranyl acetate solution was pipetted onto a drop of a fixed sample located on a grid and held for 4 min. After exposure, the excess solution was removed from the mesh surface using filter paper and placed in a vacuum chamber for final drying at room temperature.

Electron microscopic studies of bacteriophage morphology were conducted using an EM-410 transmission electron microscope (Philips, Netherlands) operated at 40 kV. The images were captured on a Fujicolor C-200 film (FUJIFILM Corporation, Japan).

Phage DNA isolation and sequencing

A precipitate of the solution (4% PEG-6000, 1 M NaCl) was added to the bacterial lysate samples. Incubation was conducted at 4°C for 3 h. After the incubation, the tubes were centrifuged (12,000 *g*) for 15 min at 4°C. The supernatant was selected, and the precipitate was resuspended in 180 μL of PBS. Then, 1.25 μL of Proteinase K (20 mg/mL) was added to the samples and the mixture was incubated at 56°C for 1.5 h without shaking. DNA was isolated using a QIAamp Viral DNA kit (Qiagen, Germany), according to the manufacturer's protocol. The DNA concentrations and quality were evaluated using Nanodrop and Qubit.

The NEBNext Ultra II DNA Library Prep Kit for Illumina (New England BioLabs, USA) was used to create DNA libraries according to the manufacturer's protocol. Sequencing of the obtained libraries was performed on a NovaSeq 6000 high-performance sequencer (Illumina, USA).

Genome analysis

The FastQC 0.12.1 software was used to assess the quality of raw reads. They were then preprocessed using the fastp 0.23.2 tool. Additionally, taxonomic read classification was performed with the standard Kraken 2 database. Reads were assembled using SPAdes 4.0.0. Host genomes were obtained by applying the – isolate flag, while the – metaviral flag was specified for viral genome assembly. The QUAST 5.2.0 tool was used to evaluate the genome assembly quality.

Viral genomes were validated using CheckV 1.0.1, and complete ones were subsequently annotated with Pharokka 1.6.1.

To analyze CRISPR spacers, 562 genomes from the starter cultures of the species *Lacticaseibacillus casei*, *Lacticaseibacillus paracasei*, *Lacticaseibacillus rhamnosus*, *Lactiplantibacillus plantarum*, *Lactobacillus helveticus*, and *Propionibacterium freudenreichii* from the NCBI GenBank database were used [20].

Bacterial genomes were examined for the presence of immune systems using the MinCED 0.4.2 and PADLOC 2.0.0 software tools.

Data accession

The whole-genome sequences of vL-20A and vL_296 were deposited into GenBank under the accession numbers PQ062249 and PQ062250.

RESULTS

Isolation and the morphological characteristics of phages

The phages vL_20A and vL_296 were isolated from subcutaneous serum using the indicator cultures *L. lactis* subsp. *lactis* 393-8 and *L. lactis* subsp. *lactis* 345-8 as host bacteria. Transmission electron microscopy (*Fig. 1*) revealed that phage vL_20A had an icosahedral head with a diameter of 39 ± 3 nm and a tail 107 ± 6 nm long. In turn, phage vL_296 had an icosahedral head with a diameter of 45 ± 4 nm and a tail 125 ± 8 nm long. This morphology is similar to that of *Caudoviricetes*. According to the International Code of Virus Classification and Nomenclature [21], these phages were designated as *L. lactis* phage vL_20A and *L. lactis* phage vL_296 (Viruses; Duplodnaviria; Heunggongvirae; Uroviricota; Caudoviricetes; Ceduovirus; Ceduovirus vL_20A and vL_296).

Host range test analysis

Four strains of *L. cremoris* were lysed by vL_20A; eight, by vL_296 (*Fig. 2*). The lytic activity against *L. cremoris* was 11.8% (4/34) for vL_20A and 22.9% (8/35) for vL_296. The lytic activities against *L. lactis*

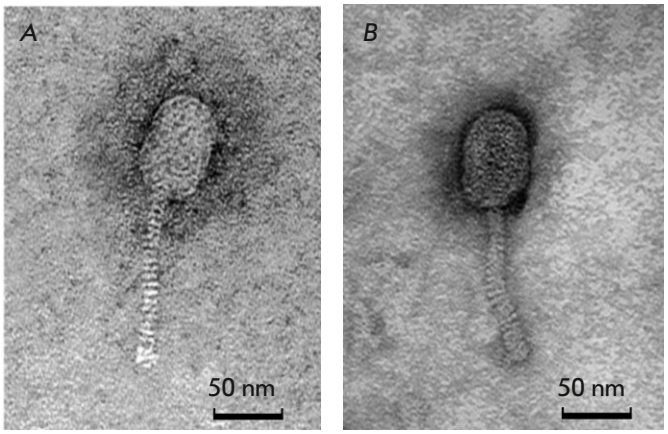

Fig. 1. Transmission electron microscopy images of *Lactococcus lactis* phage vL_20A (*A*) and *Lactococcus lactis* phage vL_296 (*B*)

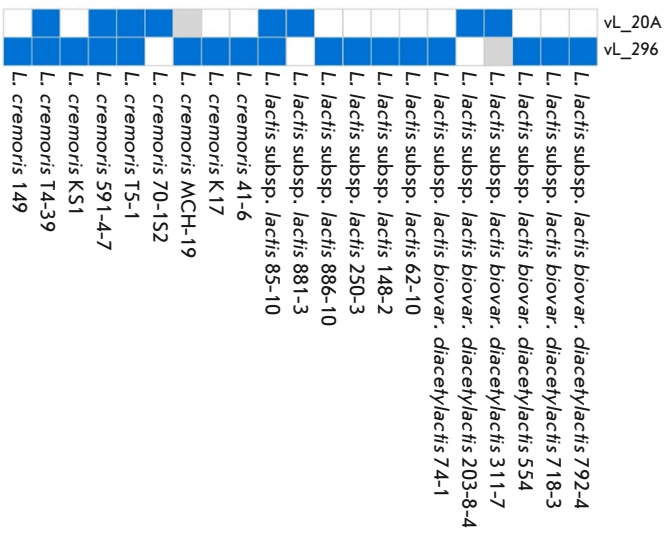

Fig. 2. Host ranges of the vL_20A and vL_296 phages. Blue: presence of plaque; white: absence of plaque; gray: no analysis was conducted

subsp. *lactis* were 5.7% (2/35) and 14.3% (5/35), respectively. For *L. lactis* subsp. *lactis* biovar. diacetylactis, the lytic activities of vL_20A and vL_296 were 5.7% (2/35) and 14.3% (4/28), respectively. It can be noted that vL_20A and vL_296 have unique host ranges. Of the 21 identified host bacteria, only four were common between them (*L. cremoris* T4-39, *L. cremoris* 591-4-7, *L. cremoris* T5-1, and *L. lactis* subsp. *lactis* 85-10).

Genome analysis

The whole-genome sequences of the vL_20A and vL_296 genomes were obtained using the Illumina NovaSeq 6000 platform. Their genomes consisted of linear double-stranded DNA with a length of 21,909 bp (GC 35.75%) and 22,667 bp (GC 35.89%), respectively. Forty-seven open reading frames (ORFs) were predicted for vL_20A and 43 ORFs, for vL_296; of those, 11 ORFs were similar to the genes encoding known functional proteins (*Fig. 3*), while the remaining ORFs encoded putative proteins.

According to functional activity, all the predicted proteins were divided into four groups (*Fig. 3*): DNA metabolism proteins (2 ORF each), packing and head formation proteins (5 ORF each), lysis proteins (two ORFs each), and tail proteins (two ORFs each). The remaining ORFs presumably encoded proteins with unknown activity. Searching across the VFDB and CARD databases revealed no virulence or antibiotic resistance genes.

Comparative genome analysis

The main criterion for identifying new virus species was the identity of the phage genome with other species within the genus by less than 95% [21]. To determine the genomic similarity of vL_20A and vL_296 to other phages, we first performed a BLASTn search across the NCBI database. The genomes of the *L. phage* genus of viruses were obtained from the Nucleotide NCBI database, and the average nucleotide identity (ANI) was evaluated.

Figure 4 shows the ANI for the ten most similar phages among the 254 analyzed genomes. The vL_20A and vL_296 phages were the closest to the *L. phage* bIL67 (ANI 93.3 and 92.6, respectively). Note that the ANI between vL_20A and vL_296 is lower than that of the *L. phage* bIL67 and is 92.5 (*Fig. 5*). It can be assumed that vL_20A and vL_296 represent separate species not described previously.

The ANI between these two phages is only 92.5. When we compare the vL_20A and vL_296 genomes, we find a high number of polymorphisms in the major tail protein, which is crucial for the phage to attach to the host cell (*Fig. 6*). Furthermore, variations in the nucleotide sequence of phages may potentially impact the efficiency of bacterial cell defense mechanisms designed to break down the viral genome.

CRISPR spacer analysis

Bacteria possess a range of defense mechanisms, including the widespread defense system against phages, CRISPR-Cas. CRISPR spacers are involved in adaptive immunity, ensuring complementary binding of RNA to the nucleic acids of foreign elements and

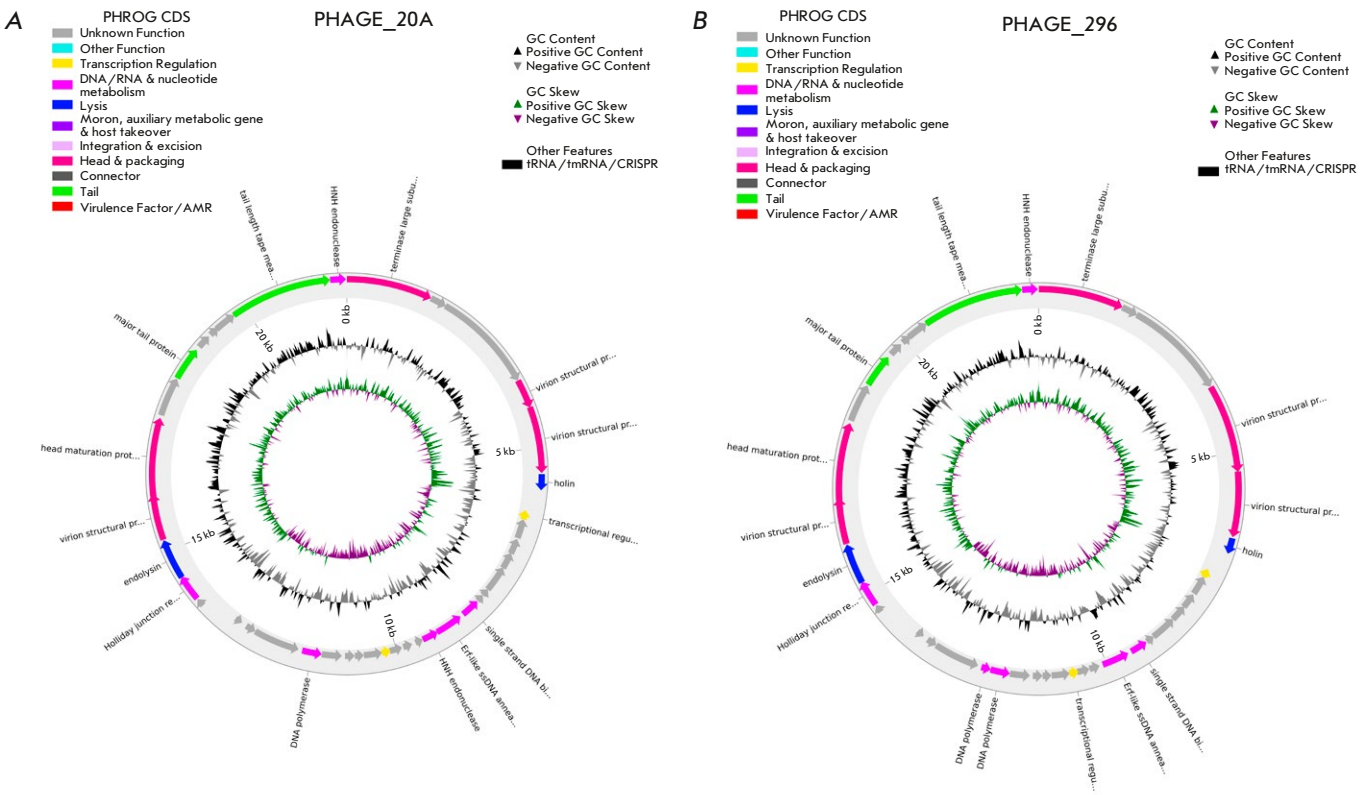

Fig. 3. Visualization of the known functional proteins encoded in the genome of *Lactococcus lactis* phage vL_20A (*A*) and *Lactococcus lactis* phage vL_296 (*B*)

their subsequent destruction by Cas proteins. This system is present in most starter cultures (*Fig.* 7).

We analyzed the presence of spacers specific to the vL_20A and vL_296 phages in the genomes of starter cultures. Among the 562 genomes analyzed, it was impossible to identify any spacers specific to the vL_20A and vL_296 phages. It can be the case that the new phage species we have identified had not been in contact with the analyzed starter cultures for a long time.

DISCUSSION

Phage attacks on the acid-forming microflora of cheeses are extremely dangerous from a product safety perspective, since there is a threat of more intensive development of residual post-pasteurization microflora. To reduce the risk of a release of substandard and dangerous products to consumer health due to phage attacks, it is particularly important to limit the reproduction of phages through the use of multi-strain starter cultures, as well as their systematic rotation and the inclusion of phage-resistant cultures in the starter microflora.

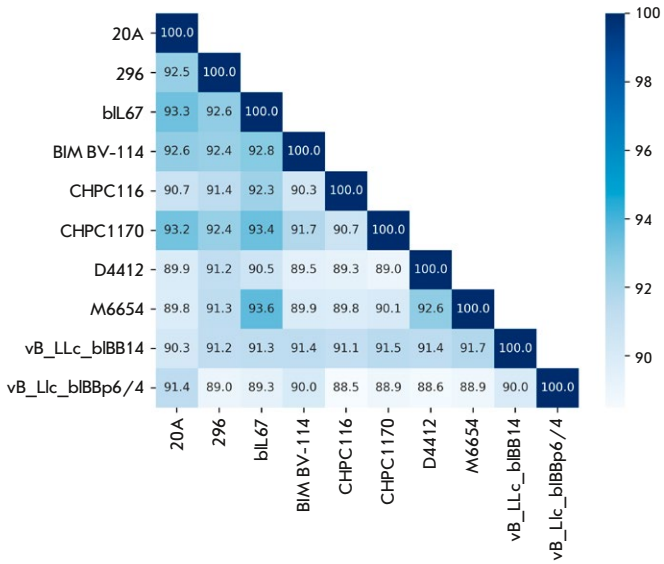

Fig. 4. Heatmap of average nucleotide identity between ten genomes of *Lactococcus lactis* phages

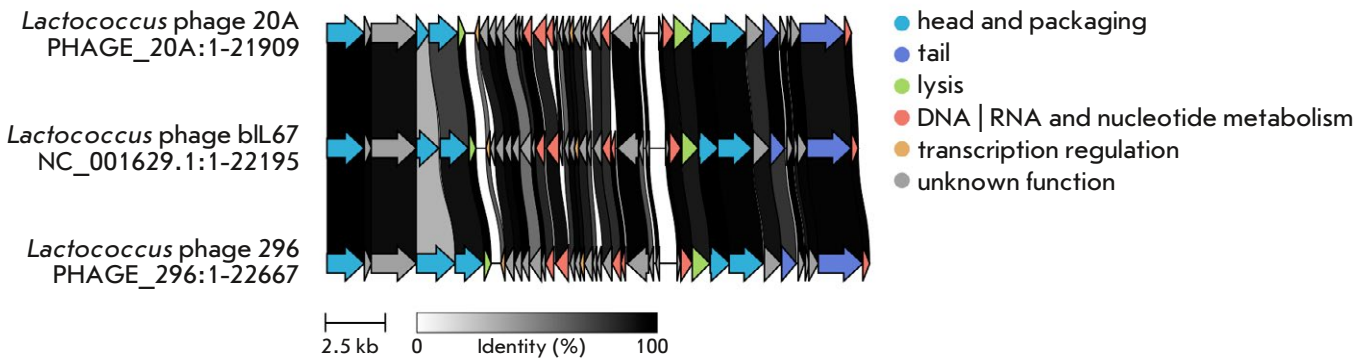

Fig. 5. Schematic diagram of the genome structure of the *Lactococcus lactis phage vL_20A* and *Lactococcus lactis phage vL_296* compared to the most similar *Lactococcus phage bIL67*

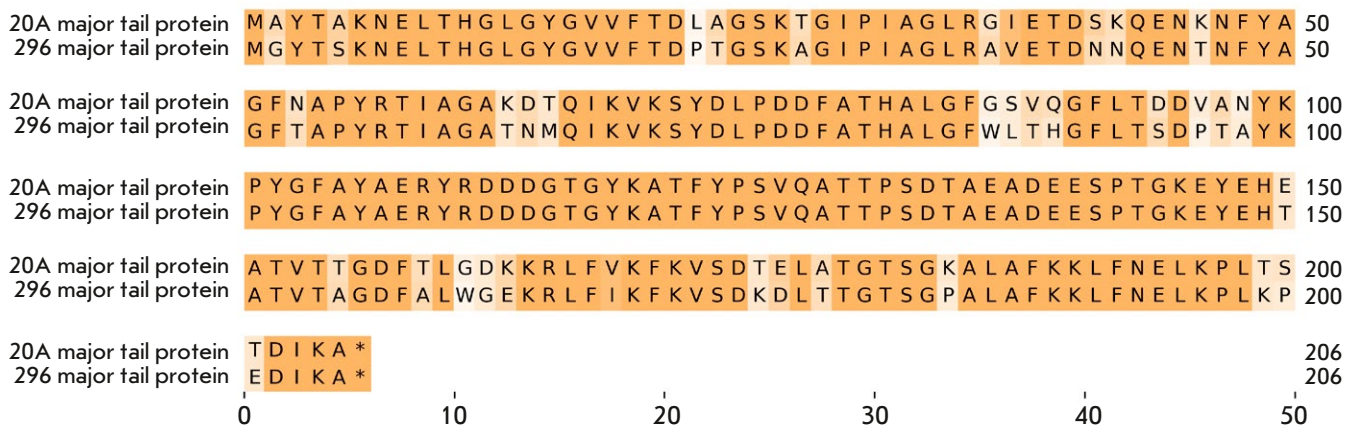

Fig. 6. Alignment of major tail protein DNA sequences in the vL_20A and vL_296 genomes

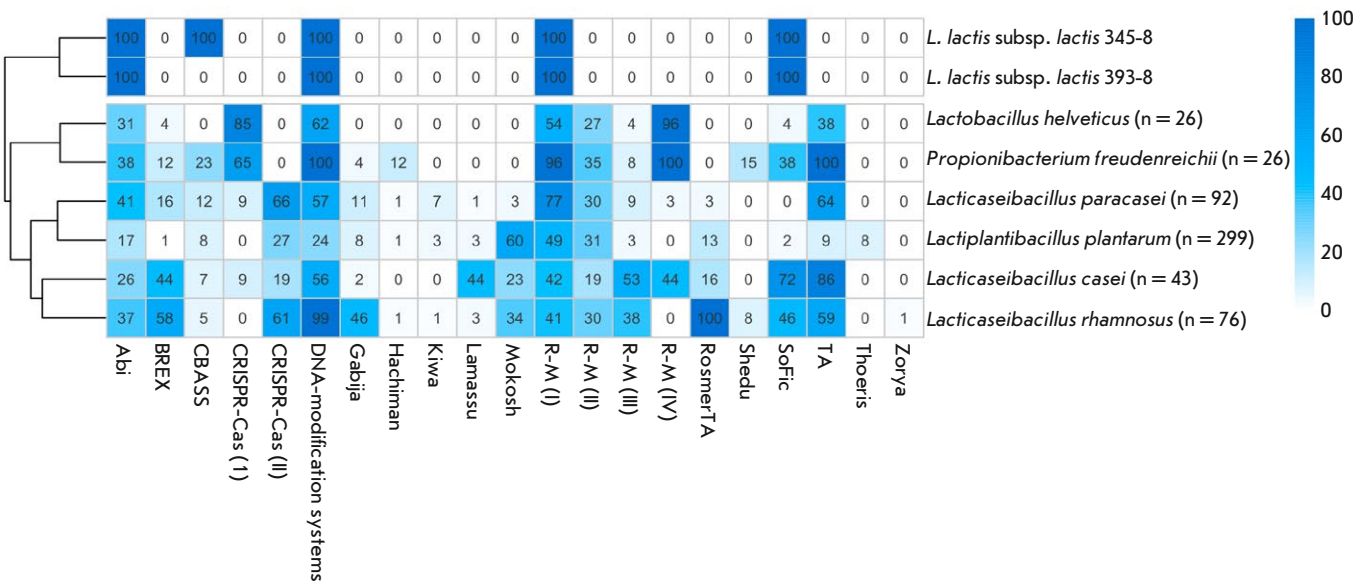

Fig. 7. The immune system of lactic acid bacteria. The cells indicate the frequency of the occurrence (%) of the immunity mechanism in starter cultures. The genus name indicates the number of analyzed genomes

In order to be able to select phage-resistant strains in starter cultures, the diversity and properties of phages capable of infecting starter cultures need to be studied. In particular, the phages described in this paper were isolated from cheese whey with an interval of 37 years and caused problems with the fermentation of raw materials. This indicates that phages and bacterial strains that are sensitive to them continue to exist in starter cultures, as shown in previous studies [22]. Considering that the ANI similarity level for the newly isolated phages was significantly below 95, it is fair to assume that we have described two new phage species for the first time.

The closest representative of the genus for these phages is the species *L. phage* biL67 [23]. We established that the genomes of the new phages *Lactococcus lactis* phage vL_20A and *L. lactis* phage vL_296 are linear double-stranded portions of DNA with lengths of 21,909 and 22,667 bp, respectively. In the genomes, 47 and 43 ORFs can be distinguished for vL_20A and vL_296, of which 11 are similar to the genes encoding known functional proteins.

The lytic spectra of the phages are quite narrow and virtually do not overlap. Only four common strains of the host bacteria could be distinguished: *L. cremoris* T4-39, *L. cremoris* 591-4-7, *L. cremoris* T5-1, and *L. lactis* subsp. *lactis* 85-10. These data differ from the results obtained by Stuer-Lauridsen et al., where most of the studied *L. lactis* phages were able to lyse 10–90% of the strains [24]. This can be attributed to the differences in the sources of the dairy products from which the phages were isolated in these two studies.

The analysis of CRISPR cassettes of starter bacteria failed to identify any spacer specific to the vL_20A and vL_296 phages. It can be assumed that the new phage species we have identified had not been in contact with the analyzed starter cultures for a long time. Nevertheless, CRISPR/Cas systems of types 1 and 2 have been found in the genomes of many of them. This suggests that immunity against these phages may develop when they are encountered.

CONCLUSIONS

Today, we need to move towards sustainable, inclusive, and independent agri-food systems. This can be achieved by regarding the food system as a continuous and interconnected chain, where risks are monitored and assessed at every stage, from raw materials to finished products. In this chain, the phage health of the production environment is the main cause of disrupted sustainability in the production of fermented dairy products.

Our study highlights the biodiversity of phages isolated from cheese whey and confirms their widespread presence in dairy factories and their virulence. However, the presence of bacterial strains with varying degrees of sensitivity to phages in the starter cultures balances this danger through bacterial immunity systems.

The high level of resistance of starter cultures to phage infection may prevent the mass reproduction of phages in multicomponent starter cultures. This explains why phages are found in fermented dairy products without acidification problems. However, the simultaneous presence of various active phages within a single starter culture can sometimes lead to a defective product. Additional research is needed to better understand the ecological role of phages and assess their impact on fermentation. The abundance of bacteriophages in dairy plants infecting starter cultures once again highlights the importance of developing strategies to combat phages in the dairy industry. ●

This work was supported by the Ministry of Science and Higher Education of the Russian Federation for large scientific projects in priority areas of scientific and technological development (Grant No. 075-15-2024-483).

REFERENCES

1. White K., Eraclio G., McDonnell B., Bottacini F., Lugli G.A., Ventura M., Volontè F., Dal Bello F., Mahony J., van Sinderen D. // Appl. Environ. Microbiol. 2024. V. 90. № 3. P. e02152–23.
2. Lahbib-Mansais Y., Mata M., Ritzenthaler P. // Biochimie. 1988. V. 70. № 3. P. 429–435.
3. Kelleher P., Mahony J., Schweinlin K., Neve H., Franz C.M., van Sinderen D. // International Journal of Food Microbiology. 2018. V. 272. P. 29–40.
4. White K., Yu J.-H., Eraclio G., Bello F.D., Nauta A., Mahony J., van Sinderen D. // MRR. 2022. https://www.oaepublish.com/articles/mrr.2021.04.
5. Eller M.R., Dias R.S., De Moraes C.A., De Carvalho A.F., Oliveira L.L., Silva E. a. M., da Silva C.C., De Paula S.O. // Arch Virol. 2012. V. 157. № 12. P. 2265–2272.
6. Whitehead H.R., Cox G.A. // N. Z. J. Dairy Sci. Technol. 1935. V. 16. P. 319–320.
7. Mahony J., McDonnell B., Casey E., van Sinderen D. // Annu Rev. Food Sci. Technol. 2016. V. 7. P. 267–285.
8. Roux S., Hallam S.J., Woyke T., Sullivan M.B. // eLife. 2015. V. 4. P. e08490.
9. Touchon M., Bernheim A., Rocha E.P.C. // The ISME Journal. 2016. V. 10. № 11. P. 2744–2754.

10. Bernheim A., Sorek R. // Nat. Rev. Microbiol. 2020. V. 18. № 2. P. 113–119.
11. Dimitriu T., Szczelkun M.D., Westra E.R. // Current Biology. 2020. V. 30. № 19. P. R1189–R1202.
12. Vasu K., Nagaraja V. // Microbiol. Mol. Biol. Rev. 2013. V. 77. № 1. P. 53–72.
13. Labrie S.J., Moineau S. // J. Bacteriol. 2007. V. 189. № 4. P. 1482–1487.
14. Doron S., Melamed S., Ofir G., Leavitt A., Lopatina A., Keren M., Amitai G., Sorek R. // Science. 2018. V. 359. № 6379. P. eaar4120.
15. Kronheim S., Daniel-Ivad M., Duan Z., Hwang S., Wong A.I., Mantel I., Nodwell J.R., Maxwell K.L. // Nature. 2018. V. 564. № 7735. P. 283–286.
16. Koonin E.V., Makarova K.S. // Phil. Trans. R. Soc. B. 2019. V. 374. № 1772. P. 20180087.
17. Kutter E. In: Bacteriophages / Eds Clokie M.R.J., Kropinski A.M. Totowa, NJ. Humana Press, 2009. P. 141–149.
18. Miller S.E. // J. Elec. Microsc. Tech. 1986. V. 4. № 3. P. 265–301.
19. Wyffels J.T. // Microsc. Microanal. 2001. V. 7. № 1. P. 66.
20. Sayers E.W., Beck J., Bolton E.E., Bourexis D., Brister J.R., Canese K., Comeau D.C., Funk K., Kim S., Klimke W., et al. // Nucleic Acids Research. 2021. V. 49. № D1. P. D10–D17.
21. Adriaenssens E., Brister J.R. // Viruses. 2017. V. 9. № 4. P. 70.
22. Zago M., Scaltriti E., Rossetti L., Guffanti A., Armiento A., Fornasari M.E., Grolli S., Carminati D., Brini E., Pavan P., et al. // Appl. Environ. Microbiol. 2013. V. 79. № 15. P. 4712–4718.
23. Schouler C., Ehrlich S.D., Chopin M.-C. // Microbiology. 1994. V. 140. № 11. P. 3061–3069.
24. Stuer-Lauridsen B., Janzen T., Schnabl J., Johansen E. // Virology. 2003. V. 309. № 1. P. 10–17.

GENERAL RULES

Acta Naturae publishes experimental articles and reviews, as well as articles on topical issues, short reviews, and reports on the subjects of basic and applied life sciences and biotechnology.

The journal *Acta Naturae* is on the list of the leading periodicals of the Higher Attestation Commission of the Russian Ministry of Education and Science. The journal Acta Naturae is indexed in PubMed, Web of Science, Scopus and RCSI databases.

The editors of *Acta Naturae* ask of the authors that they follow certain guidelines listed below. Articles which fail to conform to these guidelines will be rejected without review. The editors will not consider articles whose results have already been published or are being considered by other publications.

The maximum length of a review, together with tables and references, cannot exceed 50,000 characters with spaces (approximately 30 pages, A4 format, 1.5 spacing, Times New Roman font, size 12) and cannot contain more than 16 figures.

Experimental articles should not exceed 30,000 symbols (approximately 15 pages in A4 format, including tables and references). They should contain no more than ten figures.

A short report must include the study's rationale, experimental material, and conclusions. A short report should not exceed 12,000 symbols (5–6 pages in A4 format including no more than 12 references). It should contain no more than three figures.

The manuscript and all necessary files should be uploaded to www.actanaturae.ru:

1) text in Word 2003 for Windows format;
2) the figures in TIFF format;
3) the text of the article and figures in one pdf file;
4) the article's title, the names and initials of the authors, the full name of the organizations, the abstract, keywords, abbreviations, figure captions, and Russian references should be translated to English;
5) the cover letter stating that the submitted manuscript has not been published elsewhere and is not under consideration for publication;
6) the license agreement (the agreement form can be downloaded from the website www.actanaturae.ru).

MANUSCRIPT FORMATTING

The manuscript should be formatted in the following manner:

- Article title. Bold font. The title should not be too long or too short and must be informative. The title should not exceed 100 characters. It should reflect the major result, the essence, and uniqueness of the work, names and initials of the authors.
- The corresponding author, who will also be working with the proofs, should be marked with a footnote *.
- Full name of the scientific organization and its departmental affiliation. If there are two or more scientific organizations involved, they should be linked by digital superscripts with the authors' names. Abstract. The structure of the abstract should be very clear and must reflect the following: it should introduce the reader to the main issue and describe the experimental approach, the possibility of practical use, and the possibility of further research in the field. The average length of an abstract is 20 lines (1,500 characters).
- Keywords (3 – 6). These should include the field of research, methods, experimental subject, and the specifics of the work. List of abbreviations.
- INTRODUCTION
- EXPERIMENTAL PROCEDURES
- RESULTS AND DISCUSSION
- CONCLUSION

  The organizations that funded the work should be listed at the end of this section with grant numbers in parenthesis.
- REFERENCES

  The in-text references should be in brackets, such as [1].

RECOMMENDATIONS ON THE TYPING AND FORMATTING OF THE TEXT

- We recommend the use of Microsoft Word 2003 for Windows text editing software.
- The Times New Roman font should be used. Standard font size is 12.
- The space between the lines is 1.5.
- Using more than one whole space between words is not recommended.
- We do not accept articles with automatic referencing; automatic word hyphenation; or automatic prohibition of hyphenation, listing, automatic indentation, etc.
- We recommend that tables be created using Word software options (Table → Insert Table) or MS Excel. Tables that were created manually (using lots of spaces without boxes) cannot be accepted.
- Initials and last names should always be separated by a whole space; for example, A. A. Ivanov.
- Throughout the text, all dates should appear in the "day.month.year" format, for example 02.05.1991, 26.12.1874, etc.
- There should be no periods after the title of the article, the authors' names, headings and subheadings, figure captions, units (s – second, g – gram, min – minute, h – hour, d – day, deg – degree).
- Periods should be used after footnotes (including those in tables), table comments, abstracts, and abbreviations (mon. – months, y. – years, m. temp. – melting temperature); however, they should not be used in subscripted indexes (T_m – melting temperature; $T_{p.t}$ – temperature of phase transition). One exception is mln – million, which should be used without a period.
- Decimal numbers should always contain a period and not a comma (0.25 and not 0,25).
- The hyphen ("-") is surrounded by two whole spaces, while the "minus," "interval," or "chemical bond" symbols do not require a space.
- The only symbol used for multiplication is "×"; the "×" symbol can only be used if it has a number to its

right. The "·" symbol is used for denoting complex compounds in chemical formulas and also noncovalent complexes (such as DNA·RNA, etc.).
- Formulas must use the letter of the Latin and Greek alphabets.
- Latin genera and species' names should be in italics, while the taxa of higher orders should be in regular font.
- Gene names (except for yeast genes) should be italicized, while names of proteins should be in regular font.
- Names of nucleotides (A, T, G, C, U), amino acids (Arg, Ile, Val, etc.), and phosphonucleotides (ATP, AMP, etc.) should be written with Latin letters in regular font.
- Numeration of bases in nucleic acids and amino acid residues should not be hyphenated (T34, Ala89).
- When choosing units of measurement, SI units are to be used.
- Molecular mass should be in Daltons (Da, KDa, MDa).
- The number of nucleotide pairs should be abbreviated (bp, kbp).
- The number of amino acids should be abbreviated to aa.
- Biochemical terms, such as the names of enzymes, should conform to IUPAC standards.
- The number of term and name abbreviations in the text should be kept to a minimum.
- Repeating the same data in the text, tables, and graphs is not allowed.

GUIDENESS FOR ILLUSTRATIONS

- Figures should be supplied in separate files. Only TIFF is accepted.
- Figures should have a resolution of no less than 300 dpi for color and half-tone images and no less than 600 dpi.
- Files should not have any additional layers.

REVIEW AND PREPARATION OF THE MANUSCRIPT FOR PRINT AND PUBLICATION

Articles are published on a first-come, first-served basis. The members of the editorial board have the right to recommend the expedited publishing of articles which are deemed to be a priority and have received good reviews.

Articles which have been received by the editorial board are assessed by the board members and then sent for external review, if needed. The choice of reviewers is up to the editorial board. The manuscript is sent on to reviewers who are experts in this field of research, and the editorial board makes its decisions based on the reviews of these experts. The article may be accepted as is, sent back for improvements, or rejected.

The editorial board can decide to reject an article if it does not conform to the guidelines set above.

The return of an article to the authors for improvement does not mean that the article has been accepted for publication. After the revised text has been received, a decision is made by the editorial board. The author must return the improved text, together with the responses to all comments. The date of acceptance is the day on which the final version of the article was received by the publisher.

A revised manuscript must be sent back to the publisher a week after the authors have received the comments; if not, the article is considered a resubmission.

E-mail is used at all the stages of communication between the author, editors, publishers, and reviewers, so it is of vital importance that the authors monitor the address that they list in the article and inform the publisher of any changes in due time.

After the layout for the relevant issue of the journal is ready, the publisher sends out PDF files to the authors for a final review.

Changes other than simple corrections in the text, figures, or tables are not allowed at the final review stage. If this is necessary, the issue is resolved by the editorial board.

FORMAT OF REFERENCES

The journal uses a numeric reference system, which means that references are denoted as numbers in the text (in brackets) which refer to the number in the reference list.

For books: the last name and initials of the author, full title of the book, location of publisher, publisher, year in which the work was published, and the volume or issue and the number of pages in the book.

For periodicals: the last name and initials of the author, title of the journal, year in which the work was published, volume, issue, first and last page of the article, doi. Must specify the name of the first 10 authors. Ross M.T., Grafham D.V., Coffey A.J., Scherer S., McLay K., Muzny D., Platzer M., Howell G.R., Burrows C., Bird C.P., et al. // Nature. 2005. V. 434. № 7031. P. 325–337. doi: 10.1038/nature03440.

References to books which have Russian translations should be accompanied with references to the original material listing the required data.

References to doctoral thesis abstracts must include the last name and initials of the author, the title of the thesis, the location in which the work was performed, and the year of completion.

References to patents must include the last names and initials of the authors, the type of the patent document (the author's rights or patent), the patent number, the name of the country that issued the document, the international invention classification index, and the year of patent issue.

The list of references should be on a separate page. The tables should be on a separate page, and figure captions should also be on a separate page.

The following e-mail addresses can be used to contact the editorial staff: actanaturae@gmail.com, tel.: (495) 727-38-60.